UNIVERSITY OF LIVERPOOL

Oxide Structure Prediction and Synthesis

Thesis submitted in accordance with the requirements of the University of Liverpool for the degree of Doctor in Philosophy by:

Christopher Michael Collins

Supervised by

Professor M. J. Rosseinsky

Dr. G. Darling

Abstract

Abstract

Introduction: The focus of this chapter is to introduce the perovskite structure, beginning from the ideal cubit perovskite with the ABX_3 formula unit. The concept of introducing long range ordering into the material are then presented along with the driving forces behind the extension of the structure. Possible magnetic ordering and solid solutions of perovskites are then presented. This is followed by the introduction of how theoretical chemistry can provide useful information to investigations and begin to predict how new materials can be made and is followed by a summary of the techniques commonly used.

Methods: This chapter introduces the experimental methods used within this thesis, along with a description of the diffraction techniques used in the characterisation of oxide materials; including x-ray and neutron diffraction, iodometric titrations and the basic concepts behind Mössbauer spectroscopy. The second part to the chapter provides details on density functional theory (DFT) and force field (FF) calculations that are used throughout the thesis for the prediction of new materials.

Chapter 3: Details the use of a series of calculations with DFT on the chemical substitution in the $YBa_2Fe_{3-x}M_xO_8$ (where M = Co, Ni and Mn), where the calculations are first tested on doping with Co, where it has been previously been experimentally reported. Calculations for un-reported substitutions a new compound is predicted. Synthetic investigations are then undertaken across the series, and a new material found where DFT calculations predict a new compound. Characterisation of the new material reveals that it has a crystal structure in good agreement with the structure predicted by DFT.

Chapter 4: Computationally investigates doping in the $YBa_2Ca_2Fe_{5-x}M_xO_{13}$ (M = Co, Cu, Mn, Ni, Ti and Zn) solid oxide fuel cell cathode material using DFT. The results from the calculations predict stable doping for Cu and Co, with small doping levels favoured for M = Ni and Zn, with M = Mn yielding results predicting marginal doping and doping not favoured at all for M = Ti.

Chapter 5: When D. Hodgeman was experimentally investigating Cu doping of the $YBa_2Ca_2Fe_5O_{13}$ material an unknown perovskite superstructure was observed by x-ray diffraction. This chapter then focuses on the development of the Extended Module Materials Assembly (EMMA) method. The method is validated be correctly computing the correct crystal structure for the $YBa_2Ca_2Fe_5O_{13}$ perovskite and is used to predict the structure for the new $Y_{2.24}Ba_{2.28}Ca_{3.48}Fe_{7.44}Cu_{0.56}O_{21}$perovskite. The crystal structure predicted by EMMA is then used as the basis for the experimental refinement of the structure and the structures found to be in good agreement.

Acknowledgements

Acknowledgements

First and foremost I would like to thank my supervisors Prof. Matt Rosseinsky and Dr. George Darling, for all their guidance (and patience!) during the last four years along with their constant encouragement to learn new methods and techniques. I would also like to thank the rest of the research group with whom I have worked, notably Dr. Matthew Dyer for his never-ending patience with teaching me to use density functional theory, Dr. Antoine Demont and Dr. Phil Chater for their help with tutoring me in my synthetic chemistry and materials analysis and Dr. John Claridge for his seemingly infinite wisdom! I would also like to thank Dr. George Darling for getting computer time on the HECToR super computer through the Materials Chemistry Consortium (MCC), time which contributed enormously to the success of the calculations presented within chapters 4 and 5 of this thesis.

I would like to thank everyone around the surface science research centre and the MJR research group for making the time I have spent doing my PhD an enjoyable experience, especially all of those that have made cake over the years, even the 'experimental' cake – Olive oil and cake do not mix! and the 'rock' muffins!.

Outside of the workplace, I need to thank all of my friends and family for their kind support without whom I would not have made it through with any sanity remaining, along with their perseverance in telling me "It'll all be ok". Last but not least, a special mention has to go to Fiona for putting up with me all of these years, introducing me to radio comedy and finally taking the time to proof read this thesis, oh and cake, defiantly cake! I'll leave it here with arguably the most common phrase used in my general direction during my PhD:

"Don't Panic!" – Hitchhikers Guide to the Galaxy.

Acknowledgements

Contents

Chapter 1. Introduction

1.1 Concerning Perovskites

1.1.1 Cubic Perovskites

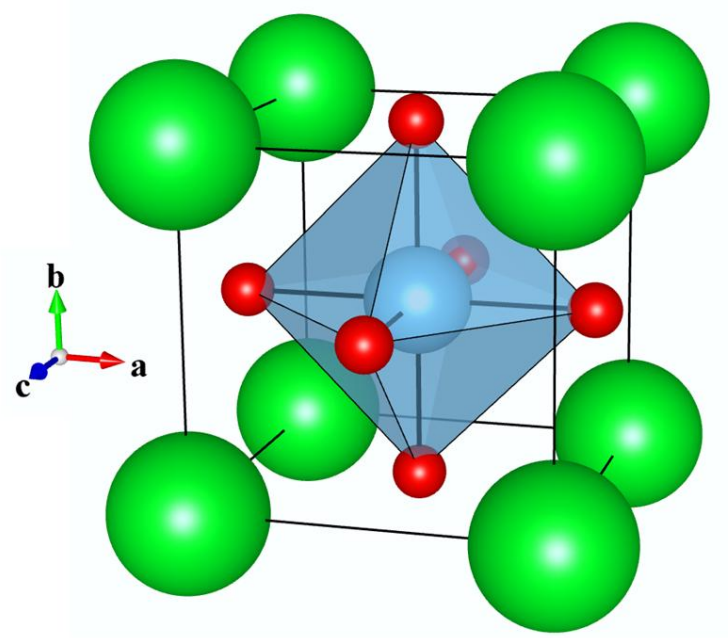

Figure 1 Structure of the cubic ABX_3 perovskite, with this example being for $SrTiO_3$[1], the A-site occupied by Sr (green) is coordinated to 12 oxygen atoms, the B-site is occupied by Ti (blue) and is in a 6 coordinate octahedral site and the unit cell also contains 3 oxygen atoms (red). In this thesis, to aid illustration of structures, polyhedra are drawn around each of the B-site cations with their coordination to oxygen anions.

Perovskites have the general formula unit ABX_3, where A and B represent different cation species that occupy different crystallographic sites and X is an anion species commonly oxygen, although other anion species are known[2]. The ideal crystal structure for perovskites is cubic, with $Pm\bar{3}m$ space group symmetry. In the ideal perovskite structure (Figure 1) there are three crystallographic sites in the asymmetric unit cell, the larger of the two cations, labelled A, is located at fractional (0, 0, 0) and is coordinated to 12 anion species. The smaller B cation is

located at (0.5, 0.5, 0.5) and occupies a six coordinate octahedral site, the third is site occupied by the anion species at (0.5, 0.5, 0), with this site having a multiplicity of three. With a typical lattice parameter for a cubic perovskite, referred to as a_p in the example of $SrTiO_3$, a_p is equal to 3.907 Å[1].

1.1.2 Extended Perovskites

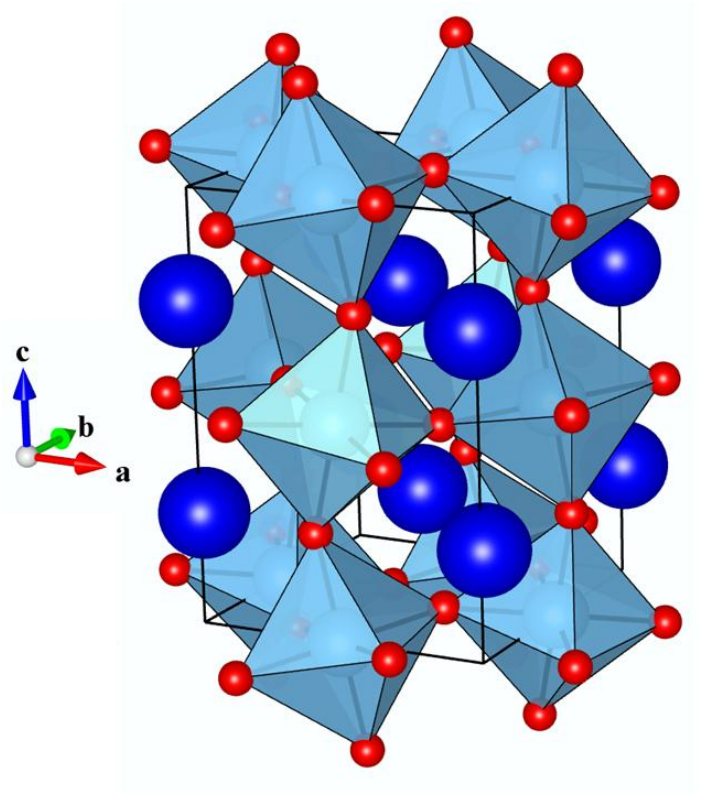

Figure 2 Orthorhombic crystal structure of $CaTiO_3$[3] where Ca (blue) occupies the 12 coordinate A-site, Ti (cyan) occupies the octahedral six coordinate site, with oxygens illustrated in red.

In the ideal perovskite structure, there is a relationship between the radii of the A, B and O cations and anions, which can be defined as follows[4]:

$$r_A + r_O = \sqrt{2}\,(r_B + r_O) \quad \textbf{(1.1)}$$

Where r_A indicates the atomic radius of the A cation, r_B indicates the B cation radius and r_O indicates the radius of an oxygen anion. For a given composition, it is therefore possible to form a ratio between the two sides of equation (1.1), referred to as the tolerance factor[4], *t*:

$$t = \frac{(r_A + r_O)}{\sqrt{2}\,(r_B + r_O)} \quad \textbf{(1.2)}$$

Perovskite type materials are known to have tolerance factors between 0.8 and 1.1, with the ideal perovskite structure having a value of 1. From a practical perspective, when deciding on a perovskite synthesis, the tolerance factor should be taken into account, as *t* moves further away from 1, the composition is less likely to crystallise into a perovskite related structure. With intermediate shifts away from the ideal tolerance factors, perovskite structures may still form albeit with a distorted and or structure extended beyond the basic cubic perovskite cell.

An example of extending the perovskite structure without altering the stoichiometry is by choice of the cations species, by selecting A and B site cations with a large difference in ionic radius, polyhedral tilting can be induced with examples reported for a number of different ABO_3 compositions[3, 5-7], including $CaTiO_3$ perovskite (Figure 2). In the $CaTiO_3$ structure, tilting of the B-site octahedra results in a unit cell expanded relative to the cubic unit cell of r45˚($\sqrt{2}a_p \times \sqrt{2}a_p \times 2a_p$) and results in a change to the observed space group to the orthorhombic *Pbnm*.

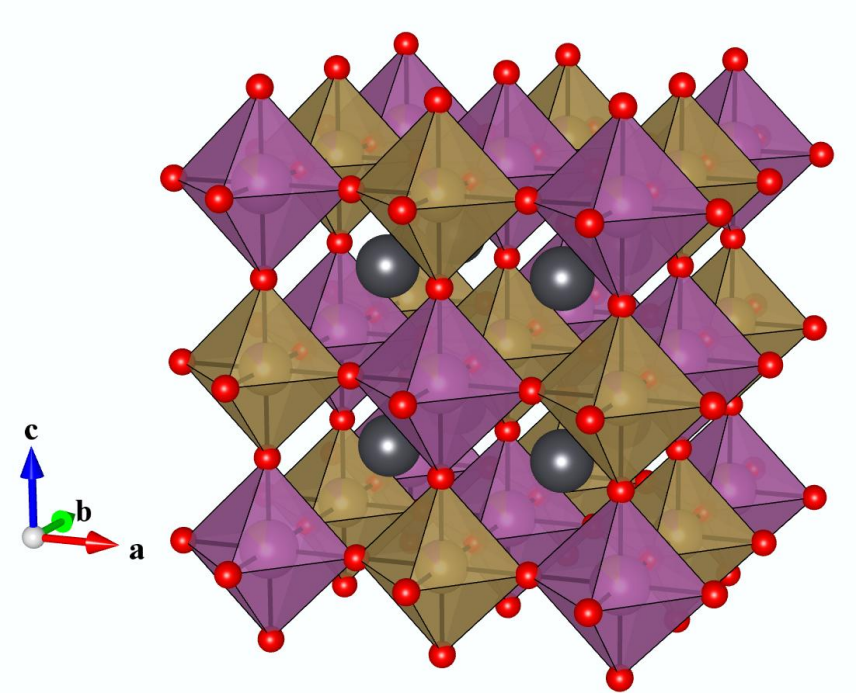

Figure 3 Crystal structure of $Pb(Sc_{0.5}Ta_{0.5})O_3$ perovskite[8] where Sc (purple) and Ta (brown) occupy the 6 coordinate octahedral B-sites and Pb (dark grey) occupy the 12 coordinate A sites, with oxygen atoms shown in red.

Extension of the perovskite structure can also be achieved by long range ordering between different cation species, as exemplified by the $Pb(Sc_{0.5}Ta_{0.5})O_3$ structure (Figure 3). The structure of $Pb(Sc_{0.5}Ta_{0.5})O_3$ is doubled in each of the crystallographic directions and the symmetry changes to the face centred cubic $Fm\bar{3}m$ space group. The doubling of the unit cell is caused by cation ordering between Ta and Sc cations, and results in an overall unit cell of ($2a_p \times 2a_p \times 2a_p$) relative to the cubic perovskite.

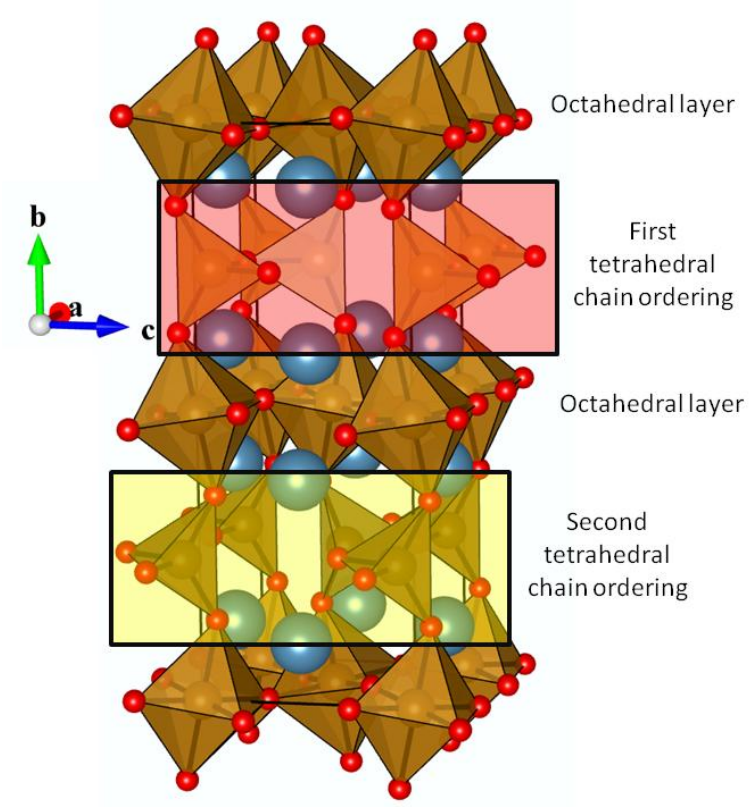

Figure 4 Crystal structure of $Ca_2Fe_2O_5$ brownmillerite[9, 10], derived from the perovskite structure, with the perovskite superstructure driven by ordering of oxygen vacancies. Ca (blue) occupies 10 coordinate A-sites and Fe (brown) occupies both four coordinate tetrahedral and six coordinate octahedral B-sites, with oxygen atoms illustrated in red.

Long range ordering in perovskites can also be induced by the reduction of the oxygen content, with the resulting oxygen vacancies becoming ordered. Experimentally this can be achieved by chemically controlling the cation composition, as is the case for $Ca_2Fe_2O_5$, where the charge states of the cation species equate to the loss of 0.5 oxygen per ABO_3 perovskite formula unit[10, 11]. Experimentally obtaining a crystal structure with oxygen vacancy ordering can also require the control of the oxygen content during synthesis (described in Chapter 3) in order to obtain a specific value required. The structure of $Ca_2Fe_2O_5$ (Figure 4), is related to brownmillerite, although with the space group *Pnma* rather than *Ibm2* as reported for Ca_2FeAlO_5 brownmillerite[11]. Long range order is induced by the ordering of oxygen vacancies every second

perovskite layer resulting in the polyhedral stacking of octahedral (O_h) followed by a tetrahedral (T_d) layer. Due to the alternating direction of tetrahedra between T_d layers the lattice parameter is quadrupled in the stacking direction, as with the $CaTiO_3$ structure discussed above, there is a rotation in the ab plane, resulting in a unit cell expansion by r45˚ ($\sqrt{2}a_p \times \sqrt{2}a_p \times 4a_p$) relative to the cubic perovskite cell.

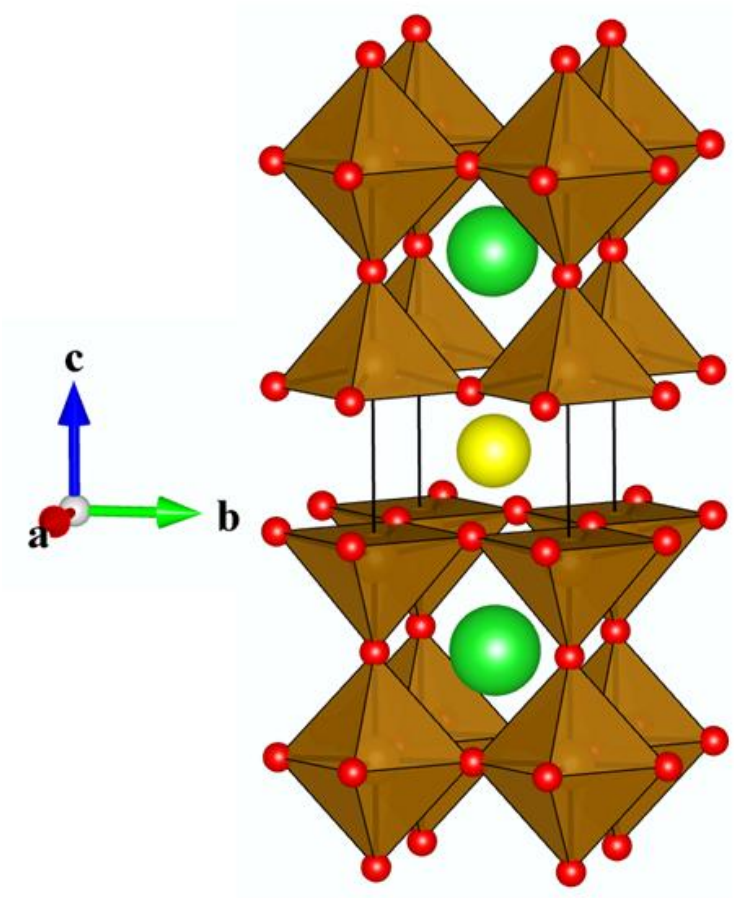

Figure 5 Crystal structure of $YBa_2Fe_3O_8$[12], with long range ordering induced by cation and vacancy ordering. Y (yellow) occupies an eight coordinate A-site, Ba (green) occupies a 12 coordinate A-site and Fe (brown) occupies both a 5 coordinate square pyramidal B-site and 6 coordinate octahedral B-site with oxygen atoms shown in red.

Long range ordering in perovskites can also be induced by a combination of effects, one example of this is in the $YBa_2Fe_3O_8$ structure[13], (Figure 5), related to the $YBa_2Cu_3O_{6.5+\delta}$ superconductor[14]. Ordering in$YBa_2Fe_3O_8$ results from the ordering of oxygen vacancies, with one oxygen missing for every three perovskite units (i.e. missing one oxygen from the $A_3B_3O_9$ formula unit), with all of the vacancies ordered within one layer in the unit cell. The ordered vacancies give rise to two distinct A-sites in the structure, being 8 and 12 coordinate, the smaller of the two A-sites, Y occupies the 8 coordinate sites and the large Ba occupies the 12 coordinate site, with Fe occupying both of the resulting B-sites, with one octahedral and two square pyramidal sites per unit cell, this ordering results in a perovskite supercell of ($a_p \times a_p \times 3a_p$) and *P4/mmm* space group symmetry and referred to as a $3a_p$ structure.

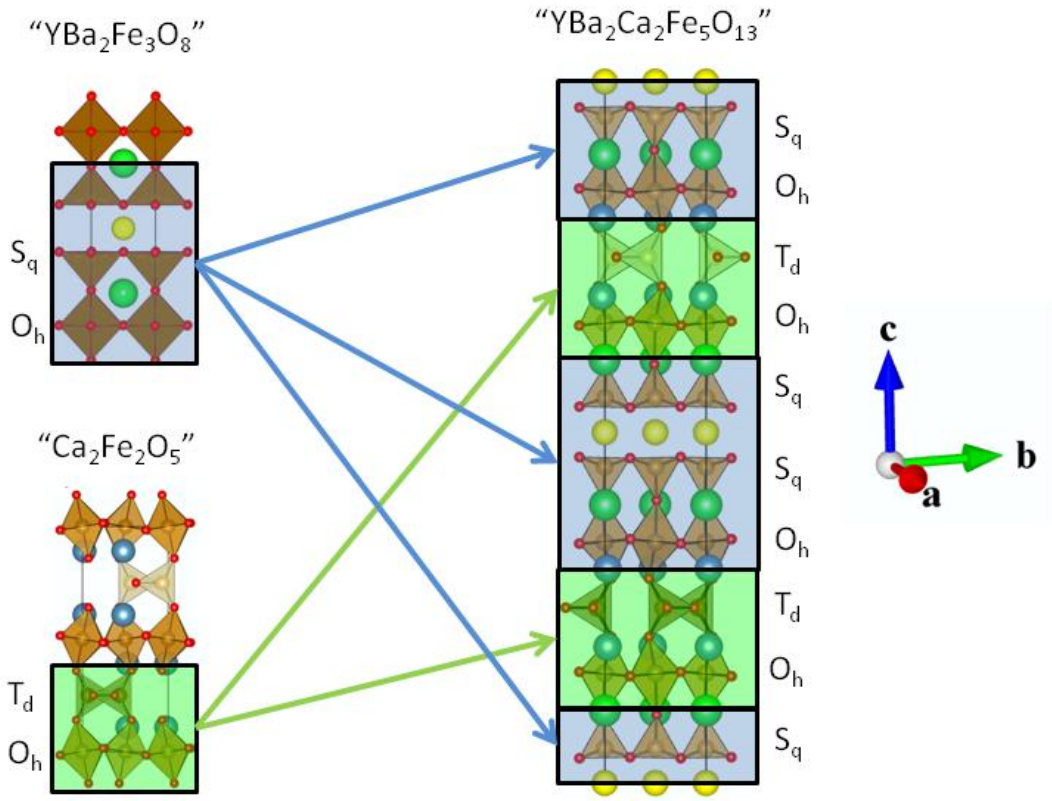

Figure 6 Idealised $YBa_2Ca_2Fe_5O_{13}$ crystal structure[15] (right), thought of as composed of blocks of the $YBa_2Fe_3O_8$ and $Ca_2Fe_2O_5$ structures[11, 13], where the structural motif of each structure is represented by blue and green blocks respectivly. Atoms colours are as follows: yttrium (yellow), barium (green), calcium (blue), iron (brown) oxygen (red).

Larger structures are possible from combinations of structural ordering as observed in the $Y_{1.1}Ba_{1.5}Ca_{2.3}Fe_5O_{13}$ material[15] first reported with the composition; $Ba_{0.81}Ca_{0.78}Nd_{0.91}Fe_{2.5}O_{6.43}$[16], having a perovskite superstructure of r45° ($\sqrt{2}a_p \times \sqrt{2}a_p \times 10a_p$), illustrated in Figure 6. Long range ordering is induced by a combination of cation ordering and vacancy ordering. This structure combines features from the $Ca_2Fe_2O_5$ (Figure 4) and $YBa_2Fe_3O_8$ (Figure 5) and structures, with oxygen vacancies causing in the formation of octahedral, square pyramidal and tetrahedral B-sites in the $10a_p$ (all occupied by Fe). Ordered oxygen vacancies also result in the

creation of three different cation sites, being 8, 10 and 12 coordinate and primarily occupied by Y, Ca and Ba respectively (Figure 6)

1.1.3 Magnetic ordering

Perovskites often containing transition metals on the B-site, can possess unpaired electrons which can lead to magnetic moments in the structure. Magnetic ordering between B-sites in perovskites has become an important consideration when performing *ab-inito* calculations in order to calculate accurate energies when unpaired electrons are present[17]. Spin polarisation in computational methods can be required when unpaired electrons are present (and therefore possibly magnetic structures) due to interaction energies being computed differently depending on whether or not spin polarisation is included[18]. Since all of the perovskites studied in this thesis contain transition metals on the B-sites magnetic ordering is relevant here to all of the systems here. Below is an overview of the types of magnetic states for solid systems relevant to the systems covered in this thesis.

All magnetic structures will be discussed in terms of a collinear model, i.e. spin moments are aligned along one crystallographic axis, being able to 'point' either way along the axis (denoted as + or – assigned to the magnetic moment). It should be noted for completion that other, non-collinear magnetic orderings are known to exist where off axis moments are reported and often result in large complex magnetic structures which are beyond the scope of the systems studied in this thesis[19].

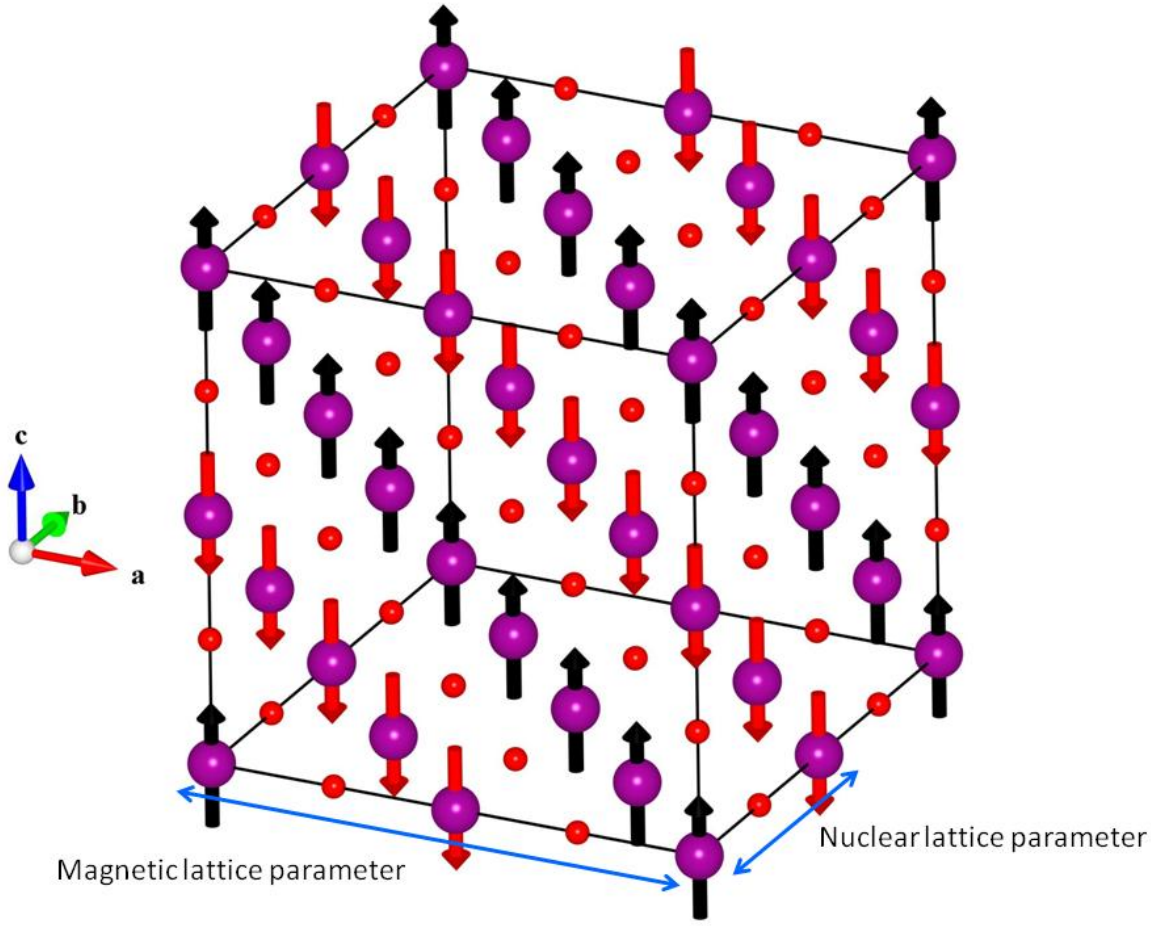

Figure 7 Reported magnetic structure of MnO, where the magnetic unit cell has a lattice parameter twice that of the nuclear structure[20], Manganese atoms coloured in purple, oxygen in red, with red and black representing differing spins.

Magnetic ordering in structure can result in an expansion of the nuclear unit cell when the spin structure is also considered. Experimentally, magnetic structures can lead to two unit cells being reported for the same material (example for MnO given in Figure 7[20]); One unit cell containing only the nuclear structure and a second larger cell including the magnetic structure, with only the nuclear or both structures being observable depending on the method of structural analysis (see Chapter 2).

Magnetic ordering in a system applies across a temperature range from 0 K upwards. At a certain temperature (material specific), magnetic coupling will break down, while the system still contains magnetic moments, there will be no overall magnetic ordering (known as a paramagnetic state), or in some cases different magnetic orderings can occur in different temperature regions. The temperature at which magnetic ordering breaks down is known as the Néel temperature (T_N). In the paramagnetic state, each of the species with unpaired electrons possess a magnetic moment, but their spin states are not coupled and therefore are not ordered in the absence of an external magnetic field and so there is no overall magnetic moment in the system[21].

For the systems studied in this thesis, four different forms of collinear magnetic ordering were considered. The first ordering, ferromagnetic (Figure 8a), all of the spin moments in the unit cell are aligned in the same direction, resulting in an overall magnetic moment in the unit cell[19]. For antiferromagnetic ordering, the magnetic unit cell contains an equal number of up and down spins (Figure 8b-d)[19] and therefore no overall magnetic moment in the unit cell. There are three different forms of antiferromagnetic ordering that are applicable to the perovskite systems in this work, which are described below.

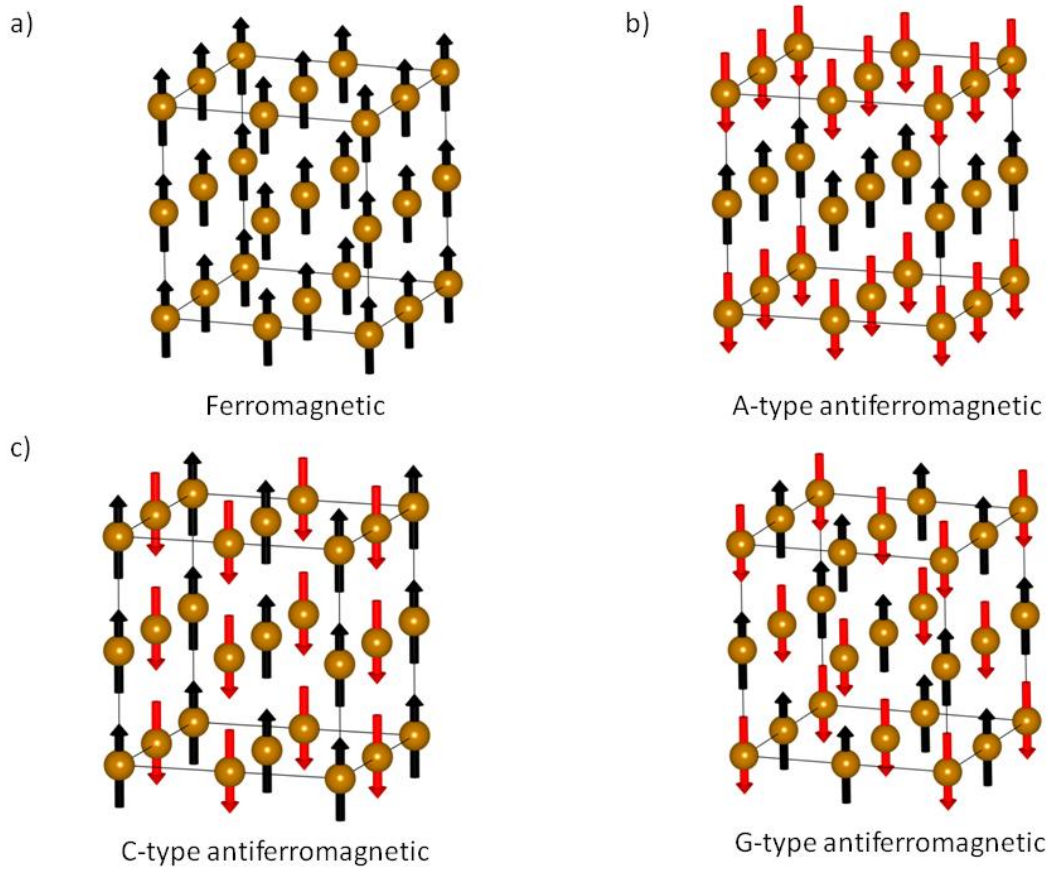

Figure 8 Magnetic orderings discussed within this thesis, on a face centred unit cell containing 8 magnetic atoms in the asymmetric cell[19], for clarity the symmetry equivalent atoms at the edges of the unit cell have been removed. a) Ferromagnetic, all of the spin moments are aligned in the same direction. b) A-type antiferromagnetic, spins are arranged in ferromagnetic sheets in the [100] plane. c) C-type antiferromagnetic, ferromagnetic sheets are aligned in the [110] direction. d) G-type antiferromagnetic, every atom has nearest neighbours with spin moments anti-aligned. The brown spheres represent arbitrary magnetic atoms.

The first type of antiferromagnetic ordering, A-type (Figure 8b), the magnetic atoms are arranged into sheets of ferromagnetism, with the spin direction changing between sheets. The ferromagnetic sheets are arranged in one plane of the unit cell (e.g. [100]). Resulting from A-type antiferromagnetic ordering, each magnetic atom has four nearest neighbours with the same spin direction (in plane) and two of opposite spin (above and below the plane).

The second type of antiferromagnetic ordering, C-type (Figure 8c), sheets of ferromagnetic ordering are observed in a diagonal crystallographic plane (e.g. [110]), with spin direction alternating between sheets. In systems with C-type antiferromagnetic ordering, each atom has four nearest neighbours with opposite spin directions (in plane with the atom) and two nearest neighbours with the same spin direction (above and below the plane).

The third type of antiferromagnetic ordering, G-type (Figure 8d), results in sheets of ferromagnetism that intersect all of the crystallographic planes (e.g. the [111] direction). G-type antiferromagnetic ordering results in magnetic atoms that have all nearest neighbours with opposite spin moments. G-type antiferromagnetic ordering is widely known in Fe containing perovskites, including all of the systems studied in this thesis[12, 15, 22].

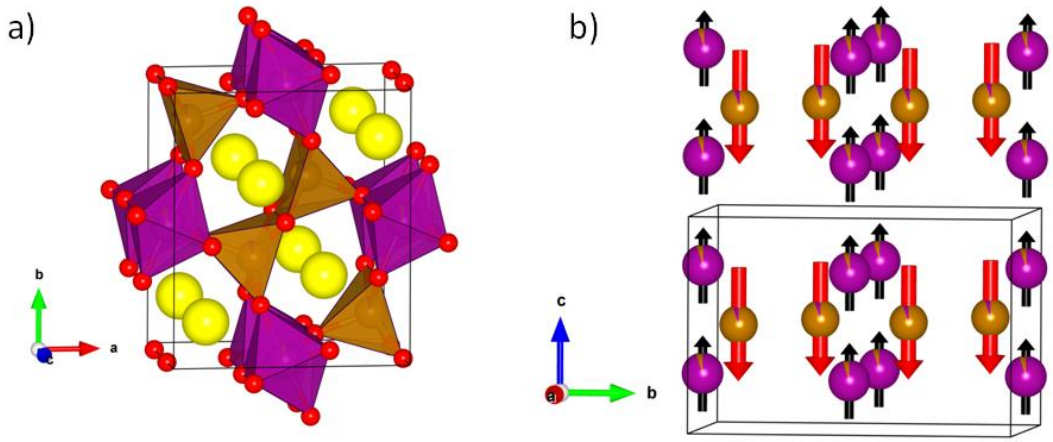

Figure 9 a) Nuclear structure of ferrimagnetic $YFeMnO_5$[23] and b) the magnetic structure of $YFeMnO_5$, with the Fe atoms having a larger magnetic moment then the Mn atoms[23], represented by the black and red arrows with the O and Y atoms omitted for clarity, colours as follows; Fe (brown), Mn (purple), O (red) and Y (yellow).

An intermediate state is known between ferro and anitferromagnetic ordering in oxide materials[23], called ferrimagnetism, with an example being the $YFeMnO_5$ (Figure 9). For a ferrimagnetic structure, magnetic spin directions are arranged as for an antiferromagnetic system, with the exception that the magnitude of the spin in one direction exceeds that of the other. The imbalance balance between the magnitudes of the magnetic moments leads to an overall magnetic moment in the unit cell, although the total magnetic moment is likely to be less than that observed for a pure ferromagnet.

1.1.4 Phase Diagrams and solid solutions

When studying systems with multiple compositions, it is often convenient to map them out onto a phase diagram so as to be able to efficiently assess ranges of experimental conditions or stoichiometries and determine regions where single or multiple phases are observed to exist (Figure 10).

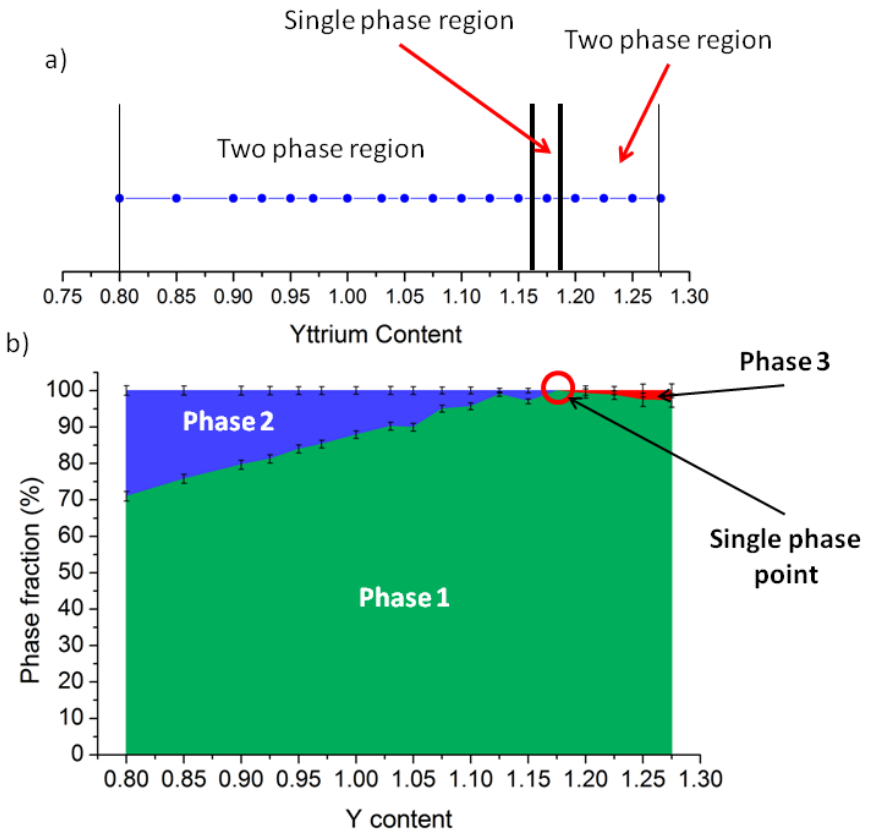

Figure 10 Phase diagrams from range of Y content in the $Y_xBa_{3-x}Fe_2MnO_8$ adapted from chapter 3 a) Representation from only the composition marking out regions according to the number of phases observed. b) Phase diagram representation with fractional quantities of each phase as a function of the Y content, with phase fractions obtained from powder diffraction data.

The example phase diagram shown in Figure 10a is for a simple phase diagram, marking out the number of observed phases against the changing yttrium content. Figure 10b shows an example

of where phase diagrams can be plotted in multiple dimensions, with the fraction of each phase as a function of yttrium content in the sample, where the system reaches an equilibrium between phases at each composition, with only a single point on the diagram favouring a single phase. Although in principle any number of additional dimensions can be included, accounting for a wide variety of parameters, including (but not limited to): plotting temperature against an oxygen partial pressure and mapping out the phase(s) observed in different regions[24]. Alternatively complex phase diagrams can be built up purely relating to the composition, in order to solely focus on which compositions can result in a single phase. For the example in Figure 10a, if one wanted to extend the investigation to include, $Y_xBa_{3-x}Fe_{3-y}Mn_yO_8$ a second axis would be added to the diagram indicating the Mn content and a similar plot produced with the number/type of phases observed in each region recorded. An example of this was critical in D. Hodgemans' synthetic work in obtaining a phase pure composition following on from computational predictions presented in chapter 5 and the subsequent publication[25].

Solid solutions of materials are the combination of two or more compounds synthesised into a single material, where a range of compositions can be formed into a single phase, typically given a form similar to $C_{1-x}D_x$, where C and D are two different compounds. Simple examples of an oxide solid solution include the reported solution between Fe_2O_3 and Cr_2O_3, to form the solution $Fe_{2-x}Cr_xO_3$ where *x* is reported between 0 and 2, with *x* values of 0.67, 1.00 and 1.33 explicitly investigated[26]. A common observation among solid solutions is the evolution of structural and physical properties across a series of *x* values, or in some cases changes to the structure, easily represented by plotting a phase diagram as a function of the solid solution composition as is represented in Figure 10b[26-29].

It is possible to construct solid solutions of more complex materials such as the perovskites discussed in the previous section (and becomes part of the focus of chapters 3 and 4), in order to create solid solutions both end members do not have to be known to exist or have the same structure type. An example of this is the doping of Co^{3+} into the aforementioned $YBa_2Fe_3O_8$ material[27], in order to form a solid solution of the form $YBa_2Fe_{3-x}Co_xO_8$. Where the first end member is the $3a_p$, $YBa_2Fe_3O_8$ and the other end member, $YBa_2Co_3O_8$ is reported as a cubic perovskite with disordered oxygen vacancies[30] and the $3a_p$ structure is retained up to a nominal x value of 1.5 (50% substitution). This study also highlights the concept of a solid solution limit, i.e. an upper limit for the value of x, where a single phase material is formed, after which the compound at the solid solution limit crystallises out with remaining material crystallising as impurities. This strategy of doping materials by the formation of solid solutions can be used to tune the properties of a material, such as the d.c. conductivity or thermal expansion properties and has become an important method for the development of functional materials.

1.1.5 Doping perovskites and applications thereof

The properties of transition metal oxides are controllable by substitution at the metal sites or via the creation of solid solutions. Doped complex metal oxides have applications in areas including; solid oxide fuel cells (SOFCs)[31], transparent conducting oxides[32] and super conducting oxides[33]. In transparent conducting oxides, doping can lead to band gap tuning and reductions in resistivity such as in doped ZnO [34-36]. With superconducting oxides it has been shown that Sn doping can result in higher T_c (where T_c indicates the temperature below which the material is superconducting) values for $Ru_{1-x}Sn_xSr_2GdCu_2O_8$ (whilst simultaneously

suppressing ferromagnetic ordering)[37], the materials presented in chapters 4 and 5, are investigated within the research group as potential SOFC cathodes (with a schematic diagram of an SOFC cathode in Figure 11a).

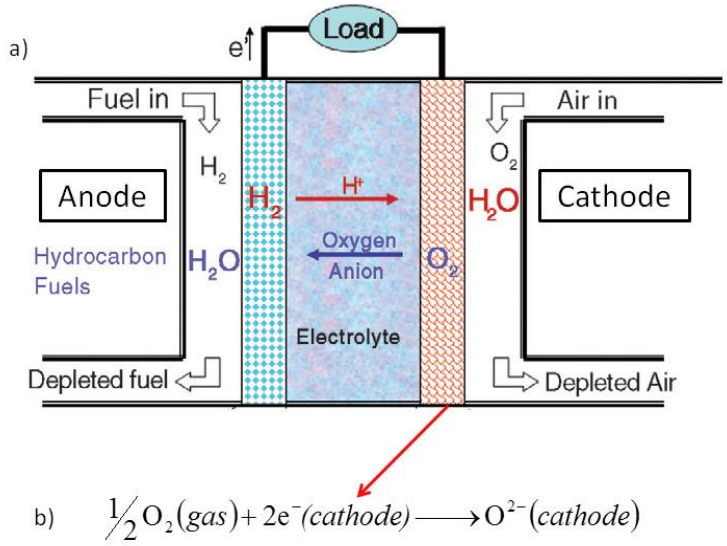

Figure 11 a) Schematic representation of an SOFC fuel cell, adapted from[38] with the corresponding overall reaction at the cathode shown in b)[4]

Therefore, for the overall reaction in (Figure 11b), a material should have a good electronic conductivity (experimentally demonstrated by d.c. conductivity/ area specific resistance (ASR)) and in order to promote the reaction only occurring at the surfaces of the material, to have the ability for oxygen ion conduction (typically demonstrated through ASR measurements), with materials containing both properties referred to as mixed-ionic-electronic-conductors (MIECs)[38], with the parent material in chapter 4; $Y_{1.1}Ba_{1.5}Ca_{2.3}Fe_5O_{13}$ shown to have good ASR values[15] the d.c. conductivity is only modest.

It has been shown that doping one of the metal species in oxides can be beneficial in order to tune desired properties, such as d.c. conductivity ASR values for SOFC cathode materials

including $Ba_{1-x}Sr_xFe_{1-y}Co_yO_{3-\delta}$[39-42]. Since metal doping has been shown to tune the properties of oxide materials, chapter 3 investigates the principle of using *ab-inito* calculations to predict where doping will be possible and it is then applied the $10a_p$ material in chapter 4 in order to guide synthetic efforts to improve the conductivity of the material. When several candidate sites are available, qualitative crystal chemical considerations may not always be capable of predicting the outcome of a substitution reaction, so in chapters 3 and 4 the concept of using *ab-initio* calculations to predict the outcome of site substitution in a structurally complex oxide is explored.

1.2 Theoretical calculations and solid state chemistry

As oxide research moves toward the discovery of new materials with increasing structural and compositional complexity, it is equally becoming more difficult to isolate such compounds by purely synthetic methods. Large and complex materials experimentally face two main problems, firstly, finding the composition at which a new structure can and will form for multiple element system can result in synthesis at a wide range of compositions and conditions with no guarantee that a new compound has not been missed. Secondly, even when new materials are formed, with large and complex structures, identifying the structure is a difficult task. Chapters 3 and 4 investigate the use of theoretical methods to calculate compositions at which new compounds can be formed, whereas chapter 5 focuses on using theoretical techniques to aid in the identification of a new complex oxide material.

Increasingly, theoretical methods have been developed in order to attempt to help with both of the problems presented above, in addition to the traditional contributions from theory such as the

calculations of band structures and corresponding density of states. The aid provided by theory covers a wide range of challenges utilising varying amounts of experimental information. At one end of the scale, where large amounts of experimental information is available are problems such as the most stable distribution of a set of cations for a given crystal structure and composition. At the opposite end, are problems where very little experimental information is known such as attempting to predict the contents of a compositional phase diagram in order to help guide future experimental synthesis. Although it should be noted that the level of experimental information available to use in the computational problem does not necessarily define problems complexity as the difficulty of the task is also reliant on the system size and number of different calculations required.

Given an infinite amount of computational power and infinite time, it would be possible to predict the structure of any compound by sheer brute force, i.e. to generate every possible permutation of a selection of atoms and to then calculate the corresponding free energy of every configuration. However in reality, in order to be able to perform calculations within a reasonable time frame and with the available computer resources, a number of different methods have been developed in order to efficiently aid experimental investigations. Although, each method either attempts to be as broad as possible or make a number of assumptions, resulting in limitations as to which systems a particular method can be applied to.

Before analysis of computed structures can be performed, the ground state structure must first be computed and methods for achieving this have become common place. Typically, the ground state structure is defined as the arrangement of a structure that has the lowest potential energy. Several different methods for finding a minimum energy structure can be reasonably performed

using modern computing resources, with the most suitable depending on the size of the system and what information is required.

In order to find a minimum energy structure, two things are required; a method by which to calculate the energy of the system and a method by which to alter the structure in order to search the energy landscape of the system[43-46].

For calculating the energy of a system, there are three main levels of theory; *ab-initio* calculations, classical mechanics and semi-empirical methods. With *ab-initio* calculations the energy of the system is computed with as few parameters as possible, with little information provided by the user apart from the atomic structure plus the number and type of atoms, with a common example of this being density functional theory (DFT, details given in the methods chapter). At the heavily parameterised end of theory is classical mechanics, whereby the energy of the system is calculated from completely parameterised atomic interactions also referred to as force fields (FF), a number of different types of force field are commonly used in simulation packages, details for the methods used in this thesis given in the methods chapter. In between these two types of theory are semi-empirical methods which combine elements from both of the above levels of theory. The most computationally expensive level of theory is the *ab-initio* methods, with force fields being the cheapest and semi-emperical methods lying somewhere in-between depending on the level of parameterisation used. All of the calculations performed in this thesis fall into either classical mechanics or *ab-initio*, with a more detailed description presented in the experimental methods chapter.

Once the energy of a system is calculated, methods can be applied in order to reduce the energy of the structure, most common methods focus on attempting to find the nearest energy minimum.

To find the nearest minimum structure (also referred to as structure relaxation), the program may attempt to find the combination of inter-atomic distances that yields the lowest energy for example (assuming that each bond length will have an energy minimum as a function of distance). There exists a larger problem however; there is the possibility that the structure that is relaxed may not be the lowest possible energy structure for the system, i.e. it may be trapped into a local minima by large energy barriers preventing the energy minimisation finding it. However, relaxing a selection of local minima may be sufficient for specific systems, such as those studied in chapters 3 and 4. A number of levels of theory have been developed in order to find this lowest possible minimum structure, also known as the global minimum structure. In addition to attempting to approximate a brute force method, three common routines have been developed addressing the issue of finding the global minimum without resorting to the generation of as many structures as possible; Monte-Carlo sampling, molecular dynamics and genetic algorithms (which are discussed in the next section).

A substantial challenge in the field of materials chemistry is the ability to be able to predict the formation of new materials or the modification of existing compounds. Computational predictions range from predicting how different cation types order within a system[47] to predicting new structures[45]. Each method will inevitably have its own advantages and drawbacks and so thus far no one method can be deemed universally applicable, each method will have systems for which it is best suited. In the following section some previously reported methods for making predictions in solid state materials are presented and summarised.

1.3 Applications of theory to solid state chemistry

1.3.1 Formation/Reaction energies and material doping

When synthesising solid solutions, it is desirable to be able to calculate regions where stable compositions are likely to exist and hence reduce the amount of compositional space that is searched experimentally. For some systems it has been possible to calculate formation energies in good agreement with experimentally determined values[17, 48]. The computation of solid solutions can be performed in at least two different ways. In the first method, formation energies are calculated from a library of relevant reference materials, so that balanced chemical equations can be found. For the second method energies can be computed relative to an ideal solid solution (if both end members are known to exist and reliable energies can be calculated). The energies of compositions are then calculated across the compositional range of interest and their energies compared to the required amounts of the end members to create balanced chemical equations.

The first method has been previously reported for the formation of ternary perovskites in the $LaMO_3$ system from binary oxides and O_2 gas[17], the computed reaction energies compared with those experimentally reported in order to test the ability of DFT to correctly calculate reaction pathways, with an example given below for $LaFeO_3$:

$$\frac{1}{2}La_2O_3 + \frac{1}{2}Fe_2O_3 \xrightarrow{\Delta E} LaFeO_3 \qquad \textbf{(1.3)}$$

In this example, the experimental and DFT calculated values for ΔE were found to be in good agreement after optimisation of the calculation. The same process was used for a number of transition metals in the same study, resulting in refined DFT calculation settings, shown to be able to calculate the relative stabilities of perovskites in reasonably good agreement with

experiment. This methodology has also been previously reported for the calculation of a number of solid solutions[48-51].

As the ability to be able to compute reaction energies has been established for some oxide systems the focus of the work presented in chapters 3 and 4 looks to utilise this capability. Firstly, formation energies are calculated for systems with larger unit cells than previously reported and containing a larger number of elements making for a complex challenge. The calculation of formation energies is used predicatively to guide the synthesis of the compounds presented to in chapters 3 and 4.

1.3.2 Convex hulls[52]

Convex hulls build on the calculation of formation/reaction enthalpies by calculating the minimum free energy[43, 45] of formation with finite temperatures (including zero Kelvin) across a compositional range, with all of the results being mapped out onto a phase diagram, (such as the ternary phase diagram in Figure 12).

Convex hull calculations are thereby required to begin by the calculation of a library of energies for reference materials, where reference should at least consist of the materials used on each axis of the proposed phase diagram (for example the elemental components on each axis in Figure 12). The list of reference materials may also be expanded to include a library of known materials within the compositional diagram of interest, where their free energies of formation are calculated relative to the components on the axes of the phase diagram.

Once the library of known materials has been computed, hypothetical compositions are additionally inserted into the system and their corresponding free energy calculated. The energy of the system can be computed from any reasonable energy minimisation method, such as DFT or force fields, although the accuracy of the resulting phase diagram will vary with the accuracy of the energy minimisation. The free energy of the system can be calculated for any given finite temperature, including zero kelvin[43] or a given range[45].

Initially, the stability of each composition on the phase diagram is measured by the calculated free energy of formation relative to the components on the diagrams axes, with the free energies at each point resulting in a contour plot across the phase diagram[52], referred to as the convex hull. Analysis of the convex hull will also allow for the identification of competing phases at each composition, based upon other compositions on the phase diagram that have similar or lower formation energies. The calculation of stability relative to competing phases allows one to predict whether the target phase is likely to form at a composition, or if it will react to form a mixture of other phases.

Using the example shown in Figure 12, adapted from[43], the highlighted composition (data point number 5), with the composition $CeIr_4In$[43], was calculated to have a total energy of -46.651 eV/FU with a resulting formation energy of -455 meV/atom from the component Ce, Ir and In metals and so is considered to be favourable. Competing compositions were identified to be Ce_2Ir_7 and $IrIn_2$ from the contours of the hull (shown as lines in Figure 12) and so a reaction between $CeIr_4In$ and Ce_2Ir_7 and $IrIn_2$ was calculated and the $CeIr_4In$ phase calculated to be marginally favoured by 8 meV/atom.

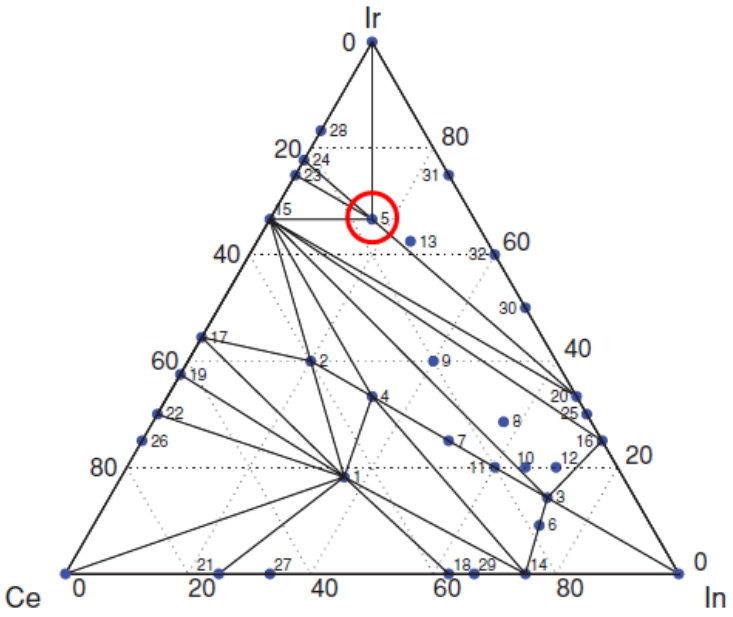

Figure 12 Adapted from[43], a convex hull constructed for the Ce-Ir-In alloy phase diagram. Each point on the hull indicates a composition calculated, low energy structures are at the vertices of the intersecting lines. Point number 5, highlighted indicates the predicted and subsequently synthesised $CeIr_4In$ alloy material.

Convex hull calculations have been employed with some success for the prediction and subsequent synthesis of new compounds[43, 52]. This methodology has been shown to achieve some success previously, although this method has the inherent drawback of the computational expense, and the convex hull becomes difficult to construct once more than three elements are involved.

1.3.3 Data mining

Data mining is an approach for crystal structure prediction ,typically focused on finding experimentally unknown compositions that crystallise into previously known crystal structure types[53, 54]. Common methods by which data mining are implemented focus on calculating the ground state structure for a range of different compositions.

An example of how a data mining run can be performed includes finding new compositions for a known structure type. Taking this example methodology as reported[55], the initial step is to determine a list of possible compositions for the structure type of interest and computing their minimum energy structure. At each composition in the diagram, once the energy has been minimised, an analysis must be performed in order to computationally assess the stability of each compound. The stability of each compound in the target structure can be assessed by the use of formation energies from combination of other known compounds, such as the components in their elemental form or from binary oxide starting materials or the same composition in a different structural type[55]. New compounds are then predicted to be favourable when they are calculated to be stable both relative to elemental materials and other competing phases, as with data points on a convex hull, this approach is exemplified by Figure 13, adapted from[55]: where a library of compositions for chalcogenide materials with the A_2BX_4 formula unit were calculated and predicting approximately 100 un-reported compositions that are likely to be stable.

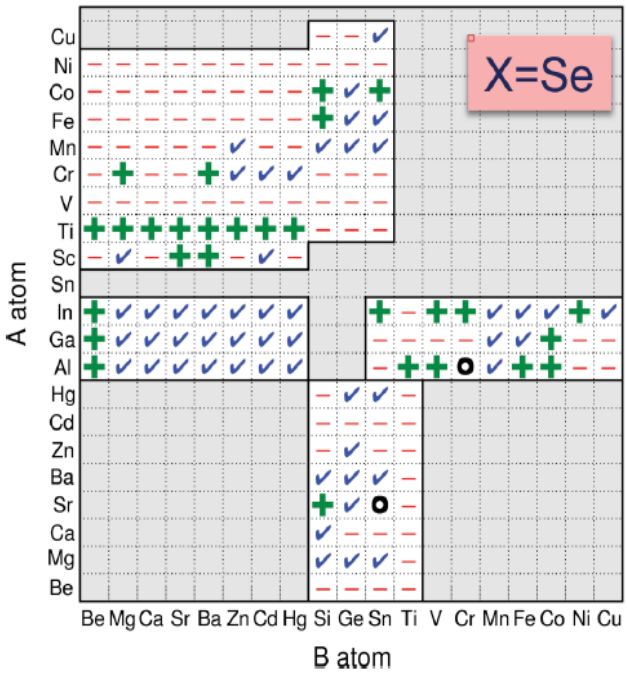

Figure 13 Adapted from[55], results from the prediction of A_2BX_4 for X = Se, + signs indicate where unreported materials are predicted to be stable, - signs indicate compounds predicted to be unstable, ticks indicate known compounds and circles indicate compounds for which the computational methods remained undecided, grey boxes indicate compositions not trailled.

Data mining methods have the drawback however, that predictions can only be made for materials that possess a previously reported structure type. This type of approach has however been used to predict whole libraries of new materials that have yet to be discovered experimentally, exemplified by the prediction of a large number of unreported metal-chalcogenide materials predicted to be stable in the same study[55] (Figure 13).

.

1.3.4 Molecular dynamics and simulated annealing

Molecular dynamics is a method to calculate the equilibrium structure of a compound at finite temperatures, rather than the lowest energy structure at zero Kelvin, these methods will allow for the calculation of structures as a function of temperature. Energy of the system is constantly updated in accordance with any of the energy calculation methods outlined above (i.e. *ab-initio* or classical mechanics).

Atoms are moved using Newtonian physics, based upon the forces calculated between atoms to calculate momentum with time and at a finite temperature. The calculation proceeds as a function of time, with a user defined time step, typically on the order of femto-seconds. The forces and energy of the system are updated at each time step and the calculation is run for a user defined simulation length.

The simulated annealing method[56] for finding the lowest energy configuration of a structure, aims to emulate what happens to experimental systems; at high temperatures, the system is typically in a highly disordered state and as the system is cooled, the material slowly becomes ordered and forms into the most stable structure. Computationally this is achieved by constant perturbation of a system with a time/temperature dependant method such as molecular dynamics. Starting from a high temperature state, the system is allowed to equilibrate and the system temperature is reduced decreasing the level of perturbation in the system until low temperatures are achieved, where the run can then be completed with a conventional energy minimisation. It generally follows, from this theory that the rate at which the temperature is reduced is important; reducing the temperature too quickly may result in the trapping of a structure into a local minimum. Reducing too slowly can result in calculations that are too slow to perform due to the

number of steps that are required to perform the calculation. Simulated annealing has resulted in the successful calculation of the global minimum of a number of structures[46, 57, 58]

1.3.5 Monte-Carlo

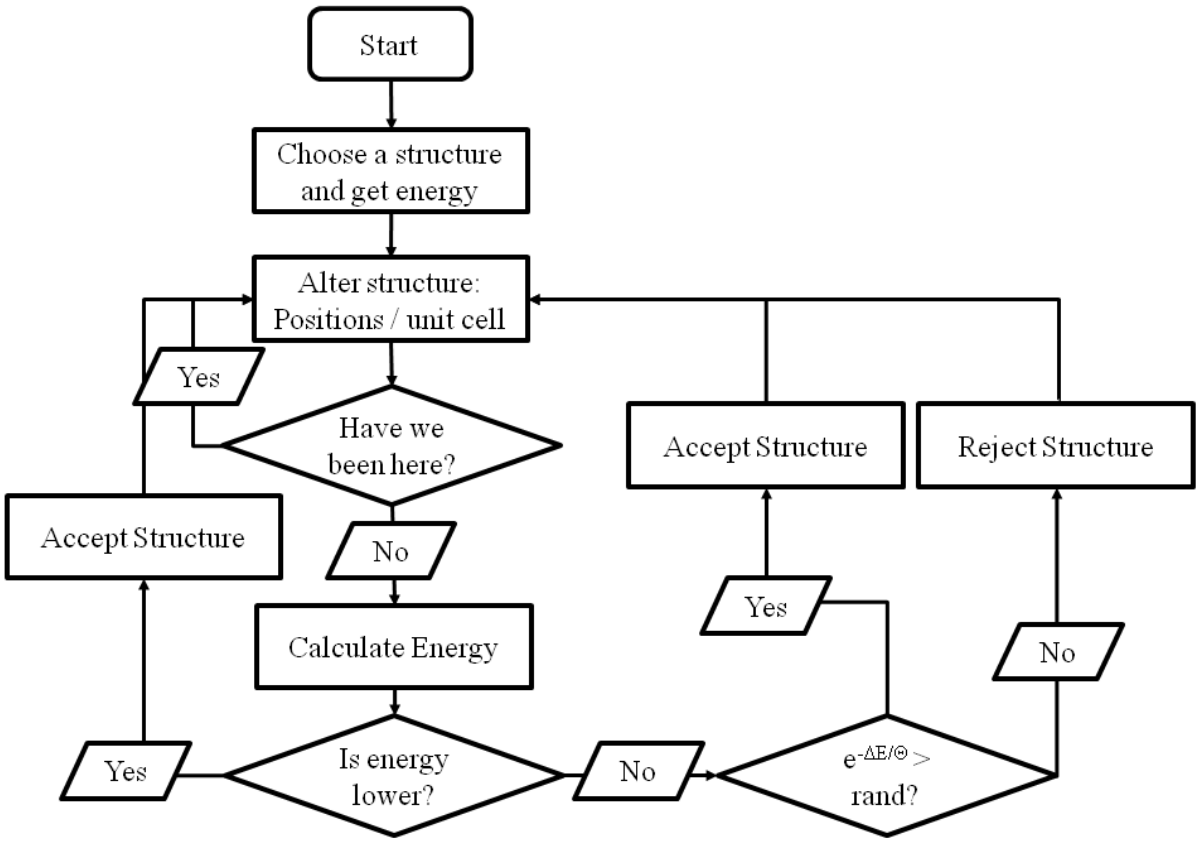

Figure 14 Example of a working Monte-Carlo routine (based upon a figure provided by M.S.Dyer, "rand" in the bottom right segment referrers to the random number generation between 0 and 1 for the probability that a higher energy structure will be accepted, with the routine typically run for either a pre-defined number of cycles or until a set number of steps rejected consecutively.

Monte-Carlo sampling (Figure 14) to find a minimum energy structure works by minimising an initial guess for the structure using one of the methods outlined above, after which a random

movement in the structure is performed, this can include moving one or more atomic positions or in a periodic system, varying the size/shape of the unit cell. The altered structure is then re-relaxed and a new energy calculated. If the new alteration to the structure is lower in energy then it is accepted. If the altered structure is found to be higher in energy the probability of it being accepted is calculated based upon a Boltzmann distribution dependent on the change in energy between steps and the probability is compared with a randomly generated number between 0 and 1, if it is less than the probability generated from the Boltzmann factor, it is accepted. Once the alteration is completed and the acceptance is determined, the cycle is repeated typically for a pre-determined number of cycles or until a user defined number of steps have been consecutively rejected.

1.3.6 Site disorder

In real solid state systems, there is often an amount of disorder on crystallographic sites, such as the disorder observed in the $10a_p$ example in the previous section. It has been shown that cation disorder in oxides can result in lower overall energy configurations, even before considering entropy contributions[15] and so for some systems it is important to be able to model this site disorder to obtain the lowest energy structure. For comparison between predicted and experimentally observed structures, the ability to estimate site disorder can decrease the difference between experimentally observed and calculated structures. Below, two separate methods for estimating site disorder for solid systems are discussed.

Previous work has examined how a Monte-Carlo routine can be implemented to approximate ordering between types of site in solid structures[59], since in most computational techniques there

is little or no allowance for fractional occupancies of sites. A successful method to get around this problem has been reported and subsequently applied to investigate B-site cation disorder in the Ca_2FeAlO_5 brownmillerite[59], where a large supercell of the material in question is generated in order to allow for statistical averaging across equivalent sites/atomic layers. Combined with the chosen method of energy minimisation, a Monte-Carlo routine is then applied for a fixed temperature, it differs from that presented above, in that instead of moving atomic positions/unit cell dimensions, each step consists of swapping pairs of non-equivalent atoms. This routine is then executed from the starting structure for a number of cycles until the lowest energy configuration is found, note that in order to eliminate very unlikely configurations it is possible to specify which atoms are allowed to swap places (e.g for a perovskite only allowing A-site species to swap with other A-site species). Once the minimum energy configuration is found from the starting structure, it is possible to then analyse each equivalent layer and estimate the fractional occupancies.

Another reported method for assessing site occupancy is the site occupancy disorder (SOD) method[47]. Starting from a given structure and its space group symmetry, a supercell can be generated, and all of the possible arrangements are generated using the symmetry operations of the parent unit cell, with the possibility to impose restrictions on which atoms can be placed into which sites. All of the generated configurations are then evaluated by a theoretical method of choice and the most stable configuration found. Since the SOD method results in the calculation of a relative energy of all possible configurations, a statistical mechanics approach must be employed to estimate the probability of finding each configuration at a given temperature, with the method outlined below[47]:

$$E_m = H_m - S_m \quad \textbf{(1.4)}$$

The starting point for the statistical mechanics approach is to compute the estimated free energy of each unique configuration, E_m. Where H_m indicates the zero Kelvin energy calculated by a chosen energy minimisation method and S_m is the calculated configurational entropy for the configuration defined as:

$$S_m = k_B T \ln \Omega_m \quad \textbf{(1.5)}$$

Where k_B is the Boltzmann constant and T is the finite temperature in Kelvin, which is then multiplied by the natural log of the number of equivalent configurations that can are generated by the symmetry of the parent structure, Ω_m. The expected population of a configuration *m*, P_m can then be estimated for the system at thermal equilibrium:

$$P_m = \frac{1}{Z} \exp\left(\frac{-E_m}{k_B T}\right) \quad \textbf{(1.6)}$$

Where Z indicates the partition function for the system, defined as:

$$Z = \sum_{m=1}^{m} \exp\left(\frac{-E_m}{k_B T}\right) \quad \textbf{(1.7)}$$

A modification to the method is used when considering materials containing magnetic atoms at high temperatures where is expected the system to be paramagnetic. In order to calculate the populations of materials expected to be paramagnetic at high temperatures, reports estimate a energy associated with the paramagnetic state as follows at zero K:

$$H_{pm} = \frac{1}{2}(H_{AF} + H_F) \quad \textbf{(1.8)}$$

Where H_{pm} indicates the paramagnetic energy, H_{AF} is the energy of the configuration in the lowest energy antiferromagnetic ordering and H_F indicates the energy of the configuration with ferromagnetic ordering; the populations for each configuration are then calculated as described as above. The statistical mechanics approach is used as part of the calculations presented in chapter 3 and becomes an important measure of how well calculations can estimate site ordering for predicted crystal structures. The SOD method has also been used in the prediction of doping within oxide systems[60, 61] as well as other systems[49, 62-64], where in the methodology outline above, after the supercell has been generated a specified number of dopant atoms are then introduced before non-equivalent configurations are generated in order to calculate the most stable configuration across a solid solution. When dopant atoms are introduced, a pre-defined number of dopant atoms are introduced into the cell and then all of the possible configurations are generated using the symmetry of the parent undoped material.

Both of the above methods have systems to which they are best suited. Since the SOD method calculates all of the possible site disorder configurations it will be the most comprehensive, although it has the drawback that as the number of atoms/elements increases the number of permutations required becomes correspondingly larger and will lead to calculations that are currently unfeasible and so is best suited to smaller systems. The Monte-Carlo sampling method is more suited to larger systems since the number of relaxations performed is entirely user defined, however, it has the drawback that there the possibility that the lowest energy structure configuration has not been found and therefore the average site occupancy calculated may not be the most favourable. In summary the SOD method has the advantage over the MC approach in that it can calculate disorder at various temperatures. However, the size of systems that SOD can be applied to is its major drawback. The MC method is more suited to larger systems but does

not calculate occupancies at different temperatures, since the temperature factor used only affects the probability of higher energy structures being accepted.

1.3.7 Genetic Algorithms

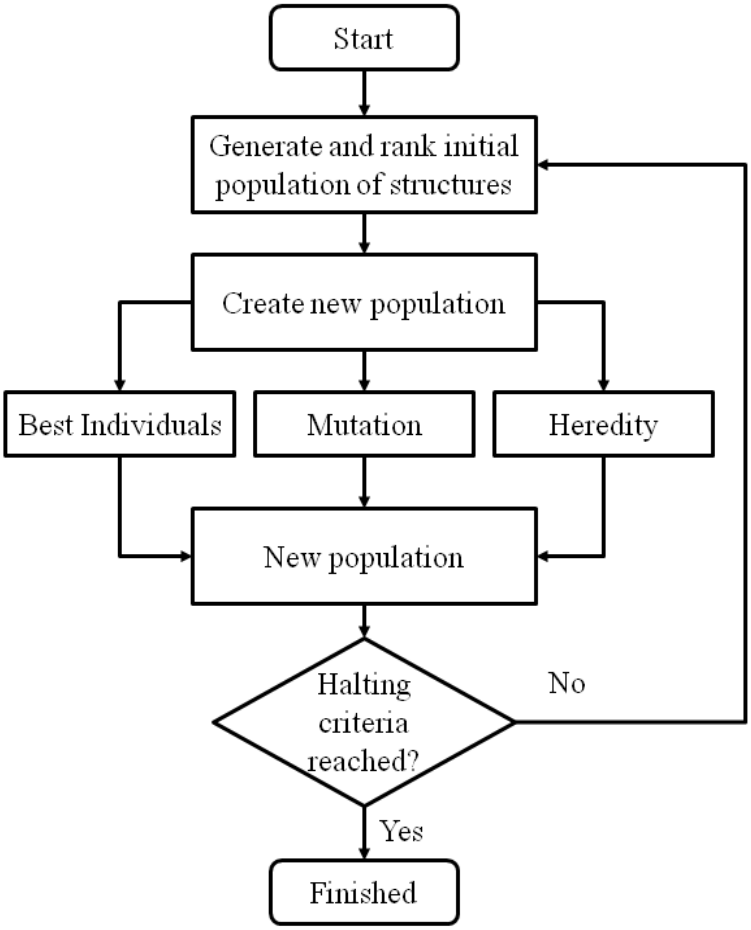

Figure 15 Typical block scheme for an evolutionary algorithm, based upon the algorithm presented in[65].

Genetic or, evolutionary algorithms have been developed as a method to calculate the global minimum structure for a given system[65], with an example algorithm presented in Figure 15.

These methods begin with a population of starting configurations, often generated by random arrangements of atoms. During the run a maximum or fixed number of structures can be specified, whereby the first and subsequent generations of structures are constrained to these limits. The number of structures can vary in the system due to generated structures being outright rejected; for example in a periodic system a criterion could be for each lattice parameter to be larger than the diameter of the largest atom in the system in order to avoid unphysical structures. Each structure is usually then relaxed and then assessed for 'fitness' for a given set of criteria, for example by the calculated energy of the structure.

Once this process is completed a second generation of structures is created, known as the procreation step, by the combination of elements from a proportion of the structures that were considered to be the 'fittest' from the first cycle, with the allowance for random mutations of the structure (random displacement of a number of atoms for example). Again the new generation of structures is relaxed and then evaluated for their fitness and the procreation cycle is repeated again. The above cycles are repeated either for a pre-determined number of cycles or until the global minimum structure is obtained (defined by a set of convergence criteria).

This method of structure prediction has been shown in the literature to be able to successfully generate structures for oxide and mineral systems[66-68] and computational packages designed specifically for the use of genetic and evolutionary algorithms with known energy minimisation techniques such as the USPEX[44] code and has also been implemented in GULP[66, 69, 70] ENREF 66. However, the drawback comes from the vast quantity of configurations that would be required to get to the global minimum structure and the problem becomes increasingly complex as the number of elements increases and consequently results in limitations being placed on the size/number of atoms that it is feasible to compute. Such algorithms do have the

advantage that it should eventually find the correct structure, and it is not limited to previously known structure types. Due to the number of generations and thus computational time that is often required the use of genetic algorithms tends to be restricted to smaller systems, although where it has been employed it has been proven to be an effective method by which to locate a global minimum structure.

1.3.8 Secondary building units

Moving away from the concept of building/generating structures in terms of a collection of atoms is the concept of constructing structures from fixed arrangements of atoms, referred to as secondary building units (SBUs); this has been developed in order to avoid the problems originating from a true brute force method for structure prediction[71-73]. SBUs can take the form of any chemically sensible way in which a structure can be broken down, by taking the basic cubic perovskite as an example, it can be thought of as assembled from two SBUs; one AO and one BO_2 layer (Figure 16). This technique can be used to construct framework materials from building units[72] or to assemble layered solid state structures from 2-D sheets[72]. In the case of the ZEBEDEE code, fragments of molecules (which fit into the description of SBUs), are used in an evolutionary method to design template molecules for the growth of frameworks and has successfully been implemented to guide the synthesis of new template frameworks[74, 75].

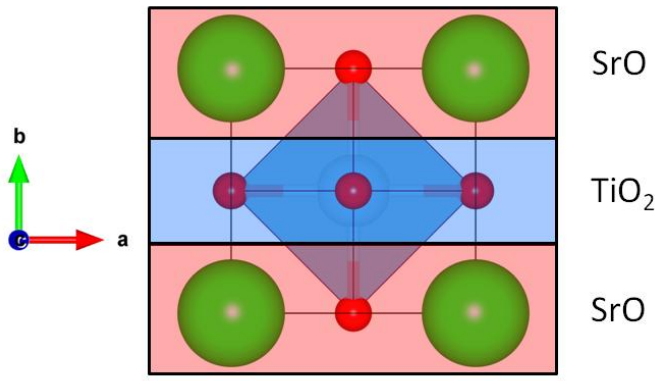

Figure 16 View of previously mentioned $SrTiO_3$ broken down into two secondary building units (SBUs), this concept of breaking structures down into SBUs can be used to simplify the problem of generating complex structures, with this example, the $SrTiO_3$ perovskite is broken down into AO layers (red) and BO_2 layers (blue).

In this second example, large layered structures can be assembled from the stacking of these 2-D sheets and so it is possible to envisage utilising this concept in the assembly of large perovskite-like structures. For perovskites this would primarily originate from the alternation of AO and BO_2 layers (from an ideal perovskite), and in order to be able to generate large perovskites such as those outlined previously oxygen vacancies would need to be included. This concept outlines the work undertaken in the discovery of a new layered perovskite presented in chapter 5.

The concept of assembling extended structures from SBUs leads to the possibility of generating and calculating previously unreported structures without the problem of having to overcome energy barriers to obtain them or rely on the chance of finding them as with other methods. Depending on the size of the SBU used, there are potentially the same drawbacks as with the SOD method for site disorder, namely the number of permutations that could be generated for large systems could become prohibitive.

When generating structures from SBUs, the resulting structures still require some form of energy minimisation, with the chosen method largely dependent on the number and size of the permutations that are generated. Once energy minimisation has been completed each of the permutations can then be ranked by their energy and the lowest energy structure determined.

1.4 Summary

In summary, there are wide choices of computational methods that can greatly assist experimental investigations, however, as outlined above, each technique has its own inherent drawbacks and therefore there is no one method that is universally applicable to every situation. Therefore when approaching a computational problem one should consider the following points before beginning:

- What is the desired outcome of the investigation?
- What level of experimental/computational information is available from which to build a starting point?
- How many atoms/electrons and how many configurations are involved in the system?

For example, if accurate energies or the electronic structure are the desired outcome, one would have to lean towards *ab-initio* level calculations, or at least combine them with classical mechanical methods. In the second point, as each computational method has its own pre-requisites before a calculation can be performed (the starting structure for example), this can govern which methods can be used, or at least require additional calculations in order to get to the starting point of the desired methodology. The last point, this will govern the practicality of the investigation, the points listed above were considered for all of the chapters within this thesis,

the desired outcomes for the computational investigations were decided upon; in chapters 3 and 4, accurate enthalpies were required to predict stable compositions and the most likely structural configurations across a solid solution. In chapter 5, accurate energies were required in order to be able to predict the crystal structure of a unknown material. These aims meant that *ab-initio* methods would have to be used in all three chapters.

Secondly, in chapters 3 and 4, it was decided that normal energy minimisation could be combined with the calculation of formation enthalpies since compositions and reasonable crystal structures were known, due to the chapters revolving around computational doping of known materials. For Chapter 5, however, only the approximate composition and unit cell size (and that the material was a perovskite) was known and so a method for finding the global minimum structure was required instead of normal energy minimisation. Due to the possible number of permutations for the atomic arrangements of the cell combined with prior knowledge about the crystal structure type, a method based on SBUs was developed, although if the crystal structure type was not known, it is likely that a combination of GA and simulated annealing methods may have been more appropriate.

Lastly, considering the size and number of the required configurations and available computing resources, it was decided that the relatively small number of configurations required for chapters 3 and 4 (on the order of tens to low hundreds) could all be completed using purely *ab-initio* methods. For chapter 5, where it soon becomes apparent that very large numbers of configurations require assessing (on the order of hundreds of thousands), pure *ab-initio* methods were impractical, and so initially all of the structures were assessed using classical mechanics methods followed by a smaller number of structures (in the order of tens) then carried forward to have accurate energies computed via *ab-initio* methods.

1.5 Aims of this thesis

In this chapter the perovskite structure has been discussed along with examples of materials with long range ordering beyond the cubic perovskite cell and the causes of ordering. Methods by which such structures can be modelled by computational chemistry have also been presented along with outlining their corresponding advantages and drawbacks, with their contribution to experimental studies detailed. This thesis moves to present work furthering the complete integration between theoretical and synthetic methods in the discovery of new functional oxide materials. The following chapter, provides an example of how theoretical techniques can be integrated with experimental investigations, leading to the discovery of manganese substitution into the $YBa_2Fe_3O_8$ $3a_p$ perovskite. The concept of predicting substitutions in oxide materials is then applied to the $10a_p$ functional SOFC cathode family in chapter 4. Finally in chapter 5 concept of SBUs is further developed a method used to successfully predict the crystal structure of a new $16a_p$ perovskite, with nothing more than an approximate composition and unit cell size as input information.

Chapter 2. Synthetic and theoretical methods

2.1 Solid state synthesis

All of the samples in this thesis were prepared via the standard ceramic methods[76, 77]. Prior to synthesis, the precursor materials were calcined to remove any moisture absorbed in the powder when stored at room temperature, in order to ensure that the correct stoichiometries are weighed out. Within this thesis and most starting materials were calcined at ~ 200 ˚C prior to weighing to evaporate any water contained in the powder, with the exception that Y_2O_3 was calcined at ~ 900 ˚C, due to Y_2O_3 being more hydroscopic than the other starting materials.

Once the starting oxides have been prepared, they were weighed out according to the stoichiometry required. Starting materials require mixing in order to ensure that the desired chemical reaction occurs efficiently and results in a homogenous product. The first step in mixing is to mill the starting powders; depending on the number of components and or the total amount of powder used, the starting materials can be milled by hand using a pestle and mortar or via a milling machine. Hand milling is typically suitable for smaller samples (a few grams) and larger samples milled mechanically. Mechanical milling has the advantage that it typically results in powders with smaller average particle sizes compared to hand milling. Consequently the finished samples can have higher densities, as is usually required for physical property measurements (e.g. d.c. conductivity measurements).

Once milled, some samples may require a calcination step in order to begin the chemical reaction and improve the homogeneity of the sample. If a calcination step is used, the temperature and time of calcination is selected in order to prevent the chemical reaction from fully occurring as

only improved mixing is required, after calcination, the sample is ground and re-mixed as described above.

Once the mixing and/or calcination step(s) have been completed, the chemical reaction is facilitated by a sintering step[77]. Sintering involves heating the sample to high temperatures (typically over 1000 ˚C for tens of hours), in order to allow the elements involved enough kinetic energy to diffuse through the sample and react. High temperature sintering is usually combined with pressing the sample into a pellet to increase contact between particles and therefore improve the solid state reaction rate. The sintering process often results in the sample density increasing significantly as particles fuse together in order to reduce the overall free energy of the system. For solid state reactions to form oxides, it is possible to adjust the atmosphere around the sample in order to manipulate the oxygen content and therefore the resulting product[24]; by either extracting oxygen from surrounding the sample with low oxygen partial pressures (e.g. by sintering the sample in a nitrogen flow), or at high partial pressures to attempt to increase the oxygen content with high oxygen partial pressures. In this thesis the concept of controlling the oxygen content in a sample becomes crucial to the successful synthesis of the target phase in chapter 3. It is common during the synthesis of oxide materials that a single sintering cycle does not provide enough energy, or inter-mixing to produce a single phase sample, and so several cycles of sintering and re-milling (also referred to as re-grinding) can be required.

For the systems studied synthetically in this work, once cycles of sintering were completed and no further reaction was observed between steps, samples were then re-ground until a fine powder was obtained. The obtained fine powders were then characterised using the methods described in the following sections.

2.2 Diffraction from crystalline solids[78]

The discovery that crystalline solids diffract x-rays was a critical in the field of material science as it now provides the basis for the identification of the atomic structure of crystalline materials. The idea that X-rays, having wavelengths similar to that of inter atomic spacings leads to the concept of solid lattices acting as a diffraction grating (with X-ray wavelengths having a magnitude of approximately 1×10^{-10} m or 1 Å) and was initially suggested by von Laue and confirmed by Friedrich and Knipping[79]. The original idea of X-ray diffraction was based from the concept that crystalline solids being 3-D arrays of atoms could act as a diffraction grating and from the way in which x-rays are diffracted information obtained about the atomic structure.

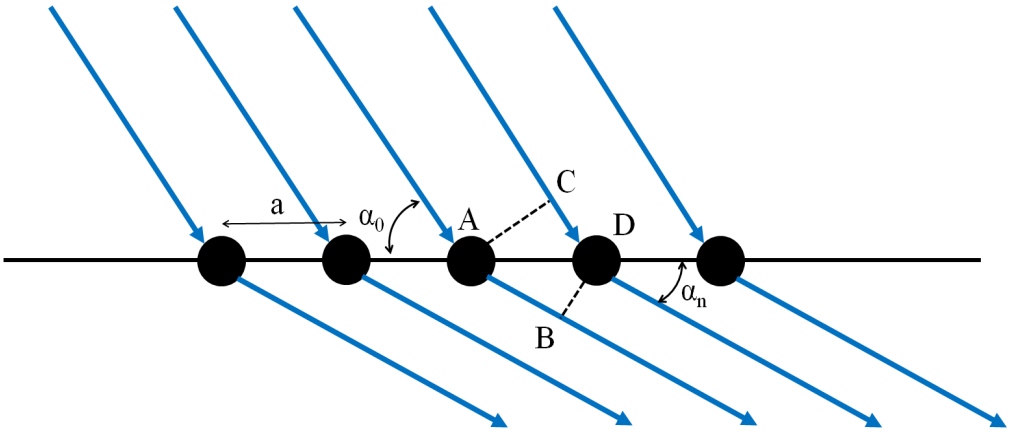

Figure 17 Schematic representation of Laue diffraction from a lattice in the *x* direction, where a is the lattice spacing, α_0 and α_n are the incident and diffracted x-ray beams, the path difference between adjacent beams is AB – CD.

The basic model of x-ray diffraction was based on a single crystal containing only a single type of atom, with each atom acting as a scattering centre at the corresponding lattice points. The crystal is constructed of rows of atoms arranged with spacings of *a*, *b* and *c* in each of the *x y* and

z axis of the crystal respectively. Diffraction is observed when constructive interference occurs between diffracted X-ray beams from adjacent atoms (Figure 17) and the path length of neighbouring x-rays is integer multiples of the wavelengths which results in the following equation:

$$(AB - CD) = X_i(\cos\alpha_n - \cos\alpha_0) = n_i\lambda \quad \textbf{(2.1)}$$

Where AB and CD are path lengths in (Figure 17), X_i denotes the atomic spacing along axis *i* (*a*, *b* or *c*), α_n and α_i indicate the angles between the diffracted and incident beam, relative to the crystallographic axis *i*, n_i indicates an integer multiple of wavelength, λ. Since diffraction can occur with a component in each of the three axis; *x*, *y* and *z*, with the corresponding atomic spacing *a*, *b* or *c* equation (2.1) can be written for the diffraction component in each axis:

$$a(\cos\alpha_n - \cos\alpha_0) = n_x\lambda \quad \textbf{(2.2)}$$

$$b(\cos\beta_n - \cos\beta_0) = n_y\lambda \quad \textbf{(2.3)}$$

$$c(\cos\gamma_n - \cos\gamma_0) = n_z\lambda \quad \textbf{(2.4)}$$

Where angles β_n, β_0, and integer n_y correspond to the angles and wave length multiples relative to the *y* axis, likewise for γ_n, γ_0 and n_z for the *z* axis. The scheme in Figure 17, only illustrates diffraction in the plane of the page, in reality, so long as the diffracted angle to the atomic row remains α_n, then the diffraction conditions can still be met, this results in diffracted beams actually forming a cone centred on the atomic row, with the apex of the cone having angle α_n. Since the same result can occur in the other two axes, diffracted beams are only observed where the diffraction cones from each axis intersect with each other resulting in well defined beams. For this analysis, in order to compute the direction of the diffracted beams, all of the angle,

spacing and integers from equations (2.2 – 2.4) need to be determined. A simpler model was proposed by W. L. Bragg[80], where diffraction was considered to be a reflection of the incident beam from planes of atoms (Figure 18), reducing the problem to two dimensions; although this is not physically correct, it makes geometrical sense, and substantially simplifies the problem.

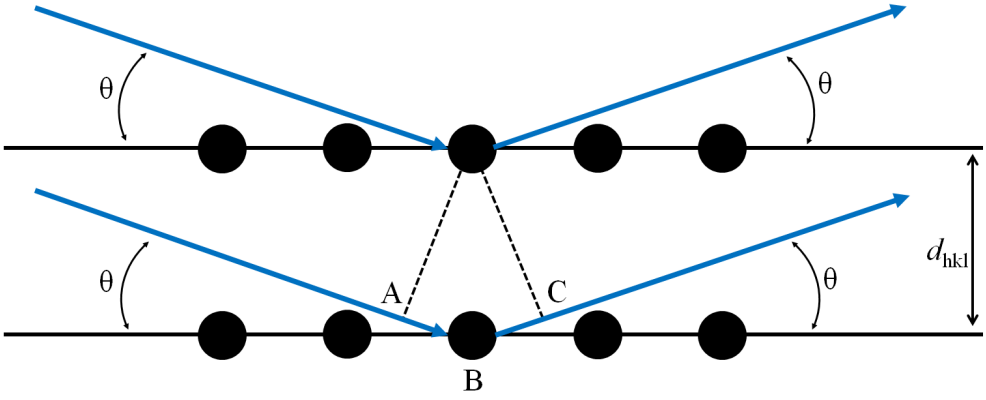

Figure 18 Schematic representation of Bragg diffraction from planes of atoms, with the path difference between adjacent beams being (AB+BC), θ indicates the incident and diffracted beam angles and d_{hkl} indicates the inter layer spacing within the crystal with miller indices *hkl*.

From Braggs' image of X-ray diffraction, the path difference between the beams scattered from adjacent planes of atoms, separated by the inter plane spacing d_{hkl} is given by (2.5), where *hkl* indicates the miller indices of the plane of atoms from which the x-ray beam is diffracting:

$$(AB + BC) = (d_{hkl}\sin\theta + d_{hkl}\sin\theta) = 2d_{hkl}\sin\theta \qquad \textbf{(2.5)}$$

For constructive interference to occur, the path difference has to equate to an integer number of wavelengths, resulting in the following condition for constructive interference:

$$n\lambda = 2d_{hkl}\sin\theta \qquad \textbf{(2.6)}$$

Where, *n* remains an integer number. Typically, experimentally collected diffraction patterns are plotted with observed intensity against the diffraction angle, 2θ, another common representation, especially when considering multiple data sets is *Q*, which is the momentum transfer on scattering and is defined by[78]:

$$Q = \frac{4\pi \sin\theta}{\lambda} = \frac{2\pi}{d_{hkl}} \qquad \textbf{(2.7)}$$

For Braggs law, the separation of the atomic planes is the governing factor for constructive interference, rather than the specific atomic coordinates. The equations described above additionally show that Braggs description of x-ray diffraction, unlike von Laue's, is only in two dimensions, dramatically reducing the number of parameters that require determination.

2.3 Powder Diffraction[81]

In practice, one commonly wants to use X-ray diffraction for the analysis of polycrystalline solids due to the difficulty of growing single crystals. Because of the nature of polycrystalline samples, each crystallite will exist in a random orientation, using the assumption that each possible crystallite orientation (relative to each other) will occur with equal probability results in each crystallographic plane diffracting a cone of X-rays according to Braggs's law. Diffraction planes are therefore observed as cones (or rings on a detector) instead of spots, which results in the obtained diffraction pattern changing from a 3-D data set into a 1-D profile as a function of the diffraction angle. The reduction in dimensionality results in the overlap of multiple

diffraction planes, as it is possible to have multiple crystallographic planes with equivalent d_{hkl} spacings, therefore regardless of the quality of the resolution of instrumentation, this overlap inevitably leads to an overall loss of information.

In spite of the inherent drawbacks of diffraction from powders, with the development of the Rietveld method[78, 82-84], it has become possible to refine the crystal structure for polycrystalline materials successfully from powder diffraction data. As instrumentation has improved, combined with the introduction of powerful software packages for powder diffraction refinement, such as GSAS[85, 86] or Topas[87, 88], structure solution from powder diffraction data for even the most complex materials has become a reality, where previously structure solution could only originate from single crystal data.

X-ray diffraction is primarily used to solve the structure of crystalline materials, since amorphous materials are lacking in the regular repeating structure which results in a diffraction pattern. The interaction of the oscillating electric field of the incident x-ray beam interacting with electrons associated with the atoms in the material. X-ray diffraction analyses the X-rays scattered from the material retaining the incident beams wavelength. The observed d_{hkl} values provide information regarding the size and shape of the unit cell, while the absolute intensities provide information regarding the location and type of atoms within the cell. The width of the reflections in a powder diffraction pattern also contains information regarding crystallite size, strain and thermal motion in the system. It follows that every material will have a diffraction pattern indicative of the structure and composition of the specific material. Given a good quality diffraction pattern, comparison against known materials combined with refinement of structural parameters can lead to the identification of materials solely from their diffraction pattern.

To refine the structure from a powder diffraction pattern, a number of considerations are required, at least initially. The first observed fact is that the electron density for an atom falls very rapidly with increasing distance from the atoms centre. The assumed fall in electron density therefore leads to the conclusion that there is no overlap between neighbouring atoms. Secondly, it is assumed that the electron density for a given atom is spherically symmetrical. Lastly, each atom within a crystal structure of the same element type is assumed to have the same number of core electrons. This coupled with the assumption that bonding electrons do not contribute to scattering, results in the conclusion that the intensity of scattered X-rays from a given element is independent of the environment of the atom.

2.4 Laboratory based Powder X-ray Diffraction (PXRD)[78]

Laboratory based x-rays are generated in a non uniform spectrum of wavelengths from an X-ray tube (Figure 19). To generate an X-ray beam, electrons are accelerated through high voltages (in the order of kV) through a vacuum tube into a metal anode material. Once electrons impact into the anode, a number of electronic transitions are initiated within the metal, resulting in a range of photons being emitted, with the spectrum comprising of two distinct components. Firstly, at most voltages, a broad spectrum of x-rays are emitted with relatively low intensities, known as the white x-ray emissions. Secondly at a high enough voltage (the exact voltage required depends on the metal the anode is made from), sharp emissions are observed at wavelengths characteristic for each metal. The characteristic x-ray emissions result from the electron beam expelling core electrons from the anode target and another electron falling down from a higher energy state, to take its place, causing the emission of distinct photons with a specific wave

length. It is common however, for a metal target to have multiple characteristic emissions, with each emission being labelled according to the electronic state from which the electron is ejected (for example the most intense emission from a Cu target being labelled $K_{\alpha 1}$ radiation, with an s to p shell transition, with a wavelength of 1.54 Å).

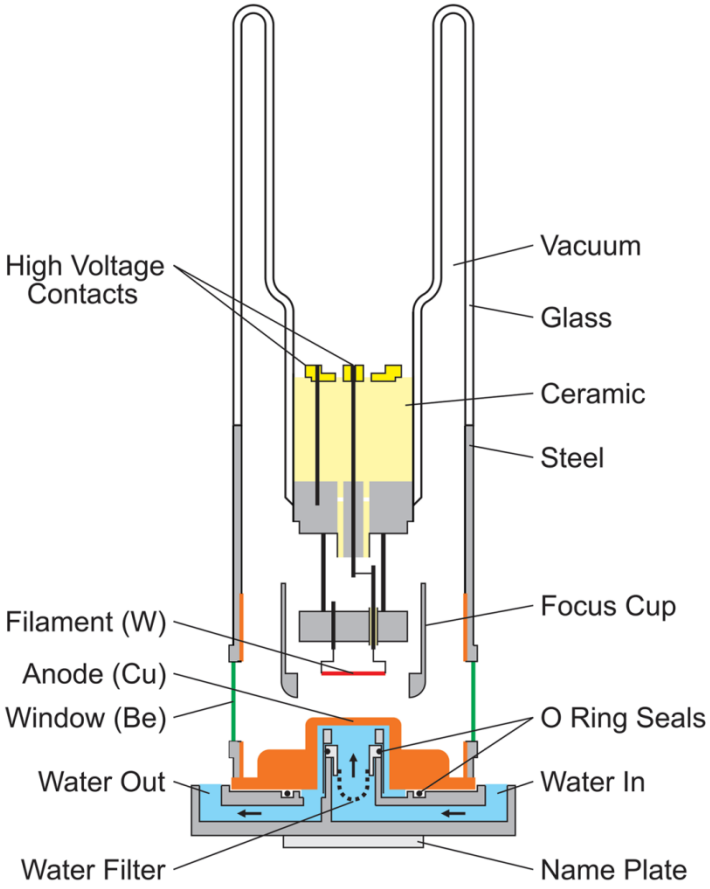

Figure 19 Schematic representation of a Cu x-ray tube, adapted from[78], when electrons pass from the filament (at high voltages), electronic excitations in the anode cause the release of x-ray photons, these x-rays pass through the Be window to the diffractometer optics and onto the sample.

Once an x-ray emission is generated, the photons pass out of the tube through a Be window into the optics of the diffractometer, using a selection of monochromators and filters (before and after the beam is diffracted from the sample) discrete wavelengths can be selected for the diffraction

experiment. A number of different geometries are commonly used in powder diffraction, with two being used within this thesis. The first is, known as Bragg-Brentano reflection[78], the x-ray beam is diffracted from a sample held on a rotating flat plate (Figure 20a). The second geometry type is known as Debye-Scherrer transmission[78], in which the sample is held in a rotating glass (typically borosilicate or silica) capillary of a known radius and is named geometry (Figure 20b). In both situations, the diffracted x-ray beam is typically detected by a moving detector (and/or sample) arm that will move through a 2θ range, on the circumference of the circle in Figure 20 measuring the diffracted intensity, thus generating the X-ray diffraction pattern.

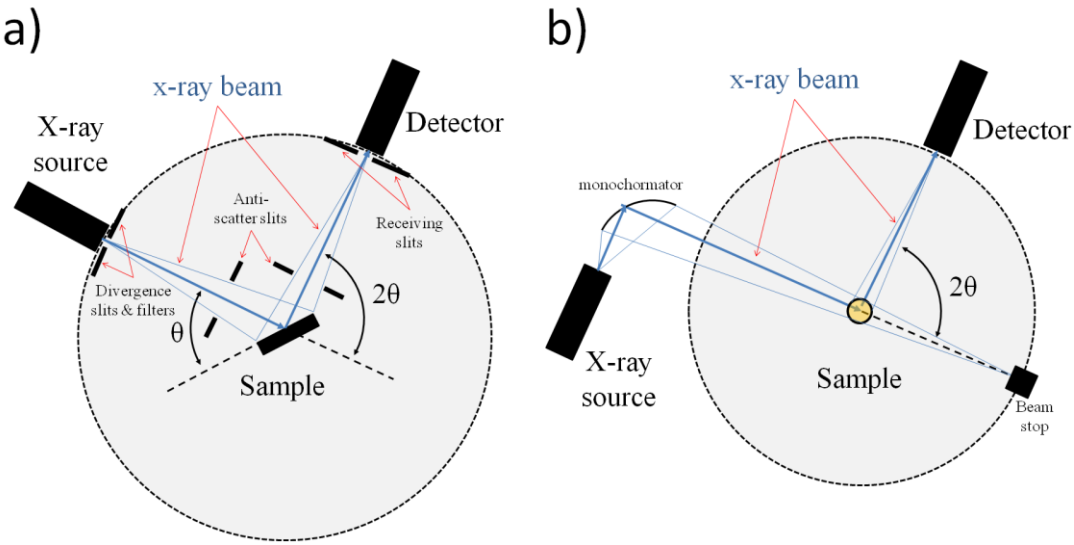

Figure 20 Schematic representations of Bragg-Brentano (A) and Debye-Scherrer geometries for powder diffraction[78]. A) For Bragg-Brentano geometry, the sample is a thin layer of powder attached to a flat plate sample holder, note that both the incident and diffracted beam can additionally be passed through a monochromator before entering the circle (incident beam) or reaching the detector (diffracted beam). B) For Debye-Scherrer geometry, the sample is either loaded into a transparent capillary or mounted on a thin transparent film.

2.5 Neutron Powder Diffraction (NPD)[78, 81]

Neutrons, like x-rays can have wavelengths with a magnitude similar to that of the inter-atomic spacing in crystalline materials, so it is also possible to perform diffraction experiments similar to those performed using X-rays. Unlike PXRD however, neutrons interact with the nucleus of an atom and therefore the technique is very sensitive to the atomic number, rather than electron number. As neutrons interact with the nucleus of an atom it makes it easier to observe lighter elements in the presence of metal atoms, thus making it an ideal technique for the study of oxides. Additionally diffracted neutrons do not have decreasing intensity with the scattering angle like x-rays do and so reflections with higher angles are easier to observe. Being able to measure smaller d_{hkl} (higher θ) values compared to PXRD results in better refinement of structural quantities that are dependent on the width of diffracted reflections (e.g. thermal parameters).

Since neutrons have an inherent spin moment, a neutron beam will interact with spin moments within a sample. It follows that if a sample has a magnetic ordering then, that a neutron diffraction pattern will have additional d_{hkl} reflections and this allows for the identification of a materials magnetic structure. A simultaneous refinement against PXRD and NPD data will contain an increased level of information compared to either of the data sets individually; since x-rays and neutrons interact with different components of the atom resulting in two independent sets of information about the same sample. An example of this is the structural refinement for the $Y_{1.1}Ba_{1.5}Ca_{2.3}Fe_5O_{13}$ ten layer perovskite[15] wherein, the combination of x-ray and neutron powder diffraction allow for the accurate refinement of up to three elements on the same site.

2.6 NPD at the ISIS neutron source on the High Resolution Powder Diffractometer (HRPD)[89, 90]

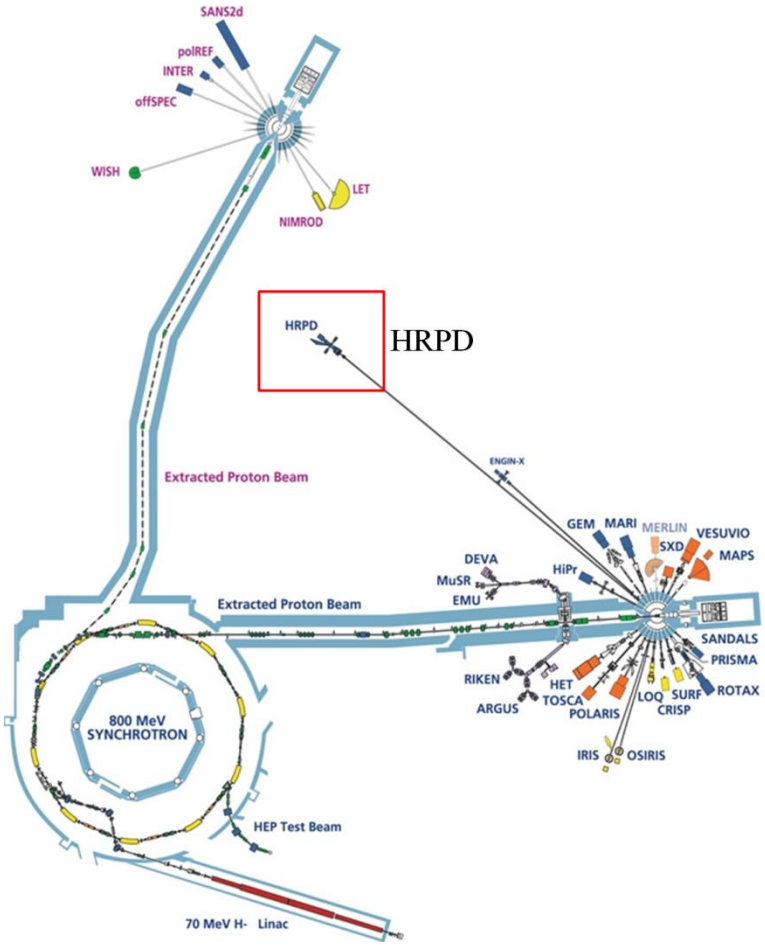

Figure 21 Schematic of the ISIS neutron source, with all of the associated neutron diffraction instrumentation, adapted from figure presented on the STFC-ISIS webpage.

At the ISIS spallation source (Figure 21), neutron generation begins with the formation of hydride ions, which are then accelerated in a linear accelerator and stripped of their electrons in order to produce protons, using an aluminium oxide target. The protons are then accelerated through a synchrotron ring, until they reach energies of 800 MeV. The high energy protons then

collide with a tungsten target, forcing an intra-nuclear cascade, resulting in neutron production. The resulting neutrons have a wide range of energies, the spread of neutron energies generated results in a range of wavelengths which can then be reduced by hydrogen containing moderators, typically water or methane. HRPD is a time of flight (TOF) diffractometer, utilising the entire range of wavelengths produced and therefore relying on solving Braggs law by utilising a continuum of wavelengths rather than diffraction angles, with the diffractometer using a bank of fixed detectors at known angles with respect to the sample. During a TOF experiment, the neutron wavelengths are calculated from the time taken for the neutrons to reach the detector from the source, with the relationship formalised in the following equation:

$$\lambda = \frac{ht}{mL} \qquad \textbf{(2.8)}$$

where h is Planck's constant, m is the mass of a neutron, L is the path length to the diffractometer and t is the time taken to reach the diffractometer. For the HRPD diffractometer (Figure 22), the moderator is methane which is maintained at 100 K. Any error caused by the neutron moderation is reduced substantially by the use of a long path length of 100 m, and therefore aids in achieving high resolution in the machine as the level of error in the path length is very low. The HRPD instrument has three fixed banks of detectors at 30, 90 and 168˚ (Figure 22), with the 168˚ 'backscattering' bank offering the highest resolution. Two choppers operate on the line at 50 Hz and 50/n Hz (where n is typically 5 or 10), these choppers reduce the overlap between neutron pulses. The instrument set up, allows for a wide range of wavelengths to be accessible, with diffracted d-spacings between 0.3 – 16.5 Å observable in diffraction patterns across the three detector banks.

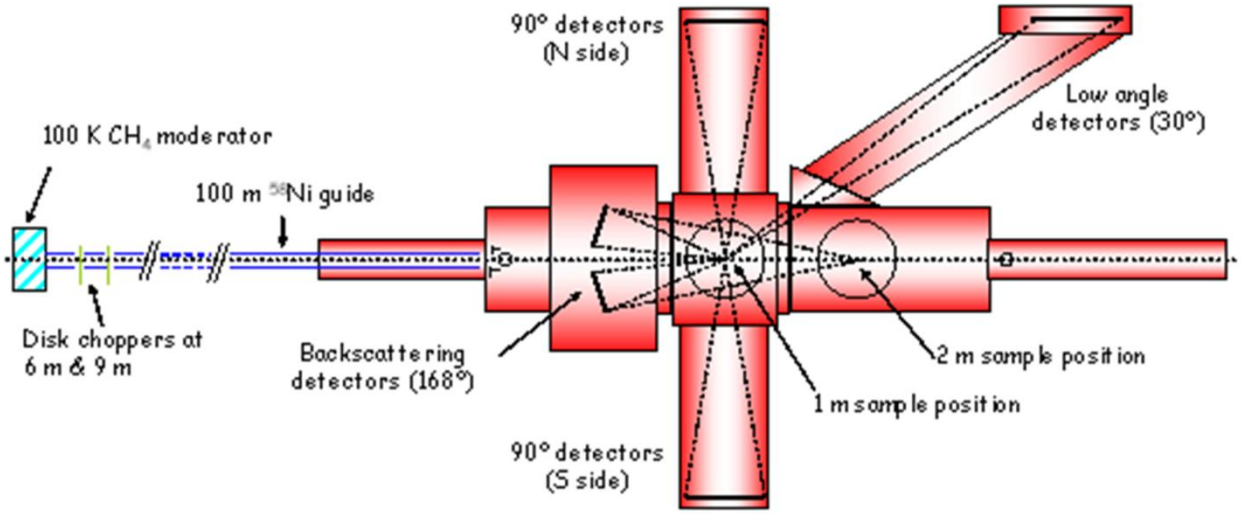

Figure 22 Schematic for the HRPD instrument at the ISIS neutron source, adapted from[90]

2.7 Structure refinement[78, 81]

A refinement consists of computing the expected diffraction pattern from a model structure with the addition of functions to cover contributions to the pattern that are independent of the material, such as a pattern background from the sample holder. Once a pattern for the material is calculated, the differences between the theoretical and observed patterns are calculated. Refinements then take place, adjusting the structural or machine parameters in order to minimise the difference between the two, typically this is performed via a least squares routine[78]:

$$S_y = \sum_i w_i \left(y_i - y_{ci} \right)^2 \qquad \textbf{(2.9)}$$

Where

$$w_i = \frac{1}{y_i}$$

Where S_y is the total residual, w_i is the weighting factor in order to normalise the residual for the number of data points, y_i indicates observed data points, y_{ci} indicates the calculated data points. During the course of the refinement, a number of R factors can be used as a measure of how good the current fit is. The first R weighted pattern (referred to as R_{wp}), is often favoured as there is no bias toward the structural model[78]:

$$R_{wp} = \left\{ \frac{\sum w_i (y_i - y_{ci})^2}{\sum w_i (y_i)^2} \right\}^{1/2} \quad \textbf{(2.10)}$$

A second R factor, R_{exp} can also be calculated for a diffraction pattern, which can be deemed as the best expected fit for the pattern[78]:

$$R_{\exp} = \left[\frac{(N - P)}{\sum w_i y_{ci}^2} \right]^{1/2} \quad \textbf{(2.11)}$$

Where N is the number of observations and P is the number of parameters being refined.

Finally, at the end of a refinement, it is common to quote a 'goodness of fit' (GOF) or χ^2 parameter, both of which related to the combination of R_{wp} and R_{exp}[78]:

$$\text{GOF} = \left[\frac{S_y}{N - P} \right]^{1/2} = \frac{R_{wp}}{R_{\exp}} = \sqrt{\chi^2} \quad \textbf{(2.12)}$$

In order to perform a structure refinement, a pre-requisite is a starting model for the structure. A starting model can be provided from a number of sources, such as a known material, suspected to be analogous to the sample, or as is the case in the results chapters in this thesis, a structural model is provided from theoretical calculations. A number of different refinement methods are available, depending upon what information is sought, with methods available to obtain anything

from just accurate d_{hkl} values to the refinement of the crystal structure; although in all methods, (aside from simply assigning *hkl* values to reflections), refinement of parameters and functions that are machine dependant must be performed[78, 81].

2.7.1 Background, zero shift and peak shape

In most refinement methods, there are three main factors to be accounted for. First is the diffraction pattern background, contributions to the background can come from the sample environment, such as the sample holder or depending on the wavelength an increased background may be observed for samples that fluoresce in the beam. Additionally, some samples will have a background component from structures which have local structures that deviate away from the long range average, or from amorphous phase fractions. Diffraction refinement software contain a number of different functions to fit the background of a diffraction pattern, such as the commonly used Chebechev polynomial function[82].

Secondly, all diffractometers will have the some form of zero error, originating from such factors as the sample holders being misaligned, and is manifested in a uniform shift in all observed d_{hkl} values. If there is concern about the zero error of a diffractometer, when preparing the powder sample with a standard material with known cell dimensions can be mixed in, which can then be fixed during in a refinement. Lastly, the observed peak shape requires refinement, the peak shape contains contributions both from the diffractometer setup and the sample. The sample contribution can come from some structural features, such as the thermal motion of atoms or micro-structure strain in the sample. Due to the complex nature of the contributions toward the

peak shape a wide range of complex peak shape functions have been derived to model them during refinements with several variations implemented within each refinement package[81, 82, 91].

2.7.2 Unit cell size and shape

In some instances only the refinement of the unit cell size and shape is required, for example in initial samples during an experimental investigation or tracking a change in cell dimensions with an increasing temperature for example. Two common methods for refining just the unit cell size and shape, called LeBail[92] and Pawley[93] refinements have been developed, both of these methods focus on accurately determining the unit cell shape and size while using structural models that contain no atomic information and fit an arbitrary intensity to the observed reflections whilst also refining the peak shape. Using such phase refinements can also be useful during the course of investigating a new crystal structure, as it will allow the user to refine the unit cell parameters, zero error and provides a good starting point for the peak shape before taking the atomic structure into account.

2.7.3 Atomic structure – peak intensity and the structure factor

As discussed above, the observed intensity in a diffraction pattern originates from atoms within the unit cell, with the intensity observed at a given *hkl* reflection defined by[81]:

$$I_{hkl} = k \times \left|F_{hkl}\right|^2 \qquad \textbf{(2.13)}$$

Where the F_{hkl} term includes variables that include information about the contents of the unit cell (the form of which is described below) and k includes a number of system dependent terms that are constant for a given structure. The components of the constant k are as follows[81]:

$$k = K \times p_{hkl} \times L_\theta \times P_\theta \times A_\theta \times T_{hkl} \times E_{hkl} \quad \textbf{(2.14)}$$

Where parameters with a subscript *hkl* have a dependency on the d_{hkl} for the reflection in question and a subscript θ indicates a parameter with a dependence on the angle of reflection, each of the parameters is defined as follows:

- K indicates the scale factor, a multiplier used to normalise the calculated intensity against the observed intensities.
- p_{hkl} is the multiplicity factor and takes into account multiple, equivalent *hkl* reflections at a given *hkl* value, for example for a cubic unit cell reflections for the miller indicies [0,0,1], [0,1,0] and [1,0,0] will be equivalent.
- L_θ is the Lorentz multiplier, which is defined for the diffraction geometry.
- A_θ is the absorption multiplier accounting for possible absorption of the beam by the sample in question, this value can be calculated from tablulated values for the composition and sample thickness.
- T_{hkl} is the preferred orientation factor and is a multiplier that accounts for the possibility of the crystallites in the sample having a distribution of orientations which deviates from an ideal distribution.
- E_{hkl} is the extinction multiplier that accounts for deviations away from ideal diffraction, typically this value is very small and usually neglected for powder samples.

The second component of the calculated intensity, the structure factor, containing information on the atomic scattering contribution at each reflection from all the atoms in the unit cell is defined as follows[81]:

$$F_{hkl} = \sum_{j=1}^{n} g^j t^j(s) f^j(s) e^{[2\pi i(hx^j + ky^j + lz^j)]} \quad \textbf{(2.15)}$$

Where:

- *n* indicates the number of atoms in the unit cell.
- g^j indicates the fractional occupancy of atoms *j*, where atom *j* fully occupies the site g^j equals 1.
- *(s)* indicates the angular dependence, $\frac{sin\theta_{hkl}}{\lambda}$ (where λ indicates the wavelength), although as mentioned previously, this angular dependence does not occur for neutron diffraction.
- f^j indicates the atomic scattering factor and is dependent on the type of diffraction being performed (x-ray or neutron), with the values for isolated atoms tablulated.
- The components of the exponential term include the scalar products of the fractional coordinates (x, y, z) for atom *j* by the corresponding *h, k or l* value.

This summation for all atoms in the unit cell at each of the observed reflections combined with the constant *k* is refined along with all of the other components to a calculated pattern described previously. The Rietveld method[83, 84], was developed in order to efficiently refine all of the parameters simultaneously using a least squares method and has become the primary choice for the refinement of powder diffraction patterns. The development of the Reitveld methodology

and the subsequent implementation in a number of software packages has lead to the refinement of complex crystal structures now becoming a reality[78].

2.8 Iodometric titrations[94]

Titrations are an analytical method by which quantitative information may be obtained about a chemical substance. The technique is reliant on the addition of a precisely known quantity of standardised compound. A colour change or change in the conductivity of the sample, indicates a the endpoint to the reaction. The addition of the standard compound induces some physical change in the sample to indicate the end point of the reaction, since the standard is well characterised, information can then be calculated for the sample. Examples of information gained from titrations include the relative molecular mass of a sample or oxygen content of an oxide.

In this thesis, iodometric titrations (titrations dependent on the generation and subsequent reduction of iodine) have been used in order to obtain accurate oxygen contents for oxide materials. Iodometric titrations are dependent on the following reaction with a standardised thiosulphate solution occurring in an acidic solution:

$$I_2 + 2S_2O_3^{2-} \xrightarrow[H^+,H_2O]{} 2I^- + S_4O_6^{2-} \qquad \textbf{(2.16)}$$

Where I_2 is generated by the reduction of the sample by an excess quantity of I^- that has been formed from a salt (typically KI), prior to the reaction:

$$KI \xrightarrow[H^+,H_2O]{} K^+ + I^- \quad \textbf{(2.17)}$$

In an iodometric titration, the end point of the reaction is indicated by a colour change (in the presence of a starch indicator) with the solution changing from indigo to colourless. For the titration of oxide materials and for oxygen content determination, the first step is to standardise the thiosulphate solution concentration by titrating against potassium iodate, with the following iodine generation reactions:

$$KIO_3 \xrightarrow[H^+,H_2O]{} K^+ + IO_3^- \quad \textbf{(2.18)}$$

$$IO_3^- + 5I^- + 6H^+ \xrightarrow[H^+,H_2O]{} 3I_2 + 3H_2O \quad \textbf{(2.19)}$$

Where the generated I_2 is titrated against thiosulphate (equation 2.19), resulting in the overall reaction of 1 mole of KIO_3 with 6 moles of S_2O_3. The concentration is determined since the KIO_3 is accurately weighed prior to the reaction. A pre-requisite for oxygen content determination is knowing what the reduced product is, including the resulting oxidation states, the titrations in this thesis are based upon the reduction of Fe and Mn from unknown oxidation states to 2+. Using the knowledge of the reduced state of the oxide, the following reaction equations can be constructed in order to determine the oxygen content for an oxide:

$$M^{\left(2+\frac{x}{2}\right)+}O_{1+x} + 2xI^- \xrightarrow[H^+,H_2O]{} M^{2+}O + xI_2 + xOH^- \quad \textbf{(2.20)}$$

$$xI_2 + 2xS_2O_3^{2-} \xrightarrow[H^+,H_2O]{} 2xI^- + xS_4O_6^{2-} \quad \textbf{(2.21)}$$

Where M indicates the transition metals of interest in the metal oxide, where the total quantity of transition metals in the oxide is normalised to be 1 (e.g. Fe_2O_3 becomes $FeO_{1.5}$). Note that the

hydroxide species generated on the right hand side of equation (2.20) are assumed to combine with H^+ to form H_2O. For the perovskite material titrated in chapter 3, the A-site species do not react under the titration conditions and so the above reaction equation is still valid. In order to determine the oxygen content, the desired quantity is the moles of oxygen generated (η_{ex}) per mole of starting oxide (η_{mo}):

$$x = \frac{\eta_{ex}}{\eta_{mo}} = \eta_{ex} \times \eta_{mo}^{-1} \qquad \textbf{(2.22)}$$

From equation (2.20) we know that the number of moles of reduced oxide (η_{red}) is equal to the number of moles of the starting oxide, so (2.21) can be written as:

$$x = \eta_{ex} \times \eta_{red}^{-1} \qquad \textbf{(2.23)}$$

From (2.20) it follows that η_{ex} is equal to the number of moles of I_2 that are titrated (η_I) and so η_{ex} is experimentally determined from the quantity of thiosulphate used;

$$\eta_I = \eta_{ex} = \frac{C_s \times V_s}{2} \qquad \textbf{(2.24)}$$

Where C_s and V_s indicate the concentration and volume of thiosulphate solution used in the titration. In order to determine x, η_{red} requires definition relative to the known experimental quantities, which can be achieved as follows:

$$\eta_{red} = \frac{m_{red}}{M_{red}} \qquad \textbf{(2.25)}$$

Where m_{red} indicates the mass of the reduced oxide and M_{red} is the molar mass of the reduced species (given in $gmol^{-1}$), the mass of the reduced oxide can be expressed relative to the sample mass and the mass of the evolved oxygen (m_o) during the titration reaction:

$$m_{mo} = m_{red} + m_o \Rightarrow m_{red} = m_{mo} - m_o$$
$$m_{red} = m_o - (\eta_{ex} \times M_o) \quad \textbf{(2.26)}$$

Where M_o is the molar mass of an oxygen atom, this is the substituted into (2.25) to give:

$$\eta_{red} = \frac{m_s - \eta_{ex} M_o}{M_{red}} \Rightarrow \eta_{red}^{-1} = \frac{M_{red}}{m_s - \eta_{ex} M_o} \quad \textbf{(2.27)}$$

Then equation (2.27) is substituted into equation (2.23), allows for the determination of x:

$$x = \eta_{ex} \times \eta_{red}^{-1} = \frac{\eta_{ex} M_{red}}{m_s - \eta_{ex} M_o} \quad \textbf{(2.28)}$$

Which can then be rearranged to give:

$$x = \frac{M_{red}}{\frac{m_s}{\eta_{ex}} - \frac{\eta_{ex} M_o}{\eta_{ex}}} = \frac{M_{red}}{\frac{m_s}{\eta_{ex}} - M_o}$$
$$x = \frac{M_{red}}{m_s \times \left(\frac{1}{\eta_{ex}} - \frac{M_o}{m_s} \right)} \quad \textbf{(2.29)}$$

With (2.29) used to calculate the oxygen content of samples produced in Chapter 3.

2.9 Mössbauer Spectroscopy[95]

The Mössbauer spectra presented in this thesis were collected by Dr. M. Thomas (University of Liverpool; Department of Physics) who also fitted the data to nuclei environments, working with myself on their interpretation. Mössbauer developed the technique[95, 96] and is based upon a Gamma Ray (GR) beam of varying wavelengths being passed through a solid sample and the absorbance of the sample measured, where absorption is observed information about the target nuclei in the sample can be obtained.

The GR beam is generated from a radioactive source held within a solid state matrix. The decay of the source then emits GRs, with a known wavelength and energy for a stationary source. The wavelength of the emission can be controlled by exploiting the Doppler effect; motion of the source will alter the wavelength of the emitted GRs, from this the absorbance of the GR beam is typically quoted across a range of velocities of the source motion (mm/s), and the shift from zero referred to as the isomer shift.

Mössbauer spectroscopy is reliant on the Mössbauer effect[95, 96] recoilless emission and absorption of GRs; if either the source or the sample were to recoil the energy of the GR would be affected due to a quanta of energy lost to recoil motion. Therefore a requirement for the technique is for both the source and the sample to be locked in the solid state, since in a solid lattice there is little possibility for the nuclei to recoil. The Mössbauer effect is most prevalent at low temperatures where there is little thermal motion in the sample. As temperature and thermal motion increases the Mössbauer effect drops and the level of recoilless absorption in the sample decreases, until ultimately the effect is not observable, although the temperature at which this occurs is sample dependant.

The absorption of a GR by the sample is reliant on the incoming GR having the correct energy to excite the target nuclei. Mössbauer spectra are typically calibrated against a standard sample, recorded at 0 mm/s; the ^{57}Fe nuclei spectra included in this thesis, were calibrated using bcc iron metal, with ^{57}Co used as the GR source.

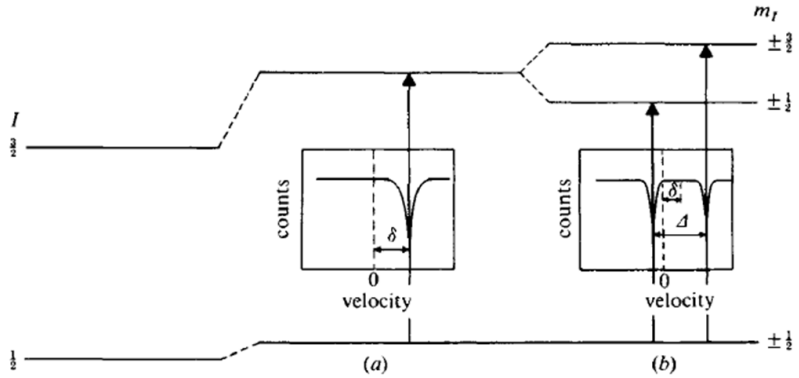

Figure 23 Schematic of ^{57}Fe Mössbauer spectra[95]; a) for a single transition with an isomer shift from zero caused by the chemical environment of the ^{57}Fe atoms. b) For a quadrupole splitting centred around an isomer shift, with the splitting caused by two accessible excited states for the ^{57}Fe atoms.

The signal from each target atom is dependent on the number of allowed transitions of the target nuclei, giving rise to one peak in the spectrum for each transition (Figure 23a). Where multiple transitions are allowed the signal will split into multiple peaks centred on a velocity in the spectrum. The velocity at which an atom absorbs a GR is dependent on the local environment, such that different geometries will give rise to a different signal in Mössbauer spectra, with the quantities of each environment being refine-able (as used in chapter 3). The absorption of a GR in a system containing a nuclear quadrupole moment has two allowed transitions (Figure 23b). Systems with magnetic ordering such as those described in the introduction chapter, give rise to six possible transitions[95, 97] (Figure 24a). As with signal intensity, there is also a temperature effect on the velocity by which signals are split, this can be caused by thermal motion. In the

case of magnetic splitting, the extent of magnetic ordering varies with temperature; stronger magnetic moments and coupling results in larger splitting, hence typically splitting will decrease with increasing temperature, until they combine into a single peak when magnetic ordering breaks down (Figure 24b)[97].

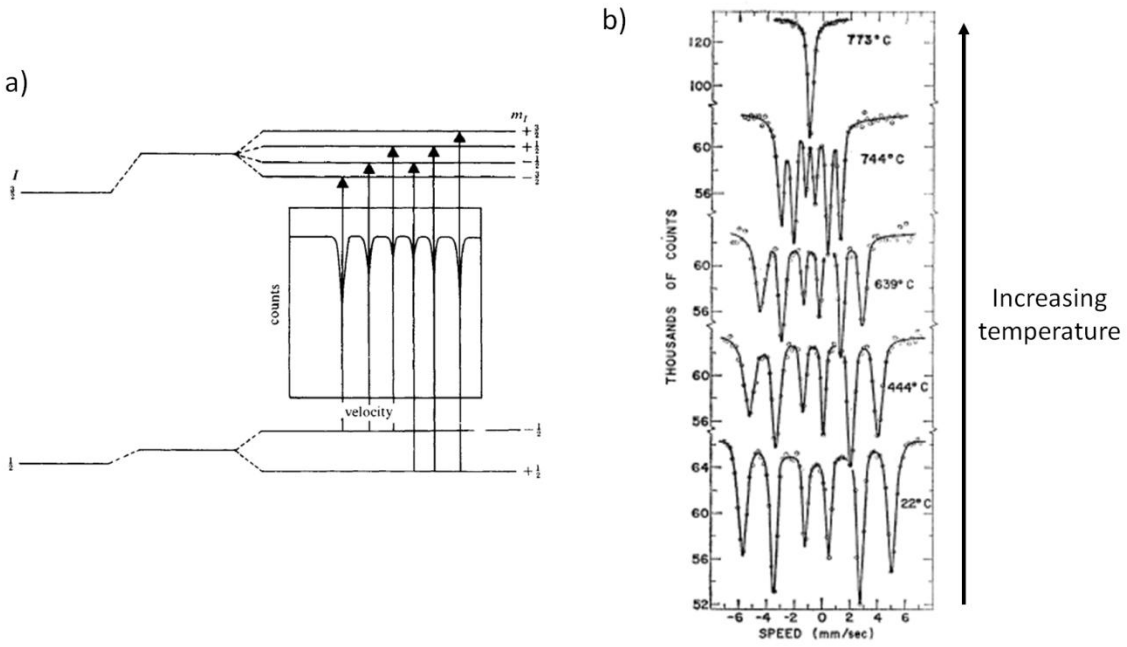

Figure 24 a) Representation of splitting for ^{57}Fe Mössbauer for a magnetically ordered system[95]. b) Typical splitting of ^{57}Fe Mössbauer spectra with varying temperature as the level of magnetic ordering changes[97].

2.10 Density Functional Theory[18, 98] (DFT)

In this thesis force field methods (detailed in the next section) are combined with *ab-initio* methods; in chapters 3 & 4, DFT is used exclusively and in chapter 5, DFT is used to calculate relative energies for a small number of structures after initial screening of large libraries of structures using force fields.

In order to calculate the ground state for a many electron system from first principles, one would seek to solve the time-independent many-body Schrödinger equation for the system of *N* interacting electrons[18]:

$$\left\{-\frac{1}{2}\sum_{i=1}^{N}\nabla_i^2+\sum_{i\neq j}\frac{1}{\left|\vec{\mathbf{r}}_i-\vec{\mathbf{r}}_j\right|}+\sum_{i=1}^{N}v_{ext}(\vec{\mathbf{r}}_i)\right\}\Psi(\vec{\mathbf{r}}_1,\vec{\mathbf{r}}_2,...,\vec{\mathbf{r}}_N)=E\Psi(\vec{\mathbf{r}}_1,\vec{\mathbf{r}}_2,...,\vec{\mathbf{r}}_N) \qquad \textbf{(2.30)}$$

Where v_{ext} is the external potential experienced by the electrons from interactions with the nuclei given the form:

$$v_{ext}=\frac{-Z}{\mathbf{r}}-\frac{Z}{\left|\mathbf{r}-R\mathbf{z}\right|} \qquad \textbf{(2.30a)}$$

Where Z equals the nuclear charge and **z** equals a unit vector along an inter-nuclear bond at separation R, and ψ indicates the many-body wavefunction. The ground state results in a ground state potential energy given by the term *E* in (2.30), however, since the dimension of the wavefunction grows with 3*N* electrons the computational cost grows very quickly and even simple systems become difficult to compute. This rapid increase in computational cost means that compromises must be made between how accurately the problem is solved and how much computational effort is required.

The most common approach to solving this problem, developed by Hohenberg, Kohn and Sham[99, 100], is referred to as DFT. The interacting particle equation (2.30) is replaced by a non-interacting one, with the many electron wavefunction replaced by electron density and the electron-electron Coulombic component of the equation replaced by a effective background potential of the electron density[18]. These modifications result in the problem being reduced from 3*N* dimensions to *N* non-interacting one electron problems. In this section the basics of DFT and modifications to the basic theory that are utilised for the systems studied in this thesis are detailed.

2.10.1 The energy functional

The development of DFT began with Hohenberg and Kohn showing that the ground state energy of a system can be expressed relative to its electron density ($n(\mathbf{r})$) with the system in an external potential ($v(\mathbf{r})$) at coordinates, **r**:

$$E[n] = \int d\mathbf{r}\; v(\mathbf{r})n(\mathbf{r}) + \frac{1}{2}\int d\mathbf{r}\, d\mathbf{r}'\; \frac{n(\mathbf{r})n(\mathbf{r}')}{|\mathbf{r}-\mathbf{r}'|} + G[n] \qquad \textbf{(2.31)}$$

Where the first term is a function of the density and external potential, describing the interaction between electrons and nuclei, the second includes the Coulomb (or sometimes referred to as the Hartree) energy and *G[n]* is an (as yet) unknown universal functional of the electron density ($n(\mathbf{r})$) and it was shown by Hohenberg and Kohn that the energy, *E[n]* will have a minimum at the unique ground state electron density[99].

Later, it was suggested by Kohn and Sham[100] that the universal functional could be divided into two components; the kinetic energy of the system of non-interacting electrons ($T_s[n]$) and the exchange and correlation (XC) component of the energy in a separate term, E_{XC}:

$$G[n] \equiv T_s[n] + E_{XC}[n] \tag{2.32}$$

This can then be substituted back into (2.31) to give the energy functional of the electron density in the form:

$$E[n] = T_s[n] + \int dr\, v(\mathbf{r})n(\mathbf{r}) + \frac{1}{2}\int dr\, dr' \frac{n(\mathbf{r})n(\mathbf{r}')}{|\mathbf{r}-\mathbf{r}'|} + E_{XC}[n] \tag{2.33}$$

This results in the ground state energy now being split into four individual terms, from left to right on the right hand side of the equation;

- Electron kinetic energy,
- Electron – nuclear interactions
- Electron – electron Coulomb interactions
- Exchange correlation term

It is possible to determine the first three terms and a number of commonly used approximations to account for the exchange correlation term (see the Exchange Correlation sub-section below). To obtain the ground state of a system, the objective then becomes to find the minimum energy for equation (2.33), with respect to the electron density (n), under the constraint that the number of electrons in the system remains constant. In order to determine this minimum, the electron density that satisfies the following equation must be sought[99]:

$$\frac{\delta E[n]}{\delta n(\mathbf{r})} = \frac{\delta T_s[n]}{\delta n(\mathbf{r})} + \varphi(\mathbf{r}) + \mu_{XC}(\mathbf{r}) = \mu \qquad \textbf{(2.34)}$$

Where μ is a lagrange multiplier, and is equal to the fermi energy:

$$\varphi(\mathbf{r}) = v(\mathbf{r}) + \int dr' \frac{n(\mathbf{r}')}{|\mathbf{r} - \mathbf{r}'|} \qquad \textbf{(2.35)}$$

And:

$$\mu_{XC}(n) = \frac{\delta E_{XC}}{\delta n(\mathbf{r})} \qquad \textbf{(2.36)}$$

Resulting in equation (2.34) having the full form:

$$\frac{\delta E[n]}{\delta n(\mathbf{r})} = \frac{\delta T_s[n]}{\delta n(\mathbf{r})} + v(\mathbf{r}) + \int d\mathbf{r}' \frac{n(\mathbf{r}')}{|\mathbf{r} - \mathbf{r}'|} + \frac{\delta E_{XC}}{\delta n(\mathbf{r})} \qquad \textbf{(2.34a)}$$

Where μ_{xc} indicates the exchange correlation contribution to the potential with respect to the electron density, it follows that for a given μ_{xc} and φ the electron density that fulfils equation (2.34) can be found by solving the one particle (or electron) Schrödinger equation:

$$\left\{ -\frac{1}{2}\nabla^2 + \left[\varphi(\mathbf{r}) + \mu_{XC}(n(\mathbf{r}))\right] \right\} \psi_i(\mathbf{r}) = \varepsilon_i \psi_i(\mathbf{r}) \qquad \textbf{(2.37)}$$

Where the electron density is given by:

$$n(\mathbf{r}) = \sum_{i=1}^{N} |\psi_i(\mathbf{r})|^2 \qquad \textbf{(2.38)}$$

In order to find the ground state of the system the equations (2.35-2.38) are solved via using a self-consistency loop, as outlined in Figure 25, where the loop is repeated and updated until a break (or convergence) criteria is met, where the energy at each iteration is found by[100]:

$$E = \sum_{i}^{N} \varepsilon_i - \frac{1}{2} \iint d\mathbf{r} d\mathbf{r}' \frac{n(\mathbf{r}) n(\mathbf{r}')}{|\mathbf{r} - \mathbf{r}'|} + E_{XC} - \int d\mathbf{r}\, n(\mathbf{r}) \mu_{XC}(n(\mathbf{r})) \quad \textbf{(2.39)}$$

The ground state energy for the current nuclei configuration of the system is then defined by the energy obtained from the last iteration.

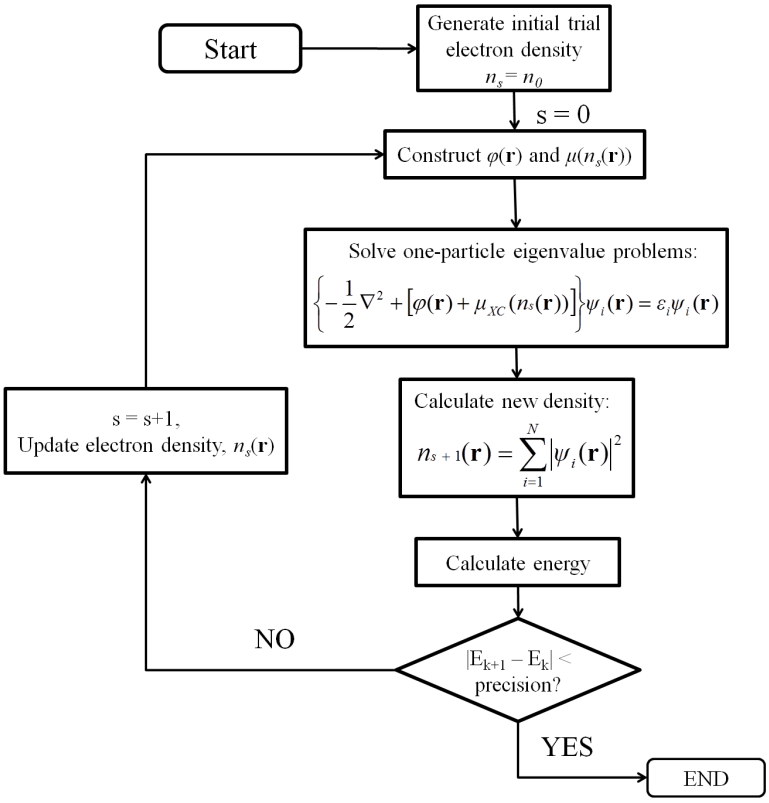

Figure 25 The basic self-consistent algorithm for finding the minimum energy with respect to electron density within the framework of the equations set out in this chapter, with the routine as outlined in[98] formulated to converge on the systems energy with s indicating the iteration number for the calculation, it is possible to write out the same routine to converge on either the energy or the electron density.

2.10.2 Exchange Correlation (XC) Functionals[18, 101]

Several different methods have been developed to approximate the XC component of DFT, with two approximations commonly used; the Local Density Approximation (LDA) and the Generalised Gradient Approximation (GGA). For LDA, one assumes that the nature of the 'electron gas' in the system varies slowly across space, such that the XC term can be approximated as follows[18]:

$$E_{XC}^{LDA}[n] = \int d^3r\, n(\mathbf{r})\varepsilon_{XC}^{\text{hom}}(n(\mathbf{r})) \qquad \textbf{(2.40)}$$

Where ε_{XC}^{hom} is the XC energy per electron in a homogeneous electron gas with the electron density $n(\mathbf{r})$. This formulation of the XC energy is exact in the case of a uniform electron gas, where the electrons move within a uniform positive background (in order to maintain charge neutrality). For a GGA XC functional, the XC adds in a term for electron density variation in the system[18];

$$E_{XC}^{GGA}[n] = \int d^3r\, \varepsilon_{XC}^{\text{hom}}(n(\mathbf{r})F_{XC}s(\mathbf{r})) \qquad \textbf{(2.41)}$$

This differs from the LDA functional by the inclusion of the $F_{XC}(s(\mathbf{r}))$ term which defines how much the exchange enhances with the term $s(\mathbf{r})$, which indicates how the electron density gradient varies. If the $s(\mathbf{r})$ term is equal to zero, then one returns to the LDA XC functional. There exist a number of implementations of GGA, with the two most commonly used forms being the Perdew-Wang 91 (PW91)[102] and Perdew-Burke-Ernzerhofer (PBE)[103].

Note that the above equations assume that there is no overall spin polarisation in the system, however, there are published forms including collinear spin polarisation for both GGA[103] and LDA[101] known as the local spin density approximation, LSD XC functionals. In both cases the

inclusion of spin modifies the XC term to be related to the relative spin polarisation, ζ, defined as[103]:

$$\zeta = \frac{\left(n_{\uparrow} - n_{\downarrow}\right)}{n} \tag{2.42}$$

Where $n_{\uparrow}$ and $n_{\downarrow}$ indicates the spin up and spin down density and n is the total spin density.

2.10.3 Plane wave solutions to the Kohn Sham equations[18, 101, 104]

As described in the previous section, the problem of many interacting electrons from the Schrödinger equation is simplified to a series of non-interacting electrons acting in an effective potential, $V(\mathbf{r})$ by using DFT, we are searching for solutions to the one particle time-independent Schödinger equation:

$$\left[-\frac{1}{2}\nabla^2 + V(\mathbf{r})\right]\psi_n(\mathbf{r}) = \varepsilon_n\psi_n(\mathbf{r}) \tag{2.43}$$

For a periodic system, $V(\mathbf{r})$ is also periodic:

$$V(\mathbf{r}+\mathbf{R}) = V(\mathbf{r}) \tag{2.44}$$

Where **R** is a lattice vector:

$$\mathbf{R} = n_1\mathbf{a}_1 + n_2\mathbf{a}_2 + n_3\mathbf{a}_3 \tag{2.45}$$

Where $\mathbf{a_1}$, $\mathbf{a_2}$ and $\mathbf{a_3}$ are the unit cell vectors of the system. The first assumption is that the system is confined to the volume Ω, which contains N unit cells each with volume Ω_N and therefore $\Omega = N\Omega_N$. According to Blochs theorem, a wavefunction for such a system can be

written as a product of plane waves and a periodic function, $\mu_k(\mathbf{r})$ retaining the same periodicity as the potential, such that:

$$\psi_k(\mathbf{r}) = e^{i\mathbf{k}\cdot\mathbf{r}}\mu_k(\mathbf{r}) \quad \textbf{(2.46)}$$

Which, then placed in a periodic system becomes:

$$\psi_k(\mathbf{r}+\mathbf{R}) = e^{i\mathbf{k}\cdot\mathbf{R}}\mu_{\mathbf{k}}(\mathbf{r}) \quad \textbf{(2.47)}$$

k indicates a wavevector in the first Brillouin zone, which is the primitive unit cell in reciprocal space containing all of the unique values of ***k*** and results in N discrete values due to the periodic system. The result of this is that the wavefunction is the same at the positions **r** and **R** except for a phase shift caused by the exponential term and it also results in the electron density having the same periodicity as the potential. The function $\mu(\mathbf{r})$ can be expanded in terms of plane waves to give:

$$\mu_{\mathbf{k}}(\mathbf{r}) = \sum_{\mathbf{G}} c_{\mathbf{k}}(\mathbf{G}) e^{i\mathbf{G}\cdot\mathbf{r}} \quad \textbf{(2.48)}$$

Where **G** is a reciprocal lattice vector, defined by:

$$\mathbf{G} = \sum_i m_i \mathbf{b}_i \quad \textbf{(2.49)}$$

Where m_i are integer values and $\mathbf{b_i}$ are the parameters of the reciprocal lattice. The reciprocal lattice is defined such that $\mathbf{R}\cdot\mathbf{G} = 2\pi l$, where l is an integer, so the full wavefunction can then be written by:

$$\psi_{\mathbf{k}}(\mathbf{r}) = \sum_{\mathbf{G}} c_{\mathbf{k}}(\mathbf{G}) e^{i(\mathbf{k}+\mathbf{G})\cdot\mathbf{r}} \quad \textbf{(2.50)}$$

The periodic potential equation (2.44) can also be expanded in terms of plane waves in reciprocal space to give:

$$V(\mathbf{r}) = \sum_{\mathbf{G}} V(\mathbf{G}) e^{i\mathbf{G}\cdot\mathbf{r}} \qquad \textbf{(2.51)}$$

By insertion of equations (2.50) and (2.51) into the one particle time independent Schrödinger equation (2.43), the problem is transformed into a number of independents equation, with one for each point sampled in *k* space. Equation (2.43) is solved numerically by plane wave DFT packages such as the Vienna *ab-inito* Simulation Package (VASP)[105, 106] used within this thesis. In order to compute these plane waves however, two parameters are required, firstly the set of plane waves need to be truncated with a kinetic energy cutoff (also referred to as the plane wave cutoff). Secondly, the number of points in *k* space within the first Brillouin zone to be sampled needs to be specified. The exact number of *k*-points required is determined in preliminary calculations or by starting from defaults suggested by the specific DFT package used. The number of *k*-points used within each chapter is specified in the corresponding methods section.

2.10.4 Pseudopotentials[98]

As the number of atoms increases in a system, especially when atoms with large number of electrons are included (e.g transition metals, or the heavy A-site species found in perovskites) the computational cost increases. A method commonly used in DFT calculations to lighten the computational load is to create a pseudopotential, typically containing two approximations: firstly the core electrons are treated as a frozen core. The frozen core approximation assumes that the interactions of core electrons with the surrounding chemical environment are minimal

and are therefore ignored and therefore only the valence electrons interact with the chemical environment.

In practice the core electron wavefunctions are generated from calculations on the isolated atoms, libraries of which are provided by most DFT packages. The core electron wavefunctions are then fixed throughout the DFT calculation and only the valence electron wavefunctions are updated throughout the calculation. Although it should be noted that for some systems, libraries exist where some of the sub-valent orbitals are treated as if they were valence in order to improve the accuracy of the calculation.

Valence electron wavefunctions, when in the core region of the atom, have very rapid oscillations due to interactions with core electrons, however, outside the core region the wavefunction is much smoother since the core electron wavefunctions are essentially zero. In order to reduce the complexity of a valence wavefunction is the exact wavefunction is replaced with a node less function in the core region retaining the electron density of the exact wavefunction[98] (also referred to as the all electron wavefunction, Figure 26). Once the pseudo wavefunction leaves the core region of the atom the pseudo function is designed such that it returns to match the exact electron wave function. There are a number of different methods by which pseudo potentials have been implemented[106-109], with the method utilised within this thesis being the Projector Augmented Wave method (PAW)[106] as implemented in VASP.

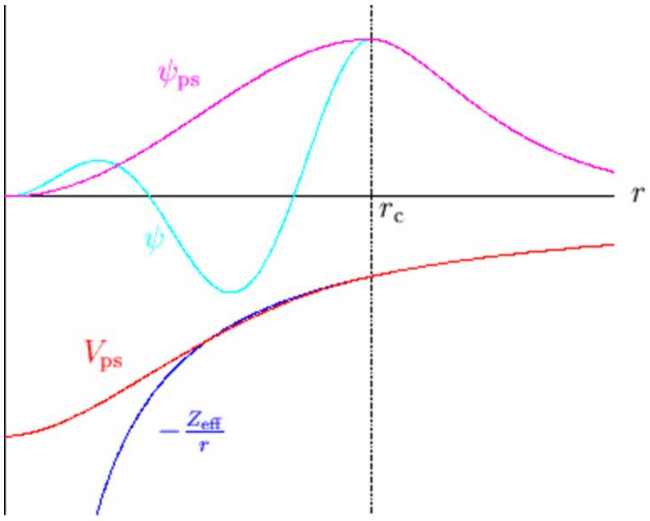

Figure 26 Schematic representation of pseudo wavefunctions and potential energies, relative to those generated by an all electron method[110] the all electron wavefunction and potential is denoted in cyan and blue respectively, and the pseudo wavefunction and potential in magenta and red respectively, with the pseudo potential and wavefunction also denoted by a subscript "ps".

2.10.5 DFT + U[98]

An inherent problem of the DFT method arises from the Coulomb term in the Kohn-Sham equations, in which an electron interacts with the total electron density. As the electron in question contributes to the total electron density, it follows that the electron is interacting with itself, known as the self interaction error (SIE), the error is introduced due to not knowing the exact form of the XC functional[98]. The SIE causes localised electron orbitals to be destabilised and so DFT often results in orbitals being spread out spatially in order to minimise self-interaction. When modelling systems that should have localised orbitals, such as in semiconductors with partially filled *d* or *f* orbitals (including the perovskite systems studied in this thesis), no localised orbitals would be calculated, this results in incorrect computation of band structures and total energies[15, 111, 112].

In order to help correct for this SIE in systems with localised electrons the DFT+U method was developed. DFT+U introduces a correction to the DFT energy; for each atom we apply a numerical parameter U_{eff} to specified orbitals (*d* orbitals in the case of this thesis), with U_{eff} defined as[98]:

$$U_{eff} = U - J \quad \textbf{(2.52)}$$

Where U and J are parameterised, in this thesis J is typically equal to 1. Since U_{eff} is a numerical parameter, it requires fitting to some known property of a relevant material, typically this is done by varying the value of U, with J remaining fixed, parameters to which a U_{eff} parameter can be fitted include band gaps or calculated reaction energies. The parameter sets used in this thesis in the calculation of oxide materials, were used as published (relevant references given in each chapter), where parameters had been fitted to reproduce experimentally determined reaction energies to form ternary oxides from binary oxides and oxygen gas where available.

2.11 Force Field (FF) Calculations[69, 70]

In some instances, when information from calculations is required (such as the lowest energy configuration of atoms/ions) and the system in question contains large numbers of atoms and/or a large number of optimisations are required (as is the case in chapter 5) it is not feasible to use purely *ab-inito* methods, due to the computational cost.

FF calculations typically model atoms as a solid charged sphere with radius equal to tabulated values for the element(s) in question. Energies are then calculated according to parameterised

interactions between atoms, where parameters are fitted to known structures and properties. Geometry relaxation can then be performed in order to minimise this energy as with any other computational method.

The downside for force fields however, lies in the realisation that a parameterised force field will only successfully describe systems for which the potential and parameters were designed (e.g. a potential designed for covalent bonding will not be able to model an ionic system). These drawbacks lead to the creation of numerous types of force field potential, such as the Lennard-Jones and Buckingham potentials combined with large libraries of published interatomic potential parameters.

2.11.1 Interatomic potentials

The FF calculations used in chapter 5 were performed using the General Utility Lattice Program (GULP)[69, 70] modelling only two-body interactions, where the energy resulting from interactions between ions are comprised of two components and defined by[113]:

$$U_{ij} = U_{ij}^{short} + U_{ij}^{long} \quad \textbf{(2.53)}$$

Where U_{ij} is the total two body interaction between atoms i and j, U_{ij}^{short} is for short range interactions typically covered by potentials such as the Buckingham potential (defined below), U_{ij}^{long} is a much longer range component, covered by a long range Coulomb interaction of the form:

$$U_{ij}^{long} = \frac{q_i q_j}{4\pi\varepsilon_0 r_{ij}} \quad \textbf{(2.54)}$$

Where q_i and q_j are the formal charges on ions i and j to be specified by the user, ε_0 is the permittivity of free space and r_{ij} is the inter-atomic distance between atoms i and j. In GULP this is implemented via the Ewald method[113, 114]. In this thesis the second energy component, is described by a short range Buckingham potential with the form that models the close range interactions of ions:

$$U_{ij}^{short} = A\exp\left(\frac{-r_{ij}}{\rho}\right) - \frac{Cij}{r_{ij}^6} \quad \textbf{(2.55)}$$

Where the terms A, ρ and C_{ij} are fitted parameters, the exponential term provides a repulsive wall for the interaction and the C_{ij} term models the short range attractive component of the potential, and the interaction will have a user defined maximum cut-off distance. Some atoms in the structures studied in this thesis make use of a polarisability 'shell' model[115]. This model allows for the polarisation of some atoms, conceptually the ion is split into two components; a core and shell. The core has the mass of the atomic species, and a charge associated with it, to model the nucleus and core electrons. The shell is mass-less with an associated charge to represent the effect of valence electrons, the concept should not be taken too seriously however, since it is common for shells to have an overall positive charge (as is the case in chapter 5). The shell and core are screened from each other with a spring connecting them, with a fitted force constant (k_s). The polarisability of an atom is then defined by:

$$\alpha = \frac{q_s^2}{k_s} \quad \textbf{(2.56)}$$

When the shell model is used in a system, convention is for the long range Coulomb interaction to act on both the shell and core and thus the long range potential interacts with the full formal charge on an ion. With shells present it is also convention for the short range potential to only interact with the shells of ions. Note that when modelling a system it is possible to have a combination of atoms with and without shells present, and therefore potentials that act between the core of one atom and the shell of another.

2.11.2 Generating FF potential parameters

Due to the nature of FF calculations, choosing potential parameters governs the result and so the process by which they are chosen is of extreme importance; choosing a bad force field will only lead to bad results!

In order to test prospective force field parameters for this thesis, potential sets were first gathered from literature. Additionally, a known and well characterised related structure is required; it does not have to be the structure to be studied however. An ideal structure to which a FF can be parameterised will have a well defined structure from experimental data or a very well converged structure from *ab-initio* calculations (such as DFT). Force field parameters are then tested using the following routine:

- If the potential set with the best fit does not satisfactorily reproduce the target structure (typically obtaining the correct connectivity and obtaining the lattice parameters/unit cell volume to within a few percent), then the pair potentials are varied in order to determine which potential has the largest effect on the calculated structure, this parameter is then refined using the internal fitting routines found within GULP.

- This last point is then repeated as necessary until the structural parameters are reproduced with the desired level of accuracy and typically should only result in a small number of newly fitted parameters.

2.12 A note on computational hardware used.

All of the FF calculations used in chapter 5 were performed using the University of Liverpool's high performance computing (HPC) cluster as serial jobs, queued in batch jobs by system. Each batch job contained in the order of 10,000 structures, with upto 128 structures being allowed to run simultaneously.

For the DFT calculations in chapter 3, all were performed using the University of Liverpool's HPC cluster, running on either 16 or 32 cores, divided across computing nodes each containing 2 quad core cpus. The DFT calculations performed in chapters 4 and 5 were performed using the HECToR super computer, with access provided through G.Darling's membership of the Materials Chemistry Consortium (MCC). Structures were relaxed using upto 144 cpu cores divided across 24 core nodes.

Chapter 3. Prediction and synthesis of $YBa_2Fe_2MnO_8$

3.1 Abstract

In this chapter energies for the reaction to form $YBa_2Fe_{3-x}M_xO_8$ (where M = Co, Ni or Mn and x = 1, 2 and 3) from binary oxides and oxygen gas were calculated using Density Functional Theory (DFT). Based upon these calculations predictions were made about favourable levels of doping and B-site ordering for $YBa_2Fe_{3-x}M_xO_8$. Where dopings were calculated to be stable, these compositions were investigated experimentally. It was found that with a small optimisation of the Y: Ba ratios a new triple perovskite is formed. In addition to this, where doping is predicted to be least favourable was also investigated in order to test whether the DFT calculations can estimate the solid solution limit. The structure of the synthesised triple perovskite was then analysed using Powder X-ray Diffraction (PXRD), iodometric titrations, Mössbauer spectroscopy and Neutron Powder Diffraction (NPD). The observed structure and calculated structures were then compared and found to be in good agreement.

3.2 Introduction

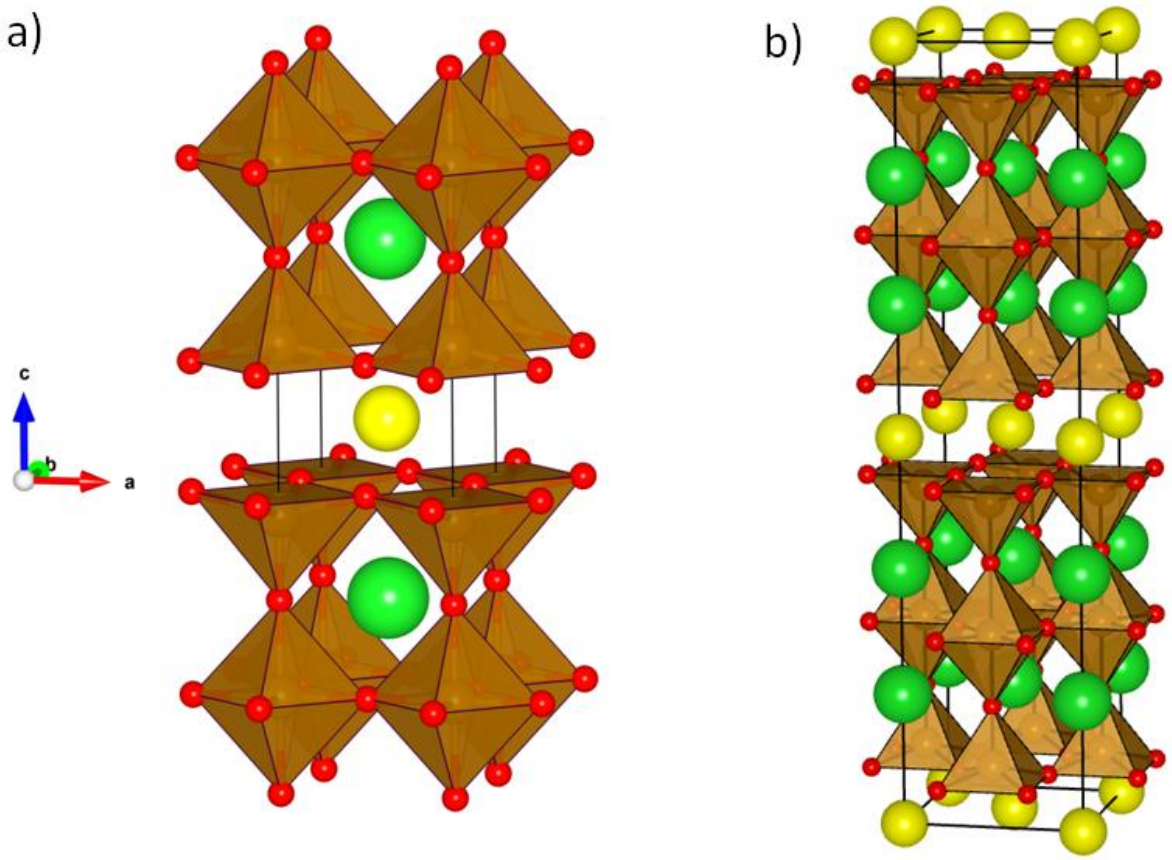

Figure 27 a) Reported structure for $YBa_2Fe_3O_8$ b) r45°(√2x√2x2) super cell used in DFT calculations. Atom colours as follows: yttrium (yellow), barium (green), iron (brown) and oxygen (red)

The focus of this chapter will be exploring how Density Functional Theory (DFT) can be used to guide the synthesis of B-site doped $YBa_2Fe_3O_8$[13]. This system was chosen as there are known experimental precedents for the system being doped[27] providing a solid solution that the calculations can be tested against, while maintaining a number of unreported substitutions. The structure of $YBa_2Fe_3O_8$ is based upon three ABO_3 perovskite units, extended in one direction to form a 3 fold super structure (Figure 27a, hereafter referred to as a $3a_p$ structure). Long range ordering in the c direction is driven by one oxygen vacancy per $A_3B_3O_9$ formula unit (FU)

(where A = Y and Ba, B = Fe), with all of the vacancies ordered in one layer. These ordered vacancies create two distinct A and B sites (coordination numbers quoted in number of co-ordinated oxygen atoms), with the A sites being one 8 co-ordinate (yttrium) and two 12 co-ordinate (barium) sites, the B-sites are either 5 co-ordinate square based pyramids and 6 coordinate octahedral iron sites, with the Fe atoms processing G-type antiferromagnetic ordering at room temperature. Note that the B-site polyhedra geometries are non-idealsed, the octahedral site has four short equatorial bonds (in the ab plane of the crystal structure 1.95 Å) and two long axial bonds (in the c axis, 2.13 Å). The square pyramidal site has one short axial bond (1.87 Å in the c direction) and four equatorial bonds (2.01 Å, in the ab plane, sitting below the iron atom in the c direction). By performing calculations on this system, in addition to predicting doping levels, it will be possible to test how well DFT can predict site preferences for dopant metals. Shifts in other structural properties such as unit cell parameters and atomic co-ordinates will also be calculated while maintaining a system with a small enough structure, such that the calculations are not computationally expensive.

Due to existing precedents for doping into each of the transition metal geometry types found in the $3a_p$ structure [22, 116, 117] for the transition metals in this work, it is possible to make arguments as to why dopant metals could go into either of the B-sites of the $3a_p$ structure or for the dopant species to go into both B-sites. If the dopant occupies both B-sites an overall dis-ordered B-site structure is formed and hence predictions in this system using multiple different dopants on the B-sites are a non-trivial problem. Given the widespread applicability of doped metal oxides it is very desirable to be able to use calculations to predict how systems can be doped and therefore greatly reduce the number of synthesises that are required experimentally. It has also been shown, that all unique configurations of a given structure can be generated using its'

corresponding symmetry. In order to find the most stable configuration for the symmetry generated structures then have an energy calculated by methods such as DFT or Force Field Methods[47]. The Site Occupancy Disorder (SOD) code[47] has previously been applied in calculating the solid solutions of both binary and ternary oxides [60, 61, 118], carbonate systems [49, 64] and other system types [62, 63, 119]. These studies typically require supercells containing large numbers of atoms. However, due to the multiple dopant species and dopant levels that are studied in this work, this approach would result in a large number of possible structures. As an example, in order to be able to predict the doping in the system, using SOD, taking the largest unit cell used in this chapter, at the composition of $YBa_2Fe_2MnO_8$ results in 24,371 in-equivalent structures. As accurate reaction energies are to be calculated with DFT, relaxations could be required on a large proportion of these structures, after first relaxing every generated structure with a computationally cheaper method (e.g. force field methods). Performing this series of calculations on each of the studied compositions is a computationally expensive route and is therefore considered to be unfeasible for the system studied in this chapter.

In this chapter, the goal was to find a simplified model by which doping can be predicted for complex oxides and have some measure of the likelihood that the material can be formed experimentally. Previously it has been shown that DFT calculations can be configured to re-produce experimental reaction enthalpies [17]. This methodology is adopted by predicting reaction enthalpies for a doping $YBa_2Fe_{3-x}M_xO_8$, in order to predict how the material can be experimentally doped and if any B-site ordering is favourable.

The reaction energy required to form the parent $YBa_2Fe_3O_8$ phase was calculated, followed by a series of doping levels and a selected number of B-site configurations, representative of the possible B-site orderings. Experimentally the following hypothesis was tested: When the

reaction energy of the doped material is lower than that of the parent material, doping will be experimentally favourable and conversely when the formation energy is greater, doping would be unfavourable. Initially the methodology is tested when M = Co which has previously been reported[27] and then predictions on when M = Mn and Ni are made.

3.3 Computational methods

Calculations were performed using the plane wave DFT package, Vienna Ab-intio Simulation Package (VASP) version 4.6.26 [105, 106] with the Perdew, Burke and Ernzerhof (PBE) [103] exchange correlation functional. For the B-site species (Fe, Mn and Ni) the first sub-valence p-orbitals were treated as valence and for the A-site species (Y and Ba) the first sub-valence s-orbital was treated as valence. The gamma centred k-point grid that was used for each calculation was determined by the first k-point grid that fulfilled the condition:

$$nk_i \times r_i \geq 20 \text{ Å} \quad \textbf{(3.1)}$$

Where k_i is the number of k-points on a lattice vector and r_i is the length of the corresponding real lattice vector, given in Å. The unit cell size, shape and atomic co-ordinates were relaxed until forces on atoms were less than 0.01 eV/Å. Wavefunctions were converged until ΔE between consecutive steps was less that 10^{-5} eV. The plane wave cut-off energy in these calculations was set to 450 eV. This computational setup was chosen as when trialled with reaction energies for the reaction of binary oxides to form of $LaMO_3$ (M = Co, Cr, Fe and Ni) it was found to give the best balance between accuracy with experimental values and the time required to perform the calculations (see appendix to this chapter for more details).

The initial atomic co-ordinates and unit cell for the calculations were used from the reported crystal structure of $YBa_2Fe_3O_8$ in the *Ib′am* magnetic supercell, r45°(√2 x √2 x 2) of the nuclear cell (Figure 27 b)[13] to allow for G-type antiferromagnetic and ferromagnetic ordering and multiple B sites (4 octahedral and 8 square pyramidal sites per unit cell), allowing for the varying levels of doping and B-site ordering.

The calculations are started by constructing a doping reaction for $YBa_2Fe_3O_8$ for each of the dopant metal species, note that these equations do make the assumption that the average oxidation state on the transition metal species in the doped material remains at 3+:

$$YBa_2Fe_3O_8 + \frac{x}{2}Mn_2^{3+}O_3 \xrightarrow{\Delta E_{Mn}} YBa_2Fe_{3-x}Mn_xO_8 + \frac{x}{2}Fe_2O_3 \quad \textbf{(3.2)}$$

$$YBa_2Fe_3O_8 + \frac{x}{3}Co_3^{2.67+}O_4 + \frac{x}{12}O_2 \xrightarrow{\Delta E_{Co}} YBa_2Fe_{3-x}Co_xO_8 + \frac{x}{2}Fe_2O_3 \quad \textbf{(3.3)}$$

$$YBa_2Fe_3O_8 + xNi^{2+}O + \frac{x}{4}O_2 \xrightarrow{\Delta E_{Ni}} YBa_2Fe_{3-x}Ni_xO_8 + \frac{x}{2}Fe_2O_3 \quad \textbf{(3.4)}$$

Each of the dopant species in equations (3.2 – 3.4) can be combined from the equations above to give a generic doping reaction equation:

$$YBa_2Fe_3O_8 + M^* \xrightarrow{\Delta E_I} YBa_2Fe_{3-x}M_xO_8 + \frac{x}{2}Fe_2O_3 \quad \textbf{(3.5)}$$

Where:

$$M^* = \left(\frac{x}{2}Mn_2^{3+}O_3\right), \left(\frac{x}{3}Co_3^{2.67+}O_4 + \frac{x}{12}O_2\right), \left(xNi^{2+}O + \frac{x}{4}O_2\right) \quad \textbf{(3.6)}$$

$YBa_2Fe_3O_8$ in equation (3.5) can also be substituted for the component binary oxides to give a reaction enthalpy from the binary oxides in order to provide a reaction pathway which is accessible from experimental solid state methods, resulting in equation (3.7):

$$\frac{1}{2}Y_2O_3 + 2BaO + \frac{3}{2}Fe_2^{3+}O_3 + M^* \xrightarrow{\Delta E_{II}} YBa_2Fe_{3-x}M_xO_8 + \frac{x}{2}Fe_2O_3 \quad \textbf{(3.7)}$$

and then in order to form a reaction pathway where only a stoichiometric amount of the desired 3_{ap} product remains on the right hand side of the equation, the total number of transition metal ions on the left hand side is fixed at, 3 resulting in ΔE_{III}:

$$\frac{1}{2}Y_2O_3 + 2BaO + \frac{3-x}{2}Fe_2O_3 + M^* \xrightarrow{\Delta E_{III}} YBa_2Fe_{3-x}M_xO_8 \quad \textbf{(3.8)}$$

Equation (3.8) was used to calculate energies for the doping levels, with units being given as electron Volts per Formula Unit, eV/FU. The most favourable configuration at each doping level is defined as the structure that yields the lowest reaction energy. This measure then gives a numerical value that can be compared across compositions.

It should be noted here that given the type of calculation performed, energies could be calculated relative to energy values for an ideal solid solution if both of the end members are known to be stable. Particularly stable compositions could be identified by energies that lay below the energy of the ideal solid solution, for a binary system energies could be calculated according to equation (3.9):

$$(1-x)C + xD \xrightarrow{\Delta E_{IV}} C_{1-x}D_x \quad \textbf{(3.9)}$$

Where *C* and *D* are the end members of the solid solution ($YBa_2Fe_3O_8$ and the un-reported $YBa_2Mn_3O_8$ for example) and $C_{1-x}D_x$ is the desired compound (e.g $YBa_2Fe_{3-x}Mn_xO_8$). In the system examined in this chapter, the end members of the solid solutions are not reported in ordered 3_{ap} structures (although $YBa_2Co_3O_{8+\delta}$ is reported as a disordered cubic perovskite[30]), as

such we will use ΔE_{III} (equation (3.8)) for predictions. For clarity in identifying the differences between conformations at each value of *x* we have used ΔE_{IV} from equation (3.9).

The initial atomic-coordinates and unit cells of the binary oxides were used as reported in the literature [29, 120-124]. Where multiple possible binary oxides are reported for the transition metals (M = Co and Mn) the oxide which gave an overall charge state as close to 3+ as possible was selected in order to minimise the amount of O_2 gas that had to be considered.

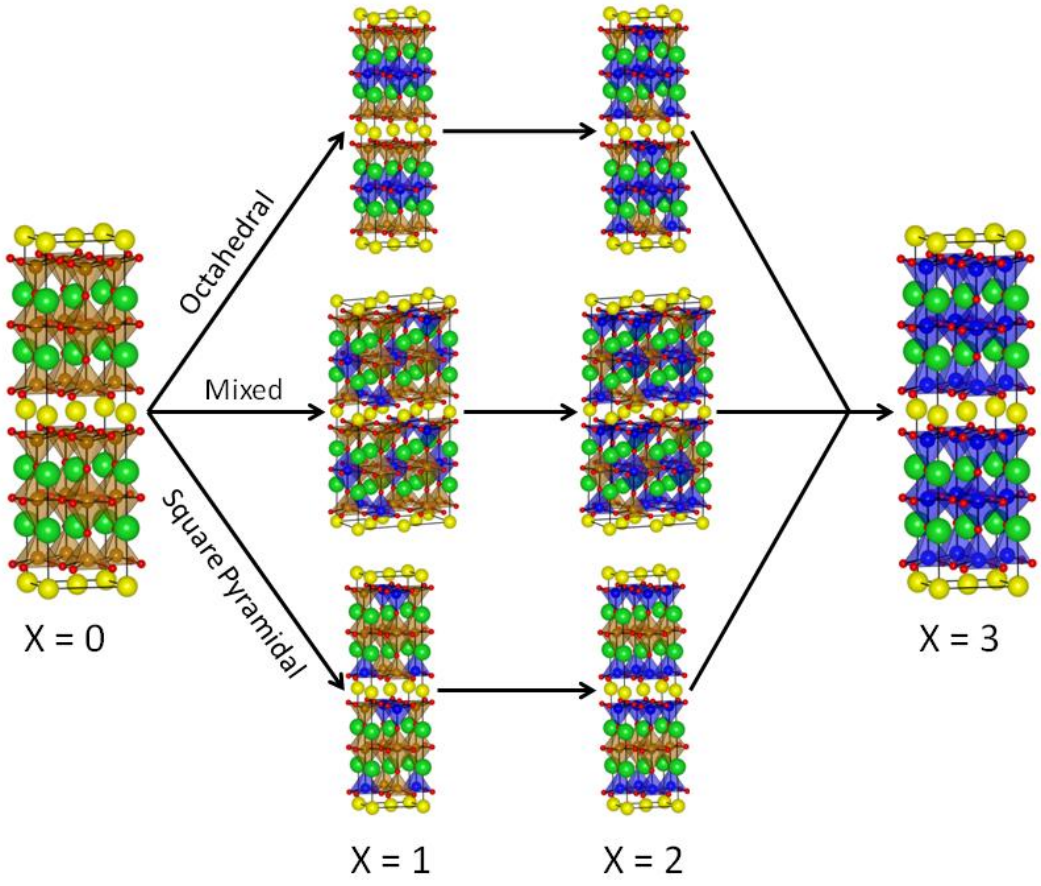

Figure 28 Structures used for DFT calculations with 3 different site preferences at doping levels x = 1, 2 and 3. Atoms coloured as follows: yttrium (yellow), barium (green), iron (brown), dopant (blue) and oxygen (red).

For a doping level of x = 3 (Figure 28) only one B-site configuration is possible as this constitutes full substitution. For doping levels of x = 1 and 2, three different B-site configurations were considered in order to approximate possible site preferences of the dopant species.

In the first site preference (named Octahedral, Figure 28) all of the dopant atoms were preferentially placed in the octahedral site. For x =1, this results in the dopant species fully occupying the available octahedral sites. When x = 2, there are too many dopant atoms to dope purely onto the octahedral sites, the remaining dopant atoms were distributed evenly amongst the square pyramidal sites, maximising the distance between the dopant atoms.

In the second site preference (named Square Pyramidal, Figure 28) the dopant atoms were distributed amongst alternating square pyramidal site when x =1, when the doping level is increased to x = 2, the square pyramidal sites are fully occupied.

The final configuration (named Mixed, Figure 28) the calculations were performed on a (2 × 1 × 1) supercell of the original calculation cell to allow for closer to statistical averaging of B-site positions, for both x = 1 and x = 2 all of the dopant atoms were evenly distributed amongst both of the B-sites.

Colinear spin-polarization was applied to the B sites for $YBa_2Fe_{3-x}M_xO_8$ as follows: when x = 0 or M = Co, the spin moments were arranged as a G-type anti-ferromagnet, as reported for $YBa_2Fe_3O_8$; when M = Ni and Mn both G-type anti-ferromagnetic and ferromagnetic arrangements were tested. Colinear magnetic structures were also applied to the binary oxide calculations in arrangements that have been experimentally reported[29, 120, 121, 124].

It has been shown in the literature that in order to be able to calculate more accurate formation energies for perovskites containing d electrons, an onsite coulomb interaction term, U must be

applied to the d-orbitals of the transition metals[17]. We have used the rotationally invariant form U_{eff} where U_{eff} = U - J. In this chapter U_{eff} values of 4.0, 4.0, 6.4 and 3.3 eV for Fe, Mn, Ni and Co respectively were used. In addition to requiring a U_{eff} it has also been shown that when using PBE functionals a corrected binding energy for O_2 gas is required[17] due to VASP over-estimating the binding energy in O_2. The energy of O_2 gas was set to -8.5 eV per FU, in line with previously reported work.

3.4 Experimental methods

Samples were synthesised from binary oxides and carbonates (Y_2O_3 (99.999%), $BaCO_3$ (99.997%), Fe_2O_3 (99.998%), MnO_2 (99.97%), NiO (99.998%) purchased from Alfa Aesar and pre-dried) weighed out in stoichiometric quantities. Samples were hand-ground using a pestle and mortar with the samples under acetone to aid grinding. Hand-grinding of samples was deemed sufficient due to the relatively small size of the samples and no requirement for dense pellets. Prior to firing the samples were pelletized using a uni-axial press at a pressure of approximately 5 tons, with the diameter of the pellet chosen to create pellets less than 5 mm thick. Samples were then heated at a temperature of 1200 °C in a tube furnace under flowing N_2 (in order to test synthesis under reducing atmospheres in addition to ambient) static air was also trialled for $YBa_2FeNi_2O_{8\pm\delta}$ and $YBaFe_2MnO_{8\pm\delta}$ materials for 72 hours in alumina crucibles, with intermediate re-grinding and re-pelletisation at 24 and 48 hours. At the end of each heating cycle the samples were allowed to cool completely to room temperature before the gas flow was removed in order to prevent sample oxidation. Initial samples were synthesised with a target

mass of 1 g. Samples used in neutron powder diffraction were synthesised using the same methodology with a target mass of 7 g under flowing N_2.

Iodometric titrations were carried out in order to determine the oxygen content and therefore the average transition metal charge state. Samples were titrated against sodium thiosulfate solution (0.1 M), standardised against potassium iodate (99.995% purchased from Sigma Aldrich), samples of Fe_2O_3 and MnO_2 (purity and supplier as used in the synthesis) were also titrated and analysed to test the titration conditions for the transition metals in question, resulting in oxygen contents of $O_{3.00(3)}$ and $O_{2.01(2)}$ respectively.

For the titrations, an approximate ratio of 1 g of potassium iodide (99.99%, purchased from Alfa Aesar) was added for every 50 mg of sample. The potassium iodate standard was dissolved in water (ca. 20 cm^3), once dissolved sulphuric acid was added (ca. 5 cm^3, 1 M). Metal oxides were dissolved in hydrochloric acid (20 cm^3, 3M), flushed with argon gas for at least 1 minute, sealed with laboratory film and stirred just above room temperature (~30 °C) until samples were dissolved. The metal oxide samples were then diluted to an acid concentration of 0.5 M and titrated immediately. Samples were titrated until a pale straw colour was obtained, and then 2 cm^3 of starch indicator solution was added, turning the solution dark indigo and the titration continued to a clear end point. All titrations were repeated a minimum of three times and the average result used, the errors were calculated from the spread of results.

Mössbauer spectra were taken in absorption mode with samples mounted between the Mössbauer source and the gamma ray detector by Dr. M. Thomas. The source motion was controlled by a waveform that gave constant acceleration motion. A double ramp waveform was used so that the folded spectra have a flat background. The source was of ^{57}Co in a Rh matrix and the 14.4 keV

gamma radiation was detected in a proportional counter filled with an argon/methane gas mixture to a pressure of about one atmosphere. The detector efficiency is about 67% for 14.4 keV radiation but is essentially zero for the 122 keV radiation that feeds the 14.4 keV state in ^{57}Fe. The spectrometer was calibrated against the known spectrum of α–iron (BCC). Values of isomer shift are quoted relative to α-iron at room temperature. The spectra are fitted with a superposition of components each of which represents a particular Fe ion in a defined environment. For each environment values of the isomer shift, electric quadrupole interaction and magnetic hyperfine field were determined.

All powder diffraction data were collected at room temperature data was collected on the initial samples using a Bruker D8 Advance diffractometer using Cu $K\alpha_1$ radiation in Bragg-Brentano or transmission foil geometry or a Phillips X'pert Panalytical diffractormeter using Co Kα1 radiation in Bragg-Brentano geometry. For the structure refinement PXRD data was collected using a Bruker D8 Advance in Debye-Scherrer geometry using a 0.3 mm capillary with Mo $K\alpha_1$ radiation (*d*-space range: 0.62 – 16.37 Å). Time Of Flight (TOF) - NPD patterns were collected at STFC-ISIS on the HRPD instrument in a 8 mm vanadium can, (with thanks to J. B. Claridge for collecting the pattern) with data collected at 168° and 90° detector banks (with *d*-space ranges 0.67 – 2.36 and 0.96 – 3.67 Å respectively). For phase identification X'Pert highscore plus software[125] was used to perform peak assignments using the pdf-2 database[126]. Phase fractions quoted in Figure 35 were calculated using the Topas academic program[87, 88] by Dr. P. Chater. Rietveld refinements were performed using the GSAS[85, 86] package, following a refinement method based upon a previously reported procedure on refining the nuclear and magnetic structure of $YBa_2Fe_3O_8$[127].

3.5 Computational results

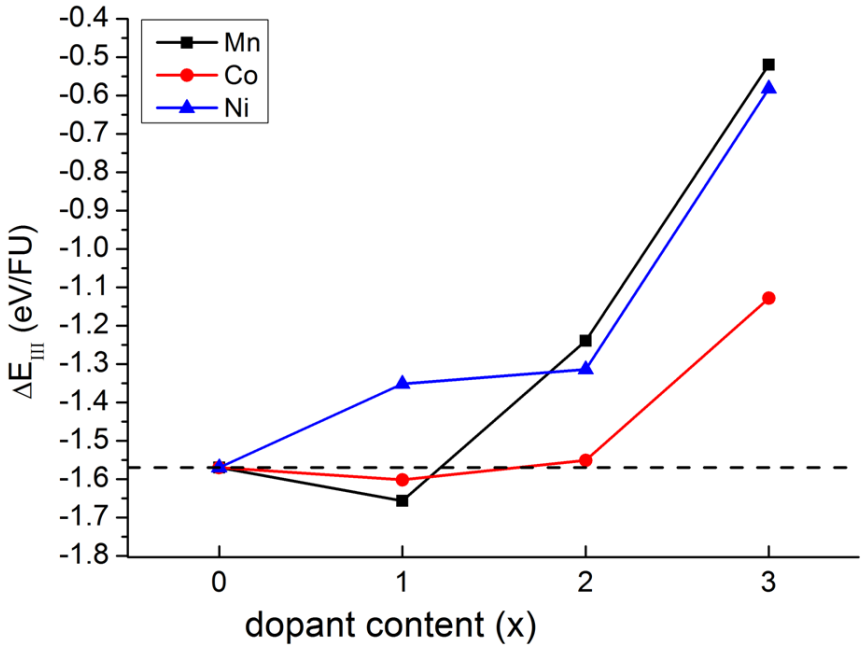

Figure 29 Reaction energies calculated for $YBa_2Fe_{3-x}M_xO_8$ from binary oxides according to equation (3.8), with the ΔE_{III} value taken for the lowest energy configuration at each value of *x*.

Balanced equations for the calculation of reaction energies were created taking into account the possibility for an overall change in oxygen content, depending on the dopant metal equation (3.6) The reaction energy for the Fe pure, $x = 0$ compound was calculated to be −1.57 eV/FU. This formation energy was used as a benchmark when attempting to predict if a calculated composition would be stable and thus likely to form experimentally. Results for the calculated formation energies suggest that favourable doping can be achieved when M = Co and Mn, although no favoured doping configuration was found when M = Ni (Figure 29).

3.5.1 Results for M = Co

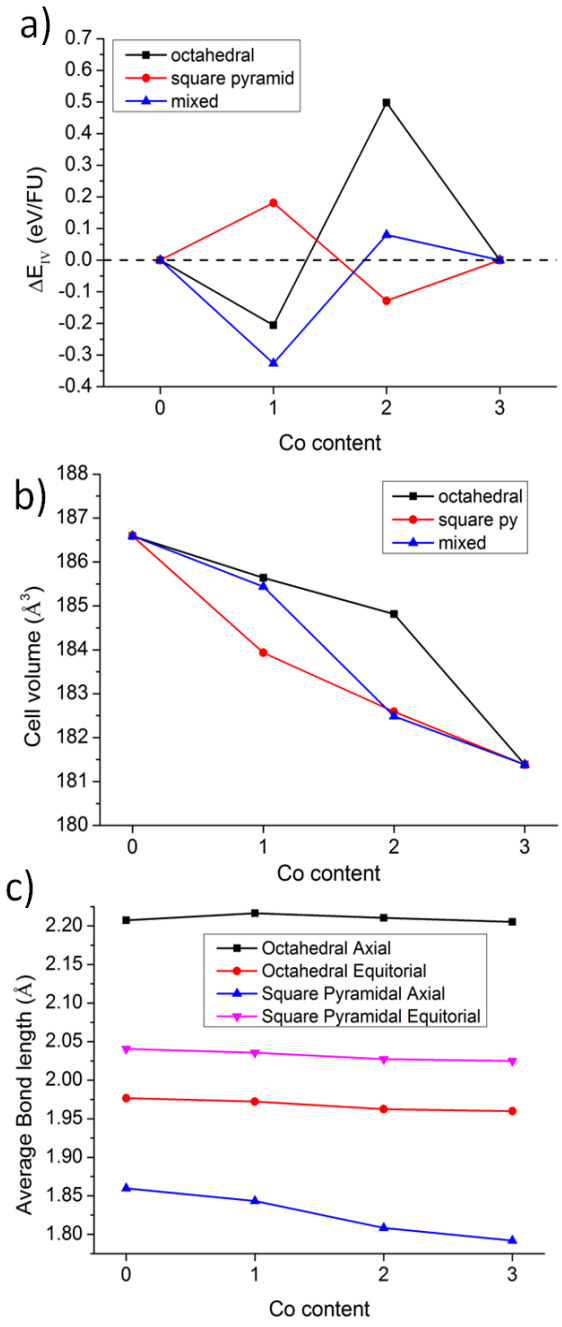

Figure 30 a) Solid solution energies calculated according to equation (3.9) when M = Co for each of the different orderings trialled in the DFT calculations. b) The DFT calculated unit cell volumes as a function of Co content. c) Average bond lengths for each of the B-site environments in the lowest energy DFT calculation at each value of *x* as a function of Co content.

When M = Co (Figure 29) the favoured doping level was when x = 1 and with the dopants in the mixed configuration (Figure 30a), the reaction energy relative to binary oxides was calculated to be 0.03 eV/FU more stable compared to the undoped material. The DFT calculations for M = Co show that the lowest energy configuration at each value of *x* is also the configuration that has the smallest unit cell volume (Figure 30b). The calculation that Co doping into this system results in a decrease in the unit cell volume correlates with reported experimental observations[27], where doping with Co causes a unit cell volume decrease of 0.80(1) %.

Looking at the bonding environments for M = Co (Figure 30c), over the doping series, on the square pyramidal site, there is little change in the average bond axial length between $x = 0$ and $x = 1$ however between $x = 1$ and 2 there is a decrease of 0.05 Å. There is very little shift in the square pyramidal equatorial bond lengths across all of the compositions. Comparison between the calculated results at $x = 1$ and the closest reported value of $x = 0.9$, show that the calculations produce similar results to those reported[27] (Table 1). The DFT results in the correct direction of shift for all but the octahedral equatorial bonds, decreasing by 0.0032 Å compared with the reported increase of 0.0032 Å.

Considering dopants on the octahedral environments, when $x = 1$, the axial and equatorial octahedral bond lengths decrease and increase respectively, to give a difference of only 0.064 Å, compared to the difference in the DFT calculation of the undoped material of 0.231 Å. As cobalt content increases to become un-favourable, the difference in the axial and equatorial bond lengths on the octahedral also increase, to return to be close to the bond lengths calculated for the undoped material. The distortion on the octahedral site reduction in the square pyramidal size may be a driving force behind doping becoming un-favourable when Co becomes the major B-site metal.

Co doping within the$YBa_2Fe_3O_8$ phase has been reported for a values of x = 0.6, 0.9, 1.2 and 1.5 [27] and that when these doping levels are achieved, the Co has no significant site preference[27]. These results confirm that the method can correctly calculate transition metal doping within this system, as our calculations suggest that doping becomes unfavourable between x = 1 and 2 as is observed experimentally.

3.5.2 Results for M = Mn

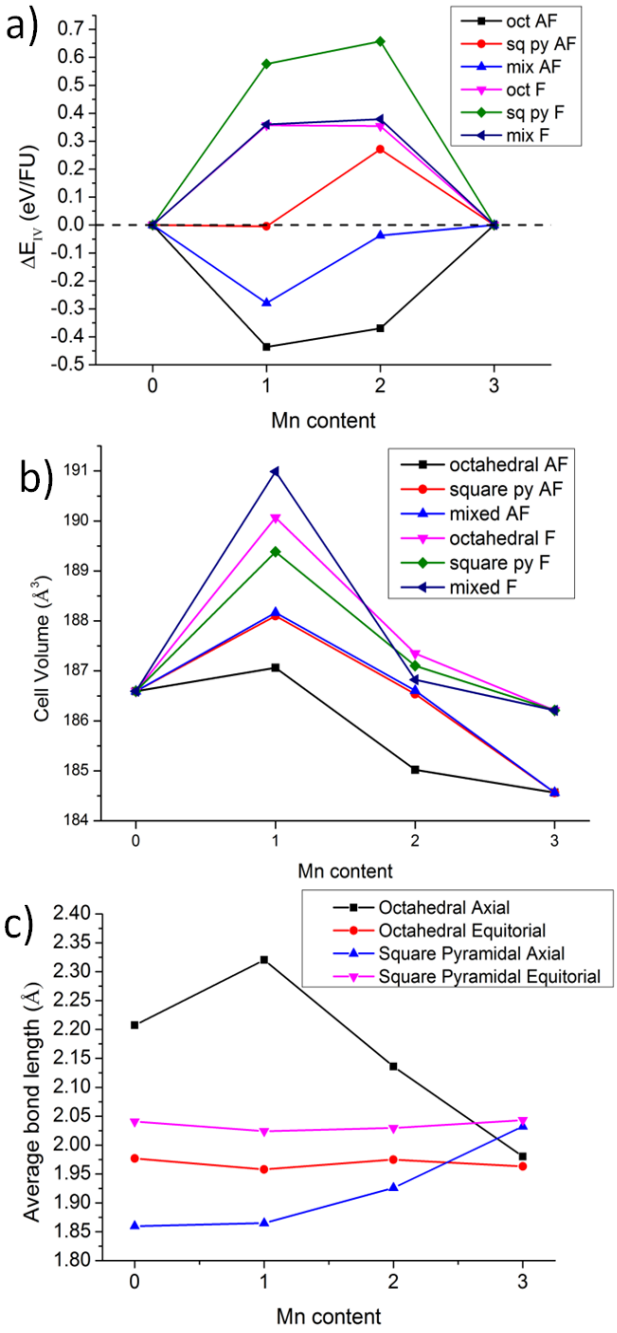

Figure 31 a) Solid solution energies calculated according to equation (3.9) when *M* = Mn for each of the different orderings trialled in the DFT calculations. b) The DFT calculated unit cell volumes as a function of Mn content. c) Average bond lengths for each of the B-site environments in the DFT calculations as a function of Mn content.

When M = Mn (Figure 29) the computationally favoured doping occurs at x = 1 with the Mn atoms in the octahedral configuration with G-type anti-ferromagnetic ordering (Figure 31a). The formation energy for the favoured configuration was calculated to be 0.09 eV/FU more stable versus the undoped material. The ferromagnetic ordering at x = 1 with Mn in the octahedral site was found to have a formation energy 0.36 eV/FU less stable versus the undoped material. When the doping level was increased to x = 2, doping becomes unfavourable, although the preference for Mn to occupy the octahedral site and have G-type anti-ferromagnetic ordering remained. At x = 2, this configuration was calculated to be 0.33 eV/FU less stable when compared to the undoped material. When M = Mn, that none of the configurations with ferromagnetic ordering were calculated to be. For x = 1 and 2 each of the lowest energy configurations was also the configuration that was calculated to have the smallest unit cell volume (Figure 31b).

When looking at the geometries (Figure 31c) of the Mn sites after doping, when x = 1, where doping is most favourable, at the preferred octahedral site, there is a sharp distortion of the site versus the undoped material. The axial bond lengths increase by 0.11 Å and a shortening of the equatorial bond by 0.02 Å is observed, in line with a Jahn-Teller distortion expected for Mn^{3+} (Figure 31c). When the doping level is increased, the length of the of the equatorial bonds change little on the octahedral site. Due to having to put Mn atoms into the square pyramidal sites the axial bond of the octahedron shortens on one side creating a irregular octahedron, with two long bonds (2.00 and 2.28 Å) and four short bonds averaging 1.91 Å each. At the doping level x = 2 having to insert Mn into square pyramidal sites results in distorted sites relative to the undoped material, with four different square pyramids each with differing bond lengths, with a similar result observed on the octahedral sites. It is suggested that when x = 2, the distortion

imposed on the Mn^{3+} octahedral sites, forcing them away from a Jahn-Teller geometry preferred is a possible driving force for the increased levels of Mn doping becoming unfavourable.

3.5.3 Results for M = Ni

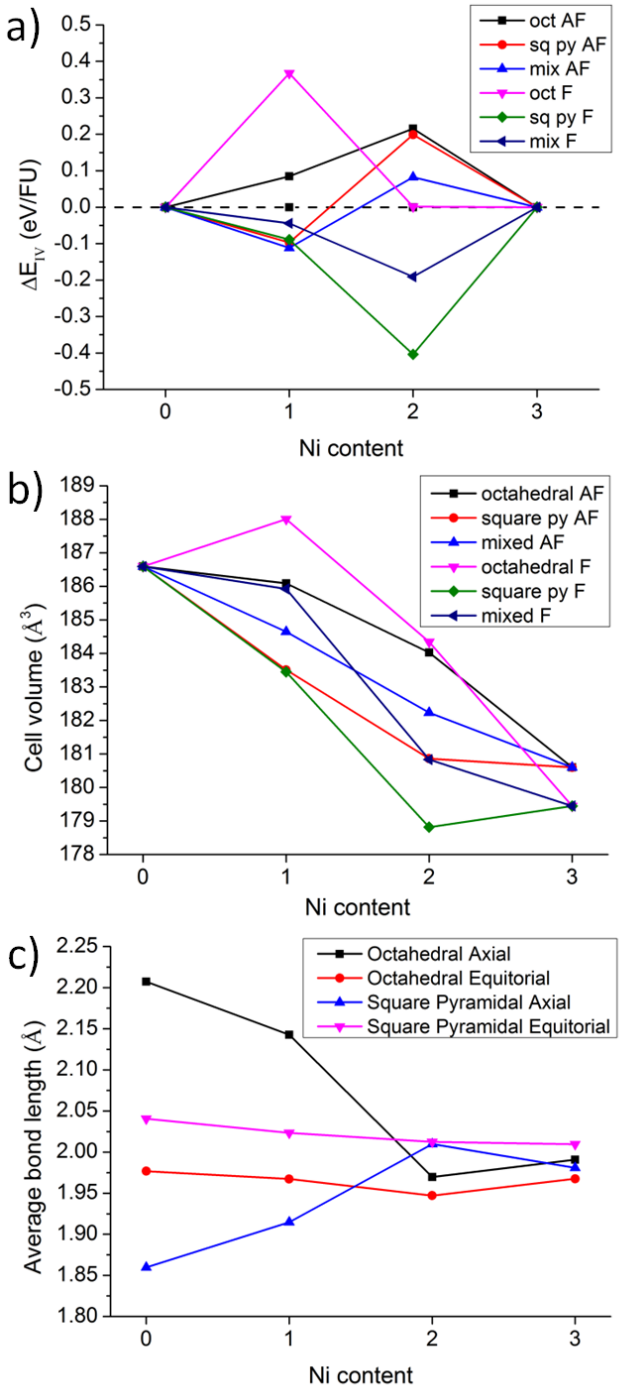

Figure 32 a) Solid solution energies calculated according to equation (3.9) when *M* = Ni for each of the different orderings trialled in the DFT calculations. b) The DFT calculated unit cell volumes as a function of Ni content. c) Average bond lengths for each of the B-stie environments in the DFT calculations as a function of Ni content.

When M = Ni (Figure 29), no structure was found to be favoured versus the undoped material, the highest energy doping level still containing Fe was x = 2, in which the Ni atoms were in the square pyramidal sites, with a reaction enthalpy of 0.26 eV/FU higher than the undoped (Figure 32a). At x = 2, where Ni becomes the dominant B-site metal the favoured magnetic ordering switches from G-type antiferromagnetic to ferromagnetic.

When x = 1 for M = Ni, the unit cell volume (Figure 32b) was almost identical between both of the magnetic arrangements when the Ni atoms were preferentially placed in the square pyramidal sites (a difference of only 0.06 $Å^3$) and have the smallest unit cell volumes, however, unlike for the other dopant species, the smallest unit cell volume does not indicate the most stable structure. The lowest energy configuration at x = 1 was found to be the mixed configuration, by a small energy difference of 0.014 eV/FU. The discrepancy with the unit cell volumes of the Ni doped structures with the other dopant species is possibly explained by looking at the bonding geometries in the configuration with the lowest volume for M = Ni. The smallest configuration, while minimising the volume of the unit cell, forces the Fe atoms (still the major B-site atom) to distort largely away from the bonding geometry of the undoped material. The bonds in the lowest energy configuration however (but not the smallest volume), do allow for the B-site environments to remain close to the undoped material (Figure 32b).

When looking at the bonding environments for the lowest energy configurations when M = Ni (Figure 32c) it was calculated that over the doping series there is little change in any of the equatorial bonding environments on either B-site. Looking at the axial bonds, there is marginal change between x = 0 and x = 1. When Ni becomes the major B-site metal (x = 2) and ferromagnetic ordering becomes favoured, the octahedral and square pyramidal axial bonds decrease and increase respectively to become close in length to the other bond lengths. The

change in bond lengths results in all of the bonds in the system being very similar, with only a gap of 0.094 Å between the biggest and smallest of the average bond lengths.

From the DFT calculations a suggested explanation as to why forming a $3a_p$ perovskite when M = Ni is not predicted to be favourable, in addition to the difficulty in forming Ni^{3+} compounds:

- When $x = 1$ the lowest energy configuration is not the configuration with the smallest unit cell volume due to how the Fe bonding environments are distorted, with the configuration with the lowest energy having the Fe environments closer to that of the undoped material.
- When $x \geq 2$ all of the bonding environments for the B-site metals become very similar and to some approximation become closer to those observed for disordered perovskites. This effective disorder may make long range ordering un-favourable, coupled with forcing the Fe atoms into a ferromagnetic state.

Therefore the DFT calculations predict that experimentally doping at $x = 1$ with Mn should be the only doping favoured in the $YBa_2Fe_{3-x}M_xO_8$ (M = Co, Ni or Mn) in addition to the previously reported Co doping[27].

3.6 Experimental results

Based upon the computational predictions outlined in the previous section, samples were synthesised for M = Mn, $x = 1, 2$ ($YBa_2Fe_2MnO_{8\pm\delta}$ and $YBa_2FeMn_2O_{8\pm\delta}$) and M = Ni, $x = 2$ ($YBa_2FeNi_2O_{8\pm\delta}$) to test the composition predicted to be favourable and to confirm that the calculations correctly predict where doping would be unfavourable.

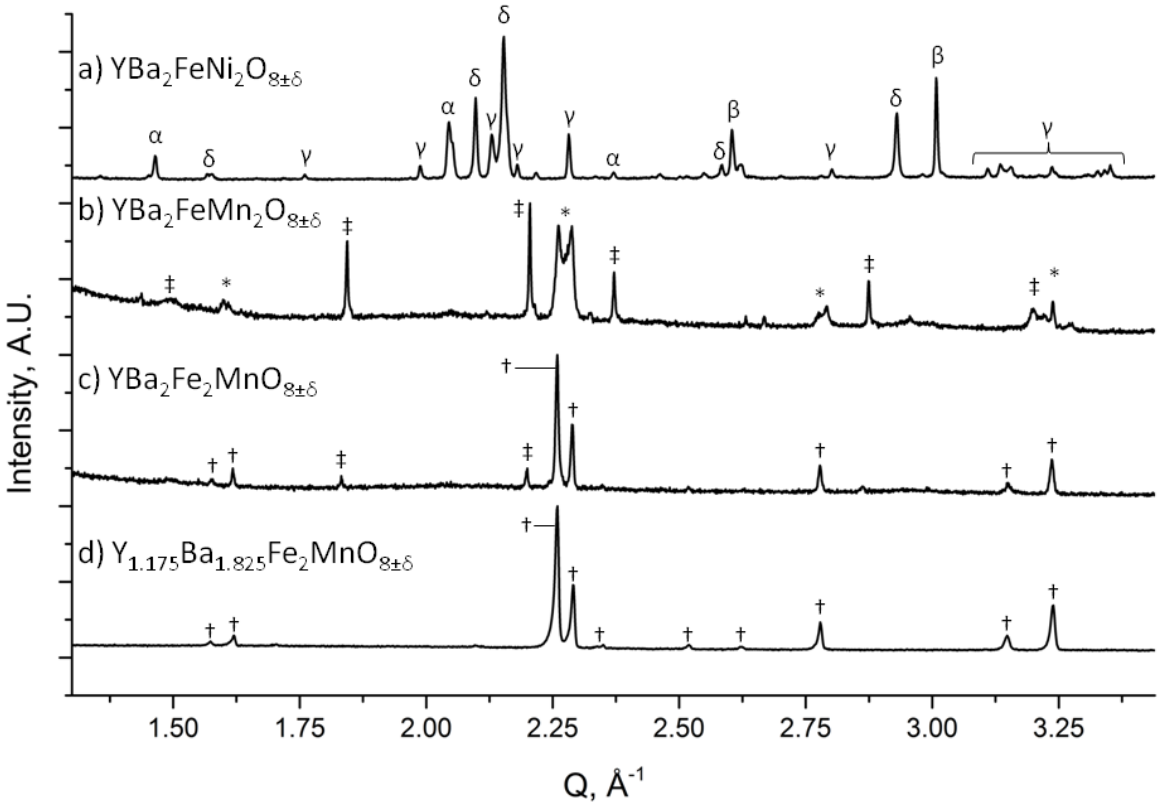

Figure 33 PXRD patterns from stiochometric samples of $YBa_2Fe_{3-x}M_xO_8$ for a) *M* = Ni & *x* = 2 ($YBa_2FeNi_2O_{8\pm\delta}$), b) *M* = Mn & *x* = 2 ($YBa_2FeMn_2O_{8\pm\delta}$) and c) *M* = Mn and *x* = 1 ($YBa_2Fe_2MnO_{8\pm\delta}$) d) $YBa_2Fe_2MnO_{8-\delta}$ with an optimised Y:Ba ratio ($Y_{1.175}Ba_{1.825}Fe_2MnO_{8.04(5)}$) when synthesised under a N_2 atmosphere. The XRD patterns show that no $3a_p$ perovskite is formed in $YBa_2FeNi_2O_{8\pm\delta}$, with a mix of oxide phases identified(α = Y_2O_3, β = NiO, γ = BaY_2NiO_5[128] and δ = $YBa_3Fe_2O_{7.5}$[129]). $YBa_2FeMn_2O_{8\pm\delta}$ contains a mix of hexagonal (‡) and two tetragonal (*) perovskite phases (where one of the phases is similar to the main phase in $YBa_2Fe_2MnO_{8\pm\delta}$). $YBa_2Fe_2MnO_{8\pm\delta}$ contains a $3a_p$ perovskite (†)as the major phase with a minor hexagonal perovskite (‡) impurity identified as a $BaMnO_3$ type hexagonal perovskite. $Y_{1.175}Ba_{1.825}Fe_2MnO_{8.04(5)}$ contains single phase $3a_p$ perovskite (†).

Samples with and the composition $YBa_2FeNi_2O_{8\pm\delta}$ fired under flowing N_2, (Figure 33a), it was observed that the sample contains a mixture of known binary and ternary oxides. In samples of composition $YBa_2FeMn_2O_{8\pm\delta}$ (Figure 33b), the major phase was indexed to be a hexagonal perovskite similar to reported 4-H $BaMnO_{3-\delta}$[118], along with two tetragonal/pseudo tetragonal phases with the first having lattice parameters of a = 3.9270(2) Å and c = 3.8380(4) Å and the second with a = 3.9004(9) Å and c = 3.926(1) Å (obtained from Pawley refinements using

topas), noting that there were no reflections observed to indicate any long range ordering for these tetragonal perovskite phases[130]. The phases observed in $YBa_2FeNi_2O_{8\pm\delta}$ and $YBa_2FeMn_2O_{8\pm\delta}$ are in agreement with the predictions from DFT in that no $3a_p$ perovskite was formed as the major phase in either sample.

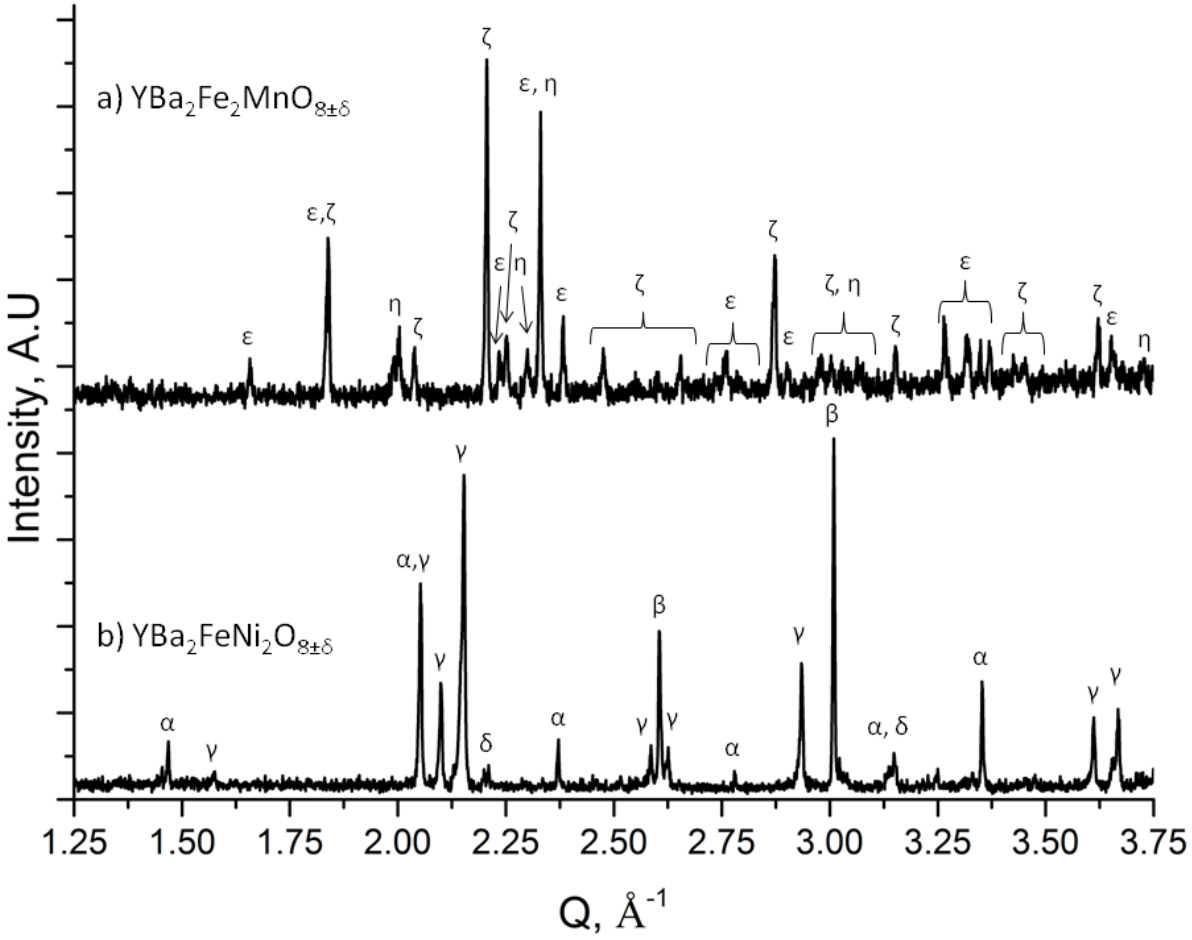

Figure 34 a) Co Kα1 XRD pattern for $YBa_2Fe_2MnO_{8\pm\delta}$ sample synthesised in static air, where η indicates $BaFe_2O_4$ type phase [13], ε indicates $YFeO_3$ perovskite type phase [131] and ζ indicates $BaMn_{0.4}Fe_{0.6}O_{2.73}$ type phase [132]. b) Co Kα1 XRD pattern for $YBaFeNi_2O_{8\pm\delta}$ sample synthesised in static air, where α indicates Y_2O_3, β indicates NiO, γ indicates a phase similar to the reported $YBa_3Fe_2O_{7.5}$ phase[129] and δ indicates reflections consistent with $BaFeO_3$ perovskite phase.

In the $YBaFeNi_2O_{8\pm\delta}$ and $YBa_2Fe_2MnO_{8\pm\delta}$ samples that were fired under static air (Figure 34), no $3a_p$ phases were observed to form. With $YBaFeNi_2O_{8\pm\delta}$ (Figure 34b) the same impurity phases were observed as for flowing N_2, although with different relative intensities in the diffraction

pattern, with the main shift being a reduction in the observed reflections for $YBa_3Fe_2O_{7.5}$. For the $YBa_2Fe_2MnO_{8\pm\delta}$ (Figure 34a) sample fired in static air, two main phases were observed by XRD, corresponding to $YFeO_3$ orthorhombic perovskite [131] and $BaMnO_3$ hexagonal perovskite (similar to that observed in the $YBaFeMn_2O_{8\pm\delta}$ sample fired under flowing N_2).

Diffraction data for $YBa_2Fe_2MnO_{8\pm\delta}$ (Figure 33c) show that the major phase is indexed to be a $3a_p$ perovskite and a hexagonal impurity identified as similar to 10H $BaMn_{0.4}Fe_{0.6}O_{3-\delta}$ [132]. The composition for $YBa_2Fe_2MnO_{8\pm\delta}$ was optimised to achieve a high purity sample by altering the Y: Ba ratio. This was achieved by searching a 1-D phase diagram covering Y_yBa_{3-y} with y values ranging between 0.8 and 1.275 while maintaining the same synthetic procedure during this search, with a reduced target mass of 0.3 g under flowing N_2. The $3a_p$ was only obtained phase pure only at the composition $Y_{1.175}Ba_{1.825}Fe_2MnO_{8\pm\delta}$ (Figure 33d), with decreases or increases in Y content resulting in impurities of 10-H hexagonal perovskite or $YFeO_3$, respectively (Figure 35a and c).

The oxygen content in the optimised composition, $Y_{1.175}Ba_{1.825}Fe_2MnO_{8\pm\delta}$, was analysed by iodometric titration. The oxygen content was determind using the following equation to find *x* in a perovskite with the formula unit ABO_{y+x}, where y is the oxygen content of the reduced compound post titration, in order to find the total sample oxygen content:

$$x = \frac{M_{red}}{m\left[\frac{1}{n} - \frac{M_O}{m}\right]} \qquad \textbf{(3.10)}$$

Where *x* indicates the excess oxygen per formula unit, *m* is the sample mass, *n* is the number of moles of oxygen calculated from the titration according to the reaction in equation (3.11). M_{red}

indicates the molar mass of the fully reduced compound, normalised such that the total number of A and B species is equal to 1 of A and B-sites and M_o is the molar mass of oxygen.

$$\frac{x}{2}I_2 + xS_2O_3^{2-} \longrightarrow \frac{x}{2}S_4O_6^{2-} + xI^- \quad \textbf{(3.11)}$$

Where the number of mols of I_2 observed from the titration (when titrated against $S_2O_3^{2-}$ from the standardised sodium thiosuphate solution) can be equated to an equal number of moles of oxygen from the dissolved oxide sample. The determined oxygen content was found to be $O_{8.04(5)}$, giving an average transition metal charge state of 2.97+, assuming a charge state of 3+ and 2+ on Y and Ba respectively.

Mössbauer spectroscopy (Figure 36c) of this sample showed the material to be magnetically ordered at room temperature (295 K). The spectrum showed the presence of two Fe^{3+} sites, which were refined as consistent with octahedral and square pyramidal geometries. From this, the occupancies of each site were refined as 80.5(9)% in square pyramidal geometry and 19.5(9)% in octahedral geometry. Assuming that the only other species on the same sites is Mn and that the ratio of octahedral to square pyramidal sites is constant at 1: 2, the percentage of Mn atoms in each environment was calculated to be 39% square pyramidal and 61% octahedral.

Successful synthesis of pure $3a_p$ $Y_{1.175}Ba_{1.825}Fe_2MnO_{8.04(5)}$ required careful control of the transition metal charge state; alteration of the A site charge and control of oxygen partial pressure during synthesis using N_2 gas were both required. Synthesis in air and synthesis with lower average A site charge state both resulted in the formation of Mn^{4+} containing species in preference to $3a_p$. The absence of oxygen deficient sites or interstitials in the $3a_p$ structure, as confirmed by iodometric titration and Rietveld refinement, indicate that the structure has a low tolerance for oxygen non-stoichiometry. The oxygen content of the DFT configurations and

therefore the B-site charge state was fixed, since only the stoichiometric composition was calculated; experimentally however, the tuning of the sample composition and atmosphere used during synthesis was required to control the average B-site charge state to near 3+ to stabilise 3ap phase relative to other competing phases containing Mn in a 4+ state. In this case performing a calculation at the exact composition was not necessary to predict the initial doping success, however experimental refinement of the composition was still required to isolate the compound.

3.7 Discussion

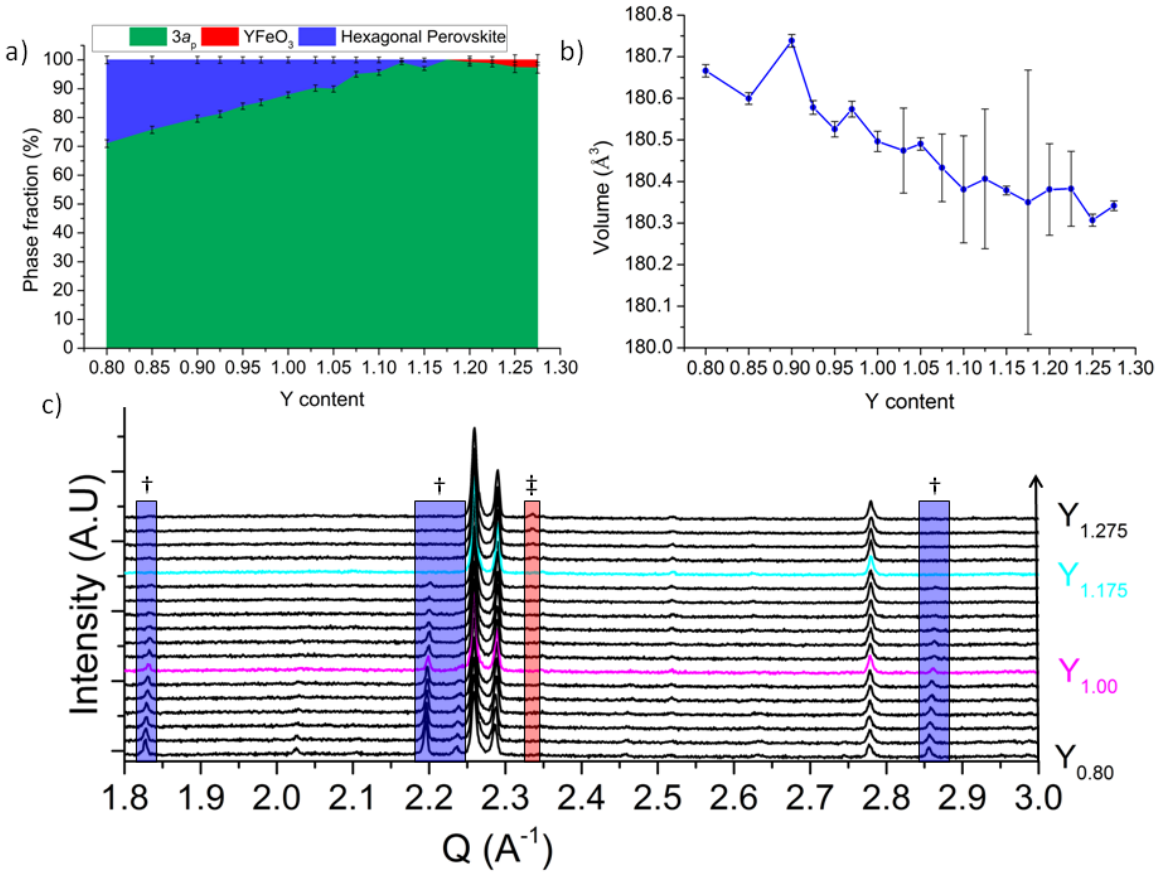

Figure 35 a) Refined phase fractions in $Y_{3-z}Ba_xFe_2MnO_{8\pm\delta}$ samples as a function of the Y content, $3a_p$ indicates the phase fraction of the desired phase, $YFeO_3$ indicates the phase fraction of a perovskite similar to the reported $YFeO_3$ material[131] and Hexagonal perovskite similar to the reported 10-H $BaMn_{0.4}Fe_{0.6}O_{3-\delta}$ material[132] b) Refined unit cell volumes for $Y_{3-z}Ba_xFe_2MnO_{8\pm\delta}$ samples as a function of the Y content. c) CuKα1 XRD patterns of $Y_{3-z}Ba_xFe_2MnO_{8\pm\delta}$ samples as a function of the Y content, blue boxes labelled with † indicate regions where hexagonal perovskite reflections are observed and the red box marked with ‡ indicates the region where the main reflection for $YFeO_3$ perovskite is observed.

Refinement of the $Y_{1.175}Ba_{1.825}Fe_2MnO_{8.04(5)}$ unit cell as a function of the Y content shows that there is a small variation in the unit cell volume (Figure 35). The variation in the cell volume implies that the structure should be accessible over a range of compositions, however in our studies we only access the structure phase pure at one specific composition, suggesting that

variation of the Fe: Mn ratio is also required at each Y: Ba ratio in order to synthesise the phase pure structure over a range of compositions. This was not attempted within this chapter as retention of Fe: Mn ratio was the focus of the DFT calculations.

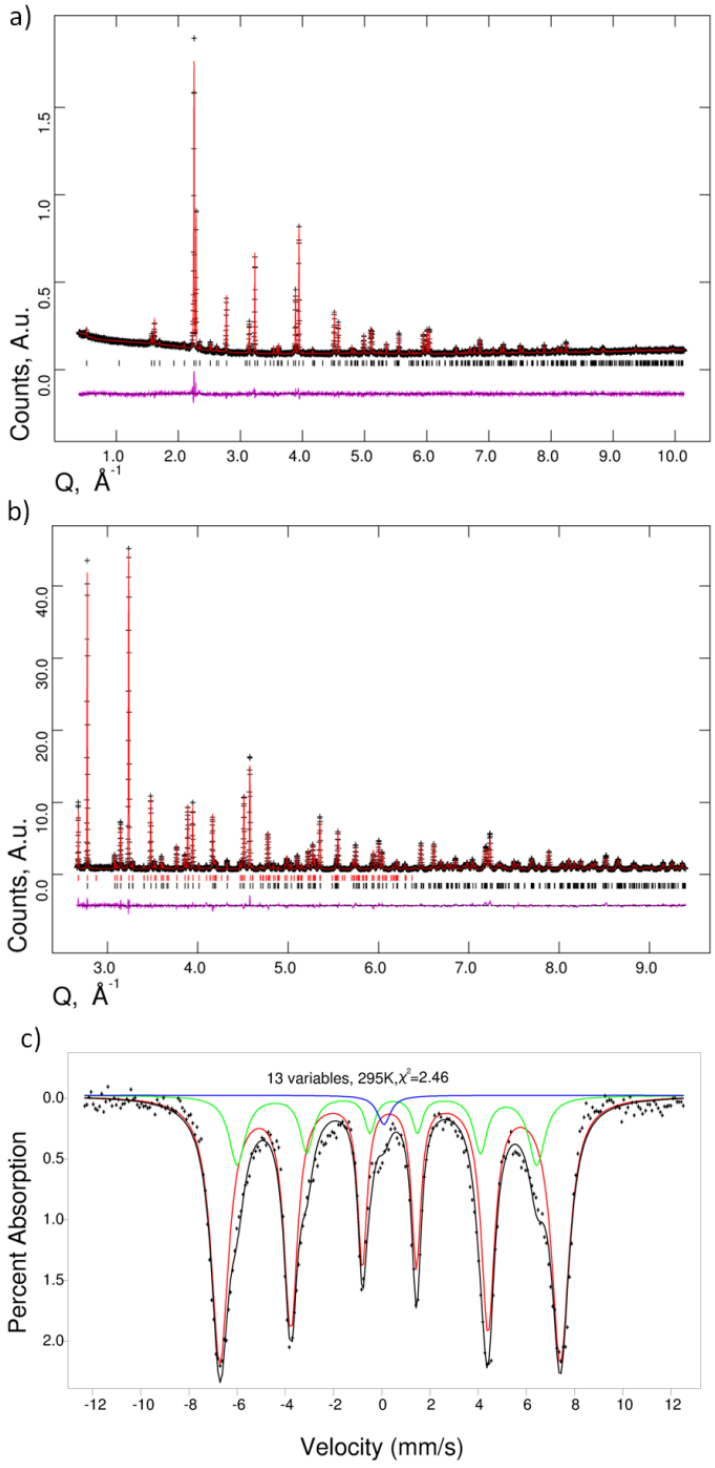

Figure 36 a) Rietveld plot for MoKα P-XRD data for phase pure $Y_{1.175}Ba_{1.825}Fe_2MnO_{8.04(5)}$.b) Rietveld plot for HRPD back-scattering bank (168˚ bank) containing both nuclear and magnetic phases for phase pure YBFM. c) Room temperature Mössbauer spectrum for phase pure $Y_{1.175}Ba_{1.825}Fe_2MnO_{8.04(5)}$, showing a fit to two Fe^{3+} environments for the refined as octahedral and square pyramidal geometries, and a signal near 0 mm/s attributed to an Fe metal impurity introduced during Mössbauer sample preparation.

Symmetry of the lowest energy DFT structure ($YBa_2Fe_2MnO_8$, Octahedral arrangement as outlined in computational setup) was determined using the FINDSYM code[133] (version 3.2.3, tolerance factor set to 0.1 Å). The highest symmetry space group was determined to be tetragonal *P4/mmm* (Figure 37a) in a unit cell a = b = 3.91603 and c = 12.19815 Å. This symmetry reduced unit cell was used as the basis for the structural refinement of $Y_{1.175}Ba_{1.825}Fe_2MnO_{8.04(5)}$. In order to be consistent with reported structures for the undoped material the origin of the unit cell was set to be on the octahedral B-site. The observed B-site occupancies from Mössbauer spectroscopy were used as the starting model for B site ordering within the structure. For the Rietveld refinement of $Y_{1.175}Ba_{1.825}Fe_2MnO_{8.04(5)}$, the structure was entered into GSAS as separate nuclear (P-XRD and NPD) and magnetic (NPD only) phases, refined diffraction patterns can be found in Figure 36a and b. The magnetic cell was refined as a 2 × 2 × 2 super cell of the nuclear cell, in the *Fmm′m′* space group configured in an G-type anti-ferromagnetic structure. The magnitude of the magnetic moment on the square pyramidal and octahedral sites allowed to refine independently with the direction of the magnetic moment refined along the a axis. Constraints were setup between the two phases in order to keep the B-site atoms consistent (positions, occupancies and thermal parameters were restrained) and the unit cells and phase fractions of the two phases were fixed, so that the ratio of the lattice parameters and total number of B-site atoms was maintained between the nuclear and magnetic phases.

As the starting model for the structure refinement of $Y_{1.175}Ba_{1.825}Fe_2MnO_{8.04(5)}$ was the most stable DFT model, the composition was initially set to close to the nominal value at $Y_{1.16}Ba_{1.84}Fe_2MnO_8$, with the additional Y inserted onto the Ba A-site. As the Rietveld refinement progressed, the composition was allowed to refine with the only restraint being that

full occupancy was enforced at each metal site. During the Rietveld refinement the space group was changed to *Pmmm* to allow an orthorhombic distortion in the lattice parameters to improve the fit of reflections with hkl values where h ≠ k. The refined orthorhombic distortion is small (the difference between the a and b lattice parameters is less than 3×10-3 Å). The space group of the magnetic cell did not need to be changed as the Fmm'm' space group is already an orthorhombic space group. The final Rietveld plots are shown in Figure 36a) and b), with the resulting structure in Figure 37b and the results of the refinement in Table 2 and Table 3, the reduced χ^2 was 4.46 for 72 variables.

Upon refinement of the structure it is shown that the DFT model calculated the unit cell volume to within 3.5% of experimental observation for $Y_{1.175}Ba_{1.825}Fe_2MnO_{8.04(5)}$, with a similar agreement between the reported and calculated cell volumes for the un-doped material. The refined structure shows that the unit cell distorts upon doping compared to the un-doped structure by a shortening of the a and b axis and a lengthening of the c axes. The shift is clearly seen by looking at the average c/a ratio before and after doping, changing from 3.018 to 3.087 (+2.29 %), this is close to the expected shift from the DFT model of +3.15 %. The unit cell distortion leads to an overall volume reduction on doping of 0.5% (DFT model calculated a reduction of 0.25%).

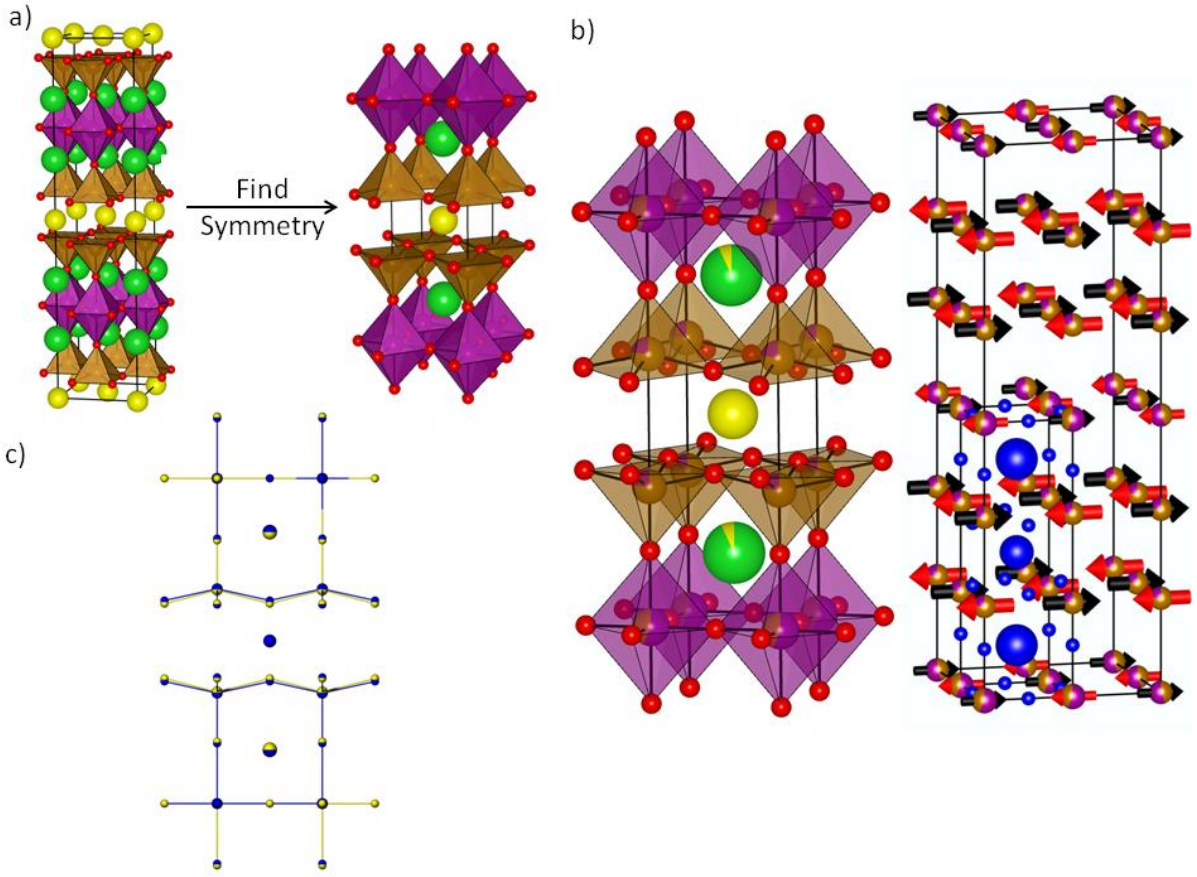

Figure 37 a) The lowest energy DFT cell for $Y_{1.175}Ba_{1.825}Fe_2MnO_{8.04(5)}$ and the symmetry reduced cell after using FINDSYM. b) The refined nuclear structure (left) of $Y_{1.175}Ba_{1.825}Fe_2MnO_{8.04(5)}$ and the refined magnetic structure (right), note that for clarity the atoms from the nuclear unit cell are overlaid in blue. c) The observed $Y_{1.175}Ba_{1.825}Fe_2MnO_{8.04(5)}$ structure (blue) overlaid with the DFT predicted cell (yellow). The unit cell sizes have been normalised to the observed cell to highlight the similarity between the observed and predicted atomic co-ordinates.

During Rietveld refinement, the A-site and B-site ratios in $Y_{1.175}Ba_{1.825}Fe_2MnO_{8.04(5)}$ changed from the starting values, to give a refined composition of $Y_{1.14(1)}Ba_{1.86(1)}Fe_{1.961(4)}Mn_{1.039(4)}O_8$, a result close to the nominal composition of $Y_{1.175}Ba_{1.825}Fe_2MnO_{8.04(5)}$. As the composition of $Y_{1.175}Ba_{1.825}Fe_2MnO_{8.04(5)}$ contains an excess of yttrium that occupies the A2 site with barium, although there was no observed disorder on the A1 site, remaining fully occupied by yttrium. The atomic co-ordinates of the refined structure show little deviation away from that of the DFT

structure (Figure 37c and Table 2), with exception of the z position of O2 (Table 2), leaving the two oxygen atoms in the equatorial position of the square pyramidal site slightly buckled.

Refinement of the oxygen content was trialled during the structural analysis. No vacancies were observed on the five oxygen positions and no extra oxygen within the structure could be found. Refinement of additional oxygen was trialled by placing an extra oxygen site in plane with the Y site (A1 in Table 2), previously reported as the O4 site in the un-doped material[13], in-plane with the A1 site. As no additional oxygen or any oxygen vacancies were found, the oxygen content was fixed to the nominal value of O_8, which is in good agreement with the oxygen content observed from iodometry of $O_{8.04(5)}$.

Ordering between the two B-site geometries in the refined structure was observed to change little from the starting values of $Fe_{0.805(9)}Mn_{0.195(9)}$ (B1) and $Fe_{0.39(2)}Mn_{0.61(2)}$ (B2) for the square pyramidal and octahedral sites respectively refined values being $Fe_{0.762(1)}Mn_{0.238(1)}$ and $Fe_{0.437(2)}Mn_{0.563(2)}$, a difference of ≈ 4% showing the refined model to be in good agreement with room temperature Mössbauer Figure 36c) spectroscopy values. Note that due to the large contrast in neutron scattering between Fe and Mn (coherent scattering lengths of 9.45 fm and −3.73 fm, respectively [134]), therefore the refinement of the occupation on this site is reliable.

In order to test how well the 0 K DFT calculations presented in this chapter represent the possible B-site ordering in the $3a_p$ structure, a statistical mechanics approach as detailed in the literature[47] was applied to calculate B-site orderings at elevated temperatures. This statistical mecahnics approach estimates the occupation of different configurations at increased temperatures based upon the energy differences between configurations while taking into

account configurational entropy and estimating energies for paramagnetic states at high temperatures (as outlined in the introduction chapter).

This approach was applied to the six configurations used in the DFT calculations of $YBa_2Fe_2MnO_8$ detailed in the computational methods when Temperature (T) was equal to 300 K. When calculating populations at high temperatures, energies for paramagnetic states were estimated, using the average energy of the ferromagnetic and anti-ferromagnetic states. Populations at two temperature values were calculated, with T equal to 300 and 1475 K in order to approximate room temperature and the synthesis temperature. From the statistical mechanics results, for each of the structures it is possible to calculate the expected population of each of the B-site environments, knowing the average population of each environment in each configuration.

When the occupations of each configuration is estimated at 1475 K the percentage of the Mn occupying octahedral and square pyramidal sites was calculated to be 71.4 % and 28.6 % respectively; compared to a completely disordered model where 33.3 and 66.7 % of the Mn atoms would be expected in the octahedral and square pyramidal sites respectively. The result at 1475 K suggests that B-site ordering, with the majority of Mn occupying the octahedral site is calculated to be favourable. At 300 K the statistical mechanics would expect the structure to be very close to fully ordered with occupancies of 99.7 % and 0.3 % for the octahedral and square pyramidal sites respectively. The higher temperature calculation was decided to be the most applicable calculation for comparison to our experimental results as experimentally cation ordering will be effectively frozen while still at relatively high temperatures. The calculated B-site ordering from the statistical mechanics show that the DFT model had calculated the correct trend when compared to the experimental Mn occupancies.

The magnetic moments for the B-sites were refined to be 3.41(3) and 2.81(4) μ_B for the square pyramidal and octahedral sites. The absence of polyhedral tilting in the experimentally observed structure leads to the conclusion that the orthorhombic distortion occurs due to the magnetic moments aligning along the a axis. The conclusion that the orthorhombic distortion is caused by the magnetic ordering accounts for why the DFT model did not calculate a distortion, as with a colinear spin model this directional magnetically induced distortion would not be possible.

Comparing the M-O bonding environments in $Y_{1.175}Ba_{1.825}Fe_2MnO_{8.04(5)}$ with $YBa_2Fe_3O_8$ (Table 4) it was observed that there is little change in the square pyramidal site. However, it is observed that on doping the $M_{oct} - O_{axial}$ bond lengthens by 0.094(3) Å, suggesting a Jahn-Teller distortion of the site as would be expected for a Mn^{3+} octahedral site; increasing the distortion of the already distorted site in the undoped material. Examining bond distances in the structure, the octahedral site distortion is the main cause of the lattice parameter distortion in the material. It was observed that DFT calculations over estimate the length of the axial bond length in the octahedral site consistently by ~ 0.1 Å in both the doped and undoped material. However the change in the axial bond length upon doping in the DFT calculation is similar to that found experimentally with an increase of 0.113 Å. The discrepancy can be attributed to the fact that the experimental structure also contains Fe on the octahedral site, causing the shift in bond length to be smaller than predicted by DFT.

The methodology reported by Baur [135] implemented in VESTA [136] was used to quantify the distortions of the polyhedra in the $3a_p$ structure by calculation of a distortion parameter according to the following equation:

$$D = \frac{1}{n}\sum_{i=1}^{n}\left\{\frac{\left|L_i - L_{avg}\right|}{L_{avg}}\right\} \quad \textbf{(3.12)}$$

Where D is the distortion parameter, n is the number of bonds in the polyhedron, L_i is the length of bond i, and L_{avg} is the average bond length in the polyhedron. An undistorted polyhedron would yield a value of zero and the heavily distorted octahedra in the reported $Bi_4Ti_3O_{12}$ phase have values of 0.078 and 0.119[137]. All calculated values can be found in Table 5, experimentally the octahedral site is observed to distort significantly upon doping, with the distortion parameter changing from 0.039 to 0.060 (an increase of 56.6%), driven by the aforementioned elongation of the axial bond. The square pyramidal site, however, sees a much smaller shift in its distortion parameter, changing from 0.023 to 0.025 (an increase of 12.4%). In the DFT structures, a similar shift in the distortion is observed on the octahedral site, with a shift from 0.049 to 0.078 (an increase of 57.8%). However, when looking at the change in distortion on the square pyramidal site with DFT, there is actually a reduction of the value of *D* from 0.029 to 0.026 (a decrease of 11.4%). When looking at the distortion parameters of all of the DFT configurations, none of the configurations trialled in this chapter resulted in an increase in the distortion parameter of the square pyramidal site.

This result of distortion of the polyhedra is similar to that observed when comparing the reported $Ca_2Fe_2O_5$ and $Ca_2Fe_{1.039(8)}Mn_{0.962(8)}O_5$ compounds found in the brownmillerite structure [10, 22], in that the distortion parameter on the Mn site increases and decreases on the Fe site when compared to the Fe pure compound. In the brownmillerite compound, the distortion parameter on the octahedral site (dominantly occupied by Mn) increases from 0.045 to 0.066 (increase of 47.6%) and the tetrahedral site (dominantly occupied by Fe) decreases from 0.026 to 0.020 (decrease of 21.0 %) relative to the Fe pure $Ca_2Fe_2O_5$ compound.

The material synthesised in this chapter can be compared to other Fe and Mn containing layered oxides, one example of a compound with B-site ordering between Fe and Mn is $Ca_2Fe_{2-y}Mn_yO_{5+z}$ brownmillerites [22, 116]. In these materials, the same level of Mn doping is also reported as the material studied in this chapter (y =⅔). At this doping level a similar site preference is observed to to that reported in this chapter, with the Mn exclusively being doped into the octahedral site. Once the value of y is increased to 1, as with the $Y_{1.175}Ba_{1.825}Fe_2MnO_{8.04(5)}$ compound, where the octahedral sites could potentially be fully occupied by Mn, some disorder between the Fe and Mn sites is observed. In previous work with the $Ca_2Fe_{2-y}Mn_yO_{5+z}$ system that when the Mn doped compound is compared to the Fe pure compound that the same distortions of the unit cell that we observe with $Y_{1.175}Ba_{1.825}Fe_2MnO_{8.04(5)}$, with the distortion of the unit cell largely driven by a distortion of the Mn octahedra. By the use of DFT it has been possible to predict strong B-site ordering within a system, when precedents have been shown to exist with the dopant metal (Mn^{3+}) with each of the possible site preferences possible within the $3a_p$ structure; octahedral geometry [22, 23], square pyramidal geometry [117] and B-site disordered [138, 139].

Although the calculations are based upon the stoichiometric compositions, this restriction was imposed as a far larger quantity of computing resources would have been required if a number of non-stoichiometric compositions were to be considered. For each composition there would be the requirement to trial larger super cells and more configurations in order to determine the most stable arrangement for each composition. For example, in the system studied in this chapter, with M = Mn, in order to calculate the Y:Ba non-stoichiometry in the steps of 0.025 that were used experimentally (calculating Y values of 0.8 – 1.2) would require an additional 48 calculations for each value of *x*, assuming that 3 B-site orderings would be trialled for each Y

content value. Under this assumption the number of calculations would increase for M = Mn from 7 (plus the undoped material) to 104 (48 for x = 1 and 2, plus 8 for x = 3). In addition, a number of A site configurations for each B-site ordering would need to be modelled, and larger super cells would be needed to model the non-stoichiometry. Hence the suggestion that a computational investigation of small changes in stoichiometry is unfeasible at present.

3.8 Conclusions

In summary, it has been shown that it is possible to use DFT to calculate reaction enthalpies of complex oxides from binary oxides; this method has also then been applied to predict a stable doping level in the $YBa_2Fe_{3-x}M_xO_8$ system and rationalise why doping becomes unfavourable when x = 2 and M = Mn. Due to the increasing amount of Mn atoms forcing the $3a_p$ octahedra away from a distorted state, favoured by Jahn-Teller distorted Mn^{3+}. These calculations have been able to predict the approximate composition, accurate atomic co-ordinates and B-site ordering of the doped structure and B-site distortions, (Figure 37c of an oxide where ordering between two similar transition metals is novel. The predicted material was then synthesised with only small deviations in the structure and composition from those calculated.

Using this methodology, compositions for which $3a_p$ structure is predicted to be unfavourable, it was not observed to form when synthesis was attempted. Therefore, it can be concluded that the methodology presented here is a powerful tool when attempting to synthesise new materials starting from a known structure or material and can be used for large and/or complex oxides where the systems are too large or complex for existing methods.

3.9 Tables

Table 1: Shifts in bond lengths between the undoped and Co doped material.

Bond	DFT shift in bond length from undoped (Å)	Reported shift in bond length from undoped(Å) [27]	Difference (Å)
M_{oct} - O_{axial}	0.0092	-0.0124	0.0032
M_{oct} - $O_{equatorial}$	-0.0045	-0.0032	0.0013
$M_{sq.py}$ - O_{axial}	-0.0163	-0.0063	0.01
$M_{sq.py}$ - $O_{equatorial}$	-0.0051	-0.0336 (average)	0.0285

Table 2: Refined crystallographic data and DFT structure parameters for $Y_{1.175}Ba_{1.825}Fe_2MnO_{8.04(5)}$ refined in *Pmmm* space group, note that all sites were constrained to be fully occupied, refined parameters shown in bold.

	Parameter	**Rietveld**	**DFT**
	a (Å)	**3.88407(5)**	3.91603
	b (Å)	**3.88125(5)**	3.91603
	c (Å)	**11.98425(9)**	12.19815
Site	**Parameter**	**Rietveld (*sg. Pmmm*)**	**DFT (*sg. P4/mmm*)**
A1	Position	0.5, 0.5, 0.5	0.5, 0.5, 0.5
	Composition	Y	Y
	U_{iso} (Å^2)	**0.0127(2)**	-
	Multiplicity	1	1
A2	Position	0.5, 0.5, **0.83558(7)**	0.5, 0.5, 0.833890
	Composition	**$Ba_{0.929(5)}Y_{0.071(5)}$**	Ba
	U_{iso} (Å^2)	**0.0127(2)**	-
	Multiplicity	2	2
B1	Position	0, 0**, 0.66045(6)**	1, 1, 0.656840
	Composition	**$Fe_{0.762(1)}Mn_{0.238(1)}$**	Fe
	U_{iso} (Å^2)	**0.013(1)**	-
	Multiplicity	2	2
B2	Position	0, 0, 0	0, 0, 0
	Composition	**$Fe_{0.437(2)}Mn_{0.563(2)}$**	Mn
	U_{iso} (Å^2)	**0.0091(2)**	-
	Multiplicity	1	1
O1	Position	0, 0.5, **0.3757(1)**	0, 0.5, 0.385130
	Composition	O	O
	U_{iso} (Å^2)	**0.0133(5)**	-
	Multiplicity	2	4
O2	Position	0, 0.5, **0.3880(1)**	Equivalent to O1
	Composition	O	-
	U_{iso} (Å^2)	**0.0175(6)**	-
	Multiplicity	2	-
O3	Position	0, 0, **0.81499(8)**	1, 1, 0.809780
	Composition	O	O
	U_{11}, U_{22}, U_{33} (Å^2)	**0.035(2), 0.024(1), 0.0224(6)**	-
	Multiplicity	2	2
O4	Position	0.5, 0, 0	0.5, 1, 1
	Composition	O	O
	U_{iso} (Å^2)	**0.0067(6)**	-
	Multiplicity	1	2
O5	Position	0, 0.5, 0	Equivalent to O4
	Composition	O	-
	U_{iso} (Å^2)	**0.0135(7)**	-
	Multiplicity	1	-

Total refined composition: $Y_{1.14(1)}Ba_{1.86(1)}Fe_{1.961(4)}Mn_{1.039(1)}O_8$

Table 3: Refined crystallographic data for the magnetic structure of $Y_{1.175}Ba_{1.825}Fe_2MnO_{8.04(5)}$ and relationships to structure parameters in Table 1, note all parameters apart from the magnetic moments are linked with equivalent parameters in the nuclear structure

	Parameter	**Rietveld**	**Relationship to nuclear**
	a (Å)	7.76814(9)	x 2 $a_{nuclear}$
	b (Å)	7.76248(9)	x 2 $b_{nuclear}$
	c (Å)	23.9684(2)	x 2 $c_{nuclear}$
Site	**Parameter**	**Rietveld**	**Equivalent nuclear site (**Table2**)**
1a	Position	0, 0, 0	B2
	Composition	$Fe_{0.437(2)}Mn_{0.563(2)}$	
	U_{iso} (Å^2)	0.0091(2)	
	μ_B	**-2.81(4)**	
	Multiplicity	4	
1b	Position	0, 0, 0.5	B2
	Composition	$Fe_{0.437(2)}Mn_{0.563(2)}$	
	U_{iso} (Å^2)	0.0091(2)	
	μ_B	**+2.81(4)**	
	Multiplicity	4	
2a	Position	0, 0, 0.33025(3)	B1
	Composition	$Fe_{0.762(1)}Mn_{0.238(1)}$	$z = z_{nuclear}/2$
	U_{iso} (Å^2)	0.013(1)	
	μ_B	**-3.41(3)**	
	Multiplicity	8	
2b	Position	0, 0, 0.33025(3)	B1
	Composition	$Fe_{0.762(1)}Mn_{0.238(1)}$	$z = ½ - z_{nuclear}/2$
	U_{iso} (Å^2)	0.013(1)	
	μ_B	**+3.41(3)**	
	Multiplicity	8	

Table 4: Observed and calculated bond lengths for $YBa_2Fe_3O_8$ (X= 0) and $Y_{1.175}Ba_{1.825}Fe_2MnO_{8.04(5)}$ *x*= 1)

Bond	**$YBa_2Fe_3O_8$ observed(Å)[13]**	**$Y_{1.175}Ba_{1.825}Fe_2MnO_{8.04(5)}$ observed (Å)**	**$YBa_2Fe_3O_8$ DFT (Å)**	**$YBa_2Fe_2MnO_8$ DFT (Å)**
M_{oct} – $O_{equatorial}$	1.9590(0)*	1.94204(3) – O4 1.94062(3) – O5 1.94133(3) average	1.9767	1.9580
M_{Oct} – O_{axial}	2.1807(17)	2.2173(10) – O3	2.2074	2.3203
$M_{sq.py}$ – $O_{equatorial}$	2.0198(4)	1.9894(4) – O 1 2.0259(5) – O2 2.0077(5) average	2.0407	2.0240
$M_{sq.py}$ – O_{axial}	1.8405(24)	1.8513(12) – O3	1.8597	1.8649

***** SD reported as zero, error likely to be very small on this distance as both atoms have fixed co-ordinates.

Table 5 Distortion parameters calculated in VESTA according to equation (3.12)[135], note that the values quoted for the distortion parameters for the $YBa_2Fe_2MnO_8$ – DFT are the averaged values when the DFT configuration contains both Fe and Mn polyhedral of the same type, configurations highlighted in bold for DFT configurations indicate the lowest energy configuration.

Geometry	**$YBa_2Fe_3O_8$ Observed (literature)[13]**	**$Y_{1.175}Ba_{1.825}Fe_2MnO_{8.04(5)}$ Observed (this chapter)**	**$YBa_2Fe_3O_8$ DFT**	**$YBa_2Fe_2MnO_8$ DFT**
Square Pyramidal	0.023	0.025	**0.029**	**0.026 (octahedral)** 0.020 (square pyramidal) 0.027 (mixed)
Octahedral	0.039	0.060	**0.049**	**0.078 (octahedral)** 0.060 (square) 0.074 (mixed)

3.10 Appendix

In preliminary work for this chapter, three different computational setups were tested. For the lowest accuracy settings (labelled Low), the plane wave cutoff energy was set to 450 eV, and electron steps converged until ΔE was less than 1.0 x10^{-5} eV and forces on atoms to less than 0.05 eVÅ^{-1}. The k-point density was set according to the condition in equation (3.13), where y = 20 on a gamma-centred mesh:

$$k_i \times r_i \geq y \quad \textbf{(3.13)}$$

Where r_i is the real lattice vector (given in Å) and k_i indicates the number of k-points along the lattice direction *i*. For the next the configuration (labelled Medium), forces on atoms were relaxed to less than 0.01 eVÅ^{-1}, the plane wave cut-off was set to 520 eV and y equal to 40, wave functions were converged as for the Low setting. For the last accuracy settings (labelled High), the initial k-point density was set such that y was increased to be equal to 55, where the computational setups are summarised in Table 6.

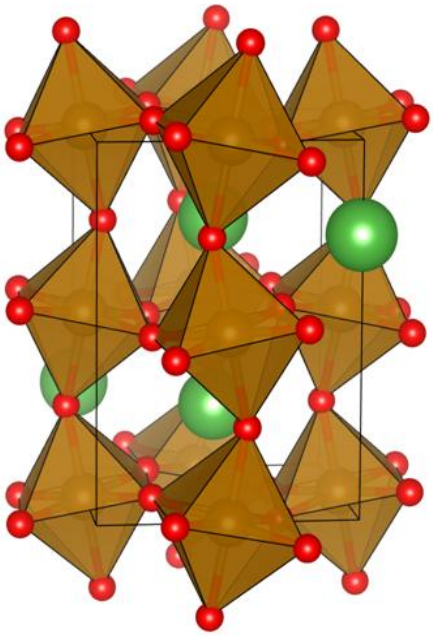

Figure 38 Structure of $LaMO_3$ used within this work for testing VASP settings, where atoms are coloured as follows: lanthanum (green), transition metal, M (brown) and oxygen (red).

In order to determine which accuracy settings should be used in VASP when performing reaction calculations for $YBa_2Fe_{3-x}M_xO_8$, reaction energies were calculated from binary oxides for the system $LaMO_3$ where M = Fe, Ni, Co and Cr. As with the $YBa_2Fe_{3-x}M_xO_8$ system, the energy for O_2 was considered and set to a value of -8.5 eV/FU in accordance with the literature[17]. The addition of the binary oxide Cr_2O_3 (when M = Cr) with the input structure used as previously reported [140]. When using a $+U_{eff}$ term for Cr, U_{eff} was set equal to 3.5 eV. Atomic co-ordinates were used as experimentally reported for $LaFeO_3$[28] (Figure 38). The atomic coordinates for the binary oxides were used as outlined in the computational setup section of this chapter. For each of the values of M, four different magnetic orderings, A, C and G type anti-ferromagnetic and ferromagnetic orderings, were trialled in a collinear spin model.

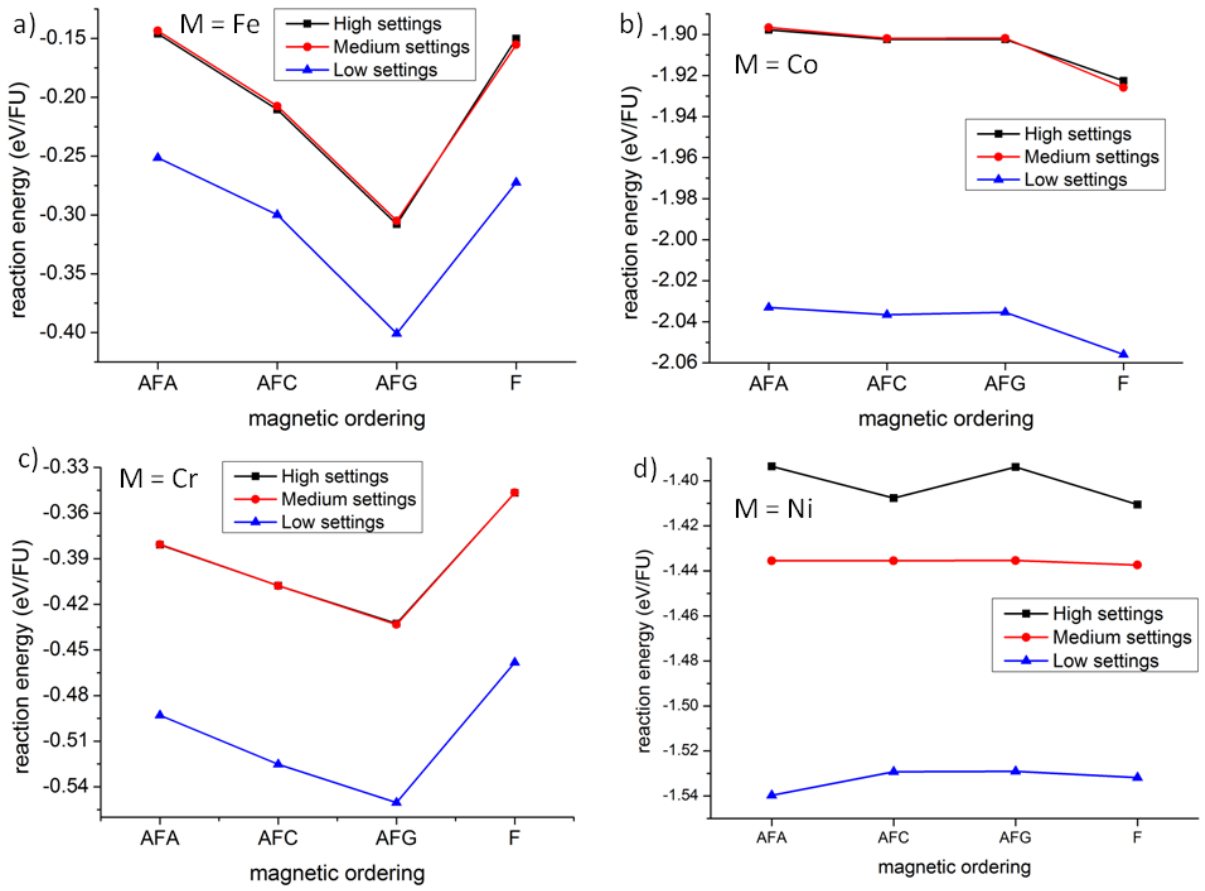

Figure 39 Calculated reaction energies for $LaMO_3$ for four different magnetic orderings and computational setups (as noted in main text) as follows: AFA equals A-type anti-ferromagnetic, AFC equals C-type anti-ferromagnetic, AFG equals G-type anti-ferromagnetic and F equals ferromagnetic.

Initially computational settings were trialled based upon the relative reaction energies calculated for each of the different magnetic orderings. Results for these calculations (Figure 39) show that for M = Fe, Co and Cr obtain very similar trends in results for all three computational setups, although when the Low settings are used the absolute reaction energy calculated is always significantly lower than the other DFT settings. When M = Ni however, the Low settings obtain a different order of stability, when compared to the Medium and High settings, calculating the A-type anti-ferromagnetic ordering as the most stable, compared to the Meduim and High

settings, which calculate the ferromagnetic ordering to be the most stable. In summary it was concluded from these computational setups, that the medium settings provided the best balance between accuracy and speed of calculation.

In order to calculate accurate, absolute values for the reaction energies, it has been shown previously that a +U term is required [17], this was applied as outlined in the computational section of this chapter. Calculations with a +U term included were calculated using the Medium settings defined previously, with the $LaMO_3$ structures setup using the G-type anti-ferromagnetic and ferromagnetic orderings. The resulting reaction energies were then calculated and compared with experimentally reported values [112].

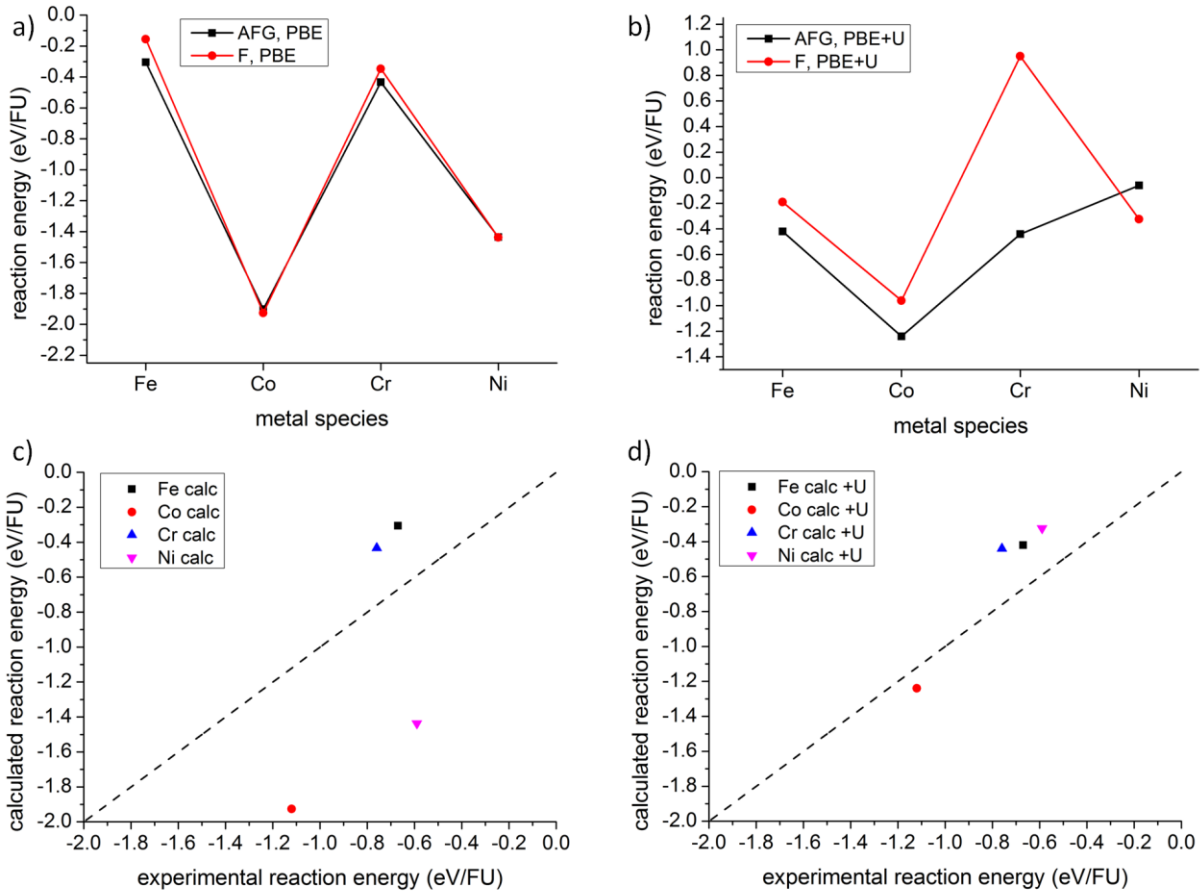

Figure 40 a) Reaction energies for the formation of $LaMO_3$ from binary oxides in G-type anti-ferromagnetic ordering (AFG) and ferromagnetic ordering (F), calculated without the +U term. b) Reaction energies calculated for the formation of $LaMO_3$ from binary oxides with the same magnetic ordering as in panel a), with the +U term included. All of these calculations were performed using the Medium calculation settings outlined in the main text. c & d) Experimentally reported reaction energies [112] plotted versus the calculated formation energies, without the +U term (panel c) and with (panel d). The imposed x = y line is plotted as a guide to the eye to help observe the difference between calculated and experimental formation energies.

The DFT calculations of $LaMO_3$ with the +U term, when compared to the calculations without, show that the introduction of the +U term results in absolute reaction energies that are much closer to those reported experimentally (Figure 40 c and d). The addition of the +U term term

also results in larger energy differences between the G-type antiferromagnetic and ferromagnetic orderings (Figure 40)

Following on from these calculations, further preliminary calculations on $YBa_2Fe_3O_8$ in the $3a_p$ structure found that a compromise in calculation settings between the medium and high settings, by reducing the plane-wave cut-off energy and the value of y in equation (3.13), named Low-Medium in Table 6.

Table 6 Input parameters for DFT calculations in VASP tested to find optimal values between fast and accurate calculations

Setting	Parameter	Value
Low	Plane wave cutoff	450 eV
	wavefunction convergence	1.0×10^{-5} eV
	forces convergence	0.05 eVÅ^{-1}
	y	20
Medium	Plane wave cutoff	520 eV
	wavefunction convergence	1.0×10^{-5} eV
	forces convergence	0.01 eVÅ^{-1}
	y	40
High	Plane wave cutoff	520 eV
	wavefunction convergence	1.0×10^{-5} eV
	forces convergence	0.01 eVÅ^{-1}
	y	55
Medium - Low	Plane wave cutoff	450 eV
	wavefunction convergence	1.0×10^{-5} eV
	forces convergence	0.01 eV Å^{-1}
	y	20

Chapter 4. Doping predictions for $YBa_2Ca_2Fe_{5-x}M_xO_{13}$

4.1 Abstract

In this chapter, doping calculations are performed on a large, functional layered oxide. The reaction energies to form $YBa_2Ca_2Fe_{5-x}M_xO_{13}$ from binary oxides and oxygen gas are calculated using density functional theory (DFT). A range of transition metals were trialled, with M = Co, Cu, Mn, Ni and Zn for x = 0.25, 0.50, 0.75, 1.00 and 1.25 and with M = Ti and x = 0.25, 0.50, 0.75 and 1.00. These calculations then allow for the prediction of stable doping levels in the system along with some estimate of the site preferences for the dopant species. The predictions made have subsequently been tested experimentally by other group members and found to be in good agreement with the predictions.

4.2 Introduction

Building upon calculations presented in the previous chapter, this work uses a similar approach on a more complex and functional material. The previously reported cathode $Y_{1.1}Ba_{1.5}Ca_{2.3}Fe_5O_{13}$[15] is shown to be stable, with good compatibility with existing electrolyte materials. While the $Y_{1.1}Ba_{1.5}Ca_{2.3}Fe_5O_{13}$ is found to have good area specific resistance (ASR) values (maximum value of 0.87 Ωcm^{-2} at 700 °C), the low reported d.c. conductivity of remains a problem for use as an SOFC cathode. Thus $Y_{1.1}Ba_{1.5}Ca_{2.3}Fe_5O_{13}$ is a good candidate for doping in order to improve the observed d.c conductivity to enhance its properties as a cathode.

The reported $Y_{1.1}Ba_{1.5}Ca_{2.3}Fe_5O_{13}$ compound forms into a perovskite superstructure, an analogue of the previously reported $Ba_{0.81}Ca_{0.78}Nd_{0.91}Fe_{2.5}O_{6.43}$[16] with a unit cell expanded by r45°($\sqrt{2}a_p \times \sqrt{2}a_p \times 10a_p$) relative to the cubic ABO_3 perovskite cell, with the resulting structure in the *Imma* symmetry space group (hereafter referred to as the $10a_p$ structure, Figure 41a) and contains three distinct A and B cation sites.

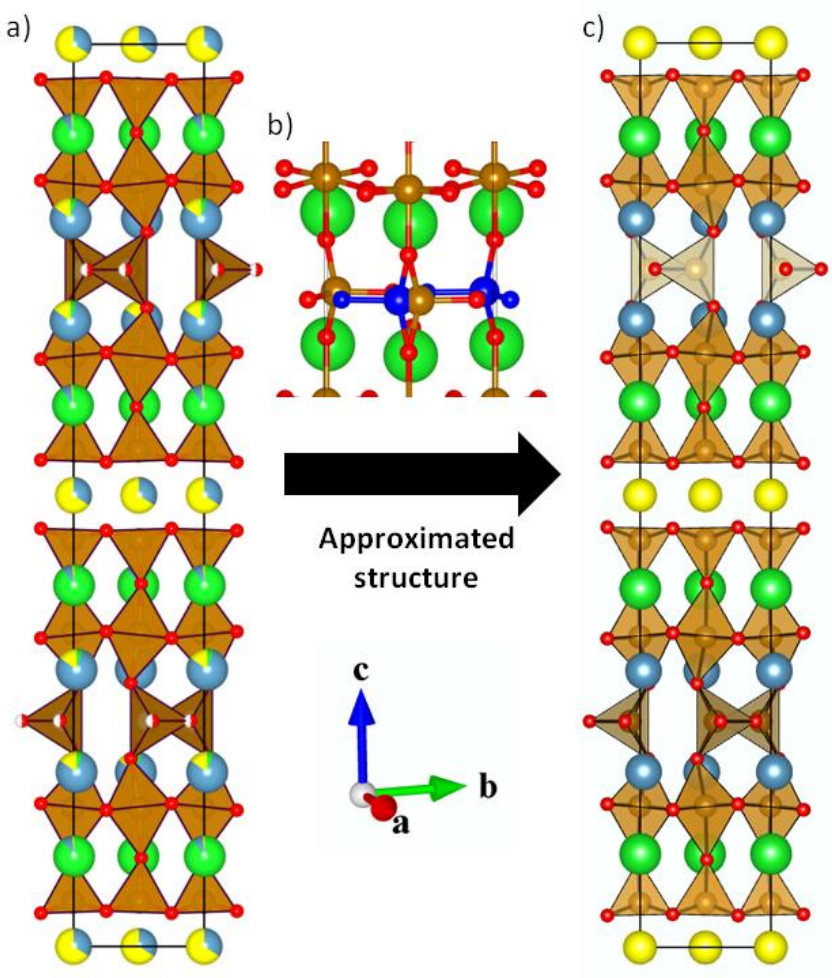

Figure 41 a) Experimental structure of $Y_{1.1}Ba_{1.5}Ca_{2.3}Fe_5O_{13}$, the pie chart representation of atoms corresponds to their refined fractional occupancies. b) Choice of tetrahedral chains, viewed along the [101] direction generated by the space group of the structure, with the chain highlighted in blue removed in one half of the cell and the non highlighted chain removed in the other. c) The idealised structure for stoichiometric $YCa_2Ba_2Fe_5O_{13}$ used for the DFT calculations within this chapter. Colours of atoms as follows (with the exception of the blue tetrahedral chain in panel b); yttrium (yellow), calcium (cyan), barium (green), iron (brown) and oxygen (red).

The A-sites are split into two 8 co-ordinate yttrium, four 9 co-ordinate calcium and four 12 co-ordinate barium sites, a significant amount of A-site disorder is observed experimentally between these sites (Figure 41a). The B-sites are separated into two 4 co-ordinate tetrahedra, four 5 co-ordinate square pyramidal and four 6 co-ordinate octahedral sites, where each of these geometries are distorted away from ideal. The octahedral site is distorted such that it has four

short equatorial bonds and two long axial bonds, the square pyramidal has one short axial bond and four long equatorial, with the plane sitting below the iron site, the tetrahedral site has two bonds of equal length in the c direction, and the two bonds in the ab plane are of differing lengths to both the bonds in the stacking direction and each other. The level of these polyhedral distortions can be quantified by calculation of each geometries distortion index, as reported by Baur[135] and implemented in VESTA[136]:

$$\mathrm{D} = \frac{1}{n}\sum_{i=1}^{n}\left\{\frac{\left|L_i - L_{avg}\right|}{L_{avg}}\right\} \qquad \textbf{(4.1)}$$

Where D is the calculated distortion index, n is the number of bonds in the polyhedron, L_i indicates the bond length i in the polyhedron and L_{avg} is the average bond length in the geometry. A calculated D value of zero indicates an ideal undistorted polyhedron and a heavily distorted polyhedron, such as the octahedra in the reported $Bi_4Ti_3O_{12}$ structure, have values of 0.078 and 0.119[137]. The polyhedra in the $10a_p$ structure as reported, have values of 0.037, 0.022 and 0.034 for the octahedral, square pyramidal and tetrahedral geometries respectively.

In this chapter a series of calculations are performed for the $YBa_2Ca_2Fe_{5-x}M_xO_{13}$ system, where M = Co, Cu, Mn, Ni, Zn and Ti. When M = Co, Cu, Mn, Ni and Zn, x values were trialled for x = 0.25, 0.5, 0.75, 1.00 and 1.25, when M = Ti doping levels were calculated for x = 0.25, 0.5, 0.75 and 1.00. Since accurate reaction energies are sought in this study, DFT energies are required at each level of doping.

A choice of preference for B-site doping is not a trivial choice, as each of the dopant species have been reported in more than one of the geometries found in the $10a_p$ structure. Examples have been reported for tetrahedral geometry for Co, Ni, Zn and Ti[141-145], square pyramidal ions

reported for Co, Cu, Ni and Mn[117, 141, 146-148] and all of the dopant species in this chapter have been reported in the octahedral geometry[3, 22, 149-152]. Although not all of the dopant species considered in this chapter have been reported as doped into the 3+ oxidation state required by the $10a_p$ structure; so for calculations with a high dopant content where Fe cannot increase its oxidation state to compensate may inhibit doping. The first challenge addressed in this chapter is generating input structures for the calculations, since a variety of configurations are required as the choice of B-site is not obvious, if indeed any B-site ordering is favoured.

An existing precedent for the generation of structures is the Site Occupancy Disorder code[47] (SOD) that has been previously used for doping and solid solution calculations on smaller systems in combination with methods for relaxing and ranking structures[60-62]. However, due to the size of the $10a_p$ structure, using SOD would result in a large number of structures that would require relaxation at each doping level for each B-site metal. For the doping range covered in this chapter, 4,216 independent configurations were found that would require relaxation for each metal (when doping goes up to $x = 1.25$), when all of the metals of interest are considered, this would result in a total of 22,175 configurations (plus the undoped material). Initially each structure generated would require some level of relaxation and energy ranking, with many requiring DFT energies, in order to calculate accurate site orderings and reaction energies. As a result of this it was decided to take a small number of configurations at each doping level that are representative of possible B-site orderings, to reduce the number of calculations at each doping level to a maximum of 5, leading to a total of 124 calculations performed in this chapter.

DFT calculations cannot be easily performed on this structure and composition as reported due to the A-site non-stoichiometry and tetrahedral chain disorder. If A-site disorder and disordered tetrahedral layers (Figure 41b) were to be considered, a large supercell of the experimental cell

would be required, considering the experimental cell already contains 92 atoms, the calculations would be very large and rapidly become unfeasible on such a cell. In order to be able to perform DFT calculations, some approximation of the reported structure and composition have to be made. First, the A-site disorder was removed from the calculations by making each A-site layer fully occupied by the A-site species which is reported to be the major A-site species. The removal of A-site disorder leads to the stoichiometric composition, $YBa_2Ca_2Fe_5O_{13}$. Secondly, disorder in the tetrahedral layers was removed as follows, when looking at the tetrahedral layer there are two choices of tetrahedral chain (with one highlighted in blue in Figure 41b), and the approximated structure was built with alternating the choice of tetrahedral chain between each tetrahedral layer as reported for this structure[16]. In the resulting approximate structure shown in Figure 41c, the unit cell axis labels for the calculations were altered from the experimental structure, so that the long stacking axis was labelled as c rather than b.

4.3 Computational Setup

The method used for calculating reaction energies in this chapter is based upon the method used in the previous chapter, which has been shown as a good method for reproducing experimental reaction energies for perovskites[17]. Calculations in this chapter were performing using plane-wave DFT implemented using the Vienna *ab-initio* Simulation Package (VASP) version 5.2.2 [105, 106], with the Perdew, Burke and Ernzerhof (PBE) exchange correlation functional[103]. For the A-site atoms (yttrium, barium and calcium) the first sub-valent s orbital was treated as valence, where the pseudo potential was available for the B-site species (Fe, Cu, Mn, Ni and Ti) the first sub-valent p orbitals were treated as valence. In all calculations within this chapter both atomic

positions and unit cell vectors were relaxed. A gamma-centred *k*-point grid was used in each calculation, with the smallest *k*-point grid that fulfils the following condition:

$$nk_i \times r_i \geq 20 \text{ Å} \quad \textbf{(4.2)}$$

Where nk_i is the number of *k*-points on the lattice vector *i* and r_i is the length of the corrisponding real space lattice vector, given in Å. The plane wave cut off energy was set to 450 eV. Wavefunctions were converged until the energy difference between electronic steps was less than 1×10^{-5} eV and forces on atoms were relaxed to less than 0.01 eV/Å.

Rotationally invariant effective U parameters were used (U_{eff}), with values of 4.0, 3.3, 4.0, 4.0, 6.4, 7.1 and 5.82 eV for Fe, Co, Cu, Mn, Ni, Zn and Ti respectively, as reported for previous calculations of oxides for each of the transition metal species[153-155]. Where U_{eff} = U – J, values for Ti were U = 6.6 and J = 0.78 to give the U_{eff} = 5.82 eV, note that J = 1.00 for all other transition metal species. Each of the $10a_p$ structures within this chapter were setup with G-type antiferromagnetic ordering, using a collinear model without including spin orbit coupling. Note that in all of the $10a_p$ structures were calculated with only G-type anti-ferromagnetic ordering as this is the magnetic ordering reported for $Y_{1.1}Ba_{1.5}Ca_{2.3}Fe_5O_{13}$[15]. As each dopant species would remain the minority B-site metal (with the highest level being 25 mol% on the B-site), it was assumed that the magnetic ordering favoured in the reported experimental structure would remain favoured. Magnetic ordering was used in the calculations of the binary oxides where magnetic ordering has been experimentally observed and reported in the literature[29, 120, 121, 124, 156].

Atomic co-ordinates for binary oxides were used as reported[29, 120-124, 153, 155-157]. The initial atomic co-ordinates for the $10a_p$ structure were created based upon generation of the full unit cell

from the asymmetric co-ordinates using the space group symmetry, with the approximations outlined previously. Four different B-site preferences were considered for each value of *x*. The number of dopant atoms placed into the unit cell is equal to the value of *x* divided by 0.25, therefore the maximum number of dopant atoms placed into the unit cell at *x* = 1.25 is five.

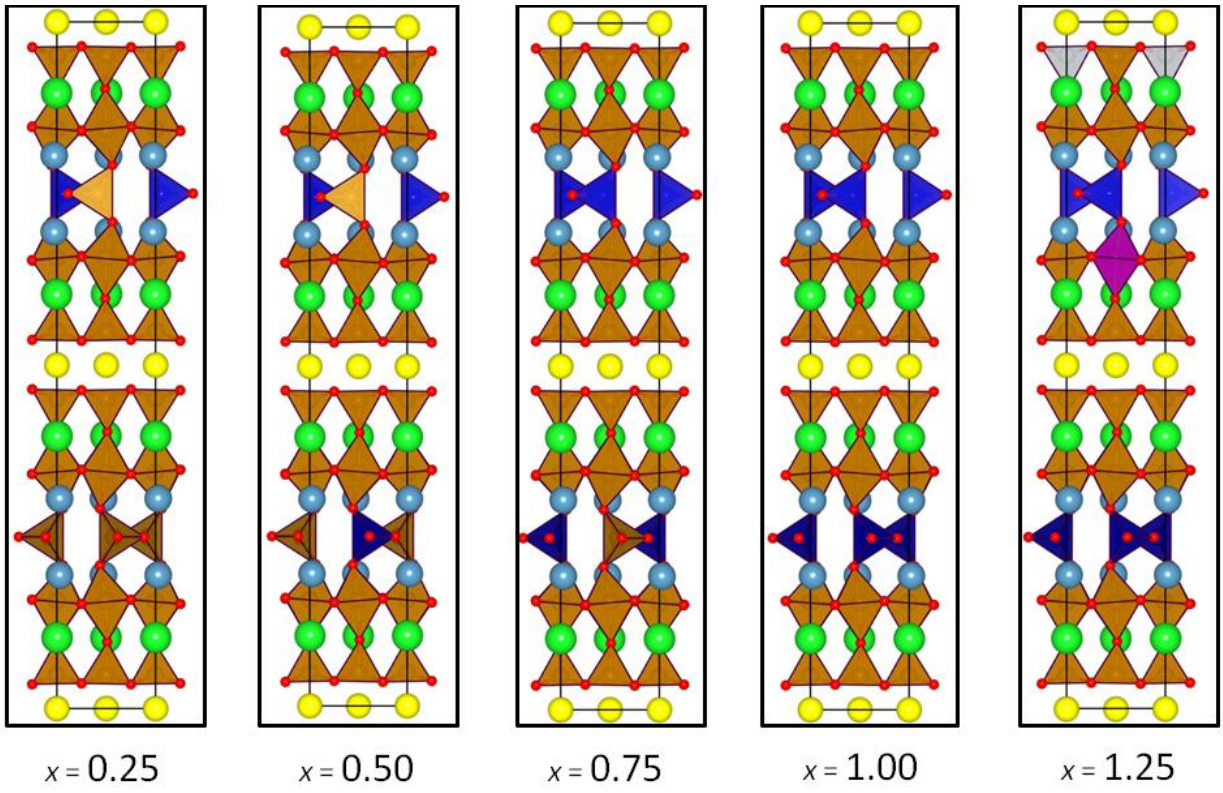

Figure 42 DFT configurations for the tetrahedral site preference at each value of *x*. Colours of atoms as follows: yttrium (yellow), barium (green), calcium (light blue), iron (brown) and oxygen (red),dark blue indicates dopant sites for all dopant species, purple indicates a dopant site when M = Mn and Zn, grey indicates a dopant site when M = Co, Cu or Ni.

For the first B-site preference, (named tetrahedral, Figure 42), all of the dopant species were placed onto the tetrahedral sites within the structure, although when *x* was equal to 1.25, all of the tetrahedral sites were occupied by the dopant species with one dopant atom remaining; when M = Mn or Zn, the additonal atom was placed on an octahedral site, when M = Co, Cu or Ni, the

extra atom was placed on a square pyramidal site. The split between dopant species at x = 1.25 was initiated based upon the literature reports for site preferences of the dopant species. Although Mn has been reported in both square pyramidal and octahedral geometries, doping calculations in the previous chapter suggest that Mn^{3+} and experimental reports for Mn^{3+} containing oxides[22] should show a stronger preference for the octahedral site, hence the additional Mn atom being placed in an octahedron. In configurations where the tetrahedral layers were not fully occupied by dopant atoms (x < 1.00), dopant atoms were placed in such a way as to maximise separation.

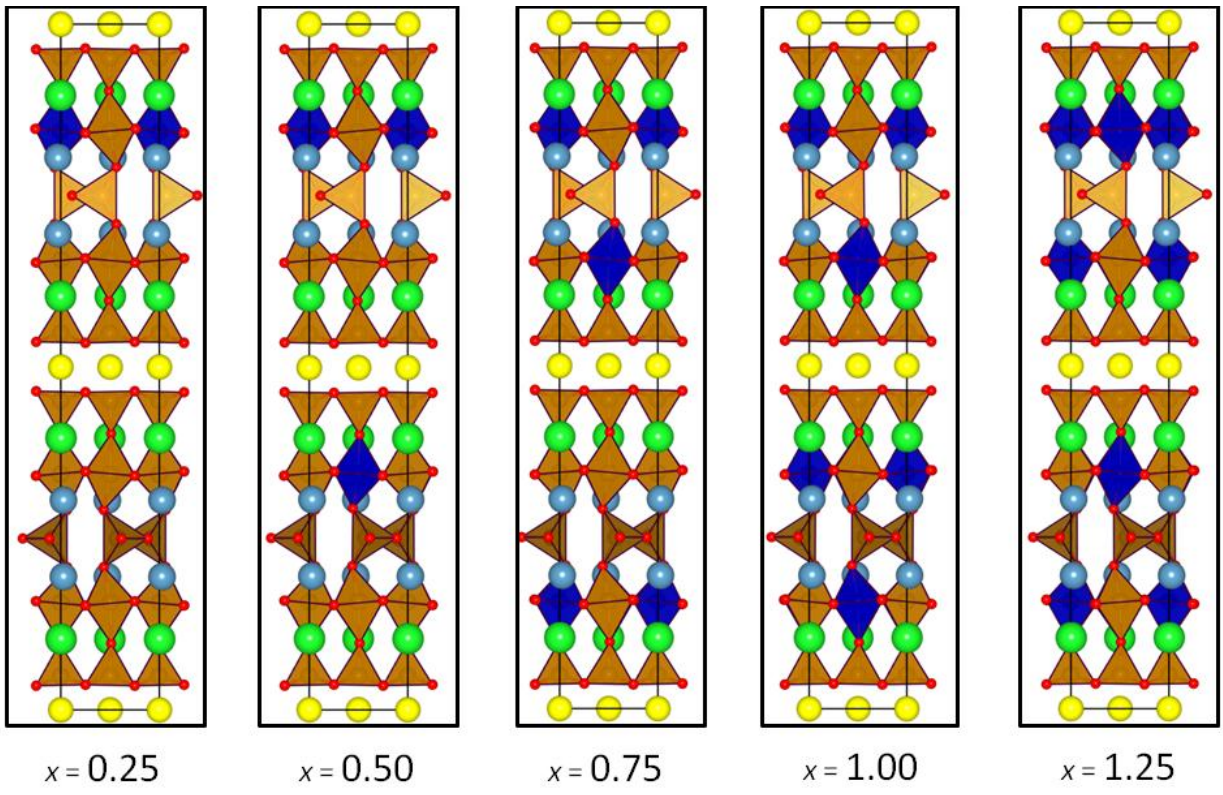

Figure 43 DFT configurations for the octahedral site preference at each value of x, colours of atoms as follows: yttrium (yellow), barium (green), calcium (light blue), iron (brown) and oxygen (red), with dark blue indicating the dopant sites.

The second site preference (named octahedral, Figure 43) has each of the dopant atom species placed onto the octahedral site at all values of *x*, with all of the dopant atoms accommodated into octahedral sites. In all of the octahedral configurations the dopant atoms were placed in order to maximise the separation between dopant species.

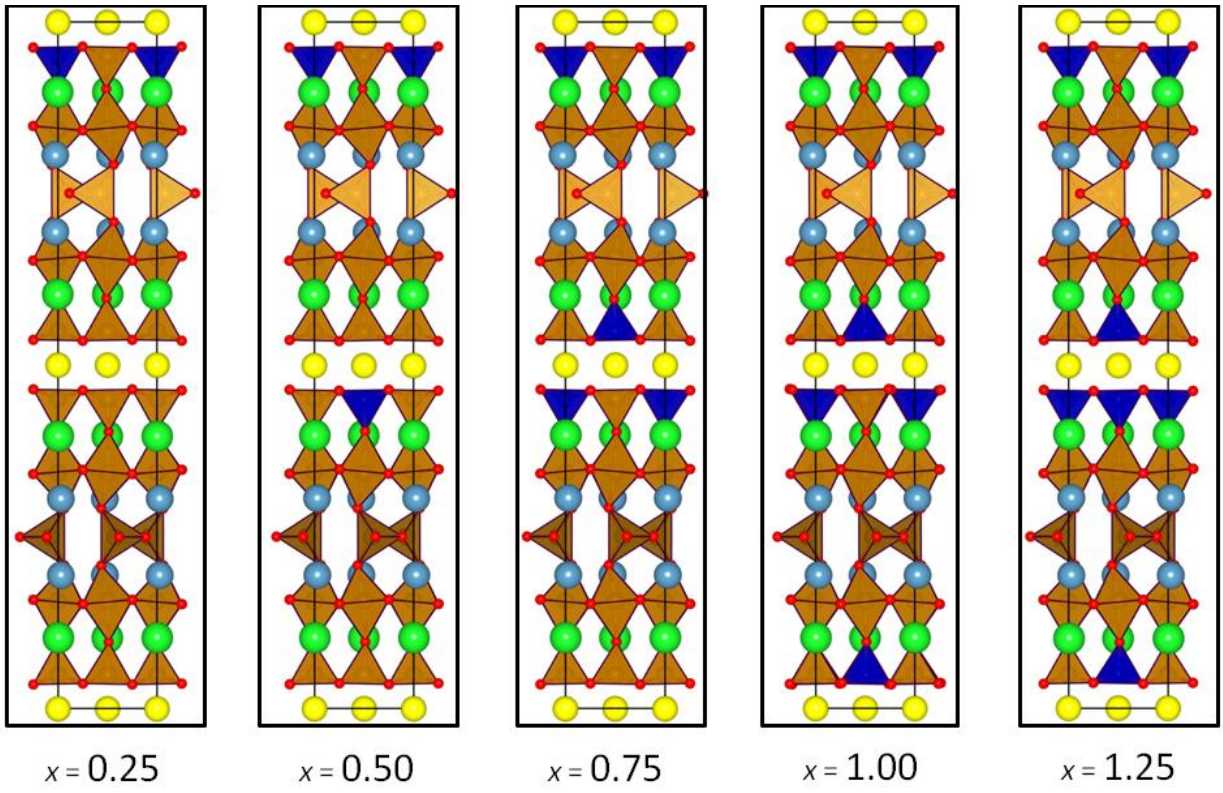

Figure 44 DFT configurations for the square pyramidal site preference at each value of *x*, colours of atoms as follows: yttrium (yellow), barium (green), calcium (light blue), iron (brown) and oxygen (red), with dark blue indicating dopant sites.

The third preference (named square pyramid, Figure 44) has all of the dopant species placed into square pyramidal sites, dopant atoms were all accommodated into square pyramidal sites at all doping levels. For the square pyramidal configurations the dopant atoms were arranged in such a way as to place them at maximum separation.

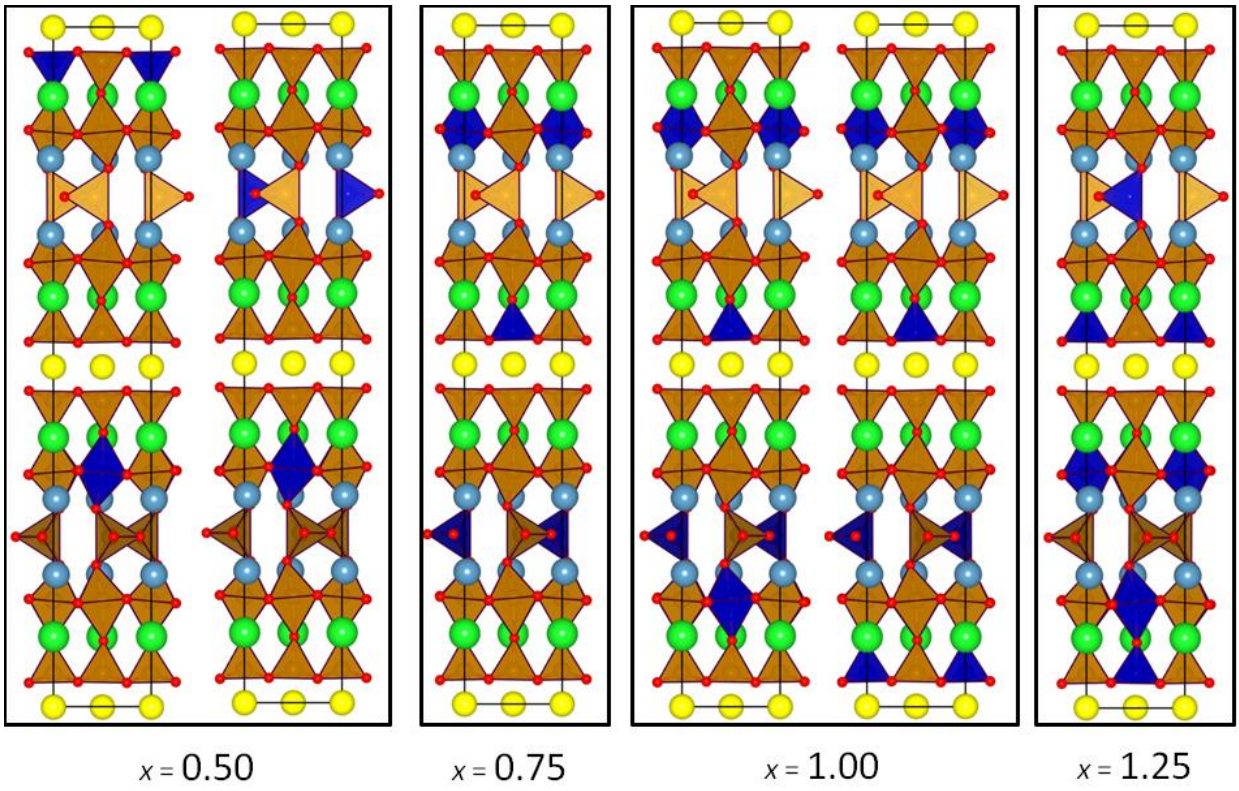

Figure 45 DFT configurations used for each doping level for the mixed site preference. Atoms colours as follows: yttrium (yellow), barium (green), calcium (light blue), iron (brown), oxygen (red) and dopant species (dark blue).

The fourth preference (named mixed, Figure 45) attempts to approximate a model for the B-site doping having little or no B-site preference. When x = 0.25 no configuration was trialled as this dopant value constituted one dopant atom per unit cell and so there is no possibility of creating a doping arrangement with no site preference in the unit cell used in these calculations. In order to be able to approximate a B-site disordered configuration a (2 × 2 × 1) cell would have been required, containing 368 atoms (to give 4 dopant atoms per unit cell) and due to its size, this calculation was not performed. When x = 0.50, two configurations were trialled, with two dopant atoms per unit cell, each configuration contains one dopant atom in an octahedral site and the second either in a square pyramidal or tetrahedral site. When x = 0.75, with three dopant

atoms, one dopant atom was placed in each of the available geometries. When x = 1.0, two configurations were trialled, with one dopant atom placed into each of the geometry types, and then two arrangements were trialled for each dopant where the last atom was placed into the octahedral or square pyramidal sites. When x = 1.25, with five dopant atoms, two dopant atoms are placed into octahedral and square pyramidal sites and one into a tetrahedral site, only this configuration was trialled as it results in the dopant atoms distributed evenly across the available B-sites in the ratios that each of the geometries appear in the structure (i.e. 2 octahedra : 2 square pyramids : 1 tetrahedron), all of the dopant configurations are summarised in Table 7.

In order to calculate reaction energies across a compositional range, energies were calculated from binary oxides and oxygen gas as required in order to maintain the average 3+ oxidation state on the B-site in the $10a_p$ product. The reaction energies were therefore calculated according to:

$$\frac{1}{2}Y_2O_3 + 2BaO + 2CaO + \frac{5-x}{2}Fe_2^{3+}O_3 + \frac{x}{3}Co_3^{2.67+}O_4 + \frac{x}{12}O_2 \xrightarrow{\Delta E_{Co}} YBa_2Ca_2(Fe_{5-x}Co_x)^{3+}O_{13}$$

(4.3.a)

$$\frac{1}{2}Y_2O_3 + 2BaO + 2CaO + \frac{5-x}{2}Fe_2^{3+}O_3 + xCu^{2+}O + \frac{x}{4}O_2 \xrightarrow{\Delta E_{Cu}} YBa_2Ca_2(Fe_{5-x}Cu_x)^{3+}O_{13}$$

(4.3.b)

$$\frac{1}{2}Y_2O_3 + 2BaO + 2CaO + \frac{5-x}{2}Fe_2^{3+}O_3 + \frac{x}{2}Mn_2^{3+}O_3 \xrightarrow{\Delta E_{Mn}} YBa_2Ca_2(Fe_{5-x}Mn_x)^{3+}O_{13}$$

(4.3.c)

$$\frac{1}{2}Y_2O_3 + 2BaO + 2CaO + \frac{5-x}{2}Fe_2^{3+}O_3 + xNi^{2+}O + \frac{x}{4}O_2 \xrightarrow{\Delta E_{Ni}} YBa_2Ca_2(Fe_{5-x}Ni_x)^{3+}O_{13}$$

(4.3.d)

$$\frac{1}{2}Y_2O_3 + 2BaO + 2CaO + \frac{5-x}{2}Fe_2^{3+}O_3 + xTi^{4+}O_2 - \frac{x}{4}O_2 \xrightarrow{\Delta E_{Ti}} YBa_2Ca_2(Fe_{5-x}Ti_x)^{3+}O_{13}$$

(4.3.e)

$$\frac{1}{2}Y_2O_3 + 2BaO + 2CaO + \frac{5-x}{2}Fe_2^{3+}O_3 + xZn^{2+}O + \frac{x}{4}O_2 \xrightarrow{\Delta E_{Zn}} YBa_2Ca_2(Fe_{5-x}Zn_x)^{3+}O_{13}$$

(4.3.f)

Note that where multiple binary oxides exist for a dopant metal, the binary oxide with oxidation closest to 3+ was used and energies from equations 4.3 a-f were calculated in electron Volts per Formula Unit (eV/FU). It was assumed that on doping that the average oxidation state on the transition metal sites would remain at 3+, either by the dopant metal changing oxidation state to 3+ or the Fe oxidation state changing to compensate (or a mixture of both effects). Doping is predicted by comparing the calculated reaction energy of the reported undoped material, doping is favourable when there is a decrease in reaction energy relative to that calculated for the undoped parent.

4.4 Results

4.4.1 Overall results

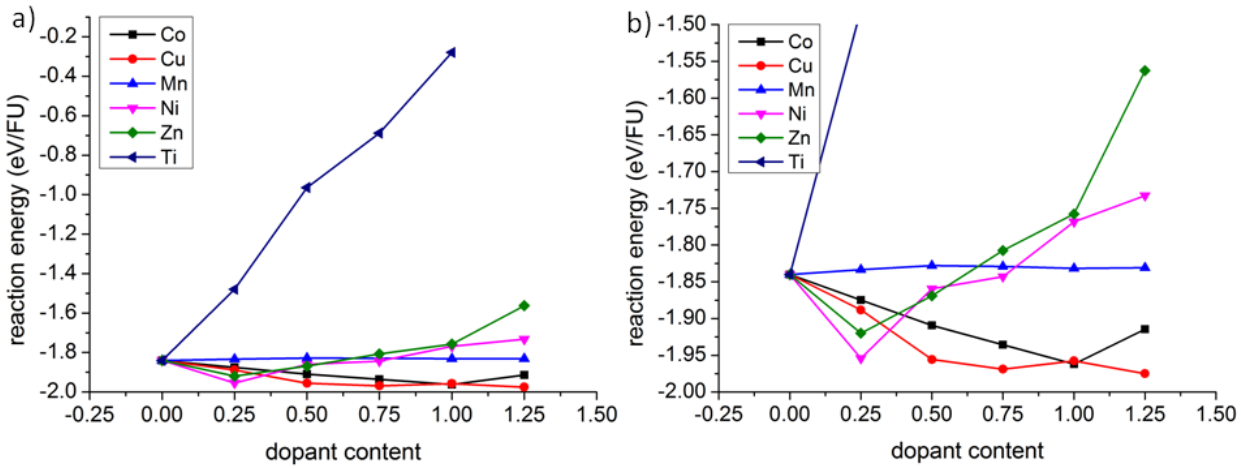

Figure 46 a) Reaction energies to form $YBa_2Ca_2Fe_{5-x}M_xO_{13}$ as a function of the dopant level, where the lowest energy configuration at each dopant level is plotted. b) Reaction energies from panel a) expanded for clarity when looking at reaction energies for M = Co, Cu, Mn, Ni and Zn, all of the reaction energies were calculated according to equations (4.3 a-f).

In order to predict whether doping should be favoured or not, calculated reaction energies are compared with the value obtained for the undoped parent structure, where a reaction energy of -1.84 eV/FU was calculated. Results are summarised in Figure 46, where for each dopant species the reaction energy of the most stable configuration is plotted as a function of the dopant content. When M = Zn and Ni, doping at x = 0.25 is calculated to have the lowest reaction energy and stable relative to the undoped material, with the reaction energy rising after this to become unfavourable. When M = Co, doping is calculated to be favourable at all doping levels, the reaction energy steadily decreases to a minimum at x = 1, with a slight increase in energy when increasing the doping level to 1.25. When M = Cu, doping is calculated to be favourable, there is an initial decrease in the reaction energy up to x = 0.75 after which the calculated reaction energy

shows little variation as a function of composition. When M = Mn, the likelihood of doping being favourable is marginal as the calculated reaction energy as a function of doping level does not change significantly. When M = Ti, no doping is calculated to be favourable as the calculated reaction energy shows a sharp increase immediately upon doping, with no minima calculated across the doping series containing Ti.

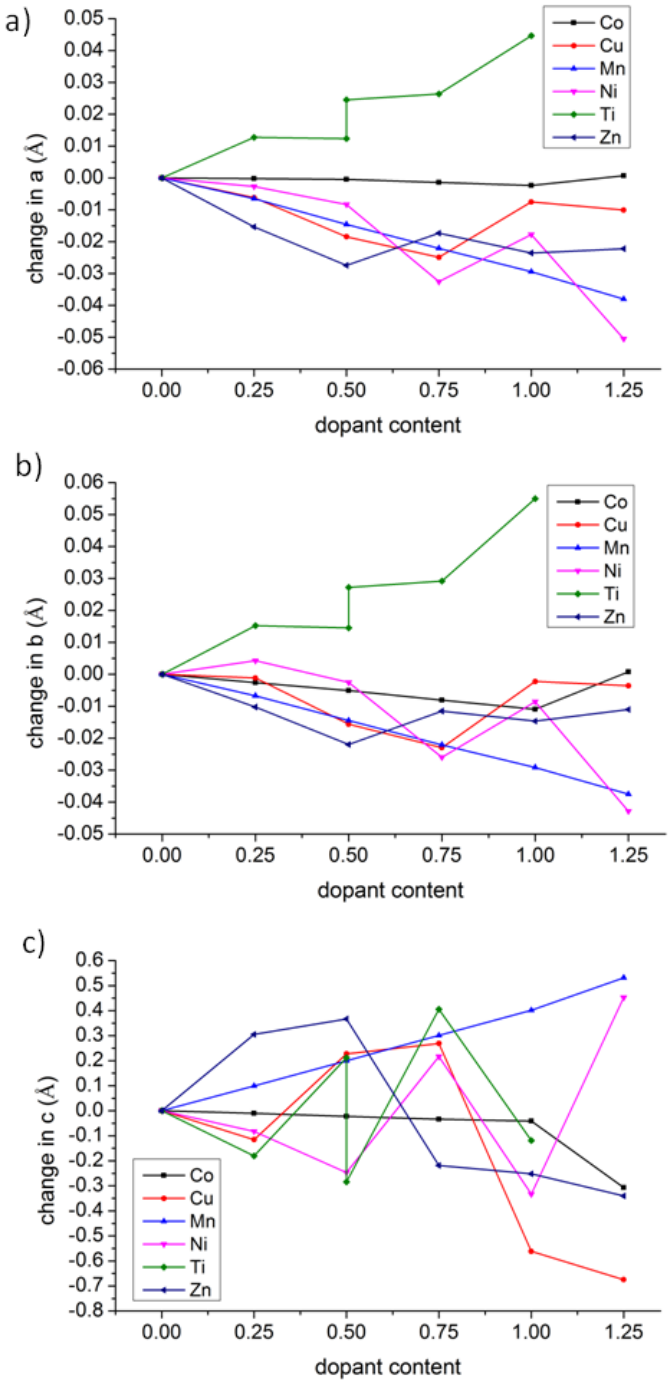

Figure 47 Changes to the calculated lattice parameters for $YBa_2Ca_2Fe_{5-x}M_xO_8$. a) Changes to the calculated a lattice parameter as a function of the dopant content. b) Changes to the calculated b lattice parameter as a function of dopant content. c) Changes to the c lattice parameter as a function of dopant content. For all panels the value reported is for the most stable configuration at each doping level.

The overall change in lattice parameters as a function of doping was calculated for each dopant species (shown in Figure 47). Shifts of all three lattice parameters for M = Co show a reduction as a function of doping, while doping is preferred on the tetrahedral site. When x = 1.25, and the square pyramidal site is favoured, the a and b lattice parameters expand and the c axis contracts (Figure 47). When M = Cu the lattice a and b lattice parameters show a decrease at x = 0.25 where doping is most favourable. For Cu doping, when doping is preferred on the square pyramidal site (x = 0.25, 1.00 and 1.25), there is a contraction in the c direction (Figure 47c), although when doping is preferred on the octahedral site the c axis expands. When M = Mn, there is a constant trend across the doping series for contraction of the a and b parameters coupled with an expansion of the c parameter. When M = Ni, at the minimum reaction energy (x = 0.25), there is little variation in the a and b lattice parameters, with a difference of less than 0.01 Å in each parameter, the a direction contracts slightly and the b direction expands slightly. For M = Ni and x = 0.25 the c parameter is calculated to contract by 0.082 Å. When M = Zn, the a and b lengths contract relative to the undoped material, when there is a Zn atom on a tetrahedral site there is an expansion in the c direction (x = 0.25 and 0.50), otherwise the c direction contracts.

4.4.2 Results for M = Co

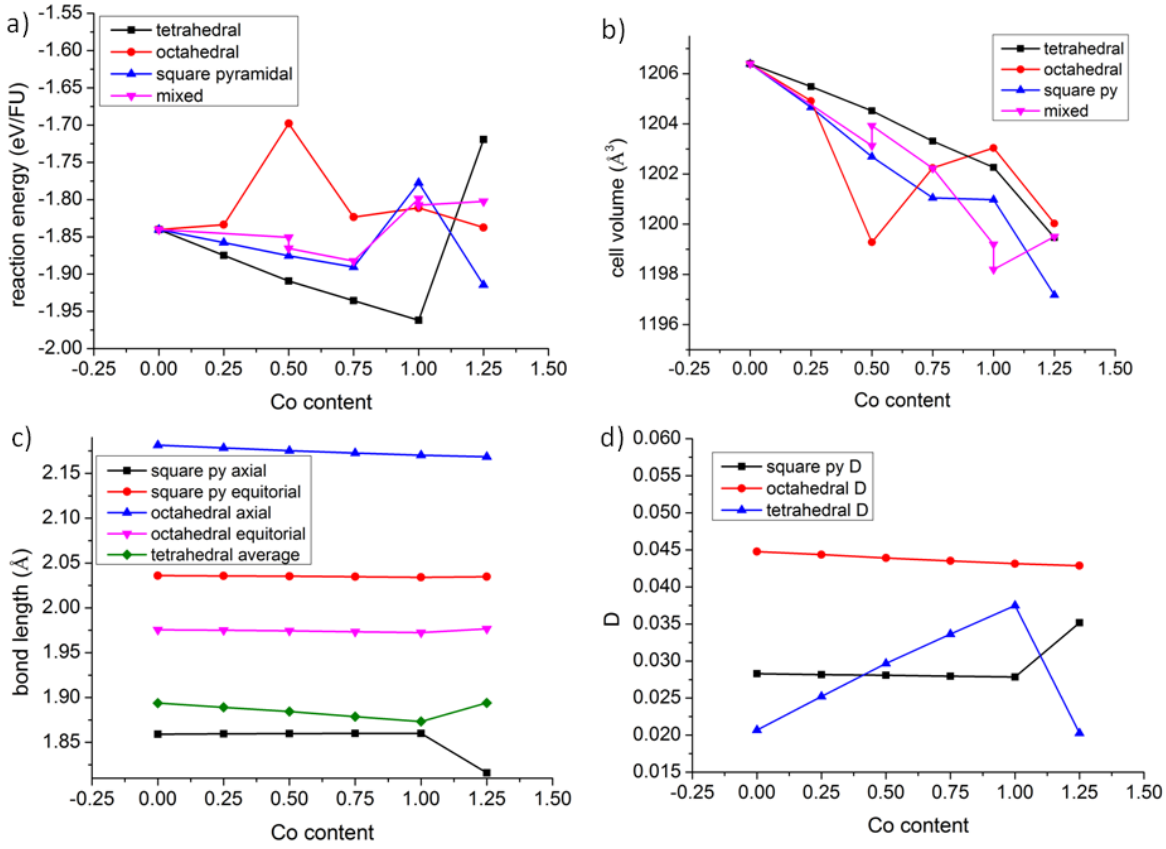

Figure 48 a) Calculated reaction energies for the formation of the $10a_p$ perovskite as a function of Co content, calculated according to equation (4.3.a), where each line indicates the calculated energy for each site doping preference. b) Calculated unit cell volumes as a function of Co doping, each line indicates the volume of the unit cell for each site preference for the Co dopant. c) Calculated average bond lengths for each geometry type in the $10a_p$ structure, calculated at each doping level for the configuration with the lowest energy. d) The average distortion index parameters calculated for each geometry type in the $10a_p$ structure, plotted as a function of the Co doping, each value is calculated for the configuration with the lowest calculated reaction energy, according to equation (4.1).

When M = Co (Figure 48a), doping is predicted to be favourable across the compositional range, there is a general decrease in reaction energy upon doping Co until x = 1.00, at this doping level Co is calculated to prefer the tetrahedral site. The reaction energy at x = 1.00 is calculated to be 0.12 eV/FU lower in energy when compared to the undoped material. On increasing the doping

level to 1.25, there is a small rise in the reaction energy of 0.05 eV/Fu compared to x = 1.00 and the site preference switches to the square pyramidal site, although the doping is still calculated to be favourable. Note that the calculated reaction energies are very close between configurations across the compositional series and therefore it would only be expected to see only a slight preference for Co to occupy the tetrahedral site. When x = 1.00 and the dopant Co can fully occupy the tetrahedral sites, at which point B-site ordering is calculated to be favourable as the next nearest configuration is calculated to be 0.15 eV/FU less stable.

As doping increases in the system it is calculated that there should be an overall reduction in the unit cell volume of the structure (Figure 48b, Table 8), with a decrease of 1.98% when doping reaches x = 1.25. There is a reduction in the unit cell volume as a function of doping, although it does not necessarily mean that the configuration with the lowest energy also has the smallest unit cell volume. The trend calculated here for unit cell volumes is in contrast to the Co doping calculations presented in the previous chapter, for $YBa_2Fe_{3-x}Co_xO_{8,}$ where the lowest energy configuration is always calculated to have the smallest unit cell volume. This suggests that site preference for Co is not driven by minimising the unit cell volume, as could have been suggested for the system investigated in the previous chapter.

Investigating the bond lengths upon doping Co in to the $10a_p$ structure, with the lowest energy configuration at each doping, the average bonding distances in the material (Figure 48c) do not alter significantly as a function of dopant content. The values calculated and referred to above are for the average of Co and Fe atoms in each environment within the structure. When looking at the tetrahedral site, there is a small decrease in the average bond length up to x = 1.00, with a decrease of 0.020 Å. When x increases to 1.25, and Co switches to preferring the square pyramidal site the decrease in the tetrahedral bond length is reversed, with the bond returning to

a similar length to the undoped material. The change in the tetrahedral site between x = 1.00 and x = 1.25 is concurrent with a decrease in the length of the square pyramidal axial bond of 0.044 Å as the Co atoms change to favour the square pyramidal site, although it is calculated that there is no substantial change in the equatorial bond length on this shift.

The distortion parameters calculated when doping with Co (Figure 48d) show little deviation away from the updoped material on the octahedral site, the square pyramidal site only observes an increase of 0.007 (+ 26.2%) when Co is doped onto the site. As the Co content is increased on the tetrahedral site there is a steady increase in the distortion of the site, with an increase of 0.017 (+ 81.2%), which reverses as soon as the doping preference switches away to the square pyramidal geometry. The observation on the Co doped sites combined with the distortion parameters not shifting significantly on the Fe sites indicates that the introduction of Co into the structure is easily accommodated; as the doping is shown to have little effect on the surrounding Fe environments whist concurrently allowing for the Co sites to distort to favour the dopant atom. Therefore, when M = Co the dopant species in the $10a_p$ only significantly effects the bonding environment of the preferred Co site.

In summary for M = Co, it is predicted that the most favoured level of doping (within the range studied in this chapter), is when x = 1.00, although doping is calculated to be favourable across the whole compositional range. The results for Co suggest that doping is favourable because Co can be doped into the structure whilst having minimal effect on Fe sites. Experimentally Co doping would be expected to manifest via a contraction in the observed unit cell volume. With x values less than or equal to 1.00, an increase in the distortion index of the tetrahedral site would be expected, when x is greater than 1.00 an increase in the distortion index of the square pyramidal site is expected.

4.4.3 Results for M = Cu

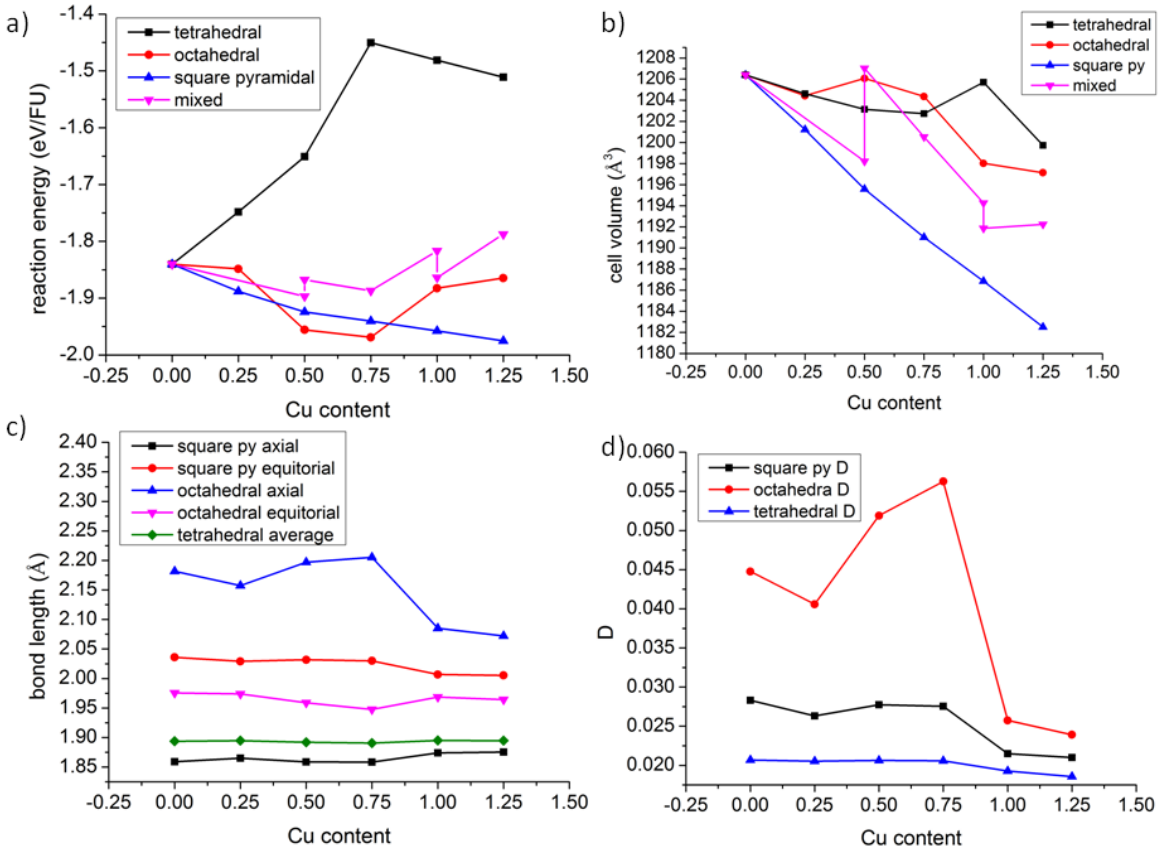

Figure 49 a) Calculated reaction energies for the formation of the $10a_p$ perovskite as a function of Cu content, calculated according to equation (4.3.b), where each line indicates the calculated energy for each site doping preference. b) Calculated unit cell volumes as a function of Cu doping. c) Calculated average bond lengths for each geometry type in the $10a_p$ structure, calculated at each doping level for the configuration with the lowest energy. d) The average distortion index parameters calculated for each geometry type in the $10a_p$ structure as a function of the Cu doping, each value is calculated for the configuration with the lowest calculated reaction energy, according to equation (4.1).

When M = Cu (Figure 49a), as the doping level increases there is an overall reduction in the reaction energy calculated, suggesting that doping should be favourable. At x =0.25, there is a slight energetic preference for the square pyramidal configuration, although this is only 0.04 eV/FU more stable than the octahedral configuration. When x = 0.50 and 0.75, there is a

preference for octahedral doping. Although the energy gap calculated between the octahedral, and square pyramidal preferences, was found to be small, calculated to be just ~ 0.03 eV/FU for both x = 0.50 and 0.75. When x = 1.00 and 1.25, the square pyramidal site preference becomes increasingly stable relative to the octahedral and mixed configurations, suggesting that when doping is less than or equal to 0.75, only small levels of B-site ordering would be expected, however, above this value, increased preference for the square pyramidal site would be expected. For all values of x the tetrahedral site preference was calculated to be unfavourable both relative to the undoped material and all other configurations.

From the calculations presented within this section the effect of Cu doping on the unit cell volume of the structure is dependent on the site preference of the Cu (Figure 49b, Table 9). When Cu doping is preferred on the square pyramidal site, (energetically favoured when x = 0.25, 1.00 and 1.25) there is a sharp reduction in the calculated unit cell volume, with the biggest drop at x = 1.25, calculated to be 23.882 $Å^3$, a decrease of 2.0%. When doping is preferred on the octahedral site (x = 0.50 and 0.75), there is only a small change in the unit cell volume, with decreases of 0.02 and 0.17 % for x = 0.50 and 0.75 respectively.

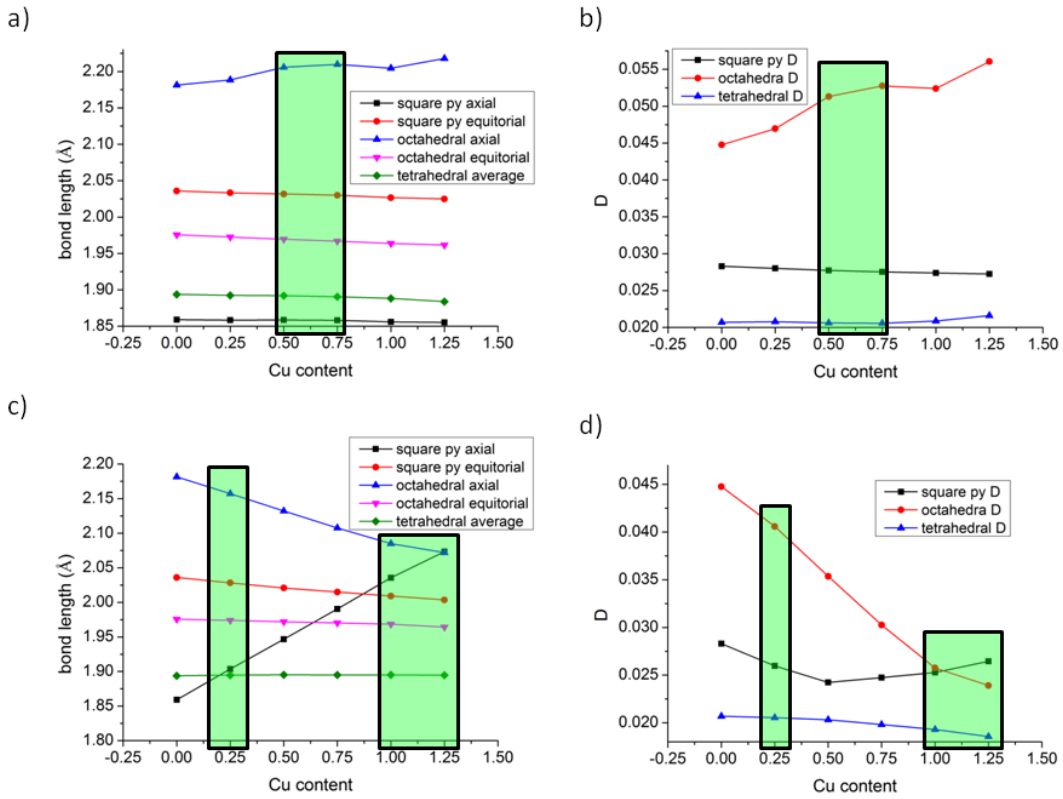

Figure 50 a) Calculated bond lengths as a function of Cu doping with the octahedral site preference. b) Calculated distortion index parameters for Cu doping with octahedral site preference. c) Calculated bond lengths for Cu doping with square pyramidal site preference. d) Calculated distortion index parameters for the square pyramidal site preference. Green boxes indicate the points that are the most energetically favourable.

Looking at the bonding environments (Figure 49c) when $x = 0.25$ with the energetically favoured square pyramidal ordering, there is a decrease in the unit cell volume. The cause of the reduction in unit the unit cell volume is a shortening of the average octahedral axial bond, combined with a small shortening of the square pyramidal equatorial bonds. The shortening of bond lengths in the system leads to a decrease in all three of the lattice parameters (Figure 47), there is also an increase in the length of the square pyramidal axial bond. The lengthening of the square pyramidal axial bond is partly caused by the Cu position at the centre of the polyhedron moving away from the axial oxygen; overall the lengthening of the square pyramidal bonds is not

sufficient to outweigh the contraction of the octahedron, resulting in the calculated contraction of the c lattice parameter. The results seen for x = 0.25 persist at other values of x when square pyramidal doping is favoured (x = 1.00 and 1.25), with the effect increasing with Cu content. At the higher doping levels for Cu, the distortion of the square pyramidal site changes such that the polyhedron has one long bond and four short, rather than the one short and four long of the undoped material (Figure 50c). The Cu doping onto the square pyramidal site has an effect on the calculated distortion index values (Figure 49d and Figure 50d) for both the square pyramidal and octahedral sites, with the D value for the square pyramidal site passing through a minima at x = 0.50. The octahedral distortion parameter decreases as a function of Cu content, until the octahedral sites are less distorted than the square pyramidal sites at x = 1.25.

When the site preference is for the octahedral site, energetically favoured at x = 0.50 and 0.75, a different trend in the unit cell volume is observed, with little shift in unit cell volume compared with the undoped material. At the highest doping level, where the octahedral site preference is calculated to be favourable, only a decrease of 2.04 $Å^3$ is observed, equating to a decrease of only 0.2%. The small changes to the unit cell volume when M = Cu and with the octahedral site preference are driven by small changes to the octahedral environments containing Cu, with these effects resulting in the increase of the average octahedral distortion index (Figure 50b).

Deciding which geometry is favoured for M = Cu appears to be related to the difference in the average axial bonds of the square pyramidal and octahedral sites for the square pyramidal doping, as there is less change in geometries when the Cu is doped into the octahedral sites. At x = 0.25, where square pyramidal doping is favoured, there is a modest change in the Square pyramidal axial bonds (Figure 50c) with a difference of 0.0443 Å. Doping onto the square pyramidal site is not favoured again until higher levels of doping (x = 1.00 and 1.25), where the

octahedral and square pyramidal sites are much more distorted away from the undoped material and the axial bond lengths much closer together, with a difference of 0.0495 Å at x = 1.00. It would therefore appear that at the intermediate doping levels (x = 0.50 and 0.75), where the difference in the average axial bond lengths is in between these two values, creates square pyramidal geometries where Cu doping is less favoured than in the octahedral sites in the Cu doping configurations.

In summary, it was calculated that Cu doping should be favourable across the range of compositions, although due to the small energy differences between doping configurations at x = 0.25 – 0.75, it is expected that little B-site ordering would be observed and above this value of x, a site preference for the square pyramidal site would become increasingly dominant. Doping with Cu is found to significantly affect the polyhedra only when it is preferred at the square pyramidal sites, when copper is in the octeahedral site, only small changes in the geometry are calculated, providing a possible method by which the site could observed.

Experimentally therefore, when doping with Cu, an overall reduction in the unit cell volume would be expected, considering there would be a mixture of doping onto the square pyramidal and octahedral sites (due to both configurations being close in energy), where the exact level of unit volume reduction would be dependent on the level of B-site ordering. As the predicted B-site ordering changes across the doping series, but remains favourable compared to x = 0, the results calculated in this work, suggest that a uniform lattice parameter and cell volume as a function of doping may not occur. When $1.00 < x > 0.25$, smaller distortions to the structure of the material would be expected due to differing predictions on the favoured B-site ordering. Due to the small energy difference between configurations, at small levels of doping ($x < 1.00$) no significant B-site ordering would be expected. When x is equal to or greater than 1.00, a large

decrease in the distortion of the octahedral site would be expected, coupled with larger reductions in the unit cell volume as preference for the square pyramidal site becomes more dominant.

4.4.4 Results for M = Mn

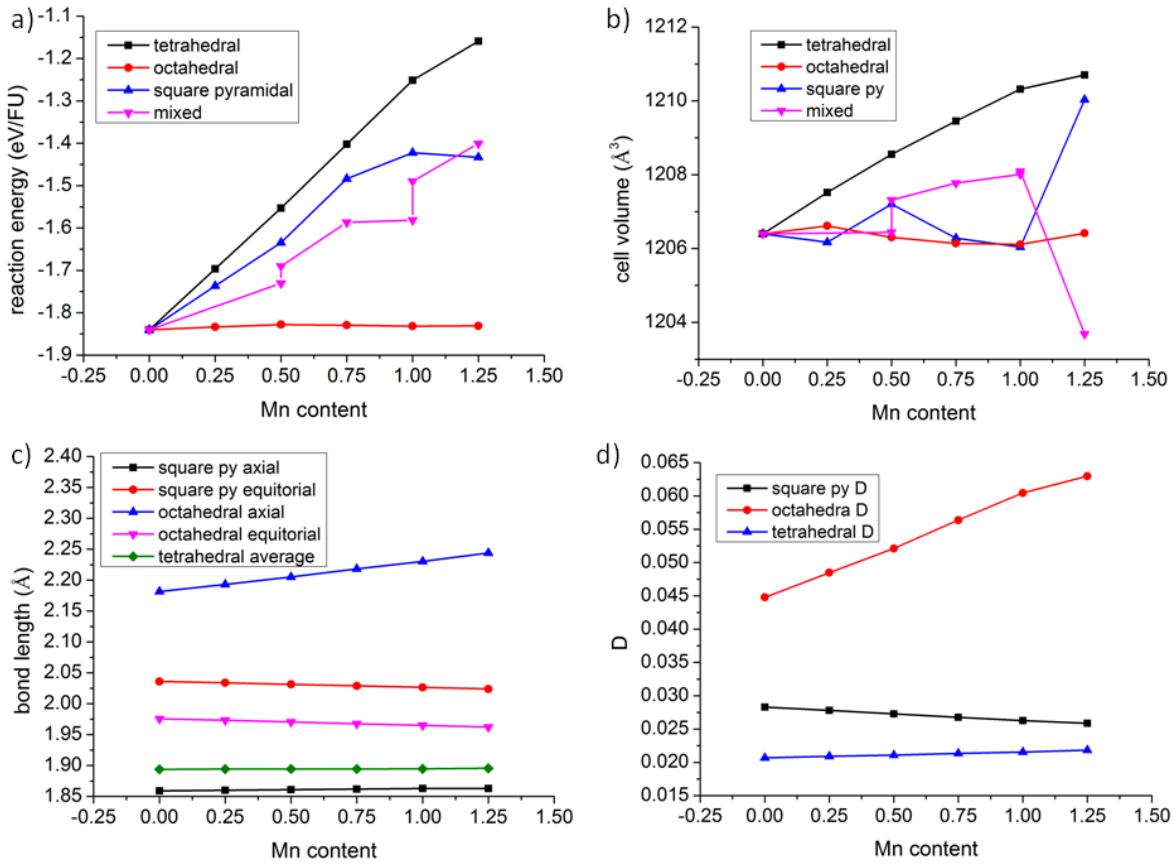

Figure 51 a) Calculated reaction energies for the formation of the $10a_p$ perovskite as a function of Mn content, calculated according to equation (4.3.c), where each line indicates the calculated energy for each site doping preference. b) Calculated unit cell volumes as a function of Mn doping, each line indicates the volume of the unit cell for each site preference for the Mn dopant. c) Calculated average bond lengths for each geometry type in the $10a_p$ structure calculated at each doping level for the configuration with the lowest energy. d) The average distortion index parameters calculated for each geometry type in the $10a_p$ structure as a function of the Mn doping, each value is calculated for the configuration with the lowest calculated reaction energy, according to equation (4.1).

When M = Mn (Figure 51a), there is very little change in the reaction energy compared to the undoped as the doping level is increased to x = 1.25, when considering the most stable configuration at each doping level. The largest change in reaction energy compared to the parent material is at x = 0.50, with the most stable configuration for the doping level calculated to be

0.01 eV/FU less stable than the parent material. It is therefore suggested that doping the system with Mn might be possible across the compositional series calculated, as no strong minimum is found at any value of *x*.

Unlike the other transition metal dopant species calculated in this chapter, if doping can be achieved, a strong site preference is calculated for M = Mn, where the Mn atoms were calculated to prefer the octahedral site (Figure 51a), with the gap in energy between the octahedral configuration and all of the other configurations growing as the Mn content increases.

Examining the calculated unit cell volumes for Mn (Figure 51b) and for the configurations with the lowest reaction energy (with the Mn preferentially placed on the octahedral site), there is little deviation from the undoped material with increasing Mn content, with the largest deviation calculated when $x = 1.00$, as a decrease of 0.29 $Å^3$ (- 0.02 %).

When considering the lowest energy configurations and the corresponding average bond lengths for each environment (Figure 51c), a steady increase in the octahedral axial bond was calculated, while simultaneously a contraction of the octahedral and square pyramidal equatorial bonds. The magnitude of the changes in bond lengths upon Mn doping results in a contraction of the a and b lattice vectors and an expansion of the c axis (Figure 47). The expansion and concurrent contraction of the lattice parameters results in the marginal overall change in the unit cell volume (Table 12).

When examining the average distortion index for each B-site environment, as a function of the Mn content (Figure 51d), it was observed that there is a slight reduction and increase of the square pyramidal and tetrahedral sites respectively. On the octahedral site there is a steady increase in the distortion index as a function of the Mn content, with a calculated increase from

0.045 to 0.063 between $x = 0$ and $x = 1.25$ (a difference of 0.018, or 40%). The calculation of an increasing distortion on doping with Mn is consistent with the inclusion of a Mn^{3+} ion into a octahedral site. Mn^{3+} would be expected to have a Jahn-Teller distortion, with two long bonds and four short, the inclusion of Mn onto the site extends the distortion already observed in the undoped material. The distortion of the octahedral site drives the shortening of the a and b lattice parameters and an expansion of the c parameter, although overall it leaves the volume relatively unchanged.

Despite having similar results on the B-site geometries as Co (i.e. the dopant only significantly effecting the site upon which it was placed), the changes in the calculated formation energy are marginal, a possible reason for this observation is that the distortion of the octahedral site and unit cell parameters described above. While being energetically favourable for Mn, the octahedral distortion may have an unfavourable effect on the rest of the cation environments. The effect of Mn on the rest of the unit cell may therefore be effectively cancelling out the energetic benefits of including Mn in the system, giving rise to only small deviations in the calculated reaction energies as a function of doping.

In summary, the calculated reaction energies being relatively flat suggest that some Mn doping into the system may be possible in the compositional range studied here, although the DFT calculations give no indication as to the maximum doping level that may be possible. When doping with Mn, only small changes in the unit cell volume would be expected, however, the unit cell axis lengths would be expected to distort with an elongation of the stacking axis and a reduction of the a and b axis, caused primarily by distortions of the octahedral site (Table 12). The doped Mn atoms are expected to be observed predominantly on the octahedral site of the structure, due to the large gap in energy between the different configurations.

4.4.5 Results for M = Ni

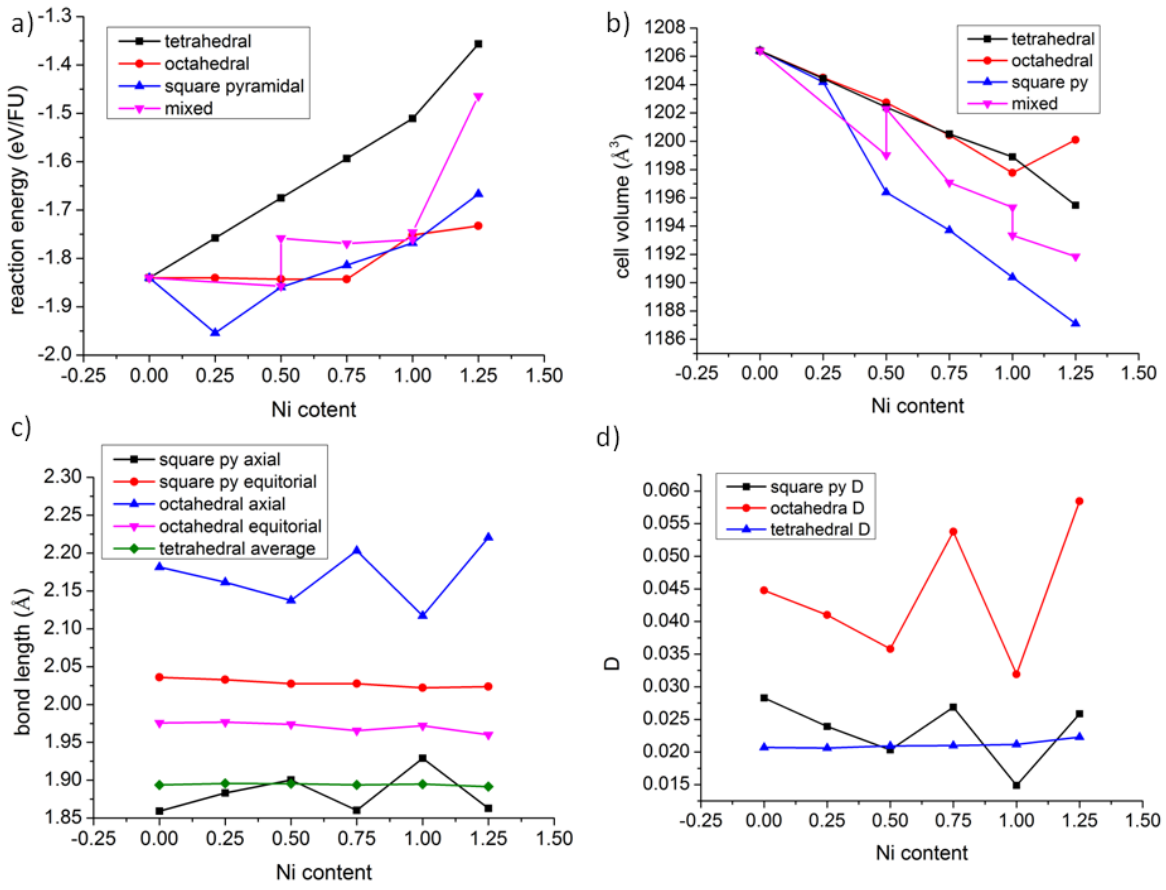

Figure 52 a) Calculated reaction energies for the formation of the $10a_p$ perovskite as a function of Ni content, calculated according to equation (4.3.d), where each line indicates the calculated energy for each site doping preference. b) Calculated unit cell volumes as a function of Ni doping, each line indicates the volume of the unit cell for each site preference for the Ni dopant. c) Calculated average bond lengths for each geometry type in the $10a_p$ structure calculated at each doping level for the configuration with the lowest energy. d) The average distortion index parameters calculated for each geometry type in the $10a_p$ structure as a function of the Ni doping, each value is calculated for the configuration with the lowest calculated reaction energy, according to equation (4.1).

When M = Ni (Figure 52a), there is an initial decrease in the reaction energy when x = 0.25 with doping Ni onto the square pyramidal site, favoured by 0.11 eV/FU compared to x = 0. When doping is increased beyond the x = 0.25 level there is an increase in the reaction energy, although this remains slightly below the reaction energy of the undoped material until x = 0.75.

After x = 0.75, the reaction energy is calculated to be higher than the undoped material and therefore unfavourable. Due to having a relatively deep minimum at x = 0.25, only small levels of doping are expected experimentally.

For the initial doping that is energetically favoured (x = 0.25), doping with Ni results in a decrease in unit cell volume of 2.2 $Å^3$ (a decrease of 0.2%, Figure 52b) compared to that calculated for the undoped material. As doping becomes increasingly unfavourable, the unit cell volume continues the same general trend toward a smaller volume.

Ni doping was found to have a significant effect on the axial bond lengths for the octahedral and square pyramidal axial bond lengths (Figure 52c). Ni atoms preferentially placed into the square pyramidal site resulted in a lengthening of the square pyramidal axial bond and a shortening of the octahedral axial bond, however, when x = 0.75 and 1.25, the octahedral site is preferred. When the site preference switches to the octahedral site, the bond lengths on the square pyramidal site revert back to close to that of the undoped material. When Ni is doped in the octahedral site, a small expansion of the octahedral axial bond coupled with a slight shortening of the equatorial bonds was observed, resulting in distinctly different distortion index parameters for the octahedral site depending on the Ni site preference.

When looking at the average distortion index for each of the B-site environments as a function of Ni doping (Figure 52d), the trends for the octahedral and square pyramidal sites follow both the Ni content and its site preference. When the square pyramidal site is preferred (x = 0.25, 0.50, 1.00), the doping results in a general trend for the calculated distortion index values to decrease from the parent material. However, when the octahedral site is favoured (x = 0.75 and 1.25), the calculated distortion index values for the octahedral site increase over the undoped material and

the square pyramidal site reverts to distortion index values very similar to that calculated for the parent material. The volumes of the polyhedra for M = Ni were calculated using VESTA[136] and implemented as previously reported[158, 159] (Table 15). Calculated polyhedral volumes indicate that the inclusion of Ni into the structure, results in Ni containing polyhedra that are significantly larger than the sites found in the undoped material. These large Ni polyhedra results in a volume reduction in the Fe containing sites. As the calculated reaction energies show an overall increase in energy as more Ni is included in the system, regardless of site preference, changes in unit cell volume etc. A possible reason for Ni doping becoming unfavourable is that it is energetically unfavourable to compress the Fe polyhedra; hence the inclusion of the larger Ni polyhedra is unfavourable.

In summary, when doping with Ni, small levels of Ni doping should be favoured, with $x = 0.25$ being particularly favoured. Aside from $x = 0.25$, where the Ni is expected to prefer the square pyramidal site, no significant level of B-site ordering would be expected. At all other values of x the energy difference between the configurations is small and so B-site ordering would not be expected. Note however, that no doping into the tetrahedral site is calculated to be favourable. Therefore experimentally, Ni doping is suggested to be most likely at $x = 0.25$ and would be expected to be manifested by a distortion of the square pyramidal axial bonds and a modest decrease in the unit cell volume, with the dopant Ni predominantly found on the square pyramidal site.

4.4.6 Results for M = Ti

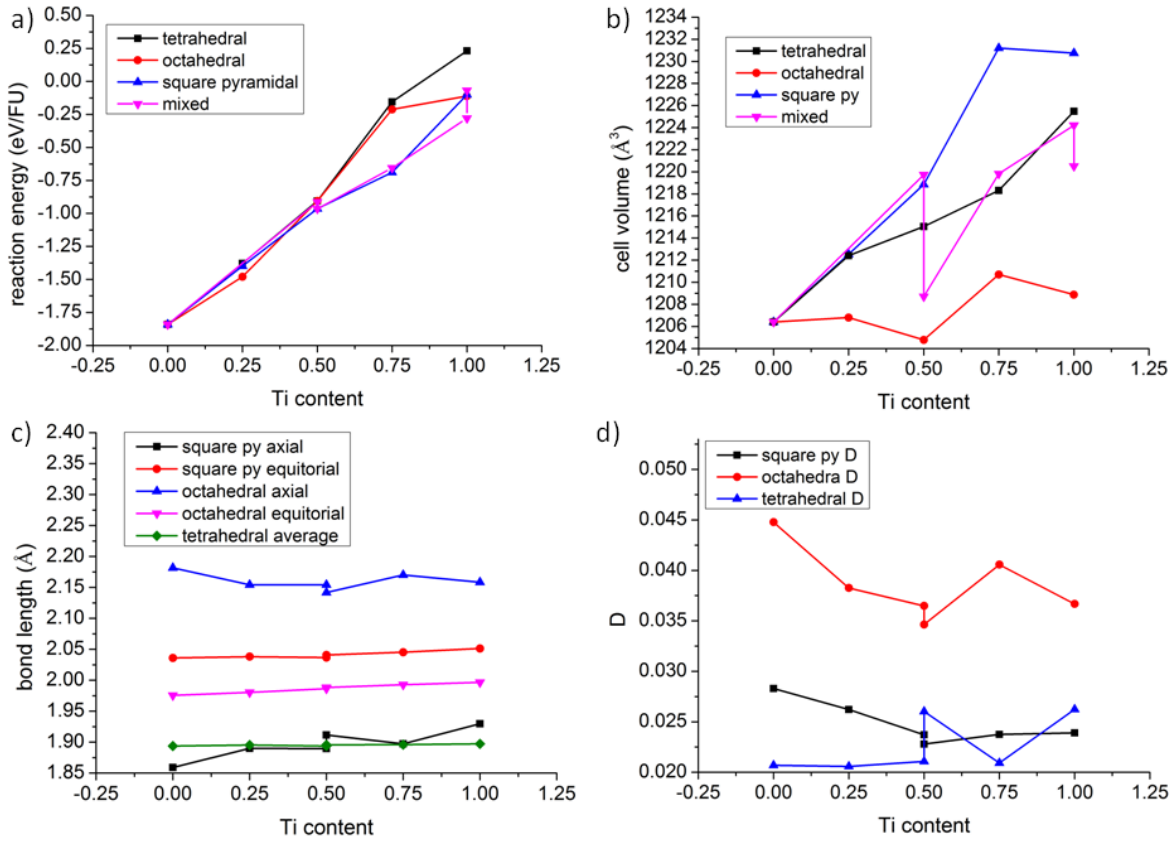

Figure 53 a) Calculated reaction energies for the formation of the $10a_p$ perovskite as a function of Ti content, calculated according to equation (4.3.d), where each line indicates the calculated energy for each site doping preference. b) Calculated unit cell volumes as a function of Ti doping, each line indicates the volume of the unit cell for each site preference for the Ti dopant. c) Calculated average bond lengths for each geometry type in the $10a_p$ structure calculated at each doping level for the configuration with the lowest energy. d) The average distortion index parameters calculated for each geometry type in the $10a_p$ structure as a function of the Ti doping, each value is calculated for the configuration with the lowest calculated reaction energy, calculated according to equation (4.1). Note that in panels c) and d), two points are presented at $x = 0.5$ as two configurations are calculated to have the same reaction energy to 3 significant figures (calculated at -0.964 eV/FU).

When M = Ti (Figure 53a), no doping level was calculated to be favourable when compared to the parent material. The calculated reaction energies increase sharply as the Ti is doped into the $10a_p$ structure. As the doping increases, all site preferences (except for octahedral), result in a

large increase in the calculated unit cell volume (Figure 53b, Table 16), with the increases driven by the expansion in the a and b parameters (Figure 47).

Doping Ti into the structure results in only small changes to the average bond distances in the structure as a function of doping (Figure 53c),. With the first two doping of Ti into the $10a_p$ there is a reduction in the calculated distortion parameters for the octahedral and square pyramidal sites (Figure 53d), after which there are only minor changes in the calculated distortion parameters. Examining the calculated polyhedral volumes (Table 17), reveals a similar trend to that of M = Ni, although the Ti atoms forcing the Fe sites to expand rapidly (possibly due to the lowering of the average Fe oxidation state) and this may be a reason for Ti doping to be unfavourable. Another possible contribution to the increase in the calculated reaction energy is the introduction of Ti^{4+} cations into the system, with the oxygen content fixed, this would result in the reduction of the oxidation state of the Fe ions to below 3+. This reduction of the Fe charge state is in contrast to the dopant that are favoured, as all of the dopant species that are favourable either maintain or increase the Fe charge state.

4.4.7 Results for M = Zn

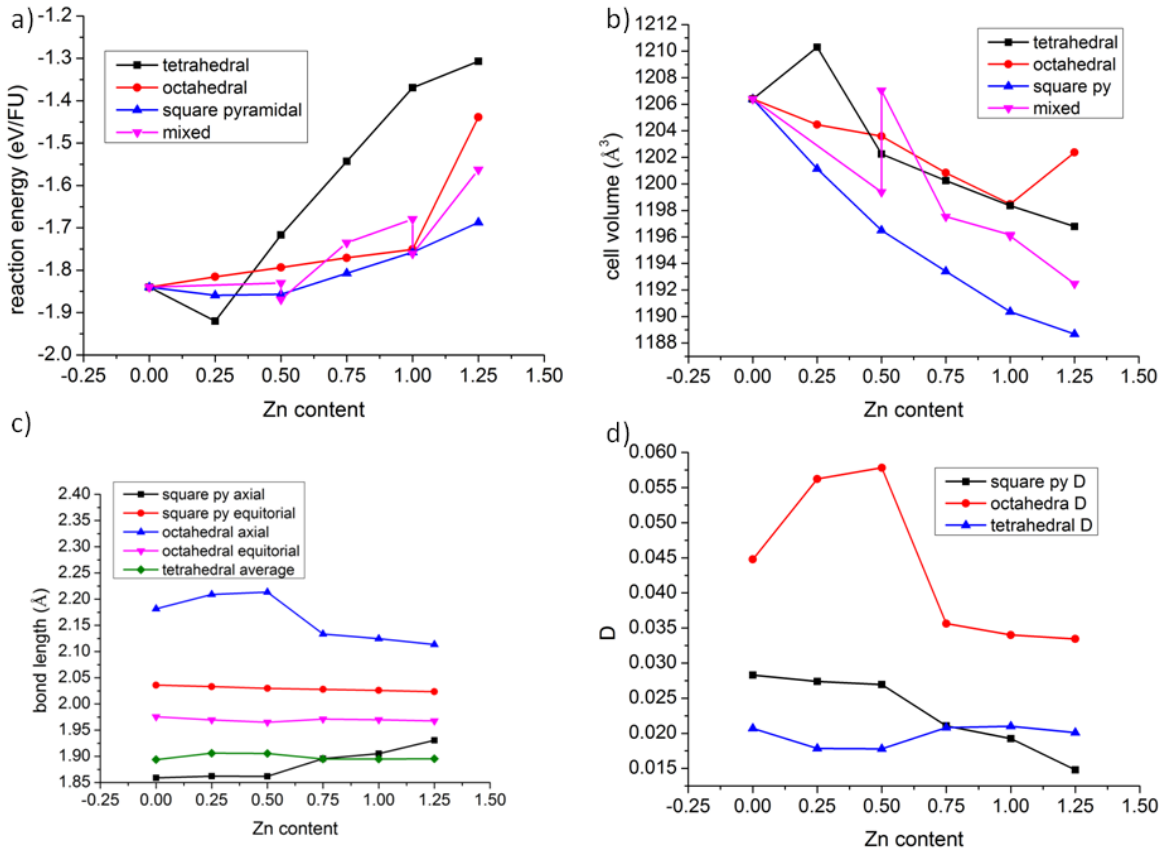

Figure 54 a) Calculated reaction energies for the formation of the $10a_p$ perovskite as a function of Zn content, calculated according to equation (4.3.f), where each line indicates the calculated energy for each site doping preference. b) Calculated unit cell volumes as a function of Zn doping, each line indicates the volume of the unit cell for each site preference for the Zn dopant. c) Calculated average bond lengths for each geometry type in the $10a_p$ structure calculated at each doping level for the configuration with the lowest energy. d) The average distortion index parameters calculated for each geometry type in the $10a_p$ structure as a function of the Zn doping, each value is calculated for the configuration with the lowest calculated reaction energy, calculated according to equation (4.1).

When M = Zn (Figure 54a), the most stable configuration is calculated at x = 0.25, with the dopant Zn atoms preferentially placed onto the tetrahedral site, with the configuration having a calculated reaction energy 0.08 eV/FU more stable than the undoped material. When doping is increased above this point, the calculated reaction energy is calculated to steadily increase for all

of the configurations. Note that the preference for the tetrahedral site is only favoured at x = 0.25, after this level, tetrahedral B-site ordering becomes the least favoured site ordering. At x = 0.50 (where the reaction energy is still calculated to be more stable than the undoped material), a mixed B-site ordering is calculated to be most stable. The most stable configuration for x = 0.50 contains one Zn in a tetrahedral site and the second in an octahedral site, the reaction energy was calculated to be 0.03 eV/FU more stable than the parent material, suggesting that having only one Zn atom on a tetrahedral site is favoured per unit cell. At x = 0.50, the square pyramidal site preference is very close in energy to the stable, mixed configuration with a reaction energy only 0.01 eV/FU higher than the undoped material. Beyond x 0.50, doping becomes unfavourable compared to the parent and the square pyramidal site becomes the preferred dopant site. With the exception of x = 0.25, each of the configurations is close in energy, suggesting that if doping could be achieved, then little B-site ordering would be expected.

It was calculated for M = Zn, that at each of the doping levels, the square pyramidal configurations have the smallest calculated unit cell volume (Figure 54b, Table 18). Doping of Zn into the structure, up to x = 0.50 results in a slight lengthening of the octahedral axial bonds (Figure 54c), combined with a minor increase in the tetrahedral bond lengths, note that in both of the lowest energy configurations at x = 0.25 and 0.50 contain a Zn atom on a tetrahedral site. After x = 0.50 there is a small decline in the axial bond length for the octahedral site, an increase in the square pyramidal site and the average tetrahedral bond length returns to the same as when x = 0.

The calculated distortion parameters for the $10a_p$ structure (Figure 54d), show that doping into the tetrahedral site results in a reduction of the tetrahedral distortion index, coupled with an increase on the octahedral site. However, when doping is preferred on the square pyramidal site

the calculated distortion parameters for both the octahedral and square pyramidal sites decline as a function of doping and the tetrahedral distortion index returns to near the value for $x = 0$.

As with M = Ni and Ti, examining the volumes of the polyhedra within the doped system (Table 19), doping with Zn forces significant changes to the volumes of the Fe sites. Doping with Zn, as with Ni results in a compression of the Fe octahedral and square pyramidal sites, it is suggested that the response of the Fe sites to Zn doping is a reason for Zn doping to be unfavourable.

To summarise, when doping with Zn, calculations suggest that a small level of doping should be favoured. When $x = 0.25$, doping would be expected to manifest in the form of a small reduction of the unit cell volume and an increase of the distortion of the octahedral site, away from that observed for the undoped material, with a slight decrease in the distortion of the tetrahedral site. If the doped material were to express B-site ordering the doped Zn, is primarily expected to be found on the tetrahedral site.

4.5 General Discussion

In summary, the calculations that are presented in this chapter suggest that some dopings should be favourable in $YBa_2Ca_2Fe_{5-x}M_xO_{13}$. The transition metals calculated to be the most favourable for doping are Cu and Co, where calculations suggest that doping should be favourable across the entire series of x values calculated. When M = Ni and Zn, small levels of doping were calculated to be favourable (in both cases, when $x = 0.25$).

When M = Mn, there is little change in the calculated reaction energy as a function of the dopant content, without the presence of any particular minima, it is suggested that doping with Mn should be possible. When M = Ti, doping was calculated to be strongly unfavourable across the whole dopant series. B-site ordering for the dopant metal was only calculated to be favoured when M = Co and Mn, where the dopants were found to prefer the tetrahedral sites (when $x \leq 1.00$) or the square pyramidal site (when $x = 1.25$) for M = Co. When M = Mn strong B-site ordering was calculated to be favourable, with Mn occupying the octahedral site. Notably, the assessment that B-site ordering is not strongly favoured for and of the other dopant metals not because mixed configurations were calculated to be especially stable, but rather because the energy gap between B-site configurations were small. The results calculated in this chapter for the dopants that are predicted to have favourable doping (M = Co and Cu) and marginal doping (M = Mn) show structural properties that are in good agreement with precedents for solid solutions involving Fe and the corresponding dopant atoms (examples discussed below).

The effect of Co doping calculated on the $10a_p$ structure is similar to that previously reported for Co doping for the $YBa_2Fe_{3-x}Co_xO_8$ triple perovskite system[27]. As with the calculations presented above, Co doping is shown to steadily decrease the overall volume of the structure, with a

reported decrease in cell volume at the highest doping level of 1.23(1)% (With a nominal metal content of $Fe_{1.5}Co_{1.5}$). Observed Co doping results in no B-site ordering (therefore having Co present at all B-sites) and culminates in a decrease in all of the observed bond lengths. Therefore, the results from the above calculations seem to give reasonable results that are consistent with existing precedents for Co doping into perovskite systems.

Solid solution systems between copper and iron have been previously reported in the $LaBa_2Cu_{3-x}Fe_xO_y$ system[160, 161], where values of x are reported between 0 and 3 (with reported values of x equal to 0.1, 0.2, 0.3, 0.5, 1, 2 and 3, note that in the reported samples, when $x > 0.2$ a slight excess of La was required[161]). The Cu pure form of the system is reported to be similar to the YBCO super conductor structure[161] and the Fe pure system reported as a disordered cubic perovskite[160]. It is has been observed that when x is greater than 1, the solid solution favours the disordered phase. There are some reports that suggest the $3a_p$ phase may be synthesised at higher values of x although the samples were not synthesised phase pure[162]. When x is equal to or less than 1, the resulting material adopts the YBCO type $3a_p$ phase.

Looking at the trends reported across the solid solutions discussed above, they yield similar results to those calculated in this chapter for the $10a_p$ material. Irrespective of the perovskite ordering observed samples are shown to have decreasing bond lengths and unit cell volumes with increased Cu content (although this is also coupled with slight decrease in oxygen content). However the calculated shifts in bond lengths for M = Cu in the $10a_p$ structure are not as substantial as for the reported systems. When the samples are reported as an ordered phase, the resulting structure contains the same trends in site distortion that are calculated here for the $10a_p$. Although assessing the literature for samples with differing charge states (i.e. a solid solution between Fe^{3+} and Cu^{2+} compounds) highlighting that any possible changes in oxygen content as

a function of B-site doping are not taken into account for the calculations in this chapter. Thus attempting to calculate varying oxygen content as a function of dopant is a possible future development of these calculations in order to improve their accuracy and applicability to real systems.

While doping calculations when M = Mn, follow the same trend highlighted above that doping only has a major effect on one of the sites in the material, . It has been shown in previous sections that Mn doping has little effect on the overall reaction energy to form the $10a_p$ structure from binary oxides. A possible reason for this result in contrast to M = Co and Cu, is that although the Mn doping significantly effects the geometry of the octahedral site (Figure 51), it also has a significant effect on the ratio of the ab : c lattice parameters caused by the Jahn-Teller distortion of the octahedral site. It is possible that the Jahn-Teller distortion changes distortions for other cations in the material which are energetically unfavourable, resulting in a combination of favourable and unfavourable distortions caused by Mn doping and hence resulting in only the small overall changes in the reaction energies calculated.

The results and conclusions drawn from Mn doping can be compared to observed results for Mn doping into the $Ca_2Fe_2O_5$ brownmillerite[10, 22] and the $YBa_2Fe_{3-x}Mn_xO_{8\pm\delta}$ reported in the previous chapter. In both of these systems it is shown that the introduction of Mn^{3+} into the structure results in B-site ordering, with the Mn atoms preferentially occupying the octahedral sites. From the resulting B-site ordering, it is observed that the octahedral site distorts toward a Jahn-Teller distortion resulting in a decrease of the a and b lattice parameters and a lengthening of the c axis.

From the conclusions drawn for the dopant species calculated to be largely unfavourable (M = Ni, Ti and Zn) and comparing them with the rest, leads to the overall conclusion that to be able

to successfully dope the $10a_p$ the dopant atoms must only cause a modest change in polyhedral volumes in the structure. The conclusions drawn here are exemplified by examining at the polyhedral volumes for the favoured dopants, M = Co, Mn and Cu, reported in Table 9, Table 11 and Table 13 respectively. Unlike the unfavoured dopants, Co, Mn and Cu cause much smaller changes to the Fe site volumes, note however, that the overall volume is allowed to expand or contract and still yield a favourable result .

The calculations also suggest it is possible for the system to accommodate dopant atoms of a reduced charge state when compared to undoped, where in this system with fixed oxygen content the introduction of a dopant with a reduced charge state is assumed to be coupled with an increase in the Fe charge state in order to maintain charge neutrality. This could therefore result in the desired effect of improving the performance of the $10a_p$ material as a SOFC cathode.

4.6 A Note on Subsequent Experimental Work Within The Research Group

Synthetic work on $YBa_2Ca_2Fe_{5-x}M_xO_{13}$ was undertaken by Mr. D. Hodgeman, also a member of the Rosseinsky research group. Samples of the doped $10a_p$ were prepared for M = Co, Cu and Mn, as other doping are predicted to either be unfavourable or favourable for only low doping levels. At the time of writing, a maximum doping level for M = Co had been found at x = 1.85, when M = Cu a maximum doping value of 0.35 had been obtained and for M = Mn, a maximum value of 0.75 attained, with all samples, as with the undoped material the A-site ratios were altered away from the stoichiometric values in order to remove impurity phases. Although not enough experimental data has been collected in order to determine if any B-site ordering is

present in the doped materials. Physical property measurements have been performed by other research group members and suggest that doping the $10a_p$ material improved upon the previously reported d.c. and area specific resistance values.

4.7 Conclusions

In summary, the work presented within this chapter has shown that the computational approach for using DFT to predict B-site doping in layered perovskites have successfully predicted doping in a large complex perovskite. The calculations within this chapter have also resulted in predictions regarding favoured B-site ordering for a variety of dopant species and doping levels. Calculations have also predicted where high levels of doping are unfavoured and for M = Ti, that doping is completely unfavoured. Conducting such a large range of calculations has also enabled conclusions to be drawn regarding the chemical reasoning as to why certain dopants are favoured, which may in turn be able to provide insights to predict the likelihood of doping the $10a_p$ with other dopants not covered in this work. Resulting from these calculations, other members of the research group have been able to dope the $10a_p$ material, although with some changes to the A-site composition.

4.8 Acknowledgements

The DFT calculations performed in this chapter on the $10a_p$ structure were performed on the HECToR super computer, with time allocated via the Materials Chemistry Consortium (MCC).

4.9 Tables

Table 7 Summary of dopant configurations for calculated doping into the $10a_p$ structure, T_d = tetrahedral, S_q = Square pyramidal and O_h = Octahedral. When M = 'all' indicates that the configuration was trialled for all of the dopant species studied.

Doping level	Dopant atoms / unit cell	Site preference	M	dopant polyhedra
***x* = 0.25**	1	T_d	all	$1 \times T_d$
		S_q	all	$1 \times S_q$
		O_h	all	$1 \times O_h$
***x* = 0.50**	2	T_d	all	$2 \times T_d$
		S_q	all	$2 \times S_q$
		O_h	all	$2 \times O_h$
		Mix-1	all	$1 \times O_h + 1 \times T_d$
		Mix-2	all	$1 \times O_h + 1 \times S_q$
***x* = 0.75**	3	T_d	all	$3 \times T_d$
		Sq	all	$3 \times S_q$
		O_h	all	$3 \times O_h$
		Mix	all	$1 \times T_d + 1 \times S_q + 1 \times O_h$
***x* = 1.00**	4	T_d	all	$4 \times T_d$
		S_q	all	$4 \times S_q$
		O_h	all	$4 \times O_h$
		Mix-1	all	$1 \times T_d + 1 \times S_q + 2 \times O_h$
		Mix-2	all	$1 \times T_d + 2 \times S_q + 1 \times O_h$
***x* = 1.25**	5	T_d-1	Co, Cu, Ni	$4 \times T_d + 1 \times S_q$
		T_d-2	Mn, Zn	$4 \times T_d + 1 \times O_h$
		S_q	all	$5 \times S_q$
		O_h	all	$5 \times O_h$
		Mix	all	$1 \times T_d + 2 \times S_q + 2 \times O_h$

Table 8 DFT calculated lattice parameters for $YBa_2Ca_2Fe_{5-x}Co_xO_{13}$ highlighting the observation that only small changes to the overall unit cell volume across the doping series are expected.

x Co	a (Å)	b (Å)	c (Å)	Volume (Å^3)	Difference from *x* = 0 (Å^3)	Percentage change
0.00	5.552	5.599	38.804	1206.397	0.000	0.000%
0.25	5.552	5.597	38.793	1205.488	-0.909	-0.075%
0.50	5.552	5.594	38.782	1204.519	-1.878	-0.156%
0.75	5.551	5.591	38.770	1203.314	-3.083	-0.256%
1.00	5.550	5.588	38.763	1202.266	-4.131	-0.342%
1.25	5.553	5.600	38.497	1197.178	-9.219	-0.764%

Table 9 Average polyhedral volumes for the lowest energy configurations for $YBa_2Ca_2Fe_{5-x}Co_xO_{13}$, calculated using VESTA.

x Co	Fe square pyramidal volume (Å^3)	Fe octahedral volume (Å^3)	Fe tetrahedral volume (Å^3)	Co square pyramidal volume (Å^3)	Co tetrahedral volume (Å^3)
0.00	6.1337	11.2980	3.4456	--	--
0.25	6.1348	11.2787	3.4460	--	3.2978
0.50	6.1391	11.2590	3.4471	--	3.2964
0.75	6.1312	11.2377	3.4457	--	3.2972
1.00	6.1262	11.2177	--	--	3.2961
1.25	6.0720	11.2325	3.4472	5.9680	--

Table 10 DFT calculated lattice parameters for $YBa_2Ca_2Fe_{5-x}Cu_xO_{13}$ and unit cell volume changes across the doping series

x Cu	a (Å)	b (Å)	c (Å)	Volume (Å^3)	Difference from *x* = 0 (Å^3)	Percentage change
0.00	5.552	5.599	38.804	1206.397	0.000	0.000%
0.25	5.546	5.598	38.688	1201.220	-5.177	-0.429%
0.50	5.534	5.584	39.031	1206.076	-0.321	-0.027%
0.75	5.527	5.576	39.073	1204.356	-2.041	-0.169%
1.00	5.545	5.597	38.242	1186.850	-19.547	-1.620%
1.25	5.542	5.596	38.129	1182.515	-23.882	-1.980%

Table 11 Average polyhedral volumes for the lowest energy configurations for $YBa_2Ca_2Fe_{5-x}Cu_xO_{13}$, calculated using VESTA.

x Cu	Fe square pyramidal volume (Å^3)	Fe octahedral volume (Å^3)	Fe tetrahedral volume (Å^3)	Cu square pyramidal volume (Å^3)	Cu octahedral volume (Å^3)
0.00	6.1337	11.2980	3.4456	--	--
0.25	6.0940	11.1524	3.4473	6.6688	--
0.50	6.1126	11.1860	3.4350	--	11.8634
0.75	6.1023	11.1012	3.4264	--	11.7574
1.00	5.9431	10.7231	3.4447	6.5975	--
1.25	5.9337	10.6094	3.4416	6.5129	--

Table 12 DFT calculated lattice parameters for $YBa_2Ca_2Fe_{5-x}Mn_iO_{13}$ highlighting the observation that only very small changes to the overall unit cell volume across the doping series.

x Mn	a (Å)	b (Å)	c (Å)	Volume (Å^3)	Difference from *x* = 0 (Å^3)	Percentage change
0.00	5.552	5.599	38.804	1206.397	0.000	0.000%
0.25	5.546	5.593	38.903	1206.616	0.219	0.018%
0.50	5.538	5.585	39.004	1206.303	-0.094	-0.008%
0.75	5.530	5.577	39.105	1206.141	-0.256	-0.021%
1.00	5.523	5.570	39.205	1206.108	-0.289	-0.024%
1.25	5.514	5.562	39.335	1206.413	0.016	0.001%

Table 13 Average polyhedral volumes for the lowest energy configurations for $YBa_2Ca_2Fe_{5-x}Mn_xO_{13}$, calculated using VESTA.

x Mn	Fe square pyramidal volume (Å^3)	Fe octahedral volume (Å^3)	Fe tetrahedral volume (Å^3)	Mn octahedral volume (Å^3)
0.00	6.1337	11.2980	3.4456	--
0.25	6.1232	11.3270	3.4467	11.3434
0.50	6.1103	11.3616	3.4471	11.3353
0.75	6.0982	11.4119	3.4475	11.3449
1.00	6.0856	11.4962	3.4483	11.3405
1.25	6.0699	11.4940	3.4515	11.4305

Table 14 DFT calculated lattice parameters and unit cell volumes for $YBa_2Ca_2Fe_{5-x}Ni_xO_{13}$..

x Ni	a (Å)	b (Å)	c (Å)	Volume (Å^3)	Difference from *x* = 0 (Å^3)	Percentage change
0.00	5.552	5.599	38.804	1206.397	0.000	0.000%
0.25	5.550	5.604	38.722	1204.186	-2.211	-0.183%
0.50	5.544	5.597	38.557	1196.390	-10.007	-0.829%
0.75	5.520	5.573	39.021	1200.429	-5.968	-0.495%
1.00	5.535	5.591	38.471	1190.387	-16.009	-1.327%
1.25	5.502	5.557	39.256	1200.108	-6.289	-0.521%

Table 15 Average polyhedral volumes for the lowest energy configurations for $YBa_2Ca_2Fe_{5-x}Ni_xO_{13}$, calculated using VESTA, the value at x = 1.00 appears to by significantly smaller than the other values as in this structure, all of the Fe square pyramidal sites are adjacent to a Ni containing square pyramidal site (see configuration for x = 1.00 in Figure 44).

x Ni	Fe square pyramidal volume (Å^3)	Fe octahedral volume (Å^3)	Fe tetrahedral volume (Å^3)	Ni square pyramidal volume (Å^3)	Ni octahedral volume (Å^3)
0.00	6.1337	11.2980	3.4456	--	--
0.25	6.0985	11.2028	3.4527	6.6102	--
0.50	6.0241	11.0509	3.4485	6.5722	--
0.75	6.0886	10.7224	3.4421	--	11.8972
1.00	5.8056	10.9203	3.4427	6.5802	--
1.25	6.0785	10.3595	3.4220	--	11.9140

Table 16 DFT calculated lattice parameters and cell volumes for $YBa_2Ca_2Fe_{5-x}Ti_xO_{13}$. Two values for x are given as they are configurations calculated to have very similar reaction energies, the first configuration with square pyramidal site preference and the second in a mixed configuration.

x Ti	a (Å)	b (Å)	c (Å)	Volume (Å^3)	Difference from x = 0 (Å^3)	Percentage change
0.00	5.552	5.599	38.804	1206.397	0.000	0.000%
0.25	5.565	5.615	38.623	1206.808	0.411	0.034%
0.50	5.565	5.614	39.016	1218.857	12.460	1.033%
0.50	5.577	5.627	38.520	1208.709	2.312	0.192%
0.75	5.579	5.629	39.210	1231.205	24.808	2.056%
1.00	5.597	5.654	38.685	1224.273	17.876	1.482%

Table 17 Average polyhedral volumes for the lowest energy configurations for $YBa_2Ca_2Fe_{5-x}Ti_xO_{13}$, calculated using VESTA.

xTi	Fe square pyramidal volume (Å^3)	Fe octahedral volume (Å^3)	Fe tetrahedral volume (Å^3)	Ti square pyramidal volume (Å^3)	Ti octahedral volume (Å^3)	Ti tetrahedral volume (Å^3)
0.00	6.1337	11.2980	3.4456	--	--	--
0.25	6.2331	11.2906	3.4553	--	10.6222	--
0.50 square pyramidal	6.5091	11.4421	3.4504	5.7400	--	--
0.50 mixed	6.3089	11.3089	3.4922	--	10.6198	3.3713
0.75	6.8371	11.5160	3.4619	5.7488	--	--
1.00	6.5323	11.6189	3.5041	5.7827	10.7131	3.3851

Table 18 DFT calculated lattice parameters and cell volumes for $YBa_2Ca_2Fe_{5-x}Zn_xO_{13}$.

x Zn	a (Å)	b (Å)	c (Å)	Volume (Å^3)	Difference from *x* = 0 (Å^3)	Percentage change
0.00	5.552	5.599	38.804	1206.397	0.000	0.000%
0.25	5.537	5.589	39.109	1210.299	3.902	0.323%
0.50	5.525	5.577	39.171	1207.032	0.635	0.053%
0.75	5.535	5.588	38.586	1193.412	-12.985	-1.076%
1.00	5.529	5.585	38.552	1190.354	-16.043	-1.330%
1.25	5.530	5.588	38.463	1188.684	-17.713	-1.468%

Table 19 Average polyhedral volumes for the lowest energy configurations for $YBa_2Ca_2Fe_{5-x}Zn_xO_{13}$, calculated using VESTA.

xZn	Fe square pyramidal volume (Å^3)	Fe octahedral volume (Å^3)	Fe tetrahedral volume (Å^3)	Zn square pyramidal volume (Å^3)	Zn octahedral volume (Å^3)	Zn tetrahedral volume (Å^3)
0.00	6.1337	11.2980	3.4456	--	--	--
0.25	6.1282	11.3511	3.4481	--	3.6813	--
0.50	6.1093	11.2086	3.4432	--	3.6745	12.1664
0.75	5.9320	10.9986	3.4434	6.5588	--	--
1.00	5.8084	10.9355	3.4424	6.5503	--	--
1.25	5.7632	10.8477	3.4433	6.4810	--	--

Chapter 5. Extended Module Materials Assembly (EMMA)

5.1 Abstract

Following on from the doping predictions and synthesis presented in the previous chapter, an unreported perovskite superstructure was discovered by members of the research group with the approximate composition of $Y_{2.1(2)}Ba_{1.8(2)}Ca_{4.1(2)}Fe_{7.4(2)}Cu_{0.6(2)}O_{21-\delta}$. This chapter describes the development of a new semi-brute force method created to assemble possible perovskite structures of this phase, known as the Extended Module Materials Assembly (EMMA). EMMA is then combined with force field and density functional theory calculations in order to predict the most stable structure. The lowest energy structure is then used as the basis for experimental identification of the phase by powder diffraction by group members. The predicted and observed structures were found to be in good agreement.

5.2 Introduction

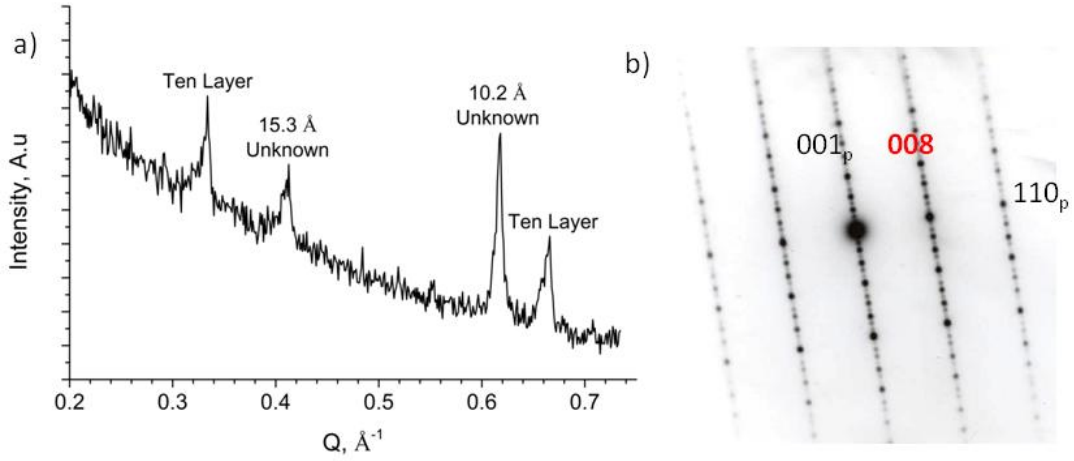

Figure 55 a) Powder X-ray diffraction collected by D. Hodgeman highlighting the unknown long range ordering *hkl* reflections. b) Electron diffraction provided by A. Demont showing the unit cell indexing to an $8a_p$ cell.

Following on from the computational predictions made in the previous chapter 4 regarding the doping of $YBa_2Ca_2Fe_5O_{13}$ ten layer perovskite (with the structure referred to as the $10a_p$) D. Hodegeman carried out synthetic work doping the material with Co, Cu and Mn. With initial samples containing Cu at a doping level of ~ 7 % for Fe, in addition to the $10a_p$ phase with the $10a_p$ structure a minor impurity phase was observed by powder X-ray powder diffraction (PXRD) with two d-spacing reflections for an unreported superstructure (Figure 55) measured at 10.2 and 15.3 Å.

The doped sample was also analysed by electron microscopy (Figure 55b) by A.Demont and found that these observed d-spacings corresponded to an eight-fold perovskite super structure, with a stacking length of approximately 32 Å (referred to as the $8a_p$ structure). Energy dispersive X-ray (EDX) analysis calculated the approximate metal composition of $Y_{2.1(2)}Ba_{1.8(2)}Ca_{4.1(2)}Fe_{7.4(2)}Cu_{0.6(2)}$. Due to the size and composition of the new structure it was

decided to attempt to use theory to attempt to calculate the most likely structure, utilising the experimental information available.

Existing methods for structure prediction include generating structures by data mining a target composition into known structural motifs[53, 163] from a database of known solid state structures, or structure types[55]. These techniques, being based on known structures would be unlikely to be able to find a new perovskite structural motif and is therefore unlikely to find the $8a_p$ structure. For some systems simulated annealing has been used to find global minimum structures[164]. The application of genetic algorithms has also been reported for structure prediction[66]. Some methods have also been presented for the generation of structures using known rigid bodies and the correct crystal structures successfully calculated[165]. Due to the size of the computational challange in this chapter, it was decided that the methods referred to above were not feasible for solving the $8a_p$ structure and a new method was sought based upon a layered description of oxide structures.

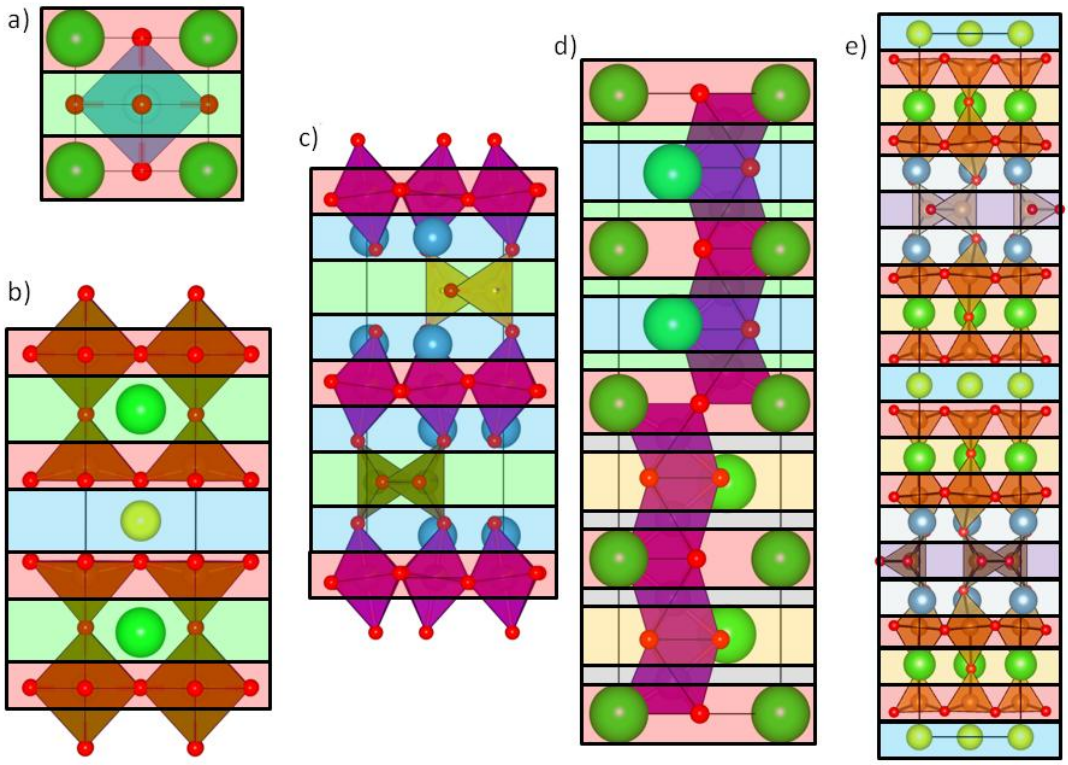

Figure 56 a) $SrTiO_3$ single perovskite[1], broken down into two different atomic layers, one for the A-site and one for the B-site. b)$YBa_2Fe_3O_8$ triple perovskite[27], broken down into one B-site layer type (formally FeO_2) and two types of A-site layer (BaO and Y). c) $Ca_2Fe_{1.039}Mn_{0.962}O_5$ brownmillerite[22] containing two types of B-site layer ($(FeMn)O_2$ and (FeMn)O) and one type of A-site layer (CaO). d) 8-H $BaMnO_3$ hexagonal perovskite[166], broken down into three different A-site layers (three different BaO layers, based on the Ba position) and two different B-site layers (containing only a Mn atom, in a different position in each layer type. e) The structure of stoichiometric $YBa_2Ca_2Fe_5O_{13}$ ten layer perovskite[15], broken into 2 types of B-site layer (FeO_2 and FeO) and three different types of A-site layer (BaO , CaO and Y).

When considering extended solid state structures such as the previously reported $10a_p$ perovskite[15] and hexagonal perovskites[166] (Figure 56), they are often considered to be a combination of structural motifs or layers. Types of layers range from only a few atoms thick or even single atomic layers, such as BaO rocksalt layers or FeO_2 layers commonly found in perovskite structures (Figure 56). Layers however can be much larger, up to many atoms thick, such as perovskite blocks, or considering large extended structures containing perovskite super structures[16].

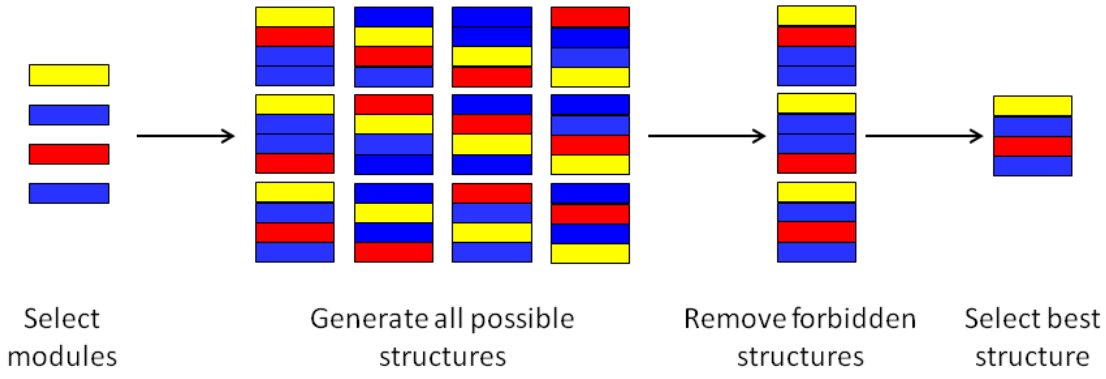

Figure 57 EMMA methodology, the structures defined as 'forbidden' are user defined and could be coded to include any chemically sensible rules. In this chapter, forbidden structures were defined as structures containing translational symmetry of other structures generated; this was used so as to only include the symmetrically unique perovskite superstructures. Note that forbidding structures that do no have perovskite stacking was not required due to structures being assembled alternating between 'A-site' and 'B-site' layers.

The concept of considering extended oxides structures as a series of layers became the basis used to identify the atomic structure of the $8a_p$ perovskite, entitled the Extended Module Materials Assembly (EMMA, Figure 57). This method begins with the selection of a module set, where each module contains chemically sensible layers, theoretically of any size, as suggested above. In the initial implementation of EMMA, the sum of all of the selected modules (including multiples of the same module) are required to achieve the composition and unit cell stacking length required. The EMMA method then takes the selected modules and assembles all possible structures from the chosen module set. The number of structures is then restricted by a given set of rules in order to ensure that the majority of structures are chemically sensible and repeat structures are not generated. An example of such a rule would be to ensure that all structures generated have a perovskite type structure by enforcing alternate stacking between A-site and B-site layers and this is enforced for all of the EMMA structures generated in this chapter. Note that since all of the modules are stacked together, all of the component modules are required to

have the same a and b axis lengths, although the length of the stacking axis will be equal to the sum of the stacking axes of all of the component modules.

Once all possible permutations are calculated it is then possible to remove structures related by translational symmetry in the stacking direction, leaving a set of unique structures. Once built, all of the structures are relaxed using some form of simulation. All of the structures can then be ranked by some calculated property (e.g. energy or calculated band gaps), in order to select the 'best' structure. In this chapter a combination of classical force field methods (FF) and density functional theory are used (DFT) with the best structure defined as the structure that has the lowest overall energy and is therefore the most stable. The EMMA method is first applied to the known $10a_p$ perovskite structure at the idealised composition used in chapter 4 in order to test the methodology; EMMA is then used to calculate the lowest energy structure and hence predict the crystal structure of the $8a_p$ material.

5.3 Computational setup

FF calculations used in this chapter were implemented using the General Utility Lattice Program (GULP)[70]. Ionic interactions are implemented with two components, firstly, long columbic interactions and a mostly repulsive short range Buckingham potential with the form:

$$\varphi_{ij}(r_{ij}) = A_{ij} exp\left(-\frac{r_{ij}}{\rho_{ij}}\right) - \frac{C_{ij}}{r_{ij}^6} \quad \textbf{(5.1)}$$

Where $\varphi_{ij}(r_{ij})$ is the potential energy for the ion pair ij, r_{ij} is the inter-atomic distance for the ion pair, A_{ij}, ρ_{ij} and C_{ij} are parameters set by the user for the force field, typically fitted so that the

potential set will reproduce a known structure. In this chapter polarizability of some atoms is taken into account by the inclusion of the shell model incorporated in GULP[115].

The force field used in this chapter was initially constructed with the help of Prof. M. S. Islam (The University of Bath). The force field was constructed in order to to replicate the $10a_p$ structure at the composition $YBa_2Ca_2Fe_5O_{13}$ when relaxed using DFT as previously reported[15] (the final potential parameters used are presented in Table 20). Initially a number of different potentials were tested from the literature covering the interactions required in the $10a_p$ structure, with different combinations also considered. The set of reported potentials that yielded the $10a_p$ structure closest to the DFT structure were selected as the basis for the potential set used in this chapter. Since Cu is not present in the $10a_p$ structure a Cu-O potential was used as previously reported to describe the $YBa_2Cu_3O_{6+\delta}$ perovskite[167] for models containing Cu atoms and was used without modification. FF calculations in this chapter were performed allowing the relaxation of the unit cell size and shape and atomic co-ordinates were relaxed. Due to the large number of structures requiring relaxation with force fields in this chapter, FF calculations were restricted to a total of 1000 ionic steps or 60 minutes CPU time.

The final force field utilised in this chapter was created by altering a small number of the parameters, initially manually in order to discover the potential parameters that had the largest impact on the structure calculated by GULP. It should be noted that with this initial parameter set the main error in the calculated structure was the overestimation of bonds in the stacking direction, which in turn resulted in a substantial overestimation of the stacking axis length. The parameters found to have the largest impact were then fitted using the fitting routines implemented in GULP, with the final parameters shown in Table 20.

In order to test the applicability of the potential set further, the DFT calculations examining A-site disorder in the $10a_p$ were repeated using GULP (configurations shown in Figure 58). The results from the FF calculations indicate that the order in which the structures are ranked matches those reported. Although the absolute values calculated by force fields differ from literature values, for example the reported difference in energy between the ideal structure and the Y/Ca mixing was only 0.22 eV/FU more stable compared to ideal[15], versus the 0.75 eV/FU calculated by the FF calculations in this chapter. Therefore it was concluded that the force field derived for this system was adequate for a 'first pass' over all of the structures to be generated by EMMA. However, due to the inaccurate energies in FF calculations, DFT calculations would be required on a proportion of the lowest energy structures from GULP, in order to be certain of the lowest energy structure, especially in cases where FF calculations only result in small energy differences.

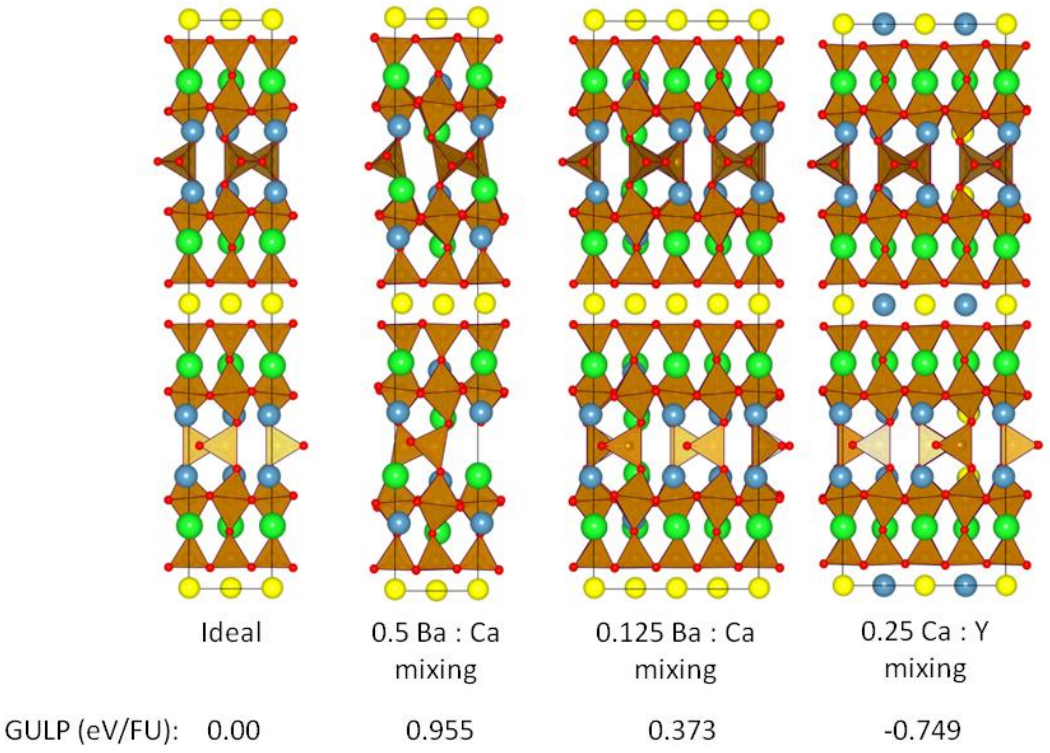

Figure 58 A-site disorder configurations trialled using FF for comparison to previously reported DFT results[15], the number indicates the fractional proportion of the first species that has been swapped for the second in each configuration. The energies indicate that the most stable configuration has Ca and Y mixing, in agreement with the results previously published[15].

DFT calculations presented in this chapter were performed using the Vienna *ab-inito* simulation package (VASP) plane wave DFT package[168, 169], using the Perdew, Burke and Ernzerhof (PBE)[103] exchange correlation functional. In all calculations the unit cell shape and size were allowed to relax along with atomic co-ordinates. Wavefunctions were relaxed until the difference in energy between steps was less than 1×10^{-5} eV and forces on atoms were relaxed to less than 0.01 eVÅ^{-1}. Calculations were setup using a Gamma centred k-point grid. The number of k-points in the a and b axis were set according to the following condition:

$$nk_i \times r_i \geq 20 \text{ Å} \qquad \textbf{(5.2)}$$

Where nk_i is the number of k-points on lattice vector i, and r_i is the real space length of lattice vector i. Colinear spin polarisation was implemented in all DFT calculations in this chapter without any spin-orbit coupling with all structures setup with G-type anti-ferromagnetic ordering. For the transition metal species a rotationally invariant U_{eff} was applied where $U_{eff} = U - J$. Values of U_{eff} were taken to be 4.0 eV for both Fe and Cu atoms, where this value has been reported in previous calculations in oxide systems[154]. For the A-site species (Y, Ba and Ca) the first sub-valent s orbital was treated as valence, for the B-site species (Fe and Cu) the first sub-valent p orbital was treated as valence.

The EMMA method was implemented in python in collaboration with M. S. Dyer, utilising the atomic simulation environment (ase) and numpy python packages[170].The input for EMMA is specified as a series of *n* modules, containing *n* A and B terminated modules. Once input modules are defined, the EMMA implementation builds all possible permutations of the input, with all of the permutations being held in the memory as 2-D numerical arrays. The permutations in this chapter were subject to the perovskite stacking, with alternating A and B-site terminated layers to be able to construct perovskite units. There is the requirement for an equal number of A and B terminated modules in the EMMA input in order to build perovskite structures.

Once all of the possible permutations were constructed, the EMMA script then searches through all of the possible permutations, finding all of the structures that are related by translational symmetry and then retaining only the first permutation found. This use of symmetry leaves just the unique stacking sequences possible from the input modules and thus greatly reduces the number of structures generated. To an approximation the use of translational symmetry reduces the resulting number of structures by a factor of *n*, where *n* is the number of perovskite layers.

Once the final set of permutations is computed, EMMA uses scripts from ase to convert each permutation into a crystal structure and writes the structure into formats suitable for use with either the VASP DFT package and the GULP FF code. Note that EMMA allows for the use of atomic 'rattling' before structures are written to file, this is a process by which all of the atoms in the unit cell are moved in a random direction around a standard deviation specified by the user. In this chapter, a standard deviation of 0.05 Å was used. Atomic rattling was found to be required, as with some module sets a large number of structures were found to be in a highly symmetrical but high energy structure and so few structures relaxed from their high energy starting point.

5.4 Validating the EMMA method by finding the $10a_p$ structure.

In order to be able to construct $YBa_2Ca_2Fe_5O_{13}$ in the $10a_p$ structure using EMMA, layers were based upon a 2 × 2 expansion of the perovskite unit cell, in the plane parallel to the stacking direction, with an a and b lattice parameter equal to 7.6 Å and each atomic layer given a height of 1.9 Å (equal to half the approximate perovskite lattice parameter of 3.8 Å). 10 single atom thick layers were used for both the A and B-sites (Figure 59a, with an example of an assembled structure shown in b) The A layers were 2 × Y_4, 4 × Ba_4O_4 and 4 × Ca_4O_4 and the B layers were 8 × Fe_4O_8 and 2 × Fe_4O_4 layers. The input layers result in structures that are a 2 × 2 ×10 supercell of the perovskite structure containing 184 atoms.

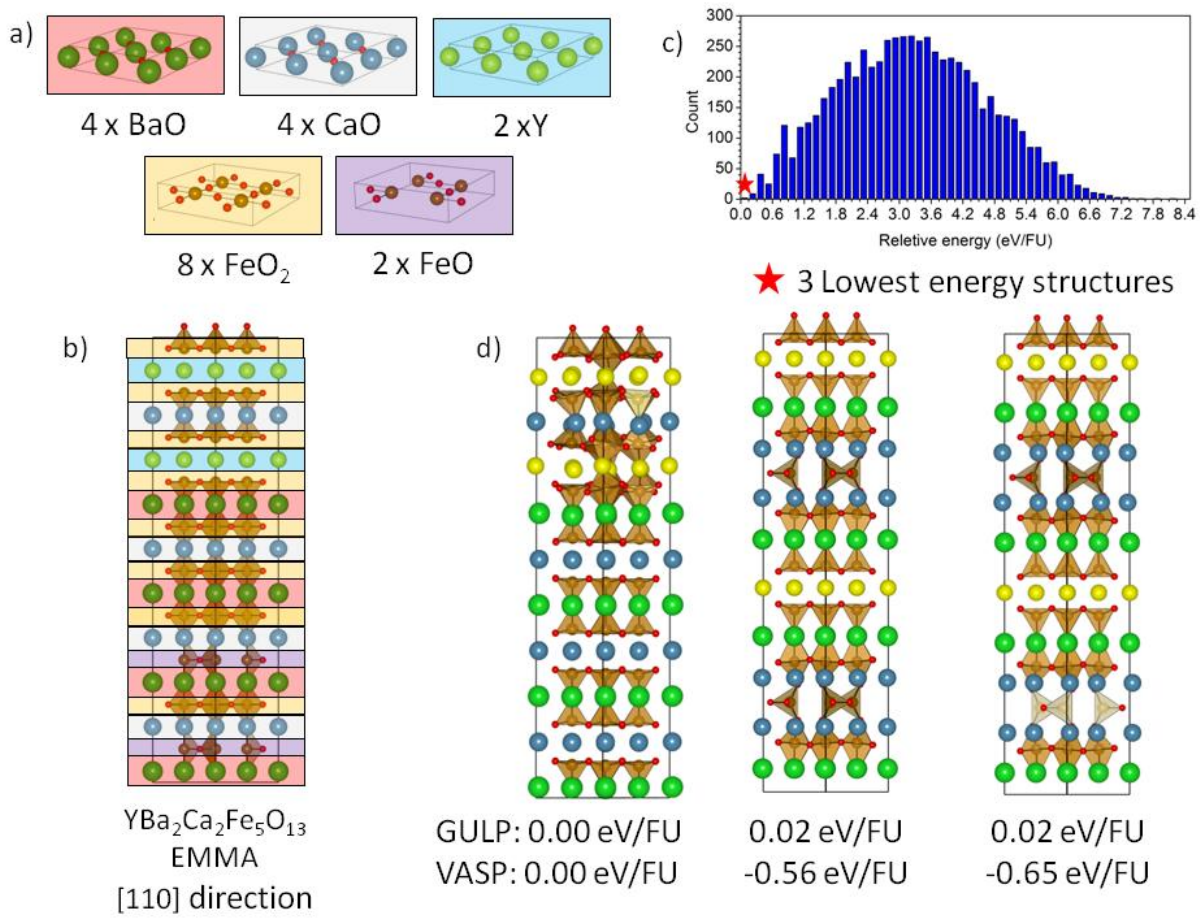

Figure 59 a) The ten A-site (BaO, CaO and Y) and ten B-site (FeO_2 and FeO) layers used for the generation of $YBa_2Ca_2Fe_5O_{13}$ $10a_p$ structures. b) Example of an assembled $10a_p$ structure from EMMA prior to relaxation, with coloured boxes corresponding to layers in panel a). c) The energy distribution of converged structures using FF calculations, divided into 0.15 eV bars. d) The three lowest energy structures from FF calculations and the energies relative to the lowest energy structure from the FF calculations, highlighting the need to use DFT calculations to correctly identify the lowest energy structure.

The module set listed above resulted in a total of 14,190 unique structures. All structures were then relaxed using the FF, with 7,628 failing to converge and therefore rejected. The remaining structures were then ranked by their total energy in order to find the most stable structure (Figure 59c). Three structures were found to be significantly more stable that the others (Figure 59d), with energies all within 0.02 eV/FU of each other, with the next nearest structure being 0.15 eV/FU less stable. Since these three structures were found to be significantly more stable than

the rest, only these three structures were re-relaxed using VASP in order to calculate accurate relative energies and therefore determine the EMMA structure for the given module set.

Once the structures were relaxed the order of stability for the lowest energy structures changed, with the structure found to be second most stable, becoming the most stable by 0.09 eV/FU, with the previously most stable GULP structure becoming the least stable of the three structures (Figure 59d). On inspection it can be seen that the lowest energy structure contains the experimentally observed $10a_p$ structure and thus validates the EMMA method (Figure 60). Calculations on the structure also highlight the requirement to utilise both DFT and FF calculations, as DFT was required to accurately separate the lowest energy structures. In this section the EMMA method has been validated by the successful calculation of the experimentally observed structure for $YBa_2Ca_2Fe_5O_{13}$, in the following section the EMMA method is applied to calculate the most likely structure for the unknown $8a_p$ material.

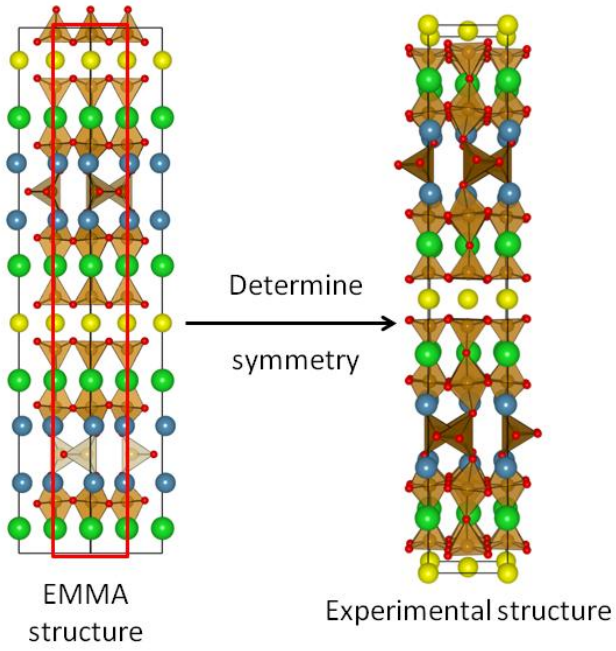

Figure 60 The $YBa_2Ca_2Fe_5O_{13}$ EMMA structure viewed down the [110] direction reveals that the experimental perovskite stacking is contained within the structure, the symmetry of the structure can then be symmetry reduced to obtain the experimental structure.

5.5 Using EMMA predict a structure for the $8a_p$.

In order to be able to test whether the presence of Cu atoms has an influence on the resulting structure, two compositions were considered; Firstly a stoichiometric form of the experimental structure, containing no Cu atoms with an approximated oxygen content of 21 per formula unit, $Y_2Ba_2Ca_4Fe_8O_{21}$. The second is a copper containing analogue, with the formula unit of $Y_2Ba_2Ca_4Fe_{7.5}Cu_{0.5}O_{21}$.

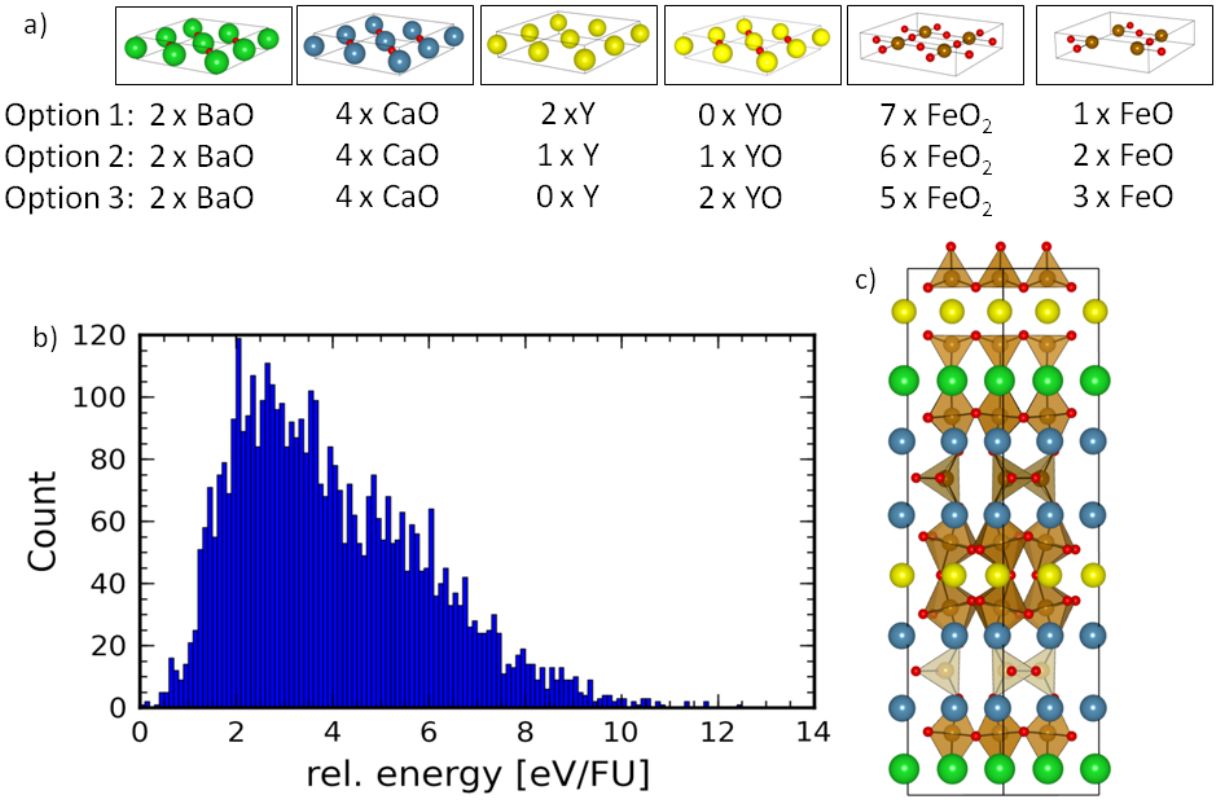

Figure 61 a) The three module sets used for the 8a_p EMMA calculations, giving variation in the location of oxygen vacancies. b) The energy distribution of the 8a_p structures for $Y_2Ba_2Ca_4Fe_8O_{21}$. c) The lowest energy structure from the EMMA calculations viewed along the [110] direction.

When using EMMA on the copper free composition, $Y_2Ba_2Ca_4Fe_8O_{21}$, the calculations were performed in collaboration with M. S. Dyer, due to the number of calculations required. The a and b lattice parameters for all layers used in this section were set to be equal to 7.6 Å equivalent to 2a_p, since the a and b lattice parameters had not been experimentally determined and this allowed for expansions in the a and b axes relative to the cubic perovskite.

Three different module sets were chosen, based primarily on the modules found in the 10a_p structure with the addition of a YO layer. All module sets contained 2 × Ba_4O_4 and 4 × Ca_4O_4 A-site modules and 5 × Fe_4O_8 B-site modules. To make the three module sets, 2 × Y_4 +Fe_4O_4 +

$2 \times Fe_4O_8$, $Y_4 + Y_4O_4 + 2 \times Fe_4O_4 + Fe_4O_8$ or $2 \times Y_4O_4 + 3 \times Fe_4O_4$ modules (Figure 61a) were added in order to make up the desired composition. Note that Y containing modules were added to the A-sites and Fe containing modules were added to the B-sites (Figure 61a). A number of different module sets were chosen for this structure in order to allow for variation in the location of the oxygen vacancies. The module sets resulted in the generation of 6,300 unique structures (FF energy distribution shown in Figure 61b), with the DFT and FF calculations yielding the same lowest energy structure (Figure 61c).

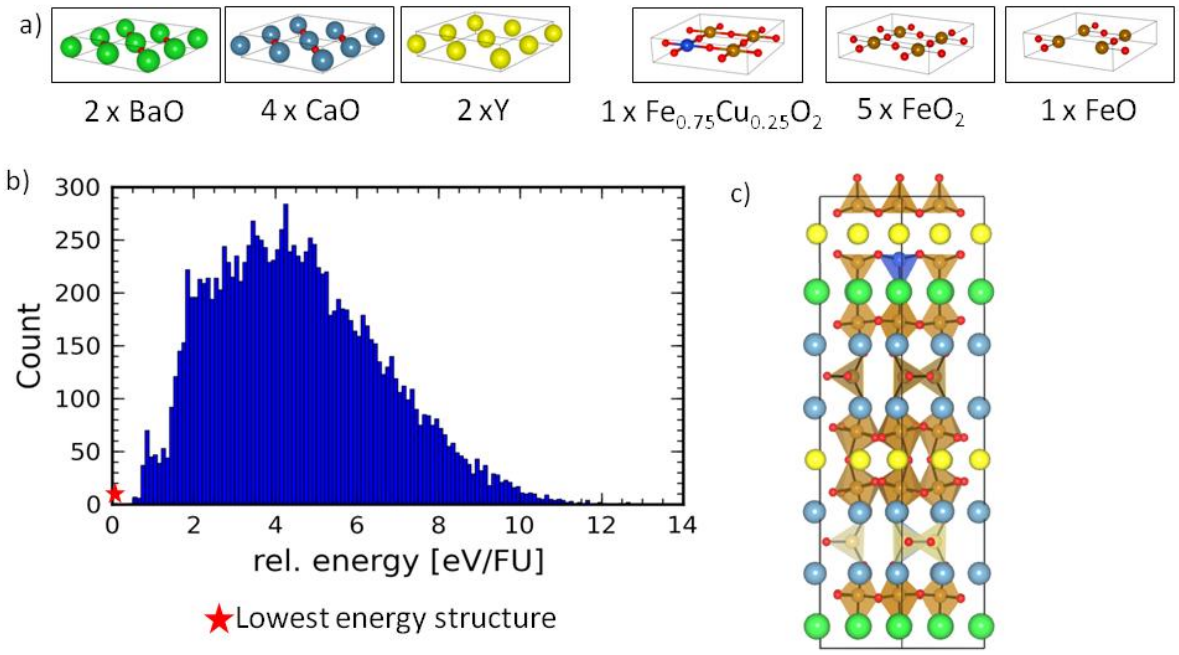

Figure 62 a) The module set used in the $Y_2Ba_2Ca_4Fe_{7.5}Cu_{0.5}O_{21}$ $8a_p$ EMMA calculations. b) FF energy distribution of structures. c) The final EMMA structure after DFT relaxation.

For the Cu containing structures, one module set was used, containing $2 \times Y_4$, $2 \times Ba_4O_4$ and $4 \times Ca_4O_4$ for the A-sites and $1 \times Fe_4O_4$, $5 \times Fe_4O_8$ and $2 \times Fe_3CuO_8$ for the B-sites (Figure 62a). Note that for the modules containing Cu, different positions were used for the Cu atom in each

module in order to maximise separation between the Cu atoms in the resulting structures. The module set generated 17,640 unique structures, with all of structures relaxed using FFs, a total of ~4,000 failed to converge (energy distribution shown in Figure 62b). One structure in this set was calculated to be especially stable, with a relative energy 0.42 eV/FU more stable than the next nearest structure (Figure 62b). DFT calculations were then performed for the lowest 20 structures from the FF calculations, this number of structures was chosen, as after the lowest energy structure, the rest of the structures only had small energy differences between them. After relaxation using DFT, the lowest energy structure from the FF calculations was confirmed as the most stable structure, with a relative energy calculated to be 0.23 eV/FU more stable than the next nearest structure. The EMMA structures calculated with compositions with and without Cu presented above are very similar and contain the same polyhedral stacking sequence with only small deviations in the atomic structure, suggesting that the inclusion of Cu in the system is not the driving force toward this particular structure.

The lowest energy $8a_p$ structure (Figure 61c and Figure 62c) has a stacking of A-site layers as follows: Y, BaO, CaO, CaO, YO, CaO, CaO, BaO. The B-site polyhedral stacking is a combination of tetrahedral (T_d), octahedral (O_h) and square pyramidal (S_q), with the calculated sequence being S_q, O_h, T_d, O_h, O_h, T_d, O_h and S_q. The tetrahedral chains in the structure, unlike the $10a_p$ structure do not alternate their orientation between tetrahedral layers. The resulting polyhedral stacking in this structure is not attainable by building structures from the layers as entered into EMMA in the case of the Cu containing composition, since initially only one T_d layer is created and all Y layers contain no oxygen atoms. Upon reviewing the relaxation of the unit cell for this structure, it is observed that the oxygen sub-lattice re-arranges upon relaxation with FF methods (Figure 63). During relaxation, initially oxygen atoms from the S_q layer below

the middle Y layer move to fill this T_d layer (to make the YO layer). Once the YO layer has been created, oxygen atoms from an O_h layer (two layers below the YO layer in Figure 63) move up one layer to make the formally S_q layer into an O_h layer, leaving the formally O_h layer as a T_d layer and creating the $8a_p$ structure created by EMMA.

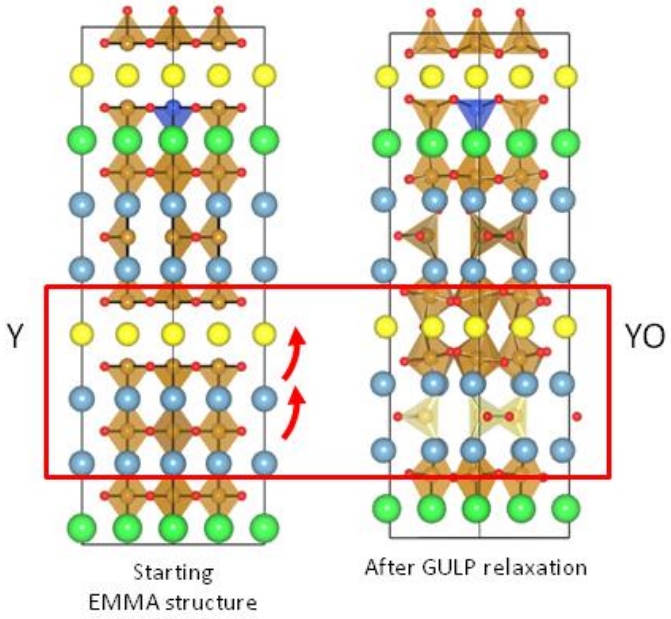

Figure 63 The lowest energy structure for $Y_2Ba_2Ca_4Fe_{7.5}Cu_{0.5}O_{21}$ before and after relaxation, showing that the oxygen positions are able to relax far away from their starting positions, indicating that the initial choice of layers does not necessarily fix the polyhedral stacking sequence in the final structures.

While the EMMA calculations were being performed, synthetic work was carried out with in the same research group by D. Hodgeman, P. Chater and A. Demont. The focus of this experimental work was aimed toward synthesising the $8a_p$ material with higher phase purity toward the unknown phase, based upon searching phase space around the EDX composition. The material was investigated using PXRD and electron microscopy. A phase pure sample was synthesised with the nominal composition of $Y_{2.24}Ba_{2.28}Ca_{3.48}Fe_{7.44}Cu_{0.56}O_{21}$ with an EDX cation

composition of $Y_{2.07(15)}Ba_{2.49(20)}Ca_{3.44(5)}Fe_{7.63(18)}Cu_{0.37(7)}$. It was also possible to form a Cu free version of the material in a polyphasic sample with the nominal composition $Y_{1.95}Ba_{2.1}Ca_{3.95}Fe_8O_{21}$. Other group members also performed selected area electron diffraction (SAED) on the sample and found that the sample had a $16a_p$ repeat. The $16a_p$ unit cell is caused by the body centring superposition of $8a_p$ blocks (here after referred to as $16a_p$, Figure 64).

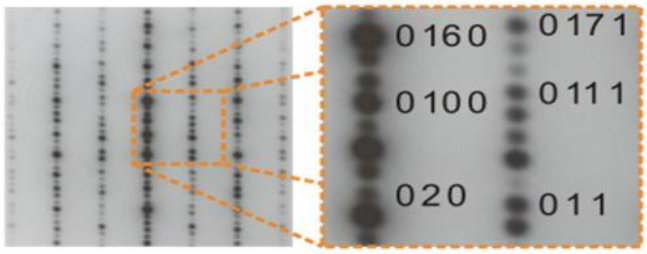

Figure 64 Electron diffraction provided and indexed by other group members on higher purity samples of the $8a_p$ material indicates that the unit cell actually has a $16a_p$ stacking length, containing body centering.

This investigation has also been able to show that the material contains an inversion centre and a r45°($\sqrt{2} \times a_p$) expansion of the perovskite cell parallel to the stacking axis. In summary the new experimental information obtained by other members of the research group is as follows; compositions were found to be nominally $Y_{2.24}Ba_{2.28}Ca_{3.48}Fe_{7.44}Cu_{0.56}O_{21}$ and $Y_{1.95}Ba_{2.1}Ca_{3.95}Fe_8O_{21}$ for phase pure and high purity samples respectively with a unit cell size of approximately 5.4 × 5.4 × 62 Å with the unit cell containing an inversion centre.

5.6 Using EMMA to identify the 16a_p structure

In order to help with the identification of the 16a_p structure, a modified version of the EMMA script was written in collaboration with M. S. Dyer to generate possible 16a_p structures. A modified version was required due to the vast number of possible permutations that could result from simply using a doubled set of modules from the 8a_p section (estimated by M. S. Dyer to be equal to ~ 10^8 before removing repeat structures) and so would be computationally un-feasible. The EMMA method was modified to include the new information made available from experimental work, namely the use of an inversion centre. As synthetic work had shown it to be possible to form the 16a_p structure without Cu, the EMMA runs for the 16a_p structure were performed without Cu in the unit cell in order to reduce the number of possible permutations. Models in this section were built such that the first 8 layers would be constructed as described previously, then the rest of the unit cell was filled by use of inversion symmetry through the centre of the unit cell.

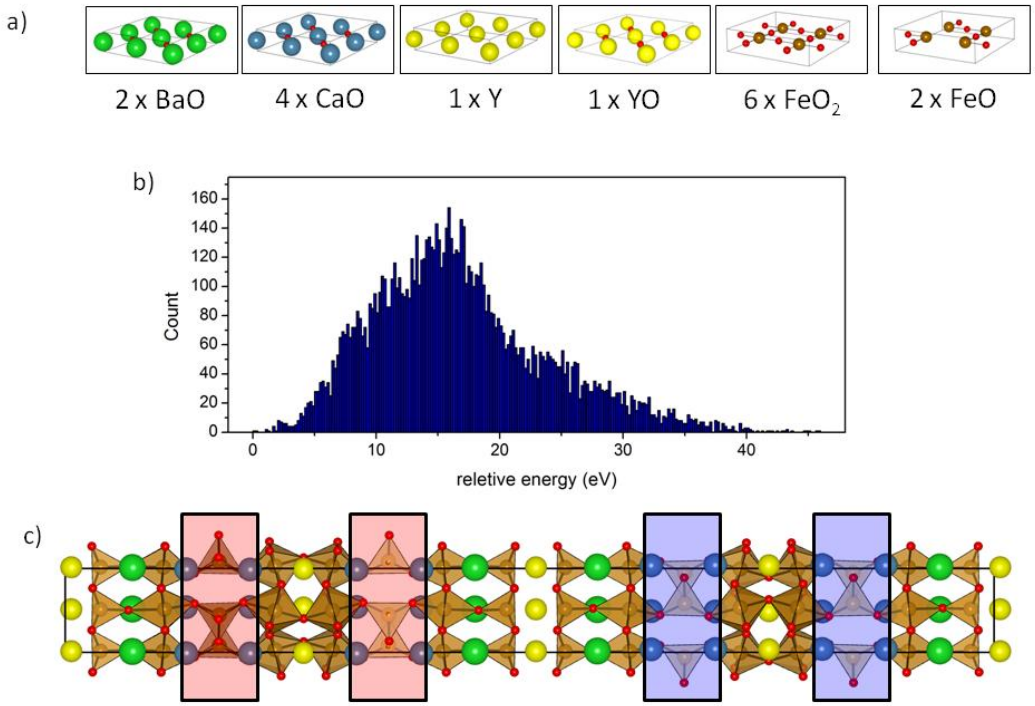

Figure 65 a) The module set used to generate the first half of the 16a_p unit cell before the rest is generated through inversion symmetry. b) The FF energy distributions of structure. c) The final EMMA structure for $Y_2Ba_2Ca_4Fe_8O_{21}$ in 16a_p cell, after DFT relaxation, with the change in tetrahedral chain directions highlighted.

In order to generate the 16a_p structures the following set of modules was chosen to fill the first half of the unit cell; for the A-sites, 2 × BaO, 4 × CaO, 1 × Y and 1 × YO. The B-sites were constructed from; 6 × FeO_2 and 2 × FeO, where the FeO layers result in tetrahedral chains and are orientated differently after the application of inversion symmetry (Figure 65a). The layers used for generating the 16a_p structure have a smaller a and b (a = b = 5.4 Å) lattice parameter than used for the 8a_p structures, to utilise the new experimental information. Using inversion symmetry to generate the 16a_p structures reduced the number of structures from the estimated 10^8 possible permutations down to 47,040. All of these structures were then relaxed using the same force field used for the 8a_p structures. Of the possible 16a_p structures only 9,864

converged (energies ranked in Figure 65b) and 16,771 failed to find an energy minima before the maximum 1000 ionic steps were completed, with the rest of the structures failing to form into a structure that GULP could report an energy for.

Of the FF structures, the lowest 5 energy structures were re-relaxed utilising DFT in order to generate accurate energy rankings. The lowest energy DFT structure was found to have the same polyhedral and A-site stacking as two of the blocks, with the direction of the tetrahedral chains alternating between each block (Figure 65c).

The final EMMA structure for the $16a_p$ with a relaxed stacking length of 61.4902 Å and contains a total of nine different cation sites. The A-site cations are divided into a 12 coordinate Ba site, Ca atoms are found in two similar 8 coordinate sites; the Y atoms occupy two different 8 coordinate sites, with the first between square pyramidal layers and the second between octahedral layers. The B-sites (all containing Fe) are divided into one 5 coordinate square pyramidal, two 6 coordinate octahedral and one 4 coordinate tetrahedral environments.

5.7 Discussion of results and comparison with experiment

The final structure from EMMA was used by P. Chater as the basis for refinement of the experimental structure, with the overall composition changed during the course of the refinement from the DFT value of $YBa_2Ca_4Fe_8O_{21}$ to $Y_{2.24}Ba_{2.28}Ca_{3.48}Fe_{7.44}Cu_{0.56}O_{21}$ to comply with that of the synthetic sample. The DFT model, with no symmetry was transformed into the *Imma* space group identified from the electron microscopy and was used as the basis for his Rietveld

refinement of the 16a_p structure using combined PXRD and neutron powder diffraction (Figure 66a).

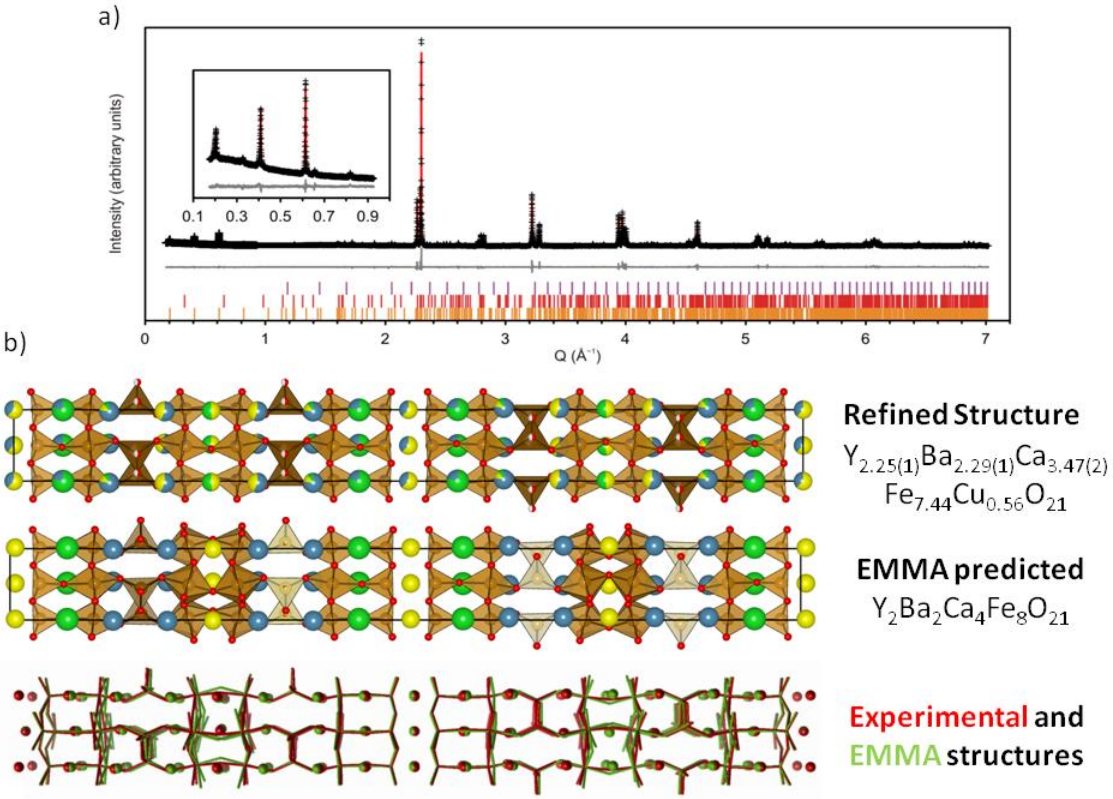

Figure 66 Rietveld refined synchrotron diffraction pattern of the 16a_p material provided by P. Chater as part of a combined XRD and NPD refinement[25]. b) Side by side comparison of the refined 16a_p structure with the EMMA predicted structure, with the A-sites shown as pie-charts in the refined structure indicating the partial refined occupancies and indicating that each A-site is occupied in majority by the atom predicted from the EMMA calculations. The overlaid structures show the close resemblance between the EMMA and refined structures, note that the unit cell parameters were normalised in order to show the comparison of fractional atomic coordinates. Colours for elements in panel b as follows; yttrium (yellow), barium (green), calcium (light blue), iron (brown), copper (dark blue) and oxygen (red)

The refined 16a_p structure bears a very close resemblance to the EMMA predicted structure, the Fe coordination sites and stacking sequence are preserved from those predicted, although some

of the oxygen positions move relative to the predicted structure (Figure 66b, refined and DFT co-ordinates shown in Table 21). The A-site stacking was retained from the predicted structure, however significant levels of A-site disorder are observed, although the majority species on each site matches that predicted by EMMA, although this disorder was expected due to the non-stoichiometry of the sample and due to entropic effects at high temperatures. Mössbauer spectra collected by M. F. Thomas agree with the refined B-site structure of the 16a_p material, confirming the 2: 1: 1 ratio of octahedral square pyramidal and tetrahedral Fe^{3+} respectively. The confirmation of the Fe geometry ratios by Mössbauer spectroscopy also confirm that the Cu atoms present in the system are disordered across the B-sites, as if the Cu atoms were ordered toward any particular geometry a significant reduction in that sites ^{57}Fe Mössbauer signal would be observed.

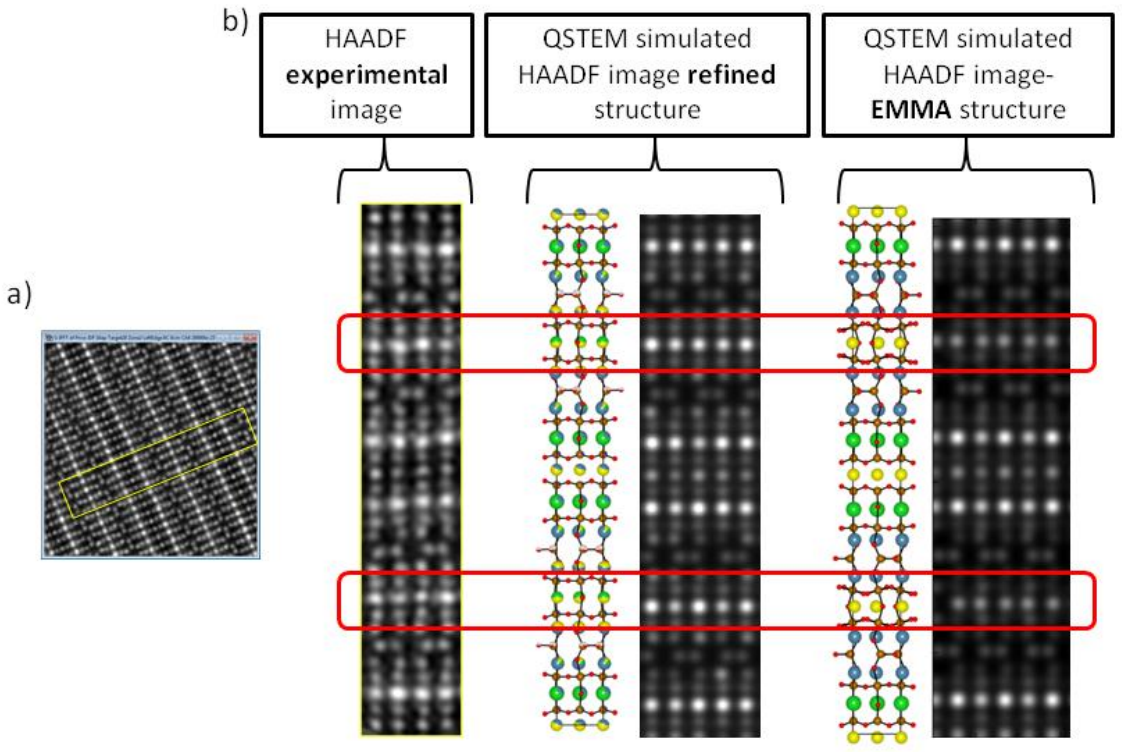

Figure 67 a) Experimental HAADF image provided by S. Romani. b) segment of the experimental image corresponding to one unit cell in the stacking direction in comparison with the refined and EMMA predicted structures, with images simulated by P. Chater, with the crystal structures provided for comparison. The red boxes highlight the layers where the largest difference is found, with the disagreement between experimental and EMMA caused by the high levels of Ba found on the Y site, resulting in increased spot intensity.

High angle annular dark field scanning transmission electron microscopy (HAADF-STEM) images were simulated by P. Chater for the EMMA predicted and refined structure for comparison against experimentally observed images (Figure 67), in order to provide a structural comparison on a shorter length scale than the long range average structure provided from powder diffraction refinements. The STEM images confirm that the refined structure and EMMA predicted structure are in good agreement, with the only notable difference being in the intensity of the spots for the formally YO layer in the EMMA predicted structure (Figure 67). The YO layer is observed to have a greater spot intensity in the simulation of the refined structure and the

experimental image due to the increase in electron density from the site disorder and the large amount of Ba included on the site.

5.7.1 Disorder matters

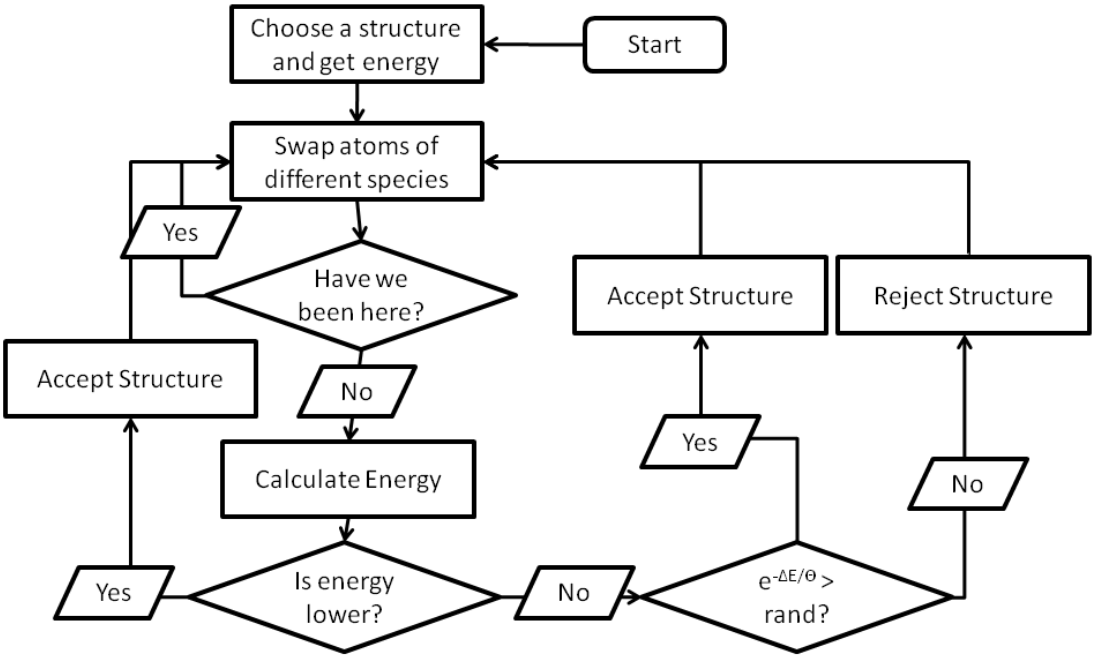

Figure 68 Finite temperature monte-carlo routine implemented in python by M. S. Dyer to allow for site mixing in 16a_p structures (see text), based upon previously implemented methods[59], the random number generated (denoted as "rand") is between 0 and 1, to allow for the probability that an atomic swap with an increase in energy can be accepted.

In order to test if A-site disorder is energetically favoured in the 16a_p structure, disorder was simulated from the 16a_p EMMA structure using finite temperature monte-carlo sampling (MC, routine outlined in Figure 68). A script for implementing this MC methodology was written in python by M. S. Dyer and relaxations performed with GULP with the aforementioned FF

parameters (Table 20). This method was based upon previously reported work for calculating expected fractional occupancies at high temperatures in a supercell[59].

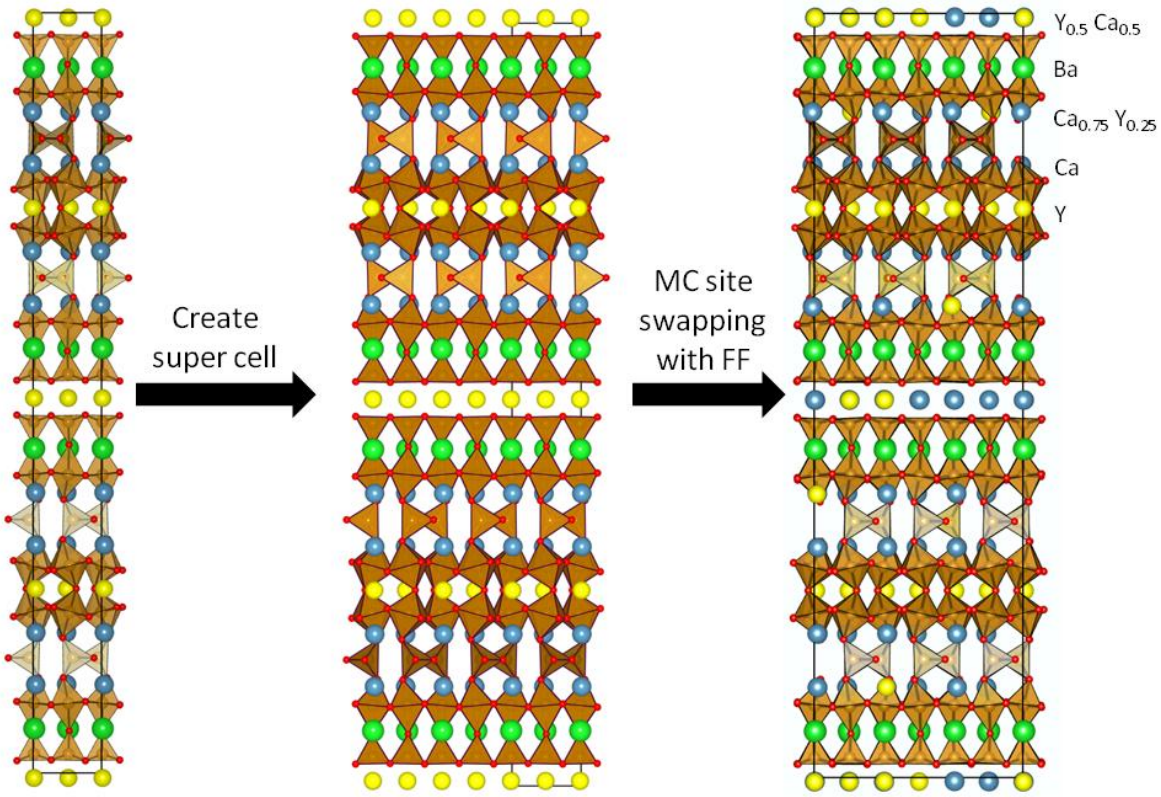

Figure 69 Results from finite temperature MC run on the $16a_p$ at the EMMA composition $Y_2Ba_2Ca_4Fe_8O_{21}$, from left to right; the EMMA structure, 3 × 3 × 1 super cell used for MC runs and the lowest energy configuration, with the layer compositions, being the average occupancy of each of the equivalent layers.

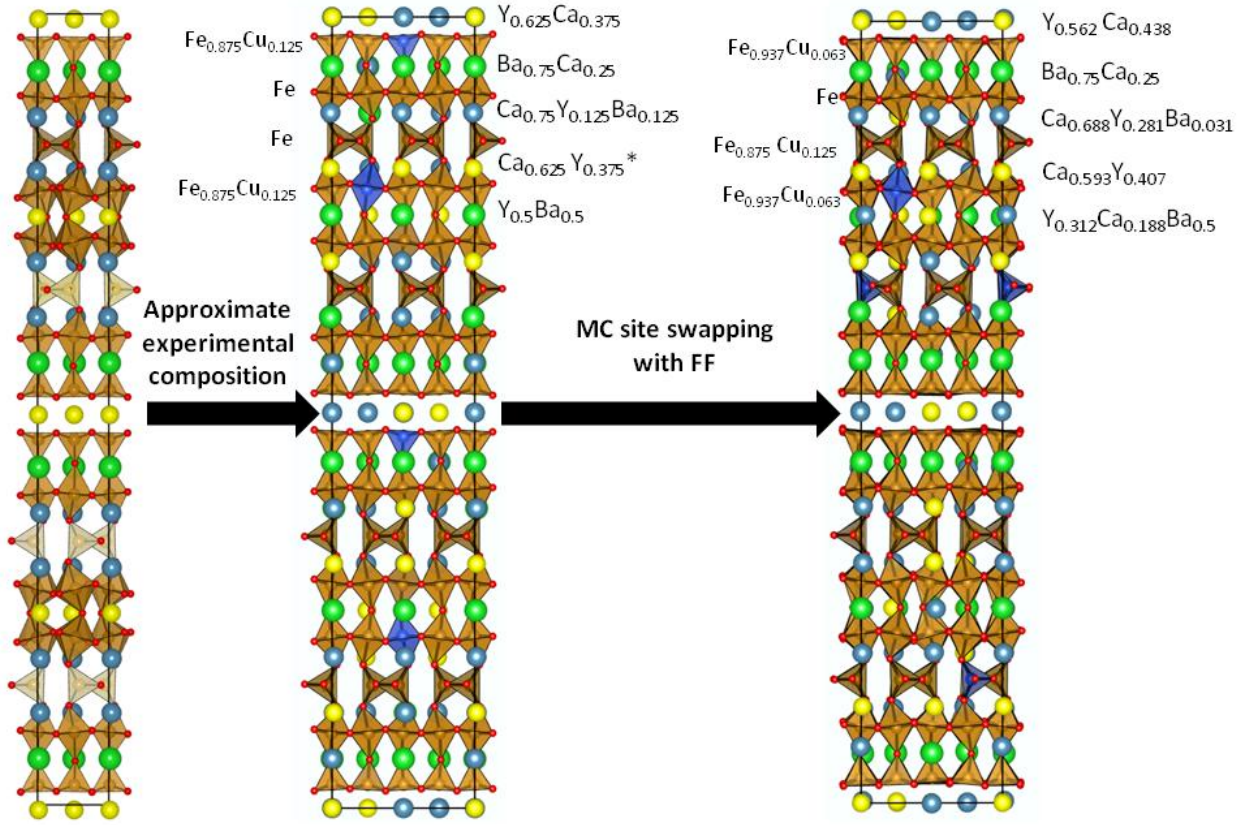

Figure 70 Results from finite temperature MC run on the $16a_p$ at the approximated composition $Y_{2.25}Ba_{2.25}Ca_{3.5}Fe_{7.5}Cu_{0.5}O_{21}$, from left to right; the EMMA structure, 2 × 2 × 1 super cell used for MC runs with the initial cation distribution based upon the refined structure (shown in **Table 21**) and the lowest energy configuration, with the layer compositions, being the average occupancy of each of the equivalent layers.

The MC script was run on two compositions, the stoichiometric $Y_2Ba_2Ca_4Fe_8O_{21}$ (referred to as the EMMA composition) and an approximation of the experimental nominal composition, $Y_{2.25}Ba_{2.25}Ca_{3.5}Fe_{7.5}Cu_{0.5}O_{21}$ (referred to as the approximated composition). For both compositions the atomic co-ordinates for the EMMA structure were used for the initial structures. For the EMMA composition, a 3 × 3 × 1 supercell used to allow for better statistical averaging of the sites. A-site occupancies for the approximated composition were set in order to give a cation distribution as close to the experimentally refined structure as possible (shown in

Figure 70) and required the use of a 2 × 2 × 1 supercell relative to the EMMA structure. For both MC runs were continued until ~ 100 configurations had been rejected consecutively, for the EMMA composition this amounted to a total of 800 swaps, for the approximated composition a total of 500 swaps were calculated, with an additional 75 steps allowed for Cu swapping with Fe, in order to determine if any significant B-site ordering would be expected.

For both compositions the temperature parameter was set equal to 1160 K, for the EMMA composition, all of the A-site species (Y, Ba and Ca) were allowed to swap sites with each other. For the approximated composition, all of the A-sites (Y, Ba and Ca) were allowed to swap and separately all of the B-sites (Fe and Cu), as to ensure that no A-site species could end up on a B-site or vice-versa. Each swap step consisted of one atom swapping for one other of a different species, but of the same type (e.g. A-site species were only permitted to swap with other A-site species).

For the EMMA composition the MC run shows that the most likely A-site disorder is between Y and one of the two types of CaO layer (Figure 69), note that the A-sites only swap between one of the two 8-coordinate Ca sites, no swapping was observed to occur in the YO layer and Ba atoms did not swap with any of the other A-sites, this disordered model was calculated to be 0.29 eV/FU lower in energy than the EMMA structure.

For the approximated composition it was observed that swapping occurred to move the site occupancies away from the starting configuration (which was an approximation of the experimentally refined structure). The main source of swapping in the approximated composition is Y for Ca in the 12 coordinate YO layer in the centre of the structure (Figure 70), although the layer retains the Ba from the starting configuration. The Cu atoms within the

material remain largely disordered throughout the structure. The site disorder calculated was found to be 1.22 eV/FU lower in energy than the approximated composition presented in Figure **70**.

The MC results from the approximated composition are in good agreement with experimental results, this is despite the Ca swapping into the YO layer in the middle of the structure, as during the refinement no Ca was allowed to refine on the A-site corresponding to this layer, as due to the complexity of the structure it would be difficult to refine the difference between the site when occupied by Y + Ba and with the site being occupied by Y + Ba + Ca (a comparison between site occupancies is shown in Table 22). In order to check the validity at this point, an additional refinement of the experimental data was performed by P. Chater using the site occupancies resulting from the MC run and was found to have little effect on the resulting fit, confirming that with the refinement process differentiation between the 12 coordinate site in question being occupied by Y + Ba and Y + Ca + Ba is unlikely.

These results indicate that cation dis-order in the $16a_p$ structure is in part at least driven by a reduction in enthalpy, rather than just by entropy as previously assumed. The additional Ba in the experimental composition, above that of the EMMA composition, causes the Y and Ba disorder in the YO layer, as no swapping between Y and Ba is observed at the stoichiometric composition. The observation that no Ba swaps with Y in the EMMA composition were calculated to be favourable but were favoured in the approximated composition suggest that while disorder between Y and Ca is generally favourable, Ba disorder is only favourable when Ba non-stoichiometry is present in the system; this agrees with previous calculations on the $10a_p$ $YBa_2Ca_2Fe_5O_{13}$ where differing calculations were performed for different A-site dis-order

conformations at the stoichiometric composition and only Y and Ca disorder was favoured, despite some Ba non-stoichiometry being observed in the experimental structure[15].

5.8 Discussion

The previously unreported 16a_p structure shown in this chapter can be compared with other layered perovskite materials such as the $YBa_2Ca_2Fe_5O_{13}$ and $YCa_4Fe_5O_{13}$ materials[15, 171]. Each of the previously reported materials adopt a perovskite structure with a large stacking length (both consisting of 10 perovskite layers) and can be thought of in terms of smaller building blocks of other smaller, known materials. In the case of the $YBa_2Ca_2Fe_5O_{13}$ structure, each of the two 5 perovskite layer blocks that make up the full unit cell can be thought of as made up of a brownmillerite $Ca_2Fe_2O_5$ block and one block of the triple perovskite $YBa_2Fe_3O_8$ (Figure 71c). The $YCa_4Fe_5O_{13}$ structure can be thought as made up of two blocks of $LaCa_2Fe_3O_8$ type blocks and two blocks of $Ca_2Fe_2O_5$ Brownmillerite blocks (Figure 71b).

As with each of the 10 layer structures, the 16a_p structure can be constructed from smaller perovskite superstructures, being constructed from two each of $YBa_2Fe_3O_8$, $LaCa_2Fe_3O_8$ type (although with La swapped for Y) and $Ca_2Fe_2O_5$ (Figure 71d). The 16a_p stacking sequence can be reproduced from the $YCa_4Fe_5O_{13}$ structure by the addition of one unit of the $YBa_2Fe_3O_8$ triple perovskite per formula unit. The 16a_p stacking sequence can also be reproduced from the $YCa_2Ba_2Fe_5O_{13}$ 10 layer perovskite by addition of $YCa_2Fe_3O_8$ in the same triple perovskite structure as reported for $LaCa_2Fe_3O_8$[172] per formula unit, although this $YCa_2Fe_3O_8$ perovskite in the $LaSr_2Fe_3O_8$ structure is currently un-reported experimentally.

The analysis of the 16a_p structure being comprised of component modules further underlines the applicability of the EMMA philosophy to layered oxide systems and therefore many other system types that can be thought of in such a manner. Building upon this, opens up the validity of utilising the method using larger starting modules, possibly beginning from perovskite superstructures as previously mentioned in the on-going search for large layered oxides. The possibility of utilising much larger starting modules than used when identifying the 16a_p structure leads to a computationally feasible way to apply the EMMA method to larger and more complex structures than those dealt within this chapter.

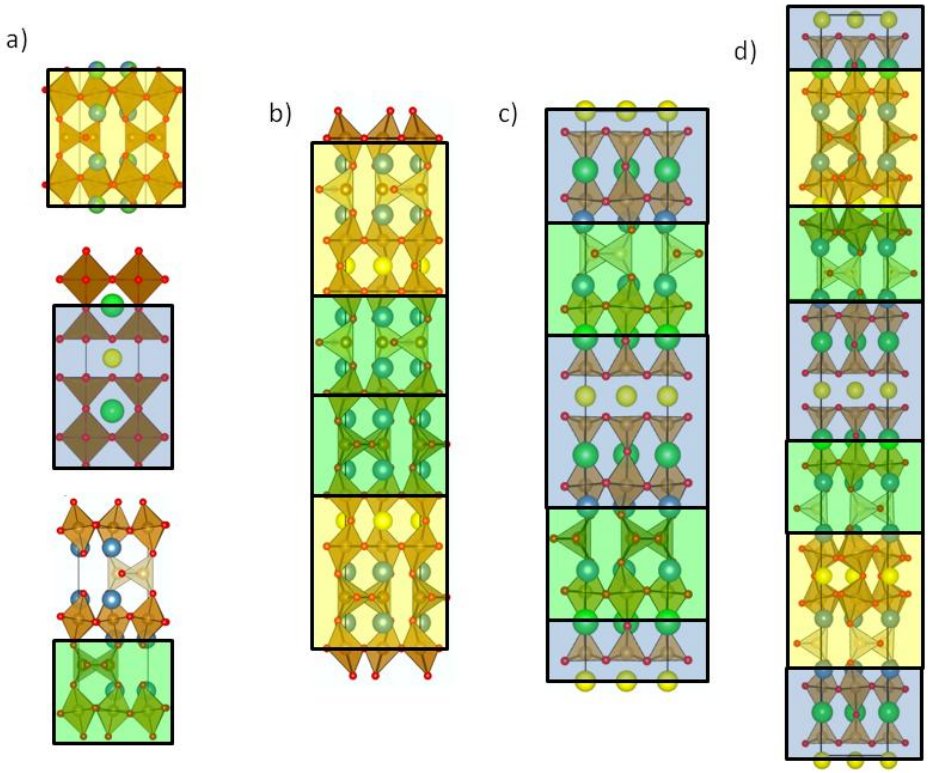

Figure 71 a) Perovskite superstructures that could be used to generate the larger superstructures in panels b, c and d, top to bottom is the $LaCa_2Fe_3O_8$, $YBa_2Fe_3O_8$ and $Ca_2Fe_2O_5$ type perovskite units, with the building block type unit highlights. b) $YCa_4Fe_5O_{13}$ perovskite structure, with the coloured boxes indicating that the structure could be generated from 2 × $LaCa_2Fe_3O_8$ and 2 × $Ca_2Fe_2O_5$ type blocks. c) $YBa_2Ca_2Fe_5O_{13}$ perovskite, showing how it could be generated from 2 × $YBa_2Fe_3O_8$ and 2 × $Ca_2Fe_2O_5$ type blocks. d) The 16a_p structure discussed in this chapter showing that the structure could be assembled from 2 × $LaCa_2Fe_3O_8$, 2 × $YBa_2Fe_3O_8$ and 2 × $Ca_2Fe_2O_5$ type units.

5.9 Conclusions

In summary, the work presented in this chapter has resulted in a new method for the construction of layered structures from chemically sensible starting modules and then combined with other theoretical techniques in order to correctly predict the crystal structure of a new inorganic compound. The EMMA method has been validated through utilising it to calculate the reported structure for the $YBa_2Ca_2Fe_5O_{13}$ $10a_p$ perovskite. The developed method was then used in the isolation and structural characterisation of the previously un-reported $Y_{2.24}Ba_{2.28}Ca_{3.48}Fe_{7.44}Cu_{0.56}O_{21}$ $16a_p$ structure and additionally it has been possible to use FF calculations to rationalise the observed cation disorder within the system, i.e. that mixing between Y and Ca is generally favourable, whereas the mixing between Ba and other species occurs as a result of the excess Ba when compared to the stoichiometric composition. The method presented in this chapter has been shown to be a powerful tool in the search for new functional materials. Resulting from this work, the research group is continuing to work towards expanding the types of system that the published EMMA code[25] is applicable to and aim to use EMMA as part of on-going research into structural prediction for complex functional materials.

5.10 Tables

Table 20 Buckingham potential parameters used for all FF calculations within this chapter.

Interaction	**A (eV)**	ρ_{ij} **(Å)**	C_{ij} **(eVÅ^{-6})**	**Reference**
$O^{2-}_{Shell} - O^{2-}_{Shell}$	22764.300	0.14900	42.000	Adapted from[173]
$Y^{3+}_{core} - O^{2-}_{shell}$	20717.500	0.24203	0.000	As published[167]
$Ba^{2+}_{Shell} - O^{2-}_{Shell}$	4818.000	0.30670	0.000	As published[174]
$Fe^{3+*}_{core} - O^{2-}_{Shell}$	1244.500	0.32990	0.000	Adapted from[175]
$Ca^{2+}_{Shell} - O^{2-}_{Shell}$	2272.741	0.29860	0.000	As published[174]
$Cu^{2+}_{core} - O^{2-}_{Shell}$	6276.000	0.22074	0.000	As published[167]

***** For calculations containing Cu, the Fe charge state was increased slightly in order to maintain charge neutrality. Shells were attached to Ba, Ca and O atoms with assigned spring constants equal to 34.05, 34.05 and 42 eVÅ^{-2} respectively and the shells charges set to 1.831, 1.281 and -2.24, with core charge states set in order to give the overall desired charge, these parameters are in line with those used in the relevant literature outlined above.

Table 21 Refined and EMMA predicted structure pameters for the $16a_p$ structure, refinement performed and results provided by P.Chater and EMMA structural parameters provided by M. Dyer.

	Parameter	**Rietveld**	**EMMA**
	a (Å)	5.484964(25)	5.56182
	b (Å)	61.25901(32)	61.5524
	c (Å)	5.550477(25)	5.57481
Site	**Parameter**	**Rietveld**	**EMMA**
A1	Position, 4a	0,0,0	0,0,0
	Occupancy	$Y_{0.627(4)}Ca_{0.373(4)}$	Y
A2	Position, 8h	0,0.062392(28),0.9977(7)	0,0.06555,0.99690
	Occupancy	$Ba_{0.787(2)}Ca_{0.213(2)}$	Ba
A3	Position, 8h	0,0.12077(5),0.9756(8)	0,0.12337,0.97632
	Occupancy	$Ca_{0.768(9)}Y_{0.132(7)}Ba_{0.100(5)}$	Ca
A4	Position, 8h	0,0.19120(5),0.9770(7)	0,0.19270,0.97272
	Occupancy	$Ca_{0.566(1)}Y_{0.434(1)}$	Ca
A5	Position, 4e	0,0.25,0.9868(9)	0,0.25,0.97795
	Occupancy	$Y_{0.488(2)}Ba_{0.512(2)}$	Y
B1	Position, 8h	0,0.030041(31),0.5008(6)	0,0.03128,0.49803
	Occupancy	$Fe_{0.86}Cu_{0.14}$	Fe
B2	Position, 8h	0,0.09470(4),0.4891(8)	0,0.09962,0.49929
	Occupancy	Fe	Fe
B3	Position, 16j	0.9450(4),0.15521(5),0.43229(32)	0.94244,0.15895,0.43195
	Occupancy	Fe	Fe
B4	Position, 8h	0,0.217745(29),0.4867(6)	0,0.21917,0.48128
	Occupancy	$Fe_{0.86}Cu_{0.14}$	Fe
O1	Position, 8g	0.25,0.02180(8),0.25	0.25,0.02234,0.25
O2	Position, 8g	0.75,0.02445(7),0.75	0.75,0.02324,0.75
O3	Position, 8h	0.5,0.06107(8),0.034(4)	0.5,0.06157,0.01199
O4	Position, 8g	0.75,0.09480(7),0.75	0.75,0.09665,0.75
O5	Position, 8h/16j	0.5,0.12861(7),0.9347(9)	0.52821,0.13255,0.93059
O6	Position, 4e/8i	0.5,0.25,0.0500(14)	0.53640,0.25,0.11429
O7	Position, 8g/16j	0.25,0.28288(8),0.75	0.29486,0.22583,0.70720
O8	Position, 8g/16j	0.25,0.28929(9),0.25	0.20219,0.21332,0.19796
O9	Position, 8h/16j	0.5,0.31872(5),0.9354(8)	0.53161,0.31444,0.92061
O10	Position, 16j	0.9024(7),0.34338(11),0.1161(7)	0.90360,0.34174,0.12207
O11	Position, 8g	0.75,0.40037(8),0.25	0.75,0.39896,0.25

Space group *Imma*. Refined composition $Y_{2.25(1)}Ba_{2.29(1)}Ca_{3.47(2)}Fe_{7.44}Cu_{0.56}O_{21}$.

Table 22 Metal site occupancies, from refined and calculated data.

Site	Refined occupancy	EMMA $Y_2Ba_2Ca_4Fe_8O_{21}$	MC $Y_2Ba_2Ca_4Fe_8O_{21}$	MC $Y_{2.25}Ba_{2.25}Ca_{3.5}Fe_{7.5}Cu_{0.5}O_{21}$
A1	$Y_{0.627(4)}Ca_{0.373(4)}$	Y	$Y_{0.5}Ca_{0.5}$	$Y_{0.562}Ca_{0.488}$
A2	$Ba_{0.787(2)}Ca_{0.213(2)}$	Ba	Ba	$Ba_{0.75}Ca_{0.25}$
A3	$Ca_{0.768(9)}Y_{0.132(7)}Ba_{0.100(5)}$	Ca	$Ca_{0.75}Y_{0.25}$	$Ca_{0.688}Y_{0.281}Ba_{0.063}$
A4	$Ca_{0.566(1)}Y_{0.434(1)}$	Ca	$Ca_{0.75}$	$Ca_{0.593}Y_{0.407}$
A5	$Y_{0.488(2)}Ba_{0.512(2)}$	Y	Y	$Y_{0.312}Ca_{0.168}Ba_{0.5}$
B1	$Fe_{0.86}Cu_{0.14}$	Fe	Fe	$Fe_{0.937}Cu_{0.063}$
B2	Fe	Fe	Fe	Fe
B3	Fe	Fe	Fe	$Fe_{0.875}Cu_{0.125}$
B4	$Fe_{0.86}Cu_{0.14}$	Fe	Fe	$Fe_{0.937}Cu_{0.063}$

Chapter 6. Conclusions

During the course of this thesis there has been a large amount of work invested in continuing the development of the integration of theoretical and synthetic investigations as a powerful philosophy, culminating in the successful discovery and isolation of the functional $Y_{2.24}Ba_{2.28}Ca_{3.48}Fe_{7.44}Cu_{0.56}O_{21}$ material; all of which are summarised in this final chapter.

In the first results chapter (Chapter 3); the computational and synthetic investigation of chemical substitution $YBa_2Fe_3O_8$ has successfully utilised the ability of well tuned DFT calculations to calculate reasonably accurate reaction enthalpies to predict a new compound in the $YBa_2Fe_{3-x}M_xO_8$ (M = Co, Mn and Ni) system. By examining the computed structures in this chapter, it has additionally been possible to provide some insight as to why doping may be favoured with Co and Mn, but not Ni. Experimental investigations subsequently were performed confirming that the new composition predicted was able to form into a $3a_p$ perovskite, albeit with some minor alteration to the A-site stoichiometry. Additionally synthetic investigations have shown that where the calculations predict doping to be unfavourable a $3a_p$ perovskite is not shown to form in any of the samples tested. Characterisation of the material by x-ray and neutron powder diffraction complimented by Mössbauer spectroscopy and iodometric titrations confirm that the crystal structure of the new material is in good agreement with that predicted.

The success with the $3a_p$ system in Chapter 3 lead to the more ambitious investigation of the functional $YBa_2Ca_2Fe_5O_{13}$ $10a_p$ material, studied in chapter 4. Chapter 4 continued to use the same methodology used in Chapter 3 in order predict substitution across the $YBa_2Ca_2Fe_{5-x}M_xO_{13}$ with x = 0.25 – 1.25 and M = Co, Cu, Mn, Ni, Zn and x = 0.25 – 1.00 with M = Ti. As well as providing insight as to which metals could be substituted into the system, the DFT calculations

were able to provide chemical reasoning as to why doping is favoured within the constraints of a system with a fixed oxygen content and therefore average cation charge states imposed by the DFT calculations. Doping was predicted to be favourable for M = Co and Cu, with Mn yielding a more mixed result, since the predicted reaction energy did not change significantly across the compositional range. When M = Ni and Zn, small levels of doping were predicted to be favoured and with Ti no doping was predicted to be favourable.

Examining the results across the whole of the series calculated, a trend became apparent; dopant species were favourable in line with the size of the polyhedra into which they were doped (after the structure was relaxed), the dopants that were found to have the polyhedral volumes similar to the undoped Fe sites were found to be the most favoured and in the case of Ti, where there was a large volume mismatch, doping was not at all favourable. Doping with Mn was the slight exception to the rule; as with Co and Cu, little overall change to the polyhedral volume were observed, however the shape of the favoured octahedral sites changed significantly, altering all of the other surrounding environments, with the suggestion that the two effects effectively out, resulting in substation having little impact on the reaction enthalpies.

The predictions from Chapter 4, lead into synthetic work performed by D. Hodgeman, with (at the time of writing), promising results for doping with Co and Cu, combined with some level of success with Mn. These investigations with M = Cu gave rise to the start of the investigation into the material at the centre of Chapter 5.

Initial experimental investigations showed that the new material had an approximate composition of $Y_2Ba_2Ca_4Fe_{7.5}Cu_{0.5}O_{21}$ ($8a_p$) with unit cell dimensions of 5.4 × 5.4 × 31 Å. The calculations presented in Chapter 5, outlined the development of a new method of computing the most likely

structure of a material given only unit cell dimensions and gave rise to the EMMA method. The method was initially validated by correctly calculating the minimum energy structure of $YBa_2Ca_2Fe_5O_{13}$ ($10a_p$), then following on to predict a structure for the $8a_p$. Subsequent experimental investigations showed the composition to have a $16a_p$ repeat, (~61 Å), with the EMMA process repeated for the new stacking length and found the same $8a_p$ structure repeated through an inversion centre. This predicted structure was then used as the basement for diffraction refinements and found to be in good agreement proving the EMMA method for an unknown material.

In summary the investigations presented in this thesis have shown that the integration of theory and synthetic investigations has proven to be a powerful philosophy for the discovery of new and functional materials. In chapter 3, the concept of integrated investigations was proven in the prediction and subsequent synthesis of $YBa_2Fe_2MnO_8$ in the $YBa_2Fe_{3-x}M_xO_8$ system and importantly been able to predict where synthesis would not be successful. Once proved, the same approach was applied successfully to the larger and more complex SOFC cathode $YBa_2Ca_2Fe_{5-x}M_xO_{13}$ system leading to the prediction of three successful dopants and outlining three others where doping would be unsuccessful. Finally in chapter 5 the approaches lead to the successful structural prediction of a large layered oxide using a new computational approach.

The work presented within this thesis has contributed to the following publications and conference presentations:

Papers:

- "Computationally-assisted Identification of Functional Inorganic Materials", published in Science May 2013: doi:10.1126/science.1226558
- "Computational prediction and experimental confirmation of B-site doping in $YBa_2Fe_3O_8$", submitted to chemical science.

Conference oral presentations:

- CCP5 (2012) – talk: "Extended Module Materials Assembly (EMMA)"
- MCC (2012) – talk: "Utilizing theory in the search for new layered oxides"

Conference poster presentations:

- RSC solid state Christmas meeting (2011) - poster: "DFT predicted synthesis of a new triple perovskite in the $YBa_2Fe_{3-x}Mn_xO_8$ system"
- CCP5 (2011) – poster: "DFT predicted doping of $YBa_2Ca_2Fe_5O_{13}$ 20 layer perovskite"
- ISACS12(2013) - poster: "Computationally-assisted Identification of Functional Inorganic Materials"

References

1. J. Brous, I. Fankuchen and E. Banks, *Acta Crystallogr*, 1953, **6**, 67-70.
2. R. H. Buttner and E. N. Maslen, *Acta Crystallographica Section C-Crystal Structure Communications*, 1988, **44**, 1707-1709.
3. S. Sasaki, C. T. Prewitt, J. D. Bass and W. A. Schulze, *Acta Crystallographica Section C*, 1987, **43**, 1668-1674.
4. T. Ishihara, *Perovskite oxide for solid oxide fuel cells [electronic book] / edited by T. Ishihara*, Dordrecht ; Springer, c2009., 2009.
5. S. Geller and E. A. Wood, *Acta Crystallogr.*, 1956, **9**, 563-568.
6. W. Marti, P. Fischer, F. Altorfer, H. J. Scheel and M. Tadin, *Journal of Physics: Condensed Matter*, 1994, **6**, 127-135.
7. W. C. Koehler and E. O. Wollan, *Phys. Chem. Solids*, 1957, **2**, 100-106.
8. W. Dmowski, M. K. Akbas, P. K. Davies and T. Egami, *Journal of Physics and Chemistry of Solids*, 2000, **61**, 229-237.
9. J. Berggren, *Acta Chemica Scandinavica*, 1971, **25**, 3616-&.
10. A. L. Shaula, Y. V. Pivak, J. C. Waerenborgh, P. Gaczyñski, A. A. Yaremchenko and V. V. Kharton, *Solid State Ionics*, 2006, **177**, 2923-2930.
11. A. A. Colville and S. Geller, *Acta Crystallographica Section B*, 1971, **27**, 2311-2315.
12. Q. Huang, P. Karen, V. L. Karen, A. Kjekshus, J. W. Lynn, A. D. Mighell, N. Rosov and A. Santoro, *Physical Review B*, 1992, **45**, 9611-9619.
13. P. Karen, E. Suard and F. Fauth, *Inorganic Chemistry*, 2005, **44**, 8170-8172.
14. G. Calestani and C. Rizzoli, *Nature*, 1987, **328**, 606-607.
15. A. Demont, M. S. Dyer, R. Sayers, M. F. Thomas, M. Tsiamtsouri, H. N. Niu, G. R. Darling, A. Daoud-Aladine, J. B. Claridge and M. J. Rosseinsky, *Chemistry of Materials*, 2010, **22**, 6598-6615.
16. C. Tenailleau, M. Allix, J. B. Claridge, M. Hervieu, M. F. Thomas, J. P. Hirst and M. J. Rosseinsky, *Journal of the American Chemical Society*, 2008, **130**, 7570-7583.
17. Y. L. Lee, J. Kleis, J. Rossmeisl and D. Morgan, *Physical Review B - Condensed Matter and Materials Physics*, 2009, **80**.
18. K. Burke, http://www.chem.uci.edu/~kieron/dftold2/materials/bookABCDFT/gamma/g1.pdf, Editon edn., 2007.
19. M. Getzlaff, Springer Berlin Heidelberg, Editon edn., 2008.
20. W. L. Roth, *Physical Review*, 1958, **110**, 1333-1341.

21. Halliday D, Resnick R and W. J, *Fundamentals of Physics*, 7th edn., Wiley international, 2005.
22. F. Ramezanipour, B. Cowie, S. Derakhshan, J. E. Greedan and L. M. D. Cranswick, *Journal of Solid State Chemistry*, 2009, **182**, 153-159.
23. A. Munoz, J. A. Alonso, M. J. Martinez-Lope and J. L. Martinez, *Chemistry of Materials*, 2004, **16**, 4087-4094.
24. K. Kosuge, *Chemistry of non-stoichiometric compounds*, Oxford University Press, 1994.
25. M. S. Dyer, C. Collins, D. Hodgeman, P. A. Chater, A. Demont, S. Romani, R. Sayers, M. F. Thomas, J. B. Claridge, G. R. Darling and M. J. Rosseinsky, *Science*, 2013, **340**, 847-852.
26. A. K. Bhattacharya, A. Hartridge, K. K. Mallick, C. K. Majumdar, D. Das and S. N. Chintalapudi, *J. Mater. Sci.*, 1997, **32**, 557-560.
27. Q. Z. Huang, V. L. Karen, A. Santoro, A. Kjekshus, J. Lindén, T. Pietari and P. Karen, *Journal of Solid State Chemistry*, 2003, **172**, 73-80.
28. E. A. Kiselev, N. V. Proskurnina, V. I. Voronin and V. A. Cherepanov, *Inorg. Mater.*, 2007, **43**, 167-175.
29. D. Rodic, V. Spasojevic, V. Kusigerski, R. Tellgren and H. Rundlof, *Physica Status Solidi B-Basic Research*, 2000, **218**, 527-536.
30. I. Felner and J. Gersten, *Czech. J. Phys.*, 1996, **46**, 1421-1422.
31. A. Aguadero, L. Fawcett, S. Taub, R. Woolley, K. T. Wu, N. Xu, J. A. Kilner and S. J. Skinner, *J. Mater. Sci.*, 2012, **47**, 3925-3948.
32. T. Minami, *Semiconductor Science and Technology*, 2005, **20**, S35-S44.
33. J. P. Attfield, *Journal of Materials Chemistry*, 2011, **21**, 4756-4764.
34. P. K. Nayak, J. Yang, J. Kim, S. Chung, J. Jeong, C. Lee and Y. Hong, *Journal of Physics D-Applied Physics*, 2009, **42**.
35. H. Agura, A. Suzuki, T. Matsushita, T. Aoki and M. Okuda, *Thin Solid Films*, 2003, **445**, 263-267.
36. R. E. Treharne, K. Hutchings, D. A. Lamb, S. J. C. Irvine, D. Lane and K. Durose, *Journal of Physics D-Applied Physics*, 2012, **45**.
37. A. C. McLaughlin, V. Janowitz, J. A. McAllister and J. P. Attfield, *Chemical Communications*, 2000, 1331-1332.
38. M. Liu, M. E. Lynch, K. Blinn, F. M. Alamgir and Y. Choi, *Materials Today*, 2011, **14**, 534-546.
39. J.-I. Jung, S. T. Misture and D. D. Edwards, *Solid State Ionics*, 2010, **181**, 1287-1293.
40. J. Pena-Martinez, D. Marrero-Lopez, J. C. Ruiz-Morales, P. Nunez, C. Sanchez-Bautista, A. J. Dos Santos-Garcia and J. Canales-Vazquez, *International Journal of Hydrogen Energy*, 2009, **34**, 9486-9495.
41. Z. P. Shao and S. M. Haile, *Nature*, 2004, **431**, 170-173.

42. A. Yan, M. Yang, Z. Hou, Y. Dong and M. Cheng, *Journal of Power Sources*, 2008, **185**, 76-84.

43. D. J. Fredeman, P. H. Tobash, M. A. Torrez, J. D. Thompson, E. D. Bauer, F. Ronning, W. W. Tipton, S. P. Rudin and R. G. Hennig, *Physical Review B*, 2011, **83**.

44. C. W. Glass, A. R. Oganov and N. Hansen, *Computer Physics Communications*, 2006, **175**, 713-720.

45. I. V. Pentin, J. C. Schon and M. Jansen, *Physical Chemistry Chemical Physics*, 2010, **12**, 8491-8499.

46. K. Doll, J. C. Schon and M. Jansen, *Physical Review B*, 2008, **78**.

47. R. Grau-Crespo, S. Hamad, C. R. A. Catlow and N. H. de Leeuw, *Journal of Physics-Condensed Matter*, 2007, **19**.

48. R. Miloua, Z. Kebbab, F. Miloua and N. Benramdane, *Physics Letters A*, 2008, **372**, 1910-1914.

49. Q. Wang, R. Grau-Crespo and N. H. de Leeuw, *Journal of Physical Chemistry B*, 2011, **115**, 13854-13861.

50. Z.-H. Liang, Y.-B. Ding, C.-M. Fan, X.-G. Hao and P.-D. Han, *Acta Physico-Chimica Sinica*, 2010, **26**, 758-762.

51. R. Miloua, F. Miloua, A. Arbaoui, Z. Kebbab and N. Benramdane, *Solid State Communications*, 2007, **144**, 5-9.

52. D. Lee, J. Choy and J. Lee, *Journal of Phase Equilibria*, 1992, **13**, 365-372.

53. C. C. Fischer, K. J. Tibbetts, D. Morgan and G. Ceder, *Nature Materials*, 2006, **5**, 641-646.

54. S. Curtarolo, D. Morgan, K. Persson, J. Rodgers and G. Ceder, *Physical Review Letters*, 2003, **91**, 1355031-1355034.

55. X. Zhang, V. Stevanovic, M. d'Avezac, S. Lany and A. Zunger, *Physical Review B*, 2012, **86**.

56. S. Kirkpatrick, C. D. Gelatt and M. P. Vecchi, *Science*, 1983, **220**, 671-680.

57. M. A. C. Wevers, J. C. Schön and M. Jansen, *Journal of Solid State Chemistry*, 1998, **136**, 233-246.

58. C. M. Freeman, J. M. Newsam, S. M. Levine and C. R. A. Catlow, *Journal of Materials Chemistry*, 1993, **3**, 531-535.

59. M. O. Zacate and R. W. Grimes, *Philos Mag A*, 2000, **80**, 797-807.

60. B. J. Morgan and G. W. Watson, *Journal of Physical Chemistry Letters*, 2011, **2**, 1657-1661.

61. S. Benny, R. Grau-Crespo and N. H. de Leeuw, *Physical Chemistry Chemical Physics*, 2009, **11**, 808-815.

62. Y. Seminovski, P. Palacios, P. Wahnon and R. Grau-Crespo, *Applied Physics Letters*, 2012, **100**.

63. D. O. Scanlon and A. Walsh, *Applied Physics Letters*, 2012, **100**.

64. Q. Wang and N. H. de Leeuw, *Mineralogical Magazine*, 2008, **72**, 525-529.

65. V. A. Blatov, S. E. Boulfelfel, G. S, R. G. Hennig, M. Jansen, L. S, L. A.O, M. R, A. R. Oganov, P. D.M, J. C. Schoen, W. W. Tipton, M. Valle, W. D. J and S. M. Woodley, *Modern Methods of Crysal Structure Prediction*, Wiley-VCH, 2011.

66. S. M. Woodley, P. D. Battle, J. D. Gale and C. R. A. Catlow, *Physical Chemistry Chemical Physics*, 1999, **1**, 2535-2542.

67. A. R. Oganov, Y. Ma, A. O. Lyakhov, M. Valle and C. Gatti, eds. R. Wentzcovitch and L. Stixrude, Editon edn., 2010, vol. 71, pp. 271-298.

68. A. R. Oganov and C. W. Glass, *Journal of Physics Condensed Matter*, 2008, **20**.

69. J. D. Gale, *Journal of the Chemical Society-Faraday Transactions*, 1997, **93**, 629-637.

70. J. D. Gale and A. L. Rohl, *Molecular Simulation*, 2003, **29**, 291-341.

71. L. Cario, H. Kabbour and A. Meerschaut, *Chemistry of Materials*, 2004, **17**, 234-236.

72. C. Mellot-Draznieks, S. Girard, G. Férey, J. C. Schön, Z. Cancarevic and M. Jansen, *Chemistry - A European Journal*, 2002, **8**, 4102-4113.

73. C. Mellot-Draznieks, J. Dutour and G. R. Ferey, *Angew. Chem.-Int. Edit.*, 2004, **43**, 6290-6296.

74. D. W. Lewis, G. Sankar, J. K. Wyles, J. M. Thomas, C. R. A. Catlow and D. J. Willock, *Angew. Chem.-Int. Edit.*, 1997, **36**, 2675-2677.

75. D. W. Lewis, D. J. Willock, C. R. A. Catlow, J. M. Thomas and G. J. Hutchings, *Nature*, 1996, **382**, 604-606.

76. D. Segal, *Journal of Materials Chemistry*, 1997, **7**, 1297-1305.

77. A. J. Moulson and J. M. Herbert, *Electroceramics: materials, properties, applications*, London: Chapman & Hall, 1990., 1990.

78. R. E. Dinnebier, S. J. L. Billinge and A. Le Bail, *Powder Diffraction [electronic book] ; Theory and Practice / Edited by R E Dinnebier, S J L Billinge; Contributions by Armel Le Bail [et al.]*, Cambridge, Royal Society of Chemistry, 2008., 2008.

79. W. Friedrich, P. Knipping and M. Laue, *Annalen Der Physik*, 1913, **41**, 971-988.

80. W. L. Bragg and J. J. Thomson, *Proceedings of the Cambridge Philosophical Society*, 1914, **17**, 43-57.

81. V. K. Pecharsky and P. Y. Zavalij, *Fundamentals of powder diffraction and structural characterization of materials [electronic book] / Vitalij K. Pecharsky and Peter Y. Zavalij*, New York : Springer, c2009.

2nd ed., 2009.

82. A. C. Larson and R. B. Von Dreele, *The GSAS technical manual*, 2004.

83. H. M. Rietveld, *Acta Crystallographica*, 1967, **22**, 151-&.

84. H. M. Rietveld, *Journal of Applied Crystallography*, 1969, **2**, 65-&.

85. A. C. Larson and R. B. Von Dreele, *General Structure Analysis System (GSAS)*, 1994.

86. B. H. Toby, *Journal of Applied Crystallography*, 2001, **34**, 210-213.

87. A. A. Coelho, *Journal of Applied Crystallography*, 2003, **36**, 86-95.

88. A. A. Coelho, 2007.

89. R. M. Ibberson, W. I. F. David and K. S. Knight, *The High Resoultion Powder Diffractometer (HRPD) at ISIS, a user guide*, 2013.

90. S.-. ISIS, *HRPD Manual*, http://www.isis.stfc.ac.uk/instruments/hrpd/documents/hrpd-documents4439.html, 2013.

91. A. A. Coelho, Packaged with Topas academic version 5, Editon edn., 2013.

92. A. Lebail, H. Duroy and J. L. Fourquet, *Materials Research Bulletin*, 1988, **23**, 447-452.

93. G. S. Pawley, *Journal of Applied Crystallography*, 1981, **14**, 357-361.

94. A. I. Vogel, J. Mendham, R. C. Denney, J. D. Barnes and M. Thomas, *Vogel's textbook of quantitative chemical analysis (by) Arthur Israel Vogel, fifth edition revised by G.H. Jeffery...(et al.)*, London: Longmans, 2000.

6th ed., 2000.

95. D. P. E. Dickson and F. J. Berry, *Mössbauer Spectroscopy [electronic book]. / Edited by Dominic P. E. Dickson, Frank J. Berry*, Cambridge : Cambridge University Press, 1987., 1987.

96. R. L. Mossbauer, *Zeitschrift Fur Physik*, 1958, **151**, 124-143.

97. R. S. Preston, J. Heberle and S. S. Hanna, *Physical Review*, 1962, **128**, 2207-&.

98. D. S. Sholl and J. A. Steckel, *Density functional theory [electronic book] a practical introduction / David S. Sholl and Jan Steckel*, Hoboken, N.J. : Wiley, c2009., 2009.

99. P. Hohenberg and W. Kohn, *Physical Review B*, 1964, **136**, B864-&.

100. W. Kohn and L. J. Sham, *Physical Review*, 1965, **140**, 1133-&.

101. W. Koch and M. C. Holthausen, *A chemist's guide to density functional theory / Wolfram Koch, Max C. Holthausen*, Weinheim ; Wiley-VCH, c2001.

2nd ed., 2001.

102. J. P. Perdew, J. A. Chevary, S. H. Vosko, K. A. Jackson, M. R. Pederson, D. J. Singh and C. Fiolhais, *Physical Review B*, 1992, **46**, 6671-6687.

103. J. P. Perdew, K. Burke and M. Ernzerhof, *Physical Review Letters*, 1996, **77**, 3865-3868.

104. K. Burke and L. O. Wagner, *International Journal of Quantum Chemistry*, 2013, **113**, 96-101.

105. G. Kresse and J. Furthmüller, *Physical Review B - Condensed Matter and Materials Physics*, 1996, **54**, 11169-11186.

106. G. Kresse and D. Joubert, *Physical Review B - Condensed Matter and Materials Physics*, 1999, **59**, 1758-1775.

107. P. E. Blochl, *Physical Review B*, 1994, **50**, 17953-17979.

108. D. Vanderbilt, *Physical Review B*, 1990, **41**, 7892-7895.

109. G. Kresse and J. Hafner, *Journal of Physics-Condensed Matter*, 1994, **6**, 8245-8257.

110. P. D. Haynes, University of Cambridge, 1998.

111. I. D. R. Moreira, F. Illas and R. L. Martin, *Physical Review B*, 2002, **65**.

112. J. H. Cheng, A. Navrotsky, X. D. Zhou and H. U. Anderson, *Journal of Materials Research*, 2005, **20**, 191-200.

113. J. D. Gale, http://projects.ivec.org/gulp/help/gulp3.4_manual.pdf, Editon edn.

114. P. P. Ewald, *Annalen Der Physik*, 1921, **64**, 253-287.

115. B. G. Dick and A. W. Overhauser, *Physical Review*, 1958, **112**, 90-103.

116. F. Ramezanipour, J. E. Greedan, L. M. D. Cranswick, V. O. Garlea, R. L. Donaberger and J. Siewenie, *Journal of the American Chemical Society*, 2012, **134**, 3215-3227.

117. F. Millange, E. Suard, V. Caignaert and B. Raveau, *Materials Research Bulletin*, 1999, **34**, 1-9.

118. J. J. Adkin and M. A. Hayward, *Journal of Solid State Chemistry*, 2006, **179**, 70-76.

119. B. Saha, J. Acharya, T. D. Sands and U. V. Waghmare, *Journal of Applied Physics*, 2010, **107**.

120. M. Regulski, R. Przeniosło, I. Sosnowska, D. Hohlwein and R. Schneider, *Journal of Alloys and Compounds*, 2004, **362**, 236-240.

121. M. Catti, G. Valerio and R. Dovesi, *Physical Review B*, 1995, **51**, 7441-7450.

122. M. Faucher and J. Pannetier, *Acta Crystallogr. Sect. B-Struct. Commun.*, 1980, **36**, 3209-3211.

123. L. G. Liu, *Journal of Applied Physics*, 1971, **42**, 3702-&.

124. W. L. Roth, *Journal of Physics and Chemistry of Solids*, 1964, **25**, 1-&.

125. A. PANalytical B. V, The Netherlands, Editon edn., 2006.

126. P. International Center for Diffraction Data, U.S.A, Editon edn., 2007.

127. J. Cui, Q. Huang and B. H. Toby, *Powder Diffraction*, 2006, **21**, 71-79.

128. E. García-Matres, J. L. Martínez, J. Rodríguez-Carvajal, J. A. Alonso, A. Salinas-Sánchez and R. Saez-Puche, *Journal of Solid State Chemistry*, 1993, **103**, 322-333.

129. D. A. Kudryavtsev, B. V. Mill, N. F. Vedernikov and I. S. Shaplygin, *Inorg. Mater.*, 1992, **28**, 943-946.

130. X. Zhang, C. Fan, Y. Wang, Y. Wang, Z. Liang and P. Han, *Computational Materials Science*, 2013, **71**, 135-145.

131. D. DuBoulay, E. N. Maslen, V. A. Streltsov and N. Ishizawa, *Acta Crystallogr. Sect. B-Struct. Commun.*, 1995, **51**, 921-929.

132. L. Miranda, K. Boulahya, A. Varela, J. M. Gonzalez-Calbet, M. Parras, M. Hernando, M. T. Fernandez-Diaz, A. Feteira and D. C. Sinclair, *Chemistry of Materials*, 2007, **19**, 3425-3432.

133. H. T. Stokes and D. M. Hatch, *Journal of Applied Crystallography*, 2005, **38**, 237-238.

134. V. F. Sears, *Neutron News*, 1992, **3**, 26-37.

135. W. H. Baur, *Acta Crystallogr. Sect. B-Struct. Commun.*, 1974, **30**, 1195-1215.

136. K. Momma and F. Izumi, *Journal of Applied Crystallography*, 2011, **44**, 1272-1276.

137. C. H. Hervoches and P. Lightfoot, *Chemistry of Materials*, 1999, **11**, 3359-3364.

138. N. Kallel, S. Ben Abdelkhalek, S. Kallel, O. Pena and M. Oumezzine, *Journal of Alloys and Compounds*, 2010, **501**, 30-36.

139. J. H. Shin, M. S. Song and J. Y. Lee, *Journal of Electroceramics*, 2006, **17**, 205-209.

140. H. Saalfeld, *Zeitschrift Fur Kristallographie*, 1964, **120**, 342-&.

141. A. Daidouh, J. L. Martinez, C. Pico and M. L. Veiga, *Journal of Solid State Chemistry*, 1999, **144**, 169-174.

142. J. Hornstra and E. Keulen, *Philips Research Reports*, 1972, **27**, 76-&.

143. J. R. Gunter and G. B. Jameson, *Acta Crystallographica Section C*, 1984, **40**, 207-210.

144. A. Mehta and P. J. Heaney, *Physical Review B*, 1994, **49**, 563-571.

145. T. G. N. Babu, J. D. Kilgour, P. R. Slater and C. Greaves, *Journal of Solid State Chemistry*, 1993, **103**, 472-480.

146. V. P. S. Awana, S. K. Malik, W. B. Yelon, M. Karppinen and H. Yamauchi, *Physica C: Superconductivity*, 2002, **378–381, Part 1**, 155-159.

147. T. Vogt, P. M. Woodward, P. Karen, B. A. Hunter, P. Henning and A. R. Moodenbaugh, *Physical Review Letters*, 2000, **84**, 2969-2972.

148. V. Caignaert, I. Mirebeau, F. Bourée, N. Nguyen, A. Ducouret, J. M. Greneche and B. Raveau, *Journal of Solid State Chemistry*, 1995, **114**, 24-35.

149. P. Lacorre, J. B. Torrance, J. Pannetier, A. I. Nazzal, P. W. Wang and T. C. Huang, *Journal of Solid State Chemistry*, 1991, **91**, 225-237.

150. M. R. Palacín, J. Bassas, J. Rodríguez-Carvajal, A. Fuertes, N. Casañ-Pastor and P. Gómez-Romero, *Materials Research Bulletin*, 1994, **29**, 973-980.

151. R. Ubic, Y. Hu and I. Abrahams, *Acta Crystallographica Section B*, 2006, **62**, 521-529.

152. J. A. Alonso, M. J. Martinez-Lope, C. de la Calle and V. Pomjakushin, *Journal of Materials Chemistry*, 2006, **16**, 1555-1560.

153. G. Y. Gao, K. L. Yaoa, Z. L. Liu, J. Zhang, X. L. Li, J. Q. Zhang and N. Liu, *Journal of Magnetism and Magnetic Materials*, 2007, **313**, 210-213.

154. L. Wang, T. Maxisch and G. Ceder, *Physical Review B*, 2006, **73**.

155. G. C. Zhou, L. Z. Sun, J. B. Wang, X. L. Zhong and Y. C. Zhou, *Physica B*, 2008, **403**, 2832-2837.

156. Y. G. Raydugin, V. E. Naish and E. A. Turov, *Journal of Magnetism and Magnetic Materials*, 1991, **102**, 331-338.

157. M. A. Ghebouli, B. Ghebouli, A. Bouhemadou, M. Fatmi and K. Bouamama, *Journal of Alloys and Compounds*, 2011, **509**, 1440-1447.

158. D. K. Swanson and R. C. Peterson, *Canadian Mineralogist*, 1980, **18**, 153-156.

159. M. Avdeev, E. a. N. Caspi and S. Yakovlev, *Acta Crystallogr. Sect. B-Struct. Commun.*, 2007, **63**, 363-372.

160. P. Karen, A. Kjekshus, Q. Huang, J. W. Lynn, N. Rosov, I. Natali Sora, V. L. Karen, A. D. Mighell and A. Santoro, *Journal of Solid State Chemistry*, 1998, **136**, 21-33.

161. P. R. Slater, A. J. Wright and C. Greaves, *Physica C*, 1991, **183**, 111-120.

162. X. S. Wu, X. H. Xiang, W. M. Chen, Y. Li, W. J. Liu and S. S. Jiang, *Physica C: Superconductivity*, 1998, **301**, 29-38.

163. G. Hautier, C. Fischer, V. Ehrlacher, A. Jain and G. Ceder, *Inorganic Chemistry*, 2011, **50**, 656-663.

164. M. A. C. Wevers, J. C. Schon and M. Jansen, *Journal of Solid State Chemistry*, 1998, **136**, 233-246.

165. C. M. Draznieks, J. M. Newsam, A. M. Gorman, C. M. Freeman and G. Ferey, *Angew. Chem.-Int. Edit.*, 2000, **39**, 2270-2275.

166. A. D. Potoff, Chamberl.Bl and L. Katz, *Journal of Solid State Chemistry*, 1973, **8**, 234-237.

167. R. C. Baetzold, *Physical Review B*, 1988, **38**, 11304-11312.

168. G. Kresse and J. Furthmuller, *Physical review. B, Condensed matter*, 1996, **54**, 11169-11186.

169. G. Kresse and D. Joubert, *Phys Rev B*, 1999, **59**, 1758-1775.

170. S. R. Bahn and K. W. Jacobsen, *Computing in Science & Engineering*, 2002, **4**, 56-66.

171. Y. Bando, Y. Sekikawa, H. Yamamura and Y. Matsui, *Acta Crystallographica Section A*, 1981, **37**, 723-728.

172. J. M. Hudspeth, D. J. Goossens, A. J. Studer, R. L. Withers and L. Norén, *Journal of Physics: Condensed Matter*, 2009, **21**, 124206.

173. M. S. D. Read, M. S. Islam, G. W. Watson, F. King and F. E. Hancock, *Journal of Materials Chemistry*, 2000, **10**, 2298-2305.

174. T. S. Bush, J. D. Gale, C. R. A. Catlow and P. D. Battle, *Journal of Materials Chemistry*, 1994, **4**, 831-837.

175. C. A. J. Fisher and M. S. Islam, *Journal of Materials Chemistry*, 2005, **15**, 3200-3207.